STRONG LIGHT-MATTER INTERACTION IN LITHOGRAPHY-FREE PERFECT ABSORBERS FOR PHOTOCONVERSION, PHOTODETECTION, LIGHT EMISSION, SENSING, AND FILTERING APPLICATIONS

A DISSERTATION SUBMITTED TO

THE GRADUATE SCHOOL OF ENGINEERING AND SCIENCE

OF BILKENT UNIVERSITY

IN PARTIAL FULFILLMENT OF THE REQUIREMENTS FOR

THE DEGREE OF

DOCTOR OF PHILOSOPHY

IN

ELECTRICAL AND ELECTRONICS ENGINEERING

By

Amir Ghobadi

January 2022

STRONG LIGHT-MATTER INTERACTION IN LITHOGRAPHY-FREE PERFECT ABSORBERS FOR PHOTOCONVERSION, PHOTODETECTION, LIGHT EMISSION, SENSING, AND FILTERING APPLICATIONS

By Amir Ghobadi

January 2022

We certify that we have read this dissertation and that in our opinion it is fully adequate, in scope and in quality, as a dissertation for the degree of Doctor of Philosophy.

Ekmel Özbay (Advisor)

Fatih Ömer Ilday

Hamza Kurt

Vakur Behçet Ertürk

Sefer Bora Lişesivdin

Approved for the Graduate School of Engineering and Science:

Ezhan Karaşan

Director of the Graduate School

ABSTRACT

STRONG LIGHT-MATTER INTERACTION IN LITHOGRAPHY-FREE PERFECT ABSORBERS FOR PHOTOCONVERSION, PHOTODETECTION, LIGHT EMISSION, SENSING, AND FILTERING APPLICATIONS

Amir Ghobadi
Ph.D. in Electrical and Electronics Engineering
Advisor: Ekmel Özbay
January 2022

The efficient harvesting of electromagnetic (EM) waves by sub-wavelength nanostructures can result in perfect light absorption in the narrow or broad frequency range. These metamaterial based perfect light absorbers are of particular interest in many applications, including thermal photovoltaics, photovoltaics, emission, sensing, filtering, and photodetection applications. Although advances in nanofabrication have provided the opportunity to observe strong light-matter interaction in various optical nanostructures, the repeatability and upscaling of these nano units have remained a challenge for their use in large-scale applications. Thus, in recent years, the concept of lithography-free metamaterial absorbers (LFMAs) has attracted much attention in different parts of the EM spectrum, owing to their ease of fabrication and high functionality. In this thesis, the unprecedented potential of these LFMAs will be explored. This thesis explores the material and architecture requirements for the realization of a LFMA from ultraviolet (UV) to far-infrared (FIR) wavelength regimes. For this aim, we theoretically investigate the required conditions to realize an ideal perfect absorber. Then, based on the operation wavelength and application, the proper material and design architecture is defined. Later, to experimentally realize these ideal LFMAs, lithography-free large-scale compatible routes are developed to generate nanostructures in centimeter scales. Finally, the application of these LFMAs has been demonstrated in various fields including filtering, sensing, emission, photodetection, and photoelectrochemical water splitting. This thesis study demonstrates that, by the use of proper material and design configuration, it is possible to realize

these LFMAs in every portion of the EM spectrum with a vast variety of potential applications. This, in turn, opens up the opportunity of the practical application of these perfect absorbers in large-scale dimensions. In the last section of the thesis, we discuss the progress, challenges, and outlook of this field to outline its future direction.

Keywords: Metamaterials, perfect absorbers, plasmonics, large-scales, filtering, sensing, photodetection, photoelectrochemical water splitting

ÖZET

FOTO-DÖNÜŞÜM, FOTO-ALGILAYICI, IŞIK EMİSYONU, ALGILAMA VE FİLTRELEME UYGULAMALARI İÇİN LİTOGRAFİSİZ MÜKEMMEL SOĞURUCULARDA GÜÇLÜ IŞIK-MADDE ETKİLEŞİMİ

Amir Ghobadi
Elektrik ve Elektronik Mühendisliği, Doktora
Tez Danışmanı: Ekmel Özbay
Ocak 2022

Alt dalga boyutlarındaki nanoyapılar tarafından elektromanyetik (EM) dalgaların verimli bir şekilde toplaması, dar veya geniş freakans aralığında mükemmel bir ışık soğurumu sağlar. Metamalzemeler olarak bilinen bu mükemmel soğurucular (MS); termal fotovoltaikler, fotovoltaikler, emisyon, sensör, filtreleme ve fotodedektör uygulamaları dahil olmak üzere birçok alanda oldukça ilgi görmektedirler. Nanofabrikasyon alanındaki gelişmeler, farklı optik nanoyapılarda güçlü ışık-madde etkileşimini gözlemleme fırsatını sunmuş olsa da bu nano yapıların ölçeklenebilir bir şekilde tekrarlanabilmesi ve büyütülmesi, geniş ölçekli uygulamalar için zorluk oluşturmuştur. Bu nedenle, son yıllarda, litografi içermeyen metamalzeme soğurucuları (LFMAs) kavramı, üretim kolaylığı ve yüksek işlevselliği nedeniyle EM spektrumunun farklı bölümlerinde oldukça dikkat çekmiştir. Bu tezde, bu LFMA' ların benzeri görülmemiş potansiyeli, santimetre ölçeklerinde nanoyapılar oluşturmak için araştırılmıştır. Bu amaçla, ultraviyole (UV)' den uzak kızılötesi (FIR) dalga boyu rejimlerine kadar bir LFMA' nın gerçekleştirilmesi için malzeme ve mimari gereksinimleri belirlenmiştir. İdeal bir mükemmel soğurucuyu gerçekleştirmek için öncelikle gerekli koşullar teorik olarak araştırılmıştır. Daha sonra çalışma dalga boyuna ve uygulamaya göre uygun malzeme ve tasarım mimarisi tanımlanmıştır. Ardından, bu ideal LMFA' ları deneysel olarak gerçekleştirmek için litografi içermeyen ve büyük ölçeklere uyarlanabilen yöntemler geliştirilmiştir. Son olarak, bu LFMA' ların kullanımı filtreleme, algılama, emisyon, fotodedektör, ve fotoelektrokimyasal suyun ayrıştırılması dahil olmak üzere çeşitli alanlarda gösterilmiştir. Genel olarak bu tez, uygulamaya özgü malzeme ve tasarım

konfigürasyonu sayesinde LFMA' ların EM spektrumunun tamamına yakınını soğurabileceğinin mümkün olduğunu bir çok uygulama alanında göstermektedir. Bu da metamalzemeler/mükemmel soğurucular için çok sayıda spektral özellik gerektiren büyük ölçekli boyuta sahip pratik uygulamaların yolunu açar.

Anahtar kelimeler: Metamalzemeler, mükemmel soğurucular, plazmonik, büyük ölçekli, filtreleme, algılama, foto algılama, fotoelektrokimyasal su ayırma

Dedicated to my beloved wife Gamze and son Poyraz…..

Acknowledgement

Firstly, I would like to express my greatest appreciation to my supervisor, Prof. Ekmel Özbay, for his guidance, support and encouragement throughout my entire PhD studies. His meticulous attentions to details, incisive but constructive criticisms and insightful comments have helped me shape the direction of this thesis to the form presented here. His dedication and enthusiasm for scientific research, his knowledge which is both broad-based and focused, and his stories on the successful integration of ideas across different disciplines, have always been a source of inspiration. Everyone has turning points in their life. Knowing Prof. Özbay and working under his supervision was a major turning point in my life. I am also thankful to him for his strong support in other aspects of life than research. He was much beyond an advisor to me.

I would like to express my gratitude to my mentor Dr. Bayram Butun who helped me a lot during these PhD years. Also, I would like to thank Prof. Fatih Ömer Ilday and Prof. Hamza Kurt for being in my thesis monitoring committee. Also, I would like to thank Prof. Vakur Behçet Ertürk and Prof. Sefer Bora Lişesivdin for being in my thesis committee.

I want to acknowledge support from the Bilkent University, TUBİTAK-BİDEB national PhD Fellowship Program, and NANOTAM for providing financial supports on this work.

During these PhD years, I had the honor to work with many bright colleagues and students. I would like to express my sincere thanks to all my friends and colleagues in our research group; Bahram Khalichi, Sina Abedini Dereshgi, Ataollah Kalantarifard, Ebru Buhara, Deniz Umut Yildirim, Mahmut Can Soydan, Alireza Rahimi Rashed, Zahra Rahimian, Ali Cahit Kosger, Hasan Kocer, Zeinab Eftekhari, Imre Ozbay. I am also thankful to NANOTAM engineers for their technical support in this thesis study.

I would like to express my special thanks to my lovely friends who were supporting me during my whole PhD study; Ehsan, Laleh, Alireza, Tahsin, Mert. I would like to thank my dear friend Ismail whose friendship and encouragement made my PhD study a journey of happiness.

I have no words to express my feelings towards my parents and my brothers Mehdi and Akbar. I hope that this achievement will turn to reality the dream that you had for me all those many years ago when you chose to give me the best

education you could. I hope that I will be worthy of your love. Without your support I would never be in the position that I am now.

Finally, I dedicate this thesis to my wife Gamze Ulusoy for all of her supports. Her love and encouragement light up many lonely moments in my life as a graduate student away from home and have been the source of courage when I was down. Without her, none of this would have been possible.

CONTENTS

CHAPTER 1. GENERAL INTRODUCTION 1

1.1. Preface 1
1.2. Thesis Goals 1
1.2.1. Routes and Materials. 1
1.2.2. Applications 3
1.3. Thesis Outline 7

CHAPTER 2. SCIENTIFIC BACKGROUND 9

2.1. Preface 9
2.2. Introduction 9
2.3. Theoretical Background 11
2.4. LFMAs Architectures 14
2.4.1. Metal Based LFMAs 15
2.4.2. Semiconductor Based LFMAs 22
2.4.3. Other Types of LFMAs 28

CHAPTER 3. CHARACTERIZATION METHODS AND INSTRUMENTATION 38

3.1. Material Characterizations 38
3.2. Optical Characterizations 38
3.3. Photoelectrochemical Measurements 39

CHAPTER 4. LFMAS FOR FILTERING APPLICATION 40

4.1. Preface 40
4.2. Motivation 40
4.3. Lithography-Free Planar Band-Pass Reflective Color Filter Using A Series Connection of Cavities 42
4.4. Bismuth Based Metamaterials: From Narrowband Reflective Color Filter to Extremely Broadband Near Perfect Absorber 55

CHAPTER 5. LFMAS FOR SENSING APPLICATION 64

5.1. Preface 64
5.2. Motivation 64
5.3. Lithography-free disordered metal-insulator-metal nanoantennas for colorimetric sensing… 67
5.4. Lithography-Free Random Bismuth Nanostructures for Full Solar Spectrum Harvesting and Mid-Infrared Sensing 74

CHAPTER 6. LFMAS FOR ENHANCEMENT AND ENGINEERING OF LIGHT EMISSION 83

6.1. Preface 83
6.2. Motivation..... 83
6.3. Strong Quantum Emission from Defective Hexagonal Boron Nitride Monolayer Coupled to Near-Touching Random Plasmonic Nanounits 87
6.4. Disordered and Densely Packed ITO Nanorods as an Excellent Lithography-Free Optical Solar Reflector Metasurface 95

CHAPTER 7. LFMAS FOR PHOTODETECTION APPLICATION 109

7.1. Preface 109
7.2. Motivation..... 109
7.3. Spectrally Selective Ultrathin Photodetectors Using Strong Interference in Nanocavity Design 113
7.4. Spectrally Selective Bismuth Based Photodetectors: Preliminary Results..... 118

CHAPTER 8. LFMAS FOR PHOTOELECTROCHEMICAL WATER SPLITTING APPLICATION 122

8.1. Preface 122
8.2. Motivation..... 122
8.3. Strong Light-matter Interaction in Au Plasmonic Nanoantennas Coupled with Prussian Blue Catalyst on $BiVO_4$ for Photoelectrochemical Water Splitting 125
8.4. Sub-wavelength Densely-packed Disordered Semiconductor Metasurface Units for Photoelectrochemical Hydrogen Generation..... 141

CHAPTER 9. CONCLUSIONS 155

CHAPTER 10. BIBLIOGRAPHY 159

LIST OF FIGURES

Figure 1.1 Schematic illustration of lithography-free fabrication routes. 2

Figure 1.2 Possible absorber materials for the realization of LFMAs in different portions of the optical spectrum. 3

Figure 2.1 The ideal tolerable permittivity values for (a) MIM, and (b) MIMI configurations. These ideal values (that correspond to absorption above 0.9) have been extracted for different D_M and D_I geometries for eight different discrete wavelength values. These tolerable ideal permittivity regions are compared with four different metals including Au, Bi, Cr, and Ti..... 16

Figure 2.2 Narrowband light perfect absorbers by use of Ag in (a) MIM[224] and (b) MIMI[223] configurations to realize a visible light color filter. (c) Automatically acquired different shaped nano islands during the film formation process in an MIM structure to obtain broadband perfect light absorption[4]. (d) Periodic arrangement of 16 pairs Ni/SiO_2 and Ti/SiO_2 (where the metal layer thickness is in the order of 1-2 nm) to realize light perfect absorption up to 2.5 μm[220]. (e) Formation of disordered nanohole patterns via dewetting process to realize ultra-broadband perfect light absorption in an MIMI multilayer architecture[7]. (f) Properly designed multilayer perfect absorber for ultra-broadband impedance matching[232]. (g) Schematic for an Ag-based 1D PC with two PVA layers. The dye is either located below (case A) or above (case B) the Ag film. The support of Tamm plasmons by this structure leads to the directional emission of the emitter[245]. (a) Reprinted with permission from ref. [224]. Copyright 2015 American Chemical Society. (b) Reprinted with permission from ref. [223]. Copyright 2016 Springer Nature. (c) Reprinted with permission from ref. [4]. Copyright 2015 American Chemical Society. (d) Reprinted with permission from ref. [220]. Copyright 2016 The Optical Society. (e) Reprinted with permission from ref. [7]. Copyright 2017 Springer Nature. (f) Reprinted with permission from ref. [232]. Copyright 2016 American Chemical Society. (g) Reprinted with permission from ref. [245]. Copyright 2014 American Chemical Society 20

Figure 2.3 The matching between the permittivity values of four different semiconductors (MoS_2, Ge, perovskite, and Fe_2O_3) and those of ideal material to obtain strong light absorption (absorption above 0.7) for (a) MS, (b) MIS

configurations. For the MIS case, the insulator layer thickness is fixed at 50 nm. 23

Figure 2.4 (a) Absorption of 98% of the incident light energy in a 12 nm thick Ge layer on an Ag substrate at a narrow wavelength range (λ=625 nm) over a wide range of angles[153]. (b) A dual band light perfect absorber operating at the Vis and NIR regimes using a 45 nm thick Si layer coated on AlCu alloy[73]. (c) 71% above band gap light absorption in a less than 50 nm thick Fe_2O_3 using a resonant light trapping scheme for efficient water splitting[77]. (d) A a-Ge:H solar cell with an efficiency as high as 3.6% using an absorbing layer as thin as 13 nm[78]. (e) Spectrally selective photodetector by the realization of perfect light absorption in a narrow frequency range using a single-crystalline germanium nanomembrane coated on a resonant foreign nanocavity.[79] (f) An efficient water splitting photoanode using an ultrathin $BiVO_4$ absorbing layer in an MIS configuration (Au-SnO_2-$BiVO_4$). The incorporation of a trapping scaffold could substantiate the process efficiency[72]. (g) Random coherent perfect absorption in a monolayer of MoS_2 mediated by anderson localization[83]. (a) Reprinted with permission from ref. [153]. Copyright 2014 American Chemical Society. (b) Reprinted with permission from ref. [73]. Copyright 2018 John Wiley and Sons. (c) Reprinted with permission from ref. [77]. Copyright 2012 Springer Nature. (d) Reprinted with permission from ref. [78]. Copyright 2015 John Wiley and Sons. (e) Reprinted with permission from ref. [79]. Copyright 2017 The American Association for the Advancement of Science. (f) Reprinted with permission from ref. [72]. Copyright 2016 American Chemical Society. (g) Reprinted with permission from ref. [83]. Copyright 2017 American Chemical Society 27

Figure 2.5 Schematics of different unpatterned plasmonic/phononic light absorbers. (a) An unpatterned SiO_2/bi-layer GZO/Ag multi-layer structure that acts a broadband perfect absorber within 1.24 μm to 1.49 μm[263]. (b) Multilayer metamaterial composed of alternating layers of AZO and ZnO layers that functions as a nearly perfect NIR absorber[265]. (c) Multilayer metamaterial that is composed of alternating layers of TiN and aluminum scandium nitride (Al,Sc)N. The surface of the planar metamaterial is stochastically covered by spin-coated ITO nanoparticles. This metamaterial acts as a light absorber in the NIR region[267]. (d) A graphene-based 1D PC that can act a narrow-band light absorber in the THz range[109]. (e) First

experimental demonstration of a graphene-dielectric multilayer structure that behaves as a hyperbolic metamaterial in the MIR region[110]. This structure is capable of light absorption in the MIR and FIR ranges. (f) Unpatterned layered structures in dielectric/graphene/metal and graphene/dielectric/metal arrangements for UV light absorption[268]. (g) SiC-based 1D PC that is appropriate for light absorption within 10.3-12.6 μm window in the mid-IR range[118]. (h) hBN-based 1D PC that can act as nearly perfect light absorption and coherent thermal emission within two 6.2-7.3 μm and 12-12.82 μm windows in the MIR range[120]. (i) Multilayer graphene-hBN metamaterial[122]. Due to the plasmon-phonon hybridization, this structure has multifunctional capabilities, specially promising for light absorption in a wide window in the MIR range. (a) Reprinted with permission from ref. [263]. Copyright 2016 IOP Publishing. (b) Reprinted with permission from ref. [265]. Copyright 2018 Springer Nature. (c) Reprinted with permission from ref. [267]. Copyright 2014 The Optical Society. (d) Reprinted with permission from ref. [109]. Copyright 2017 Chinese Laser Press. (e) Reprinted with permission from ref. [110]. Copyright 2016 Springer Nature. (f) Reprinted with permission from ref. [268]. Copyright 2018 American Institute of Physics. (g) Reprinted with permission from ref. [118]. Copyright 2005 American Institute of Physics. (h) Reprinted with permission from ref. [120]. Copyright 2017 The Optical Society. (i) Reprinted with permission from ref. [122]. Copyright 2017 American Chemical Society. 29

Figure 4.1 (a) The schematic representation of the MIMIS design and (b) its reflection upon excitation with a broadband light. (c) Cross sectional SEM image of the fabricated structure showing the successful formation of different layers. The proposed structure has a thick Al layer that reflects light back into the cavity, an Al_2O_3 layer that defines the spectral position of the reflection peak, a thin Al layer, a top Al_2O_3 insulator layer and top semiconductor Ge layer (d) the AFM image of the top Ge coating. The color bar spans from -2.7 nm to 2.7 nm. As we can see from this map, the top Ge layer has quite low roughness. (e) The experimentally extracted permittivity values for Al and Al_2O_3 layers in the range of 380 nm-800 nm. 43

Figure 4.2 (a) The schematic representation of the cavity structure used in TMM model to find the ideal absorber case. The dimensions of the structure have been shown using vertical arrows. The bottom metal layer has a thickness of

DR= 70 nm, the spacer Al_2O_3 layer has a thickness of DI and top ideal material has a thickness of DM. The ideal acceptable/tolerable regimes for real and imaginary portions of the permittivity to obtain an absorption above 0.8 for four different cases of (b) DI= 100 nm, DM= 5 nm, (c) DI= 200 nm, DM= 5 nm, (d) DI= 100 nm, DM= 10 nm, (e) DI= 200 nm, DM= 10 nm and their comparison with the permittivity values of Al and Ge. In these panels, the brown and green highlighted regions depict the tolerable region for real and imaginary parts of permittivity to obtain a reflection R below 0.1. If the permittivity of a material stays inside these regions, the material can absorb above 0.9 of the incident light. The red arrows show the spectral ranges that have this matching. 45

Figure 4.3 The contour plots of the absorption spectra for different (a) DM and (b) DIvalues in the Al-Al_2O_3-Ge MIS cavity. Increase in top insulator layer thickness (DM) makes the absorption strength less and the bandwidth wider. The optimum value is chosen as 3 nm. In this sweep the insulator layer thickness is fixed at 160 nm. By setting the top layer thickness at 3 nm, in the second counter plot, the insulator layer thickness is varied from 140 nm to 220 nm. This plot shows that the spectral position of light perfect absorption gets a red shift as we increase the insulator layer thickness. The absorption contour plot for different (a) DM and (b) DIvalues in the Al-Al_2O_3-Al MIM cavity. Similar to MIS case, we first sweep top metal layer thickness while fixing the insulator layer thickness in 100 nm. Considering both absorption strength and bandwidth the optimum top layer thickness is chosen as 9 nm. As shown in the other contour plot, the perfect absorption peak can be tuned by changing the insulator layer thickness. (e) The reflection spectra of the MIM (black), MIS (red), and MIMIS (blue) samples. As we can see from the schematic, the MIM structure absorbs the longer visible wavelengths while MIS cavity harvest the shorter wavelengths. In the spectral range in between these two absorption peaks both MIM and MIS cavities are inactive and light reflection occurs. Therefore, series connection these two cavities (MIMIS) could lead to a narrow light reflection. 46

Figure 4.4 The reflection spectra of the MIMIS stack for different DITvalues of (a) 10 nm, (b) 20 nm, (c) 30 nm, and (d) 40 nm. In all of these cases, the thickness of bottom insulator is swept from 100 nm to 200 nm with a step size of 20 nm. In these simulations, the bottom metal layer, the middle Al layer and top Ge layer thicknesses have been fixed at optimal values of 70 nm, 9 nm,

and 3 nm. (e) The contour plot showing the absorbed power across the MIMIS cavity as a function of incident light wavelength for the case of $DIT = 30\ nm$ and $DIB = 160\ nm$. As we can see the absorption in lower wavelengths occurs at top Ge layer while longer wavelengths are mainly harvested in the middle Al layer. The linear graph also illustrates the amount of absorbed power in the Al and Ge layers. 48

Figure 4.5 (a) The optical image of the fabricated MIMIS designs operating in different wavelengths in the visible regime. In all samples, the bottom metal layer thickness is 70 nm, the middle Al layer is 9 nm thick, the top insulator layer is 30 nm and top Ge layer is 3 nm. The bottom insulator layer thicknesses are 90 nm, 100 nm, 110 nm, 120 nm, 130 nm, 140 nm, 150 nm, 180 nm, and 195 nm. (b) The reflected green color from the fabricated sample upon excitation with white light. (c) The reflection spectra of different colored samples at normal light incidence. These data have been obtained using a reference sample of thick Al mirror as our 100% reflector. The angular response of (d) purple, (e) blue, (f) green, (g) yellow, (h) orange, and (i) red colored filters under different incidence angles (i.e. 30°, 45°, and 60°) and polarizations (S and P). In all samples, the reflection gets a blue shift as we go toward wider viewing angles. 50

Figure 4.6 (a) The simulated reflection spectra of the ZnO based MIMIS stack for different DITvalues of (a) 10 nm, (b) 20 nm, (c) 30 nm. In all the simulations the bottom metal, middle metal, and Ge top layer thicknesses have been fixed at 70 nm, 9 nm, and 3nm. The bottom insulator layer thickness is swept from 55 nm to 145 nm with a step size of 15 nm. (d) The experimentally extracted permittivity values of ZnO layer. (e) The comparison of the angular reflection response of the fabricated Al_2O_3 and ZnO based MIMIS designs. For this aim, a simple white light source was used, and the images are collected at 0°, 30°, 45°, and 60°. (f) The measured reflection response of RGB color filter samples at normal light incidence. In these designs, the top insulator layer thickness is fixed at 20 nm. The bottom insulator layer is chosen as 85 nm (blue), 100 nm (green), and 145 nm (red) to obtain all three main colors. The angular response of (g) blue, (h) green, (i) red color filters under different incidence angles and polarizations. In all of the samples, going toward wider view angles, the absorption peak experiences a blue shift. 52

Figure 4.7 (a) The schematic representation of MIM and MIMI cavity designs. The (b) real, and (c) imaginary parts of permittivity for different type of metals including Bi. The extracted ideal absorption regions for real and imaginary parts of permittivity in a MIM cavity design for three different configurations of (d) D_M = 5 nm and D_I = 120 nm, (e) D_M = 20 nm and D_I = 120 nm, (f) D_M = 20 nm and D_I = 180 nm. The extracted ideal absorption regions for real and imaginary parts of permittivity in a MIMI cavity design for three different configurations of (g) D_M = 5 nm and D_I = 120 nm, (h) D_M = 20 nm and D_I = 120 nm, (i) D_M = 20 nm and D_I = 180 nm. 57

Figure 4.8 The absorption spectra of the MIM design for different (a) D_M and (b) D_I values. The absorption spectra of the MIMI cavity for different (c) D_M and (d) D_I values. (e) The reflection spectra of the MIM and MIMI designs in visible frequency range for three different D_I values of 110 nm, 170 nm, and 230 nm. (f) The absorption contour plot across the cavity for MIM and MIMI architectures for the case of D_I = 110 nm. 58

Figure 4.9 (a) The cross sectional SEM image of fabricated Ag-LiF-Bi-LiF MIMI cavity. (b) The optical image of fabricated samples with different insulator layer thicknesses of 105 nm, 130 nm, 150 nm, 190 nm, and 220 nm. Each of these thicknesses leads to generation of a specific color in reflection mode. (c) A monolithically designed spatially variant color filter by linear variation of insulator thickness across the sample, by adjusting the geometrical parameters of the deposition system. The normal incident absorption spectra of the MIMI cavity for different D_I values of (d) 105 nm (blue), (e) 130 nm (cyan), (d) 150 nm (green), (d) 190 nm (orange), and (d) 220 nm (red). In all samples, the Bi layer thickness was 25 nm which the optimal value. 60

Figure 4.10 The angular response of (a) blue, (b) cyan, (c) green, (d) orange, and (e) red colored filters under different incidence angles (i.e. 30°, 45°, and 60°) and polarizations (s and p). In all samples, the reflection gets a blue shift as we go toward wider viewing angles. 62

Figure 5.1 (a) Schematic representation of the proposed MIM cavity with its (b) extracted spectral permittivity of Bi (both real and imaginary) in our desired range of 300 nm-1,000 nm. (c) The two-dimensional profile of the absorbed power across the MIM cavity as a function of incident light wavelength. Sweep

and optimization of reflection spectra for different geometries of (d) DM (while the $DI$is fixed at 150 nm) and (e) DI (while the $DM$is fixed at 20 nm)..... 68

Figure 5.2 (a) Schematic illustration of the real LiF NR design and its effective medium model. (b) The MIM ideal absorber used to extract the reflection contour plots. The TMM extracted reflection contour plots for three different $N_{effective}$ of 1.4, 1.3, and 1.2 for incident light wavelengths of (c) 350 nm, and (d) 800 nm..... 69

Figure 5.3 (a) Simplified schematic illustration of the disordered MIM nanoantennas design. The SEM images of the (b) bare LiF NRs and (c) the ones coated with a thin Bi layer. (d) The operation principle of our proposed biosensor. (e) The model design and (f) its cross sectional SEM image. In all of the SEM images, the bar length is 400 nm. The reflection spectra of the bare and PMMA coated MIM nanoantenna samples for three different DIvalues of (g) 140 nm, (h) 170 nm, and (i) 200 nm. At the top of this linear plots, the optical images of bare and PMMA coated samples are depicted..... 72

Figure 5.4 Parameter effect and modeling. a) The perspective view of the unit cell of designed two-layered structure. b) Contour plot of absorbance for the length parameter. c) Sweep and optimization of *L* from 50 to 400 nm while *P* = 200 nm and *R* = 80 nm. d) Contour plot of absorbance for radius parameter. e) Sweep and optimization of *R* from 20 to 90 nm while *P* = 200 nm and *L* = 300 nm. f) Absorbance performance comparison of Bi with Au, Cr, Ni, and W in FDTD simulation. g) Real and h) imaginary parts of the permittivity of the given materials. i) Generalized case of designed MM structure with a thick Al layer as a common reflector and an effective medium of metal nanorod–air composition. Contour plot of reflection of the structure in panel (i) and effective permittivity of the upper layer as a dot at the wavelengths of j) λ = 2 μm, k) λ = 3 μm, l) λ = 4 μm. In panels (j)–(l), f_1 was chosen as $f_1 = (\pi R^2)/P^2 = 0.503$ for *R* = 80 nm and *P* = 200 nm..... 75

Figure 5.5 Field Profiles. H-field profiles at a) 0.7 μm and b) 2.2 μm. E-field profiles at c) 0.7 μm and d) 2.2 μm. Absorbed power profiles at e) 0.7 μm and f) 2.2 μm..... 77

Figure 5.6 Effect of randomness on absorbance performance and EMW confinement mechanism. a) Absorbance spectra of 16 nanorod unit cell when

nanorods have no orientation and different random scenarios. H-field profile of the unit cell at the middle height of the nanorods at wavelengths of b) 0.5 μm, c) 1 μm, d) 2 μm, and e) 3 μm. f) Simulated absorbance spectrum for the range of 3.2–5 μm. g) Resonance wavelengths for different surrounding medium refractive index values and linear fit in order to find the sensitivity of the sensor. 80

Figure 6.1 (a) Schematic of modeled gold nanodiscs on quartz substrate. inset, the schematic illustration of the unit cell. Sweep and optimization of *R* for two heights of (b) H= 20 nm and (c) H= 50 nm while P = 100 nm. (d) Schematic of the unit cell with illustration of electric field profile view plane. $E2$ profiles of (e) R=25 nm, (f) R= 35 nm and (g) R=45 nm at their resonances. (h) The real device and its model for numerical simulations. (i) The Purcell factor of a DE placed at three different disc heights plasmonic design..... 90

Figure 6.2 (a) Schematic illustration of oblique-angle deposition and the formation of nanorods. (b), SEM images of 20 nm and 100 nm NRs. (c), AFM image of 20 nm NRs showing the surface roughness measurement. (d), reflectance, transmittance and absorbance spectra of NRs with heights H= 20 nm, 50 nm and 100 nm by ellipsometry. (e) The binary image of the 20 nm NRs converted from the top-view SEM image. (f), The simulated maximum field enhancement at different wavelengths. The contour plots of electric field amplitude profile of the 20 nm NRs at wavelengths of (g), 550 nm, (h), 600 nm, (i), 650 nm, and (j), 700 nm. 92

Figure 6.3 (a), Raman scattering spectrum of monolayer hBN and corresponding Lorentzian fit to the experimental data.inset, optical image of transferred monolayer hBN on the silicon dioxide substrate. (b), Scanning confocal map of a mmonolayer hBN sample illustrating bright illuminate defect centers. (c), Room-temperature PL spectra of defect centre in pristine monolayer hBN and coupled hBN with Au NRs. Inset shows the data in logarithmic scale. (d) The decay lifetime of different samples..... 94

Figure 6.4 Schematics of Devices 1 and 2 and the parameter sweeps on the geometrical dimensions of Device 2. (a) Device 1 to achieve broadband absorption in thermal-infrared and broadband reflection in solar spectrum. (b) Device 2 to test the effect of geometrical dimensions of a nanodisc on absorption spectrum, thermal emissivity, and solar absorptivity. (c) Top-view of

Device 2, showing the geometrical parameters in detail. Absorption spectrum of Device 2 under varying (d) nanodisc radius, r, (f) thickness of nanodiscs, h, and (h) thickness of the SiO_2 spacer, t_{SiO2} . OSR parameters Device 2 when (e) r, (g) h, and (i) t_{SiO2} are changed. 97

Figure 6.5 Fabrication of the metasurface OSR and the formation of ITO nanoforests. (a) Placement of samples in the sputtering chamber before coating of ITO. (b) Schematic illustration of line-of-sight coating in a sputtering system and the formation of tilted nanowires. (c) Low and (d) high resolution top-view SEM micrographs of one of the fabricated devices. (e) Cross-sectional SEM image of a sample metasurface OSR. 99

Figure 6.6 Optical characterization of the fabricated devices with disordered ITO nanorods, comparisons to numerical simulations of Device 2 and experimental results of a planar design, and physical explanations on ϵIR enhancement in the proposed device. (a) Experimental absorption results for Device 1 with h = 50 nm and tSiO2 = 2 μm compared to the numerical simulations of Device 2 with the same h and tSiO2 . (b) Experimental absorption result for Device 1 with h = 30 nm and tSiO2 = 2 μm compared to the numerical simulation Device 2 with the same h and tSiO2 . (c) Experimental absorption result for a planar device with h = 50 nm and tSiO2 = 2 μm compared to numerical simulations for the same device. (d) Comparison of the absorption spectra of the planar device and Device 1 with h = 50 nm and tSiO2 = 2 μm. (e) Contribution of each layer to the absorption in thermal-infrared. (f) Localization and enhancement of electric-field between nanodiscs of P = 300 nm, r = 142.5 nm. (g) |E| 2 /|E0| 2 value recorded at a planar ITO layer. (h) Near-field enhancement, |E| 2 /|E0| 2 values as a function of gap size between nanodiscs. In (f), (g), and (h), the |E| 2 /|E0| 2 values are recorded at 15 μm and at the midgap position. 102

Figure 6.7 Large-scale fabrication and optical characterization of the proposed device. (a) Positioning of the wafer in the sample holder as seen from the back view. (b) Measurement areas in the fabricated wafers. Experimental absorption result for Device 1 with h = 50 nm and (c) tSiO2 = 2 μm and (d) tSiO2 = 1.55 μm, when fabricated on a wafer. Absorption spectrum under obliquely incident radiation at an incidence angle of (e) 30° and (g) 45°. Device 1, as seen with the (g) naked eye and by (h) thermal camera. (i) Thermal microscope image of Device 1. The ellipsometry measurements are taken from area 5. 107

Figure 7.1 (a) The schematic representation of MIS cavity design and its geometries. (b) The reflection contour plots as a function of real and imaginary parts of permittivity in different wavelength values for (b) DS=3 nm, (c) DS=10 nm. The insulator is fixed at 60 nm. The extracted ideal regions and their matching with the permittivity data of Si and Ge for three different DIvalues of (d) 60 nm, (e) 120 nm, (f) 180 nm. 113

Figure 7.2 The absorbed power within Si slab for different DS values of (a) 1 nm, (b) 4 nm, and (c) 10 nm. (d) Average light absorption in UV and visible regimes for different design geometries. (e) The proposed MSM photodetector made on MIS cavity, (f) simulated photocurrent values of the design as a function of light wavelength, (g) light absorption across the cavity in two wavelengths of λ=370 nm, and 500 nm, and (h) representation of device operation under UV and visible light irradiation. 115

Figure 7.3 (a) Cross-sectional and top SEM images of the photodetector, (b) I-V characteristic, (c) photoresponsivity, and (d) I-t response of the photodetector for different dark and light conditions..... 117

Figure 7.4 (A) P-block elements, and (B) the permittivity values of the targeted elements and compounds. (C) The TA decay profiles for different probe signals for Bi, and Sb thin films. (D) The Ab Initio quantum calculations showing the possible electron excitation routes in four different materials of Bi, Sb, Bi2Te3, Sb2Te3 120

Figure 7.5 (A) The absorption response of Bi nanorod metaabsorber (the inset shows the optical and the scanning electron microscopy (SEM) image of fabricated sample), (B) the responsivity values for the ultrabroadband Bi PD (inset: device configuration). (C) Anodic and cathodic chopped photocurrent-voltage characteristic of the sample (inset: setup). (D) MIM based color PD for different insulator layer thicknesses of D_I. 120

Figure 8.1 (a) Schematic representation of fabrication route for preparing gold capped $BiVO_4$ photoanode by using oblique angle physical vapor deposition. The position of electrodes (with an 80-85° angle) resulted in Au nanoisland formation, yielding Au-$BiVO_4$ plasmonic photoanode. A top-view of the SEM images of the (b) bare $BiVO_4$ and (c) Au-$BiVO_4$ photoanodes, scale bar: 1 μm and the inset shows the high magnified image of the SEM, scale bar: 20 nm.

(d) Cross sectional SEM images of the Au-$BiVO_4$ photoanode, illustrating the morphology of the nanostructure photoanode. (e) Cross sectional FIB image of the Au-$BiVO_4$ sample, showing the formation of multi sized/shape Au nano capping islands. 126

Figure 8.2 (a) RAMAN spectrum and (b) XRD patterns with diffraction patterns of pristine $BiVO_4$ film conforming to its monoclinic phase, "$*$" indicates crystal planes of FTO substrate. High resolution XPS spectra of (c) Bi4f and (d) V2p spectra for the as-prepared $BiVO_4$ and Au-$BiVO_4$ electrodes. (e) The O1s spectrum of pristine $BiVO_4$ film which is deconvoluted into three different peaks indicating the presence of three types of oxygen: lattice oxygen (O_L), oxygen vacancy (O_V), and chemisorbed oxygen (O_C). 128

Figure 8.3 XPS valence band spectra of (a) $BiVO_4$ and (b) Au-$BiVO_4$. Green lines show the linear extrapolation of the curves for deriving the valance band edge position of $BiVO_4$ samples, i. e. E_f-E_{VBM}. The grey lines also show the background signal. (c) Absorption profiles for both $BiVO_4$ and Au-$BiVO_4$ photoanodes at the wavelength range of 300–550 nm. The inset shows the Tauc Plot used for the estimation of the optical bandgap (2.5 eV) of the $BiVO_4$. (d) Schematic energy band diagram of Au-$BiVO_4$ showing the band alignments and the involved water oxidation electron transfer processes..... 131

Figure 8.4 (a) Illustrative representations of a 3D schematic of the PEC-WS system consisting of Au-$BiVO_4$ coated FTO electrode (1 cm^2), as a working electrode. (b) LSV measurements, *j-V* curves, of the working electrodes under light illumination (Solid symbols), under dark (empty symbols) with a white-light source. Anodic scan rate: 50 mVs^{-1}, Electrolyte: N_2-saturated 0.1 M PBS pH 7, Light intensity: 100 mW cm^{-2}. (c) Chronoamperogram for 1 hours of illumination at 1.23 V (vs. RHE) bias. (d) OCVD measurement as a function of time for a duration of 300 s. (e) EIS Nyquist plots at a bias of 1.23 V (vs. RHE) in the frequency range 100 kHz to 0.1 Hz under solar irradiation. The inset shows the circuit model used for fitting. (f) IPCE spectra of the PECs with a 1.23 V (vs. RHE) external bias. The wavelength was scanned from 300 to 600 nm with a step size of 10 nm. 132

Figure 8.5 (a) The simulation unit cell. The normalized absorption as a function of (b) $BiVO_4$ length (D), and (c) Au capping radius (R). (d) The E-field distribution across the design at 450 nm where $BiVO_4$ is optically absorptive,

and 600 nm, in which $BiVO_4$ is transparent to incoming photons. (e) The absorbed power profile across the view line as a function of incoming wavelength..... 135

Figure 8.6 High resolution XPS spectra of (a) O2p and (b) VB spectra for ($BiVO_4$/[CoFe]), (c) VB spectra for Au-$BiVO_4$/[CoFe]. (d) Illustrative representations of the Prussian blue modified Au-$BiVO_4$ coated FTO electrode (1 cm^2), as a working electrode for photoelectrochemical water oxidation process. (e) LSV measurements under light illumination, *j-V* curves, of the bare $BiVO_4$ and 2-12 times CoFe-PBA modified $BiVO_4$ electrodes. (f) LSV curves for $BiVO_4$/[CoFe] and Au-$BiVO_4$/[CoFe] under light illumination (Solid symbols), and dark (empty symbols) with a white-light source. Anodic scan rate: 50 mV s^{-1}, Electrolyte: N_2-saturated 0.1 M PBS pH 7, Light intensity: 100 mW cm^{-2}. (g) EIS Nyquist plots at a bias of 0.8 V (vs. RHE) in the frequency range 100 kHz to 0.1 Hz under solar irradiation for both electrodes. The inset shows the circuit model. (h) OCVD temporal response throughout a 300 s duration. (i) IPCE spectra of the photoanodes with a 1.23 V (vs. RHE) external bias. The wavelength was scanned from 300 to 600 nm with a step size of 10 nm.... 139

Figure 8.7 (A) The schematic representation of the setup used for the oblique angle deposition of Cr nanounits. (B) The formation of nanoislands, (C) their transformation into the random 3D nanorods due to atomic shadowing effect, and (D) annealing induced CrO_X semiconductor nanostructures. The SEM images of the resultant (E) Cr and (F) CrO_X nanostructures..... 142

Figure 8.8 (A) The proposed periodic model for numerical simulations. (B) The dependence of absorption spectra on the periodicity of the metasurface (the background depicts the normalized solar spectrum). 2D absorption contour plots showing the effect of (C) gap, and (D) height of nanorods. (E) The E-field distributions and (F) absorption power density profiles across the metasurface design at three resonant wavelengths of 300 nm, 614 nm, and 633 nm..... 144

Figure 8.9 (A) The extracted refractive index data for planar Cr, CrO_X-30, and CrO_X-90 thin films. While 90 min. annealing fully transforms Cr into its oxide counterpart, the 30 min. annealing leads to a mixed state. This has been shown in the inset. (B) Atomic percentage of C, Cr, and O elements in the CrO_X-30, and CrO_X-90 thin films. Total etching time of 1000 seconds. (C) The XPS Cr3p profiles for CrO_X-30, and CrO_X-90 planar thin films. (D) Numerical simulation

absorption results of the optimal periodic design, using two different refractive index values of CrO_X-30, and CrO_X-90. (E) The diffuse reflectance values of the fabricated Cr, CrO_X-30, and CrO_X-90 nanorod designs. The inset shows the optical image of the samples..... 147

Figure 8.10 (A) The setup configuration of pump-probe TA spectroscopy. (B) The TA spectra of the CrO_X-30 film in different delay times. (C) The temporal decay profiles of the TA signal at four different probe wavelengths of 450 nm, 500 nm, 600 nm, and 700 nm. 149

Figure 8.11 (A) Schematic representation of the three-electrode setup used for PEC experiments. (B) The chopped LSV profiles of the planar CrO_X, and nanorod based CrO_X-30, and CrO_X-90 photocathodes. (C) Nyquist plots obtained by EIS characterizations for all three samples at a bias of -0.1V_{RHE} and a frequency range of 100 kHz-0.1 Hz under AM1.5 solar irradiation. (D) Schematic representation of field induced charge separation in the near surface region in a nanorod design. (E) The IPCE values of all three samples at the bias voltage of -0.1V_{RHE}. (F) The long-term CA expected response, considering the stronger absorption response of the CrO_X-..... 152

Figure 8.12 (A) The fabrication route of CrOx-NiOx heterostructure. (B) High resolution TEM elemental mapping of an individual CrOx-NiOx nanounit. These mapping data shows the formation of a core-crown configuration in this heterodesign. (C) The band alignment between CrOx and NiOx layers extracted using XPS characterizations, as explained by detail in SI. (D) The chopped LSV profile, (E)..... 153

Chapter 1. General Introduction

1.1. Preface

This chapter of the thesis is based on the publication ”*Lithography-free metamaterial absorbers: opinion*”, A. Ghobadi, T. G. Ulusoy Ghobadi, E. Ozbay, **Optical Materials Express.** 2022, 12, 524-532. Adapted (or “Reproduced in part”) with permission from OPTICA publishing group.

1.2. Thesis Goals

Although advancement in nanofabrication provides the opportunity to realize nanoscale geometries with high resolutions, the scalability and repeatability issues limit their large-scale applications. Lithography-free metamaterial absorbers (LFMAs) are a potential route for the upscaling of these designs. With restricted freedom in their synthesis, the importance of the proper material choice should be emphasized. In this thesis, we have developed various routes to realize nanostructured perfect absorbers in centimeter scales. Later, these perfect absorbers have been adopted in various applications including photoconversion, photodetection, light emission, sensing, and filtering. In this section, to highlight the goals of this thesis, we provide a comprehensive overview on the recently developed LFMAs, from both design and material perspectives, while considering their most promising applications.

1.2.1. Routes and Materials.

Light confinement and harvesting in dimensions much smaller than the wavelength have been the subject of many studies in the field of metamaterial-based perfect absorbers. Metals, at sub-wavelength dimensions, can undergo strong light-matter interaction in a broad spectral range[1]. This happens through the collective oscillation of free conduction electrons, so-called localized surface plasmon resonance (LSPR), or inter-band transitions.

However, the realization of plasmonic nano units requires complex and large-scale incompatible routes such as lithography-based techniques. Therefore, recently, the concept of lithography-free metamaterial absorbers (LFMAs) has attracted intensive attention[2], [3]. The most common type of these scalable LFMAs is planar multilayer designs, with the dominant absorption mechanism of Fabry-Perot (FP) resonance modes[2]. Metal-insulator-metal (MIM) and MIM-insulator (MIMI) and periodic $(MI)_N$ cavity configurations are the most common cavity absorbers. One-dimensional photonic crystal (1D-PC) based configurations are also utilized to achieve light absorption in ultrathin absorbing layers. Nanostructured LFMAs could outweigh these planar designs, especially in applications where both strong absorption and high active surface area are desired. Recently, several innovative fabrication routes have been developed to meet this requirement. Deposition induced structuring[4], [5], dewetting induced nanounit formation[6]–[8], oblique angle deposition of three-dimensional (3D) structures[9]–[14], direct laser writing[15], template-assisted etching[16], [17], and deposition[18], [19] are examples of these methods, as shown in Figure 1.1. Aside from the importance of the route, the choice of the right material is another prominent factor in LFMA design. Figure 1.2 outlines

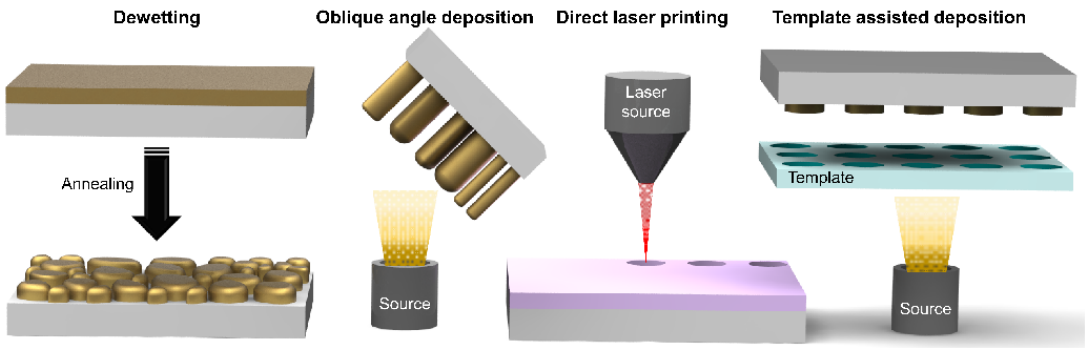


Figure 1.1 Schematic illustration of lithography-free fabrication routes.

The most suitable materials for the building of LFMAs. In the ultraviolet (UV) and visible, a vast variety of semiconductors and metals can be used to achieve this goal. To extend this functionality toward longer ranges such as near-infrared (NIR) and short-wavelength infrared (SWIR), lossy metals such as Ti, Cr, W, and Bi could be utilized in a proper configuration[2]. Moreover, doped metal oxides such as Al-doped ZnO (AZO)[20], Ga-doped ZnO (GZO)[21], In-doped SnO_2 (ITO)[22], In-doped CdO (ICO)[23], [24], and Ce-doped In_2O_3

(CIO)[25] that show epsilon-near-zero (ENZ) characteristics in the SWIR range could be used in LFMAs. Metal nitrides such as TiN, ZrN, HfN, and InN could also reveal a plasmonic response in the infrared (IR) range[26]–[29]. Moreover, these alternative plasmonic materials show tunable plasma frequency in the mid-wavelength infrared (MWIR) range. In longer wavelengths (i.e. MWIR, long-wavelength infrared (LWIR), and far-infrared (FIR)), LFMAs can be realized through the excitation of i) optical phonon in metal oxides[30], ii) plasmonics in highly doped semiconductors[31], iii) plasmonic resonances in two dimensional (2D) materials such as graphene and black phosphorus (BP)[32], [33], and iv) phonon polariton modes in polar materials[34].

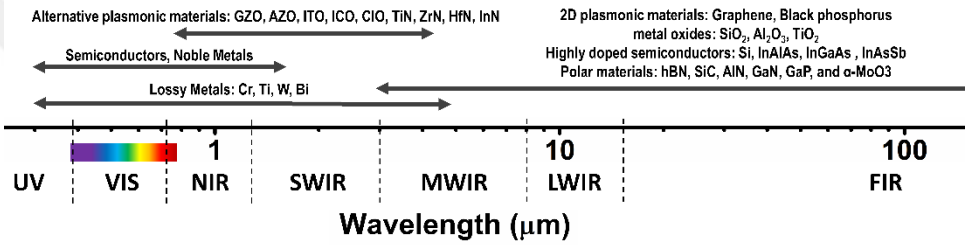


Figure 1.2 Possible absorber materials for the realization of LFMAs in different portions of the optical spectrum.

1.2.2. Applications

LFMAs are divided into two material categories: i) metallic and ii) non-metallic. Their applications are sorted based on their operational wavelength range; i) sun blackbody radiation spectrum (sun-BBRS) or so-called solar spectrum covering UV-visible-NIR-SWIR ranges, and ii) earth blackbody radiation spectrum (earth-BBRS) covering SWIR-MWIR-LWIR-FIR.

i. ***Sun-BBRS;***

Metallic LFMAs. Planar metallic LFMAs can reveal spectrally selective narrowband or broadband light absorption. The narrowband planar LFMAs are commonly utilized in color filtering applications[35]. While simple MIM cavity design can generate additive red-green-blue (RGB) colors in transmissive mode (with amplitudes much below unity), tandem shape cavity architectures can generate high-efficiency RGB colors in reflection mode[36]–[40]. These planar LFMAs can also show dynamically tunable color generation, through the

change in spacer layer index or thickness. For index modulation, phase change materials (PCMs) such as GST[41], [42], VO_2[43], Sb_2S_3[44], or even Sb[45] can be used as the spacer to generate thermally tunable colors. For nanoscale thickness tuning of the spacer, swelling/deswelling of humidity-sensitive polymers and hydrogels is employed to fabricate dynamic MIM color filters[46]–[48]. Besides filtering, the narrowband LFMAs have potential application in colorimetric sensing platforms such as bio-, and gas-sensing, where the external stimuli shifts the resonance peak of the LFMA[12], [49], [50]. However, in sensing, a high surface area is desired to maximize the interaction of light with the surrounding environment. Thus, nanostructures such as dewetted or oblique angle deposited plasmonic units offer higher sensitivities[51], [52].

On the other side, the broadband LFMAs can harvest a large portion of the solar spectrum, which is desired for photoconversion applications. In metals, photoconversion functionality can be acquired using the excitation and extraction of energetic hot electrons. However, due to the femtosecond relaxation of hot electrons with a dominant mechanism, called Landau damping, only energetic carriers can traverse the Schottky barrier[53]. This photoemission efficiency is even less in planar and large particle sizes[54] where absorption is due to non-resonant inter-band transitions rather than the LSPRs. Despite intensive efforts to find alternative high performance and low-cost plasmonic elements such as Al[55]–[57], conductive oxides[27], [58], [59], transition metal nitrides/carbides (such as TiN)[60], [61], and doped semiconductors[62]–[64], the efficiency of hot electron designs is still low. The same obstacles are present in the hot electron based photodetection and photoelectrochemical water splitting (PEC-WS) applications[65]. The alternative route is to use these metallic LFMAs in the application platforms where metals are not the photoactive layer such as thermal photovoltaic (TPV) and steam generation. In TPV, a broadband LFMA absorbs photons, transforms them into heat, and reradiates it using a selective emitter with a spectral emission peak overlapping with the PV bandgap. Based on theoretical calculations, a solar TPV, with an ideal design of absorber and emitter, can achieve efficiencies exceeding the Shockley-Queisser limit[66]. The narrowband emitter can also be realized with a multilayer dielectric-based 1D-PC design, making the overall system a lithography-free architecture[67]. Solar-driven steam generation is another promising area for broadband LFMAs.

Advancements in this area have proven efficiencies as high as 90% at 4-sun intensity (4 kW m^{-2})[68]. Different from TPV, in this application, a high area is a must to maximize the heat transfer between the LFMA and water.

Non-metallic LFMAs. Similar to metallic ones, the dominant application of non-metallic LFMAs in sun-BBRS is photoconversion and semiconductors are its main building blocks[69]. In most semiconductors, the carrier diffusion length is much shorter than the light penetration depth. Therefore, the bulk recombination of carriers limits their efficiency. However, sub-wavelength semiconductor-based LFMAs can offer optically thick, electrically thin platforms suitable for photoconversion systems, such as PV, photodetection, and PEC-WS [67]. Planar metal-semiconductor (MS) and metal-dielectric-semiconductor (MDS) cavity designs are proven to achieve near-unity absorption in deep sub-wavelength semiconductor thicknesses[70]–[80]. In 2D monolayer semiconductors, dielectric-based 1D-PC and Bragg reflector designs are the right strategy to confine the entire power in the position of the 2D layer and efficiently harvest it[81]–[83]. Besides the optical response, the electrical characteristics of these semiconductors are also a prominent factor that affects the performance outcome. Ideally, a crystalline semiconductor film should be grown in ultrathin dimensions, but it is a challenging task. The transfer of external crystalline thin films[79], [84] and the CVD growth of 2D semiconductors can provide high-quality thin films. In PEC-WS, two more factors should be adopted in the design of these LFMAs; i) surface area and ii) long-term structural integrity (or stability) of the photoelectrode[69]. While planar LFMAs have already been used as photoanode and photocathode components in PEC-WS[84], [85], nanostructured designs with a higher water-semiconductor interface can improve the activity. To have a high surface area with good crystallinity, template-assisted etching of crystalline semiconductor host seems a promising approach[16]. A thin protection layer with proper band alignment could be utilized to solve the stability issue.

ii. Earth-BBRS;

***Metallic LFMAs*.** In most metals, the LSPR excitation and interband transition happen in the UV-visible range. However, lossy metals in $(MI)_N$ and metal-1D-PC configurations, can reveal resonant light absorption in the SWIR-LWIR range[37], [86]–[89]. These planar absorbers can act as selective/broadband

thermal emitters with possible applications in radiative cooling and thermal camouflage[90]–[98]. Integration of these LFMAs with PCMs offers dynamically tunable IR emitters/absorbers[99]–[101]. Such a design could even enable passive radiative thermostat functionality by adjusting the visible and IR absorption/emission[102].

Non-metallic LFMAs. Highly doped semiconductors, doped metal oxides, metal nitrides/carbides, and 2D materials such as graphene, and BP are alternative plasmonic materials in MWIR, LWIR, and FIR range[34]. Heavily doped semiconductors such as Ge, Si, III-V compounds are appealing alternatives to metals for IR plasmonics[31]. Their plasma frequency can be tuned chemically, optically, or electrically across a broad range. Semiconductor-based hyperbolic metamaterials, made of doped-undoped pairs, can be developed to realize narrowband directional IR emission[103], [104] and ultrafast and low power all-optical switching[105]. Doped metal oxides have the advantage of visible transparency, making them compatible materials for spacecraft cooling and thermal camouflage[11], [106]. 2D materials with exceptional electrical and optical properties are another attractive category in IR plasmonics. Graphene, as the most famous member of this group, can support guided plasmonic modes in the IR range, where the spectral position of these modes can be effectively tuned by its chemical potential (μ) [33], [107]–[109]. Graphene monolayer-based LFMAs have been realized using the excitation of Tamm plasmons in 1D-PC structures[110]–[112]. Moreover, the use of distributed Bragg reflector (DBR) in a cavity design, to couple light into the graphene monolayer, has been demonstrated[109]. A similar design strategy can be utilized to achieve LFMA using a monolayer of BP[113]. Due to their high carrier mobility, LFMAs made of these 2D materials coupled with narrow bandgap semiconductors have promising applications in IR photodetector designs [114], [115]. Different from graphene, the BP monolayer shows strong in-plane anisotropy, used to design polarization selective absorbers[116]. Moreover, different from common narrow bandgap semiconductors, BP has a tunable bandgap from 2 eV (in monolayer) to 0.3 eV (in bulk). Based on recent work[117], a vertical electric field can tune the bandgap of BP and provide a wide tunability (from 3.7 to 7.7 μm) in its photoluminescence (and consequently absorption peak) spectral response. The last category of non-metallic materials is polar dielectrics. These materials

are used to make LFMAs in a wide range spanning from MWIR to FIR[2]. The IR optical response of these materials (such as hBN, SiC, AlN, GaN, GaP, and α-MoO_3) are dominated by highly reflective reststrahlen (RS) bands that are located between the longitudinal and transverse optical phonons. Within these RS bands, light can couple with optical phonons to support surface phonon-polariton (SPhPs) modes. LFMAs made of these polar materials are commonly made in 1D-PC and DBR cavity configurations and have been mainly used to realize coherent monochromatic, and directional thermal emitters[118]–[120]. The hybrid use of these polar materials with PCMs and graphene can provide tunable IR absorbers to be used in radiative cooling, adaptive thermal camouflage, and modulators[121], [122]. Moreover, some of these polar materials including BP, hBN, and α-MoO_3 have strong in-plane and out-of-plane anisotropy. This could be utilized to realize lithography-free polarization converters in the IR region[123].

1.3. Thesis Outline

This thesis work is organized as follows:

Chapter 1 summerizes this thesis goals and motivation. It provides a general overview on LFMAs and their possible applications.

Chapter 2 provides a comprehensive review on the scientific background of the proposed thesis work, with emphasize on design architecture and application.

Chapter 3 gives information about the characterization methods employed in this thesis, including structural, steady-state and transient optical, and photoelectrochemical characterization techniques.

Chapter 4 shows the application of these LFMAs in filtering.

Chapter 5 demonstrates the effictiveness of these LFMAs in sensing application.

Chapter 6 reveals the effectiveness of these large-scale compatible designs in light emission process. This chapter is devided into two parts; i) In the first part, the coupling of these plasmonic units into light emitting quantum emitters is

discussed, ii) in the second section, mid-infrared responsive LFMAs are utilized to engineer the blackbody radiation from a hot object. These designs are utilized in radiative cooling and thermal camouflage applications.

Chapter 7 puts one step forward and brings these optical designs into optoelectronic applications. These chapter summarizes our finding on application of these LFMAs in photodetection.

Chapter 8 demosntartes efficient, cost-effective, and stable operation of these LFMAs in photoconversion and photoelectrochemical water splitting applications.

Chapter 9 concludes this thesis by highlighting its achievments and highlighting the possible future directions.

Chapter 2. Scientific Background

2.1. Preface

This chapter of the thesis is based on the publication "*Strong Light–Matter Interaction in Lithography-Free Planar Metamaterial Perfect Absorbers*", A. Ghobadi, H. Hajian, B. Butun, E. Ozbay, **ACS Photonics.** 2018, 5, 4203 – 4221. Adapted (or "Reproduced in part") with permission from American Chemical Society.

2.2. Introduction

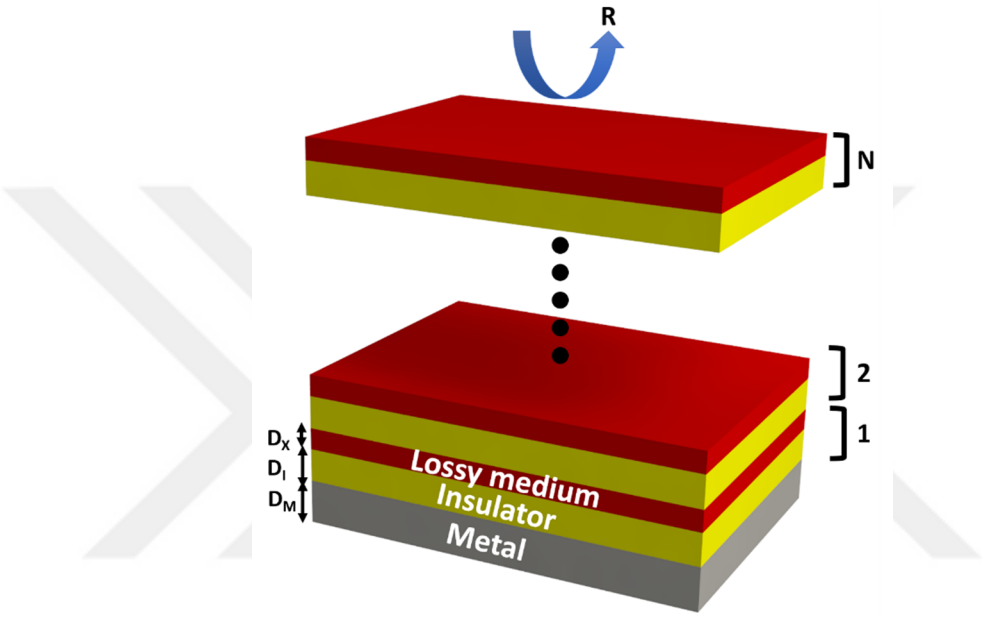
Metamaterials refer to a class of synthetic materials comprising designed inclusions that offer exotic properties. Negative refraction[124]–[126], artificial magnetism[127], [128], asymmetric transmission[129], [130], lasing[131], [132], cloak of invisibility[133]–[135], and sub-wavelength light absorption[136] are examples of these attributes. The concept of light confinement and harvesting by sub-wavelength geometries has been one of the most intensively studied areas in recent years. Efficient harvesting of this confined field utilizing an absorbing layer such as metal, or semiconductor material could lead to the realization of perfect absorption of light. These light perfect absorbers can be employed in a vast variety of applications. Metal based perfect absorbers can afford their response in narrow or broad spectral ranges. The narrowband metal perfect absorbers are of particular interest in sensing, imaging, and color filter applications[100], [137]–[143]. While their broadband counterparts have potential applications in thermal photovoltaics[66], [144], [145], radiative cooling[146]–[148], hot electron based photodetectors[149], [150], photochemistry[65], and efficient solar vapor/steam generation[68], [151], [152]. Similar to metals, ultrathin light perfect absorbers can be also realized using semiconductor based configurations where a strong light-matter interaction can harvest most of the incident light photons and go beyond the Yablonovitch limit in an ultrathin thickness[153]. The generation of high density photo carriers in dimensions smaller than the semiconductor diffusion length

can guarantee their efficient collection. Therefore, these semiconductor based metamaterials are promising choices for future performance enhanced ultrathin optoelectronics. In recent years, resonant light trapping schemes were employed in different applications including ultrathin photovoltaic solar cells, spectrally selective photodetectors, and other optoelectronic applications[149], [154]–[164]. These perfect absorbers have also been realized in other types of materials, such as polar and two dimensional (2D) materials; i.e. graphene, transition metal dichalcogenides (TMDs), and black phosphorus that will be discussed in the following. Although there are enormous efforts being made in the performance enhancement of these nanostructured perfect absorbers, the fabrication complexity of these nanostructures hinders their further upscaling.

In recent years, extensive attention has been paid to the design of lithography-free multilayer perfect absorbers of light. Strong light-matter interaction in these properly designed planar structures can provide perfect absorption in narrow or broad wavelength ranges while keeping the overall process large scale compatible. The goal of this thesis is to provide a comprehensive overview of these planar multilayer designs in three different classes of materials; metals, semiconductors, and other type of materials. It is shown that by choosing proper material and design architecture, it is possible to obtain strong light absorption in different ranges of electromagnetic (EM) spectrum. The lithography-free nature of these designed multilayer structures provides great flexibility and high-throughput manufacturing convenience and opens a new opportunity for low-cost, high performance, and robust optoelectronic devices. It should be mentioned that there are some omissions for the topics and designs discussed here. For instance, novel synthesis methods such as chemical or self-assembly techniques can be utilized to obtain lithography-free perfect absorbers. However, this thesis mainly focuses on sub-wavelength planar designs that can be fabricated with common cleanroom equipment with high fabrication throughput and repeatability. Finally, in the last section, we discuss the progress, challenges, and the outlook of this field to outline its future direction.

2.3. Theoretical Background

In order to realize nearly perfect absorption of the light, reflectance should be suppressed by matching the effective impedance of the metamaterial to that of the incident medium. Simultaneously, transmittance is eliminated by



Scheme. 1. Schematic representation of the studied $M(IX)^N$ design to find the ideal condition for light perfect absorption

Introducing another metallic plate acting as a mirror for metamaterial absorbers. In this section, an alternative analytical-numerical approach based on transfer matrix method (TMM) will be provided to predict the most appropriate permittivity of the lossy layers, labeled X, in a metamaterial absorber that comprises N two-layer elementary IX unit cells, i.e. $M(IX)^N$. The studied $M(IX)^N$ design configuration is schematically shown in Scheme. 1. In this definition, M, I, and X stand for metal mirror, insulator, and lossy medium. The lossy layer could be metal, semiconductor, or any other types of absorbing materials. We can investigate the ideal permittivity (ε_X) of the lossy layers (X) in the $M(IX)^N$ structure through an analytical-numerical approach based on TMM. Supposing that the $M(IX)^N$ metamaterial is bounded with air (ε_a) and a substrate (ε_s), and considering $z = 0$ plane as the interface of air the first insulator layer, the y component of the magnetic field can be written as

$$H_y(z) = \begin{Bmatrix} A_i e^{ik_a z} + A_r e^{-ik_a z}, z < 0 \\ I_{11} e^{ik_I z} + I_{12} e^{-ik_I Z}, 0 < z < D_I \\ X_{11} e^{ik_X (z-D_I)} + X_{12} e^{-ik_X (z-D_I)}, D_I < z < (D_I + D_X) \\ I_{21} e^{ik_I [z-(D_I+D_X)]} + I_{22} e^{-ik_I [z-(D_I+D_X)]}, (D_I + D_X) < z < L \\ . \\ . \\ . \\ M_{11} e^{ik_M [z-NL]} + M_{12} e^{-ik_M [z-NL]}, NL < z < (NL + D_M) \\ S_t e^{ik_s [z-(NL+D_M)]}, z > (NL + D_M) \end{Bmatrix}.$$

(1)

Where $L = 2D_I + D_X$ and $k_{j=(a,X,I,M,s)} = \sqrt{\varepsilon_j \omega^2/c^2 - k_x^2}$. In these formulations, D_I, D_X, and D_M are the thicknesses of the dielectric, lossy medium and bottom metal reflector layers, respectively. c is the speed of light in vacuum, k is the wave vector inside different media, and ε is the permittivity data of different layers. Applying the boundary conditions for transverse magnetic (TM) polarization (the continuity of the fields and their derivatives at the boundaries separating different media), reflection of the incident light from the structure can be obtained as $R = |F_{12}/F_{11}|^2$.[165] Here, $F = \begin{bmatrix} F_{11} \\ F_{12} \end{bmatrix} = a^{-1}(X_1 X_2^{-1} I_1 I_2^{-1})^N M_1 M_2^{-1} s$ where

$$a = \begin{bmatrix} 1 & 1 \\ ik_a/\varepsilon_a & -ik_a/\varepsilon_a \end{bmatrix}, s = \begin{bmatrix} 1 \\ \frac{ik_s}{\varepsilon_s} \end{bmatrix}$$

(2a)

$$I_1 = \begin{bmatrix} 1 & 1 \\ ik_I/\varepsilon_I & -ik_I/\varepsilon_I \end{bmatrix}, I_2 = \begin{bmatrix} e^{ik_I D_I} & e^{-ik_I D_I} \\ ik_I e^{ik_I D_I}/\varepsilon_I & -ik_I e^{-ik_I D_I}/\varepsilon_I \end{bmatrix}$$

(2b)

$$X_1 = \begin{bmatrix} 1 & 1 \\ ik_X/\varepsilon_X & -ik_X/\varepsilon_X \end{bmatrix}, X_2 = \begin{bmatrix} e^{ik_X D_X} & e^{-ik_X D_X} \\ ik_X e^{ik_X D_X}/\varepsilon_X & -ik_X e^{-ik_X D_X}/\varepsilon_X \end{bmatrix}$$

(2c)

$$M_1 = \begin{bmatrix} 1 & 1 \\ ik_M/\varepsilon_M & -ik_M/\varepsilon_M \end{bmatrix}, M_2 = \begin{bmatrix} e^{ik_M D_M} & e^{-ik_M D_M} \\ ik_M e^{ik_M D_M}/\varepsilon_M & -ik_M e^{-ik_M D_M}/\varepsilon_M \end{bmatrix}.$$

(2d)

Considering the normal light incidence and the planar nature of the design, the same response is observed for transverse electric (TE) polarization. Knowing the thickness and epsilon of the dielectric layers and the bottom metal layer as

well as the thickness of the top X layer, we can numerically obtain the real and imaginary values of $\varepsilon_X$under nearly perfect absorption condition (which we define as $R < 0.1$). More explanation will be provided in the following parts of the thesis.

Another approach to obtain nearly perfect absorption using unpatterned structures is to combine a thin film of a plasmonic/phononic lossy material with a one-dimensional photonic crystal (1D PC). In this case, Tamm plasmon/phonon modes can be supported by the lossy-based 1D PC for both TM and TE polarizations that, in turn, show themselves as nearly perfect resonant peaks (deeps) in the absorption (reflection) spectrum. Therefore, by appropriately designing the structure and obtaining the Tamm modes in the wavelength range of interest, nearly perfect absorption peaks that are supported by the system can be estimated. A typical 1D PC comprises alternating dielectric layers with permittivities ε_1 and ε_2 and thicknesses d_1 and d_2 that is separated from the lossy material by a spacer layer (ε_s and d_s). We suppose the nonmagnetic plasmonic/phononic lossy material has thickness t and, in a general form, has a uniaxially anisotropic permittivity of $\varepsilon_{lossy} = diag(\varepsilon_t, \varepsilon_t, \varepsilon_z)$. Taking the y component of a magnetic field as

$$H_y(z) = \begin{cases} ae^{-q_a(z-t/2)}, & z > t/2 \\ h_1 e^{-q_{h,TM}z} + h_2 e^{q_{h,TM}z}, & -t/2 \le z \le t/2 \\ s_1 e^{-q_s(z+t/2)} + s_2 e^{q_s(z+t/2)}, & -(t/2+d_s) \le z \le -t/2 \\ p\left\{\sinh\left(q_1\left[z+\left(\frac{t}{2}+d_s\right)\right]\right) + \gamma_{TM}\cosh\left(q_1\left[z+\left(\frac{t}{2}+d_s\right)\right]\right)\right\}, & z < -(t/2+d_s) \end{cases} \quad (3)$$

and applying the appropriate boundary conditions for TM polarization at different interfaces, dispersion of the Tamm modes of the 1D lossy-based PC can be obtained using the direct-matching procedure that is applicable for electronic and photonic layered structures[120], [166], [167]

$$\tanh\left(q_{h,TM}t\right) = -\frac{\Gamma_a+\Gamma_s}{1+\Gamma_a\Gamma_s}. \quad (4)$$

Here, $\Gamma_a = q_h\varepsilon_a/q_a\varepsilon_t$, $\Gamma_s = q_h X_{3,TM}/\varepsilon_t$, $X_{3,TM} = \varepsilon_s(1 + e^{-2q_s d_s}X_{1,TM})/q_s X_{2,TM}$, $X_{2,TM} = (-1 + e^{-2q_s d_s}X_{1,TM})$, $X_{1,TM} = \Gamma_1 + 1/\Gamma_1 - 1$, $\Gamma_1 = q_s\varepsilon_1\gamma_{TM}/q_1\varepsilon_s$, $q_{j=(a,s,1,2)} = \sqrt{k_x^2 - \varepsilon_j\omega^2/c^2}$, $q_{h,TM} = \varepsilon_t\sqrt{k_x^2 - \varepsilon_z\omega^2/c^2}/\varepsilon_z$ and

$$\gamma_{TM} = \frac{F_{TM}e^{iK_B d}\sinh(q_2 d_2) + \sinh(q_1 d_1)}{e^{iK_B d}\cosh(q_2 d_2) - \cosh(q_1 d_1)}$$

(5)

where $F_{TM} = F_{1,TM}/F_{2,TM}$. Moreover, $e^{iK_B d}$ can be calculated using the well-known dispersion relation of a 1D PC

$$\cos(iK_B d) = \cosh(q_1 d_1)\cosh(q_2 d_2) + \frac{F_{1,TE,TM}}{F_{2,TE,TM}} + \frac{F_{2,TE,TM}}{F_{1,TE,TM}}\sinh(q_1 d_1)\sinh(q_2 d_2)$$

(6)

with $F_{i,TM} = \varepsilon_i/q_i$, $F_{i,TE} = q_i$.

In order to have an estimation of the nearly perfect resonant absorption for TE polarization, we also formulate TE Tamm polaritons of the 1D lossy-based PC. To this aim, considering E_y as Eq. (3) and applying TE boundary conditions, we arrive at the following dispersion relation for the TE Tamm modes[120]

$$\tanh\left(q_{h,TE}t\right) = \frac{X_4 - X_5}{X_4 + X_5}.$$

(7)

Here, $X_4 = (-q_{h,TE} - X_{3,TE})(q_{h,TE} - q_a)$, $X_5 = (-q_{h,TE} + X_{3,TE})(q_{h,TE} + q_a)$, $X_{3,TE} = q_s(-1 + e^{-2q_s d_s}X_{1,TE})/X_{2,TE}$, $X_{2,TE} = (1 + e^{-2q_s d_s}X_{1,TE})$, $X_{1,TE} = (q_1/\gamma_{TE} + q_s)/(-q_1/\gamma_{TE} + q_s)$, $q_{h,TE} = \sqrt{k_x^2 - \varepsilon_x\omega^2/c^2}$ and γ_{TE} can be calculated using Eq. (3) by replacing F_{TE} with F_{TM}. It should be noted that a similar approach can be followed for obtaining Tamm modes that are supported by a 1D PC based on 2D materials[167].

2.4. LFMAs Architectures

Herein, a comprehensive literature review is conducted on different types of LFMAs. These designs have been devided into three main material categories including; i) metal, ii) semiconductor, and iii) other type of materials based LFMAs.

2.4.1. Metal Based LFMAs

The most commonly studied metal-insulator (MI) pair based architecture that provides perfect light absorption is sub-wavelength metal-insulator-metal (MIM) based cavity[143], [168]–[174]. In this MIM configuration, the top metal layer is a nano patterned plasmonic metal while the bottom layer is an optically thick mirror. In this design, due to strong light confinement inside the cavity in the resonance frequency, perfect absorption of light can be realized in dimensions much smaller than the incident light wavelength. Coupling of incident wave to collective oscillation of top metal electrons via the excitation of surface plasmon resonances (SPRs) leads to light harnessing in the desired frequency range[143], [174]. However, due to the fact that the SPRs can be supported in a relatively narrow frequency range, the absorption bandwidth (BW) of these plasmonic designs has a narrow spectral coverage[136], [169], [171], [175]–[189]. Many different design strategies have been employed to broaden the absorption BW of these plasmonic MIM cavities. One of the most frequently utilized ideas is to implement multi-dimensional/multi-shape pattern in the top metal layer where each unit is designed in a way that SPR excitation can be obtained in different adjacent wavelengths and the superposition of these resonance modes provide perfect absorption of light in a broad frequency range[170], [190]–[197]. The use of tightly packed arrangements of lossy metal nanounits, elongated shapes (such as ellipse) that support dual SPR modes, and structures with sharp corners are other alternatives to make plasmonic broadband perfect absorbers[198]–[203]. However, the main drawback with all of these design configurations is their complex fabrication route. To realize the top sub-wavelength nano units, electron beam lithography (EBL) is required that is inherently an incompatible approach for large scale applications. Although nano imprint lithography (NIL) could be a solution for the large scale synthesis of these samples, this system is also a complex and costly one. Therefore, to open up the opportunity of practical application of these perfect absorbers, the concept of lithography-free multilayer planar designs has attracted much attention in recent years[6], [7], [67], [204]–[229]. Unlike resonant plasmonic MIM perfect absorbers, non-resonant MIM cavities that are made of lossy metals such as chromium (Cr), titanium (Ti), Tungsten (W), and

nickel (Ni) can be used to obtain light perfect absorption in the visible (Vis) and near infrared (NIR) wavelength regimes[8], [213]. In these configurations,

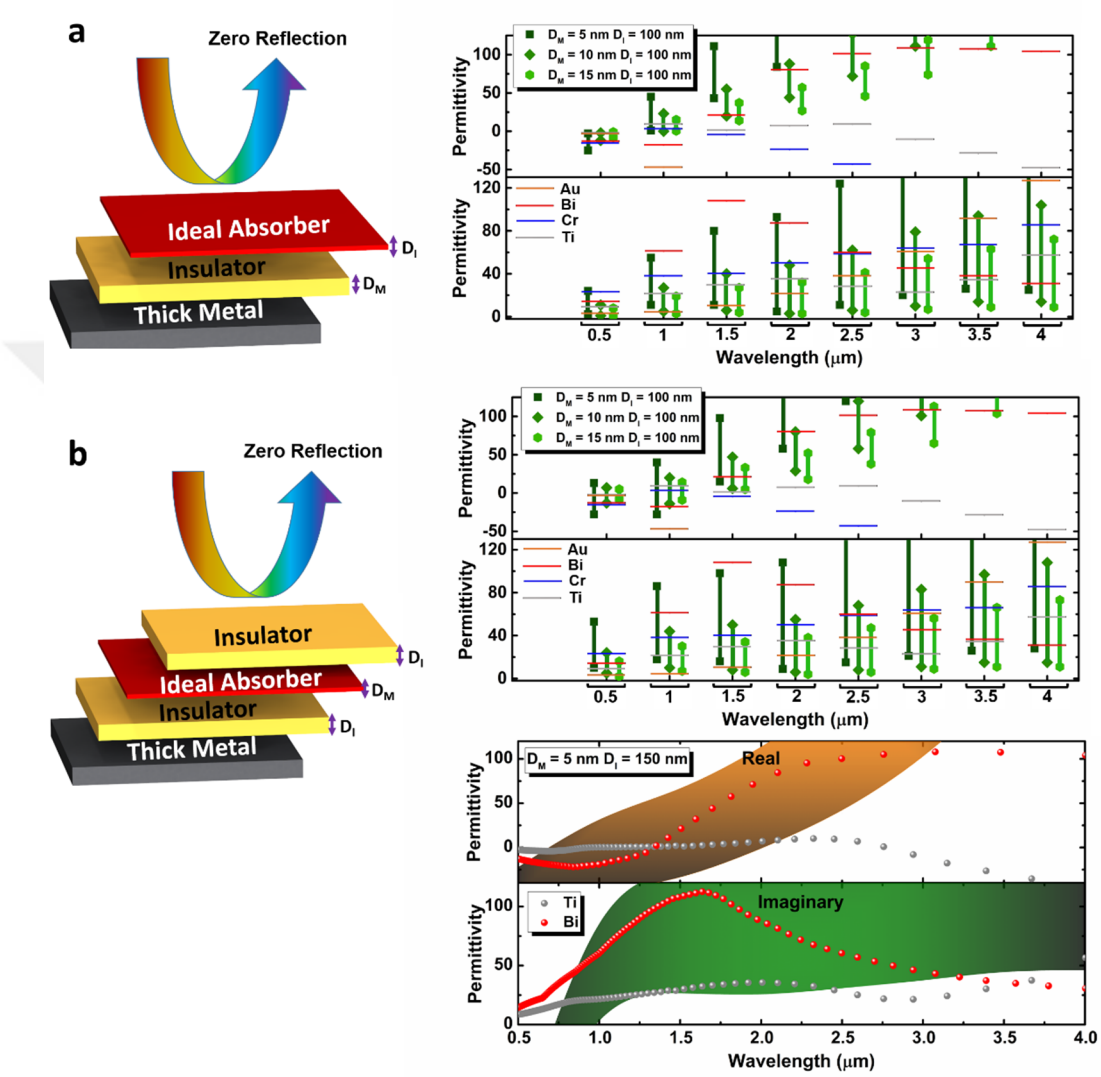


Figure 2.1 The ideal tolerable permittivity values for (a) MIM, and (b) MIMI configurations. These ideal values (that correspond to absorption above 0.9) have been extracted for different D_M and D_I geometries for eight different discrete wavelength values. These tolerable ideal permittivity regions are compared with four different metals including Au, Bi, Cr, and Ti.

the top planar lossy metal layer (with a thickness in the order of couple of nanometers) offers a low quality factor (Q_F) cavity that satisfies impedance match condition in an ultra-broadband frequency range. In this planar configuration, the use of noble metals such as gold (Au) and silver (Ag) could result in narrow absorption BW which is of great interest for the realization of

visible light color filters[206], [208], [209], [211], [224], [229]. To have a better understanding on the absorption BW limits of this configuration, above-mentioned TMM (Eq. (1)) is adopted for an MIM cavity to find the ideal top material for nearly perfect light absorption. In this model, the bottom metal layer is fixed as an optically thick metal mirror and the spacer layer is chosen as SiO_2[70]. The tolerable real and imaginary values of permittivity data, for achieving absorption above 0.9, are obtained for eight discrete wavelengths spanning from 0.5 μm to 4 μm and the results are shown in Figure 2.1. These ideal regimes have been extracted for three different top layer thicknesses of 5 nm, 10 nm, and 15 nm where the spacer layer thickness is fixed at 100 nm. Being located inside the highlighted region in every wavelength value can ensure an absorption above 90 percent that, we define it as the threshold for perfect absorption of incident light. As can be seen from Figure 2.1a, thinner top layers have wider spans for getting perfect absorption while thicker layer moves the bottom of the ideal region toward zero. These ideal permittivity ranges are compared with those of permittivity values for different metals of Au[70], Bismuth (Bi)[230], Cr[70], and Ti[70]. As Figure 2.1a clearly implies, the ideal region for real part of permittivity gets positive values as we move toward longer wavelengths. However, most of the metals (including both noble [Au] and lossy ones [Bi, Cr, Ti]) take an exponential drop toward negative values in NIR wavelengths. For noble metals, such as Au and Ag, this leads to a narrowband light absorber that has been widely explored in Febry-Perot color filter and sensing applications, as shown in Figures 2.2a-b. While for lossy metals, such as Cr and Ti, this matching can be met in broader wavelength range. Generally, however, for a planar MIM absorber, the perfect light absorption is limited to visible and the beginning of the NIR regimes (roughly $\lambda < 1000$ nm). This limit can be extended toward longer wavelength values with tuning the permittivity values of the metals, e.g. composition of a metal with a low refractive index medium such as air[4], [8], [231]. We recently adopted a method based on the dewetting process to create ultra-small nanoholes inside a layer of Cr to reduce its effective permittivity values[8]. It was proven that this modification in a Cr based MIM cavity can shift the upper absorption edge from 850 nm (for planar design) to 1150 nm (for disordered random nanohole design). Moreover, controlling metal deposition condition could be another way to create metal nanostructures[4], see Figure 2.2c. Further improvement in the absorption BW of the design can be accomplished by utilizing a metal-insulator-

metal-insulator (MIMI) configuration. As shown in Figure 2.1b, in this design, the top insulator layer acts as a broadband antireflection coating to provide a gradual impedance matching between the air and underlying MIM cavity. Extracting the ideal data for this case, it can be seen that the overlap between the ideal perfect absorption region and the metal permittivity values have been extended toward longer wavelengths (compared to that of MIM design)[6], [7], [216], [217], [222]. In fact, this configuration can make the ideal permittivity range wider compared to that of MIM design. However, similar to the MIM case, absorption toward longer wavelengths [mid infrared (MIR)] cannot be achieved by this configuration. Although increasing the number of pairs could substantially improve the absorption bandwidth but the upper absorption edge is still limited to NIR regime[67], [217], [220], [221]. Increasing the insulator layer thickness will red-shift both the lower and upper absorption edge in which the perfect absorption of light will not cover the visible region[212]. As depicted in Figure 2.2d, it has been proven that the periodic arrangement of 16 pairs Ni/SiO_2 and Ti/SiO_2 (where the metal layer thickness is in the order of 1-2 nm) could provide near unity light absorption up to 2.5 μm[220]. However, such a large number of pairs require multiple deposition processes and considering the ultrathin nature of metal layer, the repeatability could be an issue in this type of metamaterial absorbers. Therefore, it is desired to improve light absorption BW while keeping device dimensions intact. To achieve this goal, different strategies have been proposed. The optimum choice of back reflector[222], multi-thickness metal layers[6], and incorporation of randomly sized nano holes[7] (Figure 2.2e) can further improve the absorption BW in MIMI configuration. Not only the periodic arrangement of MI pairs can provide ultra-broadband light perfect absorption but also proper arrangement of different multilayers with designed thicknesses can ensure impedance matched condition. An example of such a structure is shown in Figure 2.2f [232]. Nevertheless, according to the ideal model, the absorption at longer wavelengths requires a positive real part of permittivity condition that cannot be satisfied with common lossy and noble metals. That is actually the reason why this configuration cannot go beyond some wavelength limits. However, Bi has extraordinary permittivity values in the longer wavelengths that are perfectly matched to the ideal region. As depicted in Figure 2.1b, Bi has small negative real epsilon values at wavelengths below 1.5 μm and this value moves toward positive ones as we go toward longer wavelengths. Therefore, it is envisioned

that by tuning the spacer and Bi layer's thicknesses in MIM and MIMI configurations, perfect absorption can be acquired in an ultra-broadband frequency range covering all the Vis and NIR frequencies. To prove this statement, the ideal tolerable region is extracted for the case of D_M = 5 nm, and D_I = 150 nm and its matching is compared with that of permittivity data of Bi and Ti (as two metals that have positive permittivity values in long wavelengths). As it can be deduced from this figure, the perfect absorption of incident light is retained up to 3 μm with MIMI dimensions in the order of $\lambda/10$. Therefore, not only the design configuration, but also the optimum choice of the material is essential to acquire near unity absorption in an ultra-broadband frequency range. It should be mentioned that the general approach for achieving perfect light absorption in this MI pair based multilayers, throughout NIR and MIR regimes, is to use tapered structure[221], [233]–[240]. Such architecture will provide gradual matching between the air and underlying metamaterial impedance. However, these designs require lithography and etching processes that are out of the focus of this Perspective. Moreover, some other studies realized perfect light absorption by the integration of ultrathin metal with lithography-free light trapping scaffold. [241], [242] We recently showed that a coating of a 10 nm thick Pt layer on randomly oriented TiO_2 nanowires can provide an absorption above 97% in a broad frequency range spanning from Vis to the NIRregime[241]. However, in this thesis work, we essentially investigate the light absorption in planar sub wavelength structures that operate based on strong interface effects.

Another approach to obtain light perfect absorption is the integration of a thin metal layer with a 1D PC structure. Unlike an MI pair based design configuration, this configuration could provide light absorption in a narrow frequency range and it is of particular interest in directional emission and sensing applications. In agreement with the aforementioned analytical approach for the investigation of Tamm modes supported by the lossy-based 1D PCs, here, we provide some examples regarding the nearly perfect resonant absorption observed by these structures. PCs are artificial structures with dielectric constants periodically varying in one, two, or three dimensions, and display photonic band gaps; i.e. the frequencies regions that light cannot propagate in the structure[243]. Since the pioneering work by Yablonovitch[244], control of light emission has been indicated as one of the

most promising applications of PCs. 1D PC are capable of supporting surface waves that can

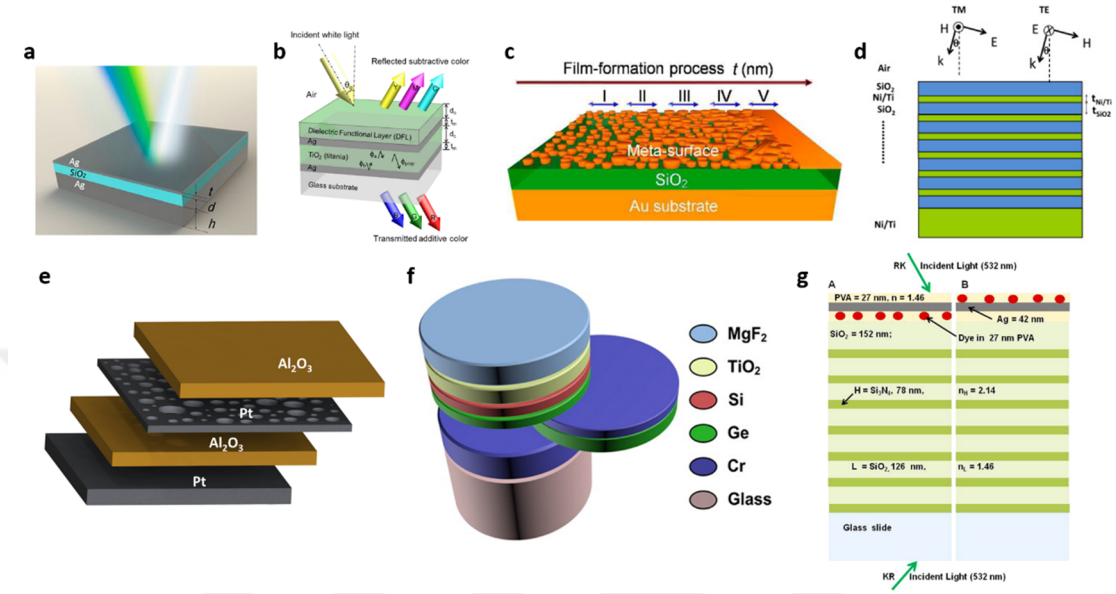


Figure 2.2 Narrowband light perfect absorbers by use of Ag in (a) MIM[224] and (b) MIMI[223] configurations to realize a visible light color filter. (c) Automatically acquired different shaped nano islands during the film formation process in an MIM structure to obtain broadband perfect light absorption[4]. (d) Periodic arrangement of 16 pairs Ni/SiO_2 and Ti/SiO_2 (where the metal layer thickness is in the order of 1-2 nm) to realize light perfect absorption up to 2.5 μm[220]. (e) Formation of disordered nanohole patterns via dewetting process to realize ultra-broadband perfect light absorption in an MIMI multilayer architecture[7]. (f) Properly designed multilayer perfect absorber for ultra-broadband impedance matching[232]. (g) Schematic for an Ag-based 1D PC with two PVA layers. The dye is either located below (case A) or above (case B) the Ag film. The support of Tamm plasmons by this structure leads to the directional emission of the emitter[245]. (a) Reprinted with permission from ref. [224]. Copyright 2015 American Chemical Society. (b) Reprinted with permission from ref. [223]. Copyright 2016 Springer Nature. (c) Reprinted with permission from ref. [4]. Copyright 2015 American Chemical Society. (d) Reprinted with permission from ref. [220]. Copyright 2016 The Optical Society. (e) Reprinted with permission from ref. [7]. Copyright 2017 Springer Nature. (f) Reprinted with permission from ref. [232]. Copyright 2016 American Chemical Society. (g) Reprinted with permission from ref. [245]. Copyright 2014 American Chemical Society

propagate along the interface of the PC and the adjacent medium over long distances and are confined in the normal direction (these modes can also be supported in two-dimensional photonic crystals (2D PCs)[243], however, their

investigation is not of our interest in this thesis). Moreover, the surface waves may be considered as dielectric analogues of surface plasmons that propagate on a metal/dielectric surface[246]. Yeh et al.[247] proved that a 1D PC is capable of supporting surface waves for both TE and TM polarizations. Due to the hybridization of those surface waves with the surface plasmons of a thin film of metal in a metal-based 1D PC, Tamm plasmons can be supported by the system. Consequently, inspired by that point, nearly perfect and directional absorption/emission was obtained by an Ag-based 1D PC due to the support of Tamm plasmons (see Figure 2.2g)[245], [248]–[250]. For the structure schematically illustrated in Figure 2.2g, 42 nm film of silver is separated from a 1D PC by 26 nm film of SiO_2, and the 1D PC comprising 14 alternating layers of SiO_2 (126 nm) and Si_3N_4 (78 nm). Since the emission of poly(vinyl alcohol) material, PVA, was interested in[245], [250], the Ag film is symmetrically bounded with two 27 nm PVA layers to incorporate fluorophores. The addition of an Ag layer to the 1D PC structure leads to a dip in reflectivity in the photonic band gap (PBG) region at 637 nm, due to excitation of Tamm plasmons. It is observed that, in this case, directional emission at normal excitation can be achieved by the structure. In return, by removing the PVA layers and impinging the light to the structure from the Ag part, directional resonant absorption can be obtained. As mentioned hereinabove, Tamm plasmons, that were reported for the first time in 2007[251], are created due to the hybridization of surface plasmons of the thin film of Ag and surface waves of the 1D PC in a hybrid structure. The electric fields for the Tamm plasmons are localized in the dielectric below the metal film and can be supported for both TE and TM polarizations at normal incidences, unlike surface plasmons. Moreover, since the wavevector of Tamm plasmons is smaller than that of light in vacuum, they can be directly excited from air without the aid of prisms or gratings. Using Eqs. (4) and (7) and by appropriate choice of the material, geometrical parameters of the 1D PC, and the spacer layer, it is possible to obtain dispersion curves of the Tamm plamons for both TE and TM polarizations for a thin film of silver with a thickness of t and $\varepsilon_{lossy} = \varepsilon_{Ag}$. Since this dispersion is in exact agreement with the directional-spectral absorption/reflection of the Ag-based 1D PC, the parameters that are taken for the dispersion curves would be a fair estimation for the design and fabrication of the directional absorber. By replacing Silver with an alternative plasmonic material[26] and designing appropriate 1D PC, it

would be possible to achieve nearly perfect resonant absorbers operating at the desired wavelength range.

2.4.2. Semiconductor Based LFMAs

Metamaterials are not only promising solutions for metal based perfect absorbers but they can also provide strong light-matter interaction in ultrathin semiconductor based designs. It should be noted that semiconductors can act as plasmonic (highly doped semiconductors) and phononic (lowly doped or intrinsic semiconductors) materials. A comprehensive discussion on obtaining absorption using unpatterned phononic structures will be provided in the next section. This section will focus on the strategies employed to obtain strong above optical band gap absorption in semiconductor based metamaterial designs. A semiconductor based metamaterial can provide strong light absorption in ultrathin layers. Therefore, near unity light absorption can be achieved in dimensions much smaller than the incident light wavelength. The absorption of light in such thin layers can also be beneficiary from the electrical perspective. Considering the short diffusion length of most of semiconductors[252], total absorption of light in nanometer scale dimensions can significantly improve the collection efficiency of these carriers by suppressing their recombination. In the other words, there is a trade-off between light absorption and carrier collection for a specific semiconductor film thickness[253]. The integration of metamaterial configurations to ultrathin semiconductor films is a promising approach to get high efficiency optoelectronic devices. Such a simple ultrathin trapping design configuration is able to exceed Yablonovitvh's theoretical limit[153]. Therefore, the application of these functional architectures in optoelectronics, such as photovoltaic, photo detectors, and photoelectrochemical devices has attracted a lot of attention in recent years.

Unlike metals that keep their large extinction coefficient values in a wide wavelength range, semiconductors can only absorb photons with energies above their inherent optical band gap. Therefore, they are only active at Vis and short wavelength NIR frequency ranges. The essential goal in the semiconductor based metamaterials is to increase the light-matter interaction to enhance light harvesting efficiency. Same as the previous section, we first

need to explore the condition for strong light absorption. For this aim, the ideal material permittivity values are extracted for metal-semiconductor (MS) and metal-insulator-semiconductor (MIS) configurations. Considering the low

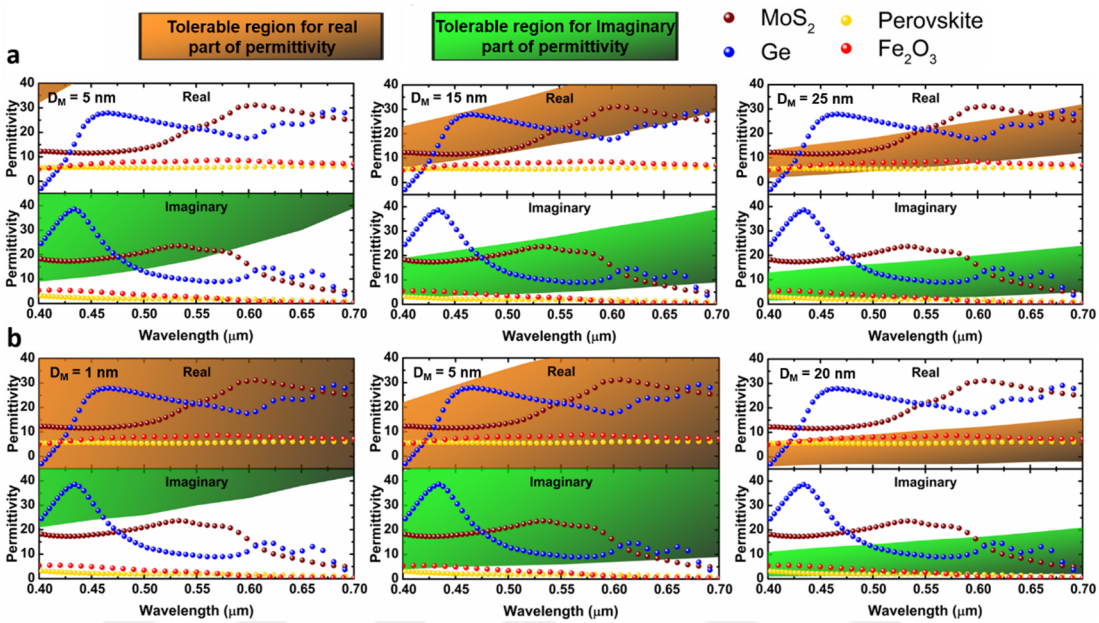


Figure 2.3 The matching between the permittivity values of four different semiconductors (MoS_2, Ge, perovskite, and Fe_2O_3) and those of ideal material to obtain strong light absorption (absorption above 0.7) for (a) MS, (b) MIS configurations. For the MIS case, the insulator layer thickness is fixed at 50 nm.

extinction coefficient of semiconductors, we chose 0.7 as the threshold for light absorption and highlighted the tolerable permittivity regions for an absorption above this value. The overlap between these ideal regions and four different materials [Germanium (Ge) as a low band gap semiconductor, monolayer of molybdenum disulfide (MoS_2) as a 2D semiconductor, $CH_3NH_3PbI_3$ perovskite (PVSK) as an organic semiconductor, iron(III) oxide (hematite, Fe_2O_3) as a low band gap metal oxide] is compared in Figures 2.3a-b. For this goal, the ideal model is obtained for three different top material thicknesses of D_M = 5 nm, 15 nm, 25 nm for MS (Figure 2.3a) and D_M = 1 nm, 5 nm, 20 nm for MIS configurations (Figure 2.3b), respectively. The bottom layer is chosen as an optically thick highly reflecting Al[70] layer and the spacer is chosen as 50 nm thick SiO_2. The simplest metamaterial design to provide strong light absorption is MS configuration. In one of the pioneer works[71], it was shown that the amorphous germanium (a-Ge) layer with a thickness below 25 nm coated on

thick Au metal can absorb around 90% of the light in a relatively narrow Vis frequency range. The spectral position of the absorption peak gets red shift as the thickness of the semiconducting layer increases. It was proven that this nearly perfect absorption is due to the coupling of Fabry-Perot (FP) resonances with excited Brewster modes, see Figure 2.4a[153]. Later studies have proven this strong interface effects for other ultrathin coatings, such as Si and Fe_2O_3 [73]–[76]. In a recent study that is schematically illustrated in Figure 2.4b[73], a perfect absorber made of an ultrathin Si coating on top of AlCu alloy was realized in the Vis-NIR frequency regime. This coating supports Brewster modes and acts as a dual band absorber where the spectral position of these peaks can be finely tuned from the Vis to the NIR by simply changing the semiconductor layer thickness. However, in the above mentioned MS structures, the perfect absorption is realized in a narrow wavelength region that is not our desire in energy related applications where higher density of absorbed photons can provide larger current values. The use of a multilayer back reflector instead of a bare metal layer in which the layers provide gradual phase matching is found to substantiate light absorption in a broad wavelength regime[77]. As shown in Figure 2.4c, this strategy is successfully applied on Fe_2O_3 based water splitting photoanode in which an estimated amount of 71% of the incident photons of energy above the band gap of Hematite can be absorbed by a coating thinner than 50 nm. Thus, most of the photogenerated holes can reach the surface and oxidize water before recombination takes place. This 1D trapping scheme can be also utilized in the design of ultrathin solar cells[78]. The a-Ge:H solar cell proposed in Figure 4d has an efficiency of 3.6% with an absorbing layer as thin as 13 nm. Further improvement in the performance of these optoelectronic devices can be attained by improving the crystalline quality of the absorber layer. PVSK as a chemically synthesized ultrathin crystalline coating can be a proper option to achieve this goal[254]–[257]. Despite all of these considerations, according to the ideal model data for a MS design at ultrathin coatings, the mismatch is generally due to the low values of imaginary permittivities of semiconductors. However, thicker layers could provide the matching for both real and imaginary parts of permittivity in a relatively narrow frequency range for all four different materials. This matching can be met in a broader frequency range for MIS configuration. In this case, similar to MS structure, ultrathin layers (~ 1nm) have poor matching. Thicker layers could shift the highlighted ideal regions toward zero but this time the real

part of permittivity values stays out of the tolerable ideal region. Therefore, each material has its own optimum condition for strong light absorption and by simultaneous tuning of semiconductor and spacer layers thicknesses, strong light absorption in a broad frequency range can be achieved. As for a material thickness of 1 nm that is around the thickness of a monolayer of a two-dimensional (2D) semiconductor, we have poor matching between the ideal case and different semiconductors. Therefore, this configuration cannot provide strong light absorption in 2D monolayers of semiconductors but rather it is useful in its few layer dimensions[258]–[260]. However, for thicker top layer thickness of 5nm, the matching condition can be achieved in a broad frequency range for materials with relatively high extinction coefficient such as Ge and MoS_2. Moving to larger thicknesses, this broad absorption can be acquired for weak absorbing materials such as metal oxides. Increasing the spacer layer thickness to larger values (comparable to $\lambda/4$) can also tune the spectral position of the matching and in general a narrow absorption response will be obtained in this case. All the above mentioned results show the potential application of this metamaterial configuration in optoelectronic applications. However, as mentioned earlier, the main problem with these lithography-free structures is the electrical behavior of the amorphous top active layer that suffers from low electron mobility and a short diffusion length. In other words, it is difficult to obtain ultrathin materials with single-crystalline quality. In a very recent work[79], authors proposed a method to fabricate single-crystalline Ge coatings in an MIS configuration and by this way spectrally selective high performance photodetectors were realized in dimensions much smaller than a bulk device, see Figure 2.4e. It has been proven that by tuning the top single crystalline Ge layer thickness, the absorption peak can be tuned throughout the optical band gap of the semiconductor coating. Moreover, it has been proven that ultrathin crystalline PVSK and metal oxide layers can also be achieved using chemical synthesis methods[255], [261], [262]. Besides the above mentioned optoelectronic applications of these metamaterial cavities, these designs can also be promising in photoelectrochemical water splitting cells. In recent years, MIS cavity configuration, for which the insulator layer thickness is below ~5nm (to facilitate carrier tunneling) and the semiconductor layer is an optically thick coating, has attracted much attention[80]. In this structure, light is absorbed by the semiconductor layer and the applied voltage facilitates the tunneling of the carrier toward the metal layer as well as at the surface of the

metal layer, in which the hydrogen evolution reaction takes place. Considering the fact that the carrier tunneling rate exponentially drops by increasing the insulator thickness and existence of any surface trap states can further hamper the efficiency of this process, this device configuration has some limitations. Moreover, surface reflection from ultrathin top metal reduces the amount of light absorbed by the semiconductor layer. This configuration can be modified by our proposed design where the spacer layer is replaced by a semiconducting metal oxide such as TiO_2 or SnO_2. In this configuration, the light is strongly absorbed by top ultrathin photoactive layer. Then, the photogenerated electron is transferred through the metal oxide spacer toward the back metallic contact and the left holes undergo water oxidation reaction. Unlike the previous case, wherein the photoactive layer is a thick coating, such an ultrathin semiconductor layer can ensure the efficient participation of the carrier in the photoelectrochemical reaction even in low mobility semiconductor materials. This design strategy has been successfully applied to $Au/SnO_2/BiVO_4$ MIS configuration where substantial improvement has been obtained by transferring this cavity on top of a pre-patterned trapping scaffold[72], see Figure 2.4f.

As mentioned hereinabove, this MIS configuration is not a good solution to get light perfect absorption in dimensions below 1 nm that corresponds to the thickness of 2D semiconductor monolayers. That is the reason why MS and MIS based 2D TMD perfect absorbers (absorption above 0.9) have been only realized in multilayer dimensions[258], [259]. The alternative strategy to obtain light perfect absorption in the monolayer of semiconductor layers is to integrate this monolayer with a photonic crystal (PC) design. In one of the pioneer works, authors proved strong light absorption in atomically thin materials through a dielectric cavity design with chirped Bragg reflectors for broadband coherent light absorption[81]. It was numerically proven that due to this cavity enhancement, a monolayer MoS_2 photodetector absorbs as much as 33% of incident visible light over a 300 nm bandwidth. Later, another study illustrated narrowband absorption above 96% in a monolayer of MoS_2. The structure is made of a 1D PC on top of a MoS_2 layer, an optically thick reflecting bottom metal mirror, and a spacer between MoS_2 and the bottom metal film[82]. Numerical simulations demonstrated that this strong light absorption is originated from the strong field confinement due to the support of Tamm plasmon modes in the MoS_2-based 1D PC. Recently, it was shown that the

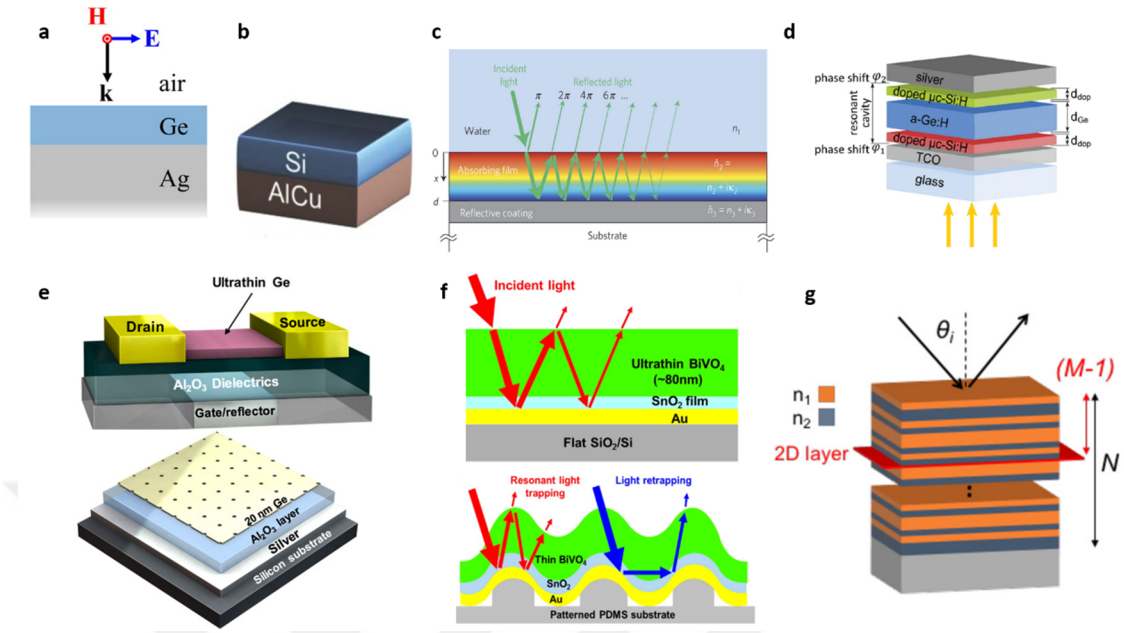


Figure 2.4 (a) Absorption of 98% of the incident light energy in a 12 nm thick Ge layer on an Ag substrate at a narrow wavelength range (λ=625 nm) over a wide range of angles[153]. (b) A dual band light perfect absorber operating at the Vis and NIR regimes using a 45 nm thick Si layer coated on AlCu alloy[73]. (c) 71% above band gap light absorption in a less than 50 nm thick Fe_2O_3 using a resonant light trapping scheme for efficient water splitting[77]. (d) A a-Ge:H solar cell with an efficiency as high as 3.6% using an absorbing layer as thin as 13 nm[78]. (e) Spectrally selective photodetector by the realization of perfect light absorption in a narrow frequency range using a single-crystalline germanium nanomembrane coated on a resonant foreign nanocavity.[79] (f) An efficient water splitting photoanode using an ultrathin $BiVO_4$ absorbing layer in an MIS configuration (Au-SnO_2-$BiVO_4$). The incorporation of a trapping scaffold could substantiate the process efficiency[72]. (g) Random coherent perfect absorption in a monolayer of MoS_2 mediated by anderson localization[83]. (a) Reprinted with permission from ref. [153]. Copyright 2014 American Chemical Society. (b) Reprinted with permission from ref. [73]. Copyright 2018 John Wiley and Sons. (c) Reprinted with permission from ref. [77]. Copyright 2012 Springer Nature. (d) Reprinted with permission from ref. [78]. Copyright 2015 John Wiley and Sons. (e) Reprinted with permission from ref. [79]. Copyright 2017 The American Association for the Advancement of Science. (f) Reprinted with permission from ref. [72]. Copyright 2016 American Chemical Society. (g) Reprinted with permission from ref. [83]. Copyright 2017 American Chemical Society

integration of lossy 2D materials with a finite all-dielectric 1D random medium can provide random coherent light absorption above 99.9% in the visible regime[83], as shown in Figure 2.4g. It was found that optical resonances, only

in the regime of Anderson localization, can provide the condition for random coherent perfect light absorption.

2.4.3. Other Types of LFMAs

Alternative plasmonic materials such as gallium doped zinc oxide (GZO), aluminum doped zinc oxide (AZO), indium-tin-oxide (ITO) and titanium nitride (TiN) can also be implemented in designing unpatterned metamaterial absorbers. The real part of permittivity of these materials is negative in the NIR region and their epsilon-near-zero (ENZ) characteristics around 1.5 μm can be tuned by doping[26]. Figure 2.5a shows schematic of an unpatterned SiO_2/bi-layer GZO/Ag multi-layer structure[263]. The bi-layer GZO is composed of two GZO layers with different carrier concentrations. This structure can act a broadband perfect absorption within 1.24 μm to 1.49 μm and its absorption remained higher than 97% for incident angles up to 60°. This NIR perfect absorber has a simple design as well as broadband and wide-angle absorption features, which is promising for practical applications. A similar ITO-based structure has also been employed for this purpose[264]. It has also been verified that a multilayer metamaterial composed of alternating layers of AZO and ZnO functions as a nearly perfect NIR absorber (see the schematics in Figure 2.5b that is taken from[265]). As mentioned in the theoretical background section, this system is another category of unpatterned metamaterial absorbers. In this structure, which does not include any bottom reflecting layer, the negative real part of permittivity of AZO allows the dielectric multilayer to meet the impendence matching condition around 1.90 μm, leading to almost 99% light absorption in this region[266]. As mentioned about, TiN is also another plasmonic material beyond gold and silver. Schematic of a multilayer metamaterial that is composed of alternating layers of TiN and aluminum scandium nitride (Al,Sc)N is shown in Figure 2.5c[267]. As seen from this schematic and the represented SEM image, the surface of the planar metamaterial is stochastically covered by spin-coated ITO nanoparticles on its top. It was reported that the presence of the plasmonic ITO nanoparticles at the surface of the metamaterials facilitates the impedance matching condition by exciting high-k propagating modes in the system and reducing the reflection.

Thus, light can penetrate inside the system with minimum reflection and finally absorbed inside the metamaterial.

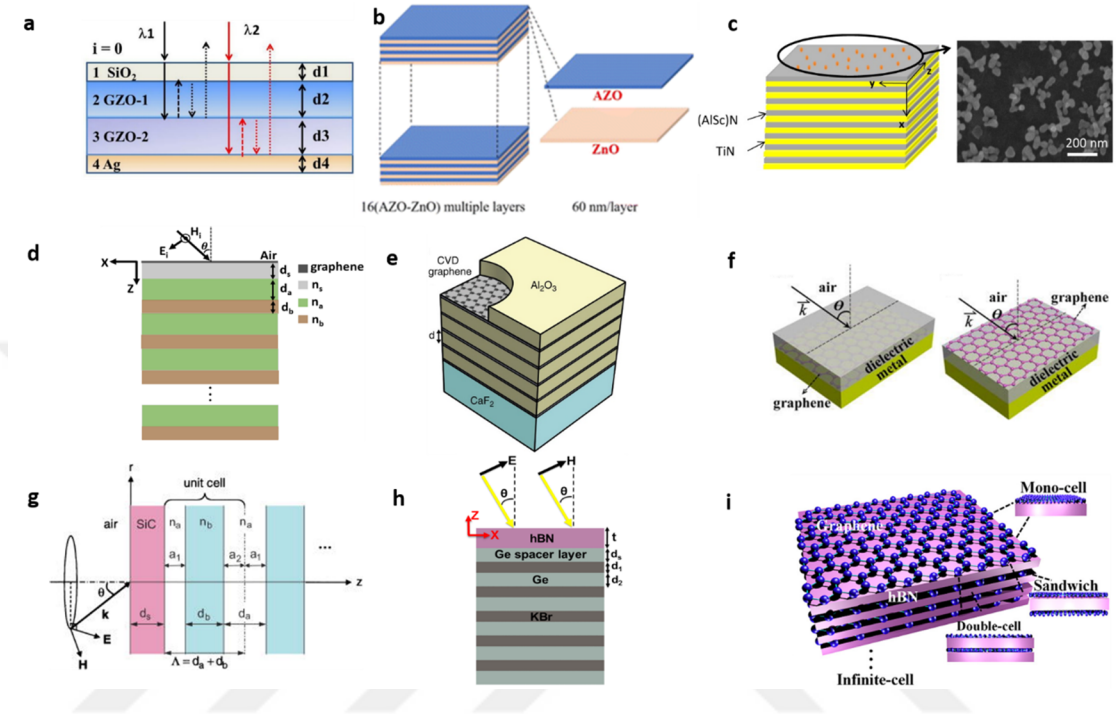


Figure 2.5 Schematics of different unpatterned plasmonic/phononic light absorbers. (a) An unpatterned SiO_2/bi-layer GZO/Ag multi-layer structure that acts a broadband perfect absorber within 1.24 μm to 1.49 μm[263]. (b) Multilayer metamaterial composed of alternating layers of AZO and ZnO layers that functions as a nearly perfect NIR absorber[265]. (c) Multilayer metamaterial that is composed of alternating layers of TiN and aluminum scandium nitride (Al,Sc)N. The surface of the planar metamaterial is stochastically covered by spin-coated ITO nanoparticles. This metamaterial acts as a light absorber in the NIR region[267]. (d) A graphene-based 1D PC that can act a narrow-band light absorber in the THz range[109]. (e) First experimental demonstration of a graphene-dielectric multilayer structure that behaves as a hyperbolic metamaterial in the MIR region[110]. This structure is capable of light absorption in the MIR and FIR ranges. (f) Unpatterned layered structures in dielectric/graphene/metal and graphene/dielectric/metal arrangements for UV light absorption[268]. (g) SiC-based 1D PC that is appropriate for light absorption within 10.3-12.6 μm window in the mid-IR range[118]. (h) hBN-based 1D PC that can act as nearly perfect light absorption and coherent thermal emission within two 6.2-7.3 μm and 12-12.82 μm windows in the MIR range[120]. (i) Multilayer graphene-hBN metamaterial[122]. Due to the plasmon-phonon hybridization, this structure has multifunctional capabilities, specially promising for light absorption in a wide window in the MIR range. (a) Reprinted with permission from ref. [263]. Copyright 2016 IOP Publishing. (b) Reprinted with permission from ref. [265]. Copyright 2018 Springer Nature. (c) Reprinted with permission from ref. [267]. Copyright 2014 The Optical

Society. (d) Reprinted with permission from ref. [109]. Copyright 2017 Chinese Laser Press. (e) Reprinted with permission from ref. [110]. Copyright 2016 Springer Nature. (f) Reprinted with permission from ref. [268]. Copyright 2018 American Institute of Physics. (g) Reprinted with permission from ref. [118]. Copyright 2005 American Institute of Physics. (h) Reprinted with permission from ref. [120]. Copyright 2017 The Optical Society. (i) Reprinted with permission from ref. [122]. Copyright 2017 American Chemical Society.

Other category of the plasmonic materials that can be employed for light absorption in the mid-IR and far-IR regions is 2D materials such as graphene[33], [107]–[109], [269]–[271] and black phosphorous[272]–[278]. The optical properties of these 2D materials are quite different than those of bulk, 3D materials, which results in significantly different plasmon dispersion relationships. After the rise of graphene, a great deal of attention has been attracted to its potential applications in optoelectronics[279] and plasmonics[33]. The surface conductivity of graphene (σ) can be effectively modulated via tuning of chemical potential through chemical doping or electrostatic/magnetostatic gating[107], [279], [280]. When Im(σ)>0, graphene behaves like a very thin metal layer capable of supporting transverse-magnetic (TM) guided plasmonic mode[33], [108], [109], [269]–[271] Tunability of its plasmon resonance through the variation of μ together with a relatively large propagation length and a small localization length of SPPs in the mid-infrared (MIR), far-IR (FIR) and terahertz (THz) ranges[108] are the key advantages of the graphene SPPs over those supported by the noble metals[246]. Consequently, neglecting graphene-based patterned metamaterials[269]–[271], it is possible to obtain nearly perfect resonant absorption in the MIR, FIR, and even THz frequency ranges by combining an unpatterned layer of graphene with a 1D PC with appropriate design, see the schematics in Figure 2.5d[109]. The basic mechanism for the observation of such a resonant behavior in this graphene-based 1D PC is the excitation of Tamm plasmons. Updating Eqs. (4) and (7) by replacing a single layer of graphene with the optical conductivity σ with a lossy film with permittivity ε_{lossy} and thickness t, we can arrive at the dispersion relations of Tamm plasmons supported by the system[167]. Taking the structural parameters appropriately, the dispersion curves of the Tamm plasmons at the desired range of frequency can be obtained and, thus, the frequency- and angle-dependency of the resonant absorption peaks of the structure can be precisely estimated. An example of

THz nearly perfect resonant absorptions using a 1D graphene-based PC is discussed in[109]. Recalling that the schematic of this structure is illustrated in panel (d) of Figure 2.5, the considered 1D PC is composed of periodic layers of SiO_2 (n_a=1.46 and d_a=51.37 μm) and poly 4-methyl pentene-1 (n_b=1.9 and d_b=39.47 μm) and the refractive index and the thickness of the spacer layer are taken to be as 2.12 and 35.35 μm. It is demonstrated in this paper that the electric field is mostly localized at the dielectric layer below graphene, i.e. the plasmonic material, for the Tamm plasmons supported by the plasmonic-based 1D PC. Moreover, the spectral-directional absorption of the structure for TM and TE polarizations verifies that the trend of the nearly perfect absorption behavior of this system is completely predictable by the dispersion of Tamm plasmons. It is noteworthy that, by the same approach, nearly perfect resonant absorption behavior is also achievable by unpatterned layer of black phosphorous. Similar to multilayer metal/dielectric metamaterial, graphene/dielectric metamaterials, that has been realized experimentally (see Figure 2.5e that is taken from[110]), are also another candidate to achieve tunable light absorption in the MIR range[110]–[112]. Notice that the designs schematically shown in panels (d) and (e) of Figure 2.5 are a couple of examples of plasmonic light absorbers based on unpatterned graphene sheet that can operate in the MIR, FIR and THz regions. However, graphene, which acts as a lossy dielectric not a plasmonic material, has also potential applications in the Vis and UV ranges. As schematically illustrated in Figure 2.5f [268], an unpatterned layer of graphene in dielectric/graphene/metal and graphene/dielectric/metal structures is a decent tool to achieve UV light absorption. It has been reported in[268] that by taking the material and structural parameters appropriately, and also by manipulating the polarization and angle of incident light, it is possible to get 71.4% and 92.2% light absorption in the planar structures that composed of single and four layers of graphene, respectively.

Alongside the noble metals, highly doped semiconductors, alternative plasmonic materials, graphene and the other 2D materials, polar dielectrics also offer an opportunity of simultaneous sub-diffractional confinement, low optical losses, and operation in the MIR to THz spectral ranges through the stimulation of surface phonon polariton (SPhP) modes[281]. SPhPs originate from the interaction of optical phonons with long-wavelength incident fields,

creating a surface excitation mediated by the atomic vibrations. Depending on the type of the polar material, SPhPs have many applications in a wide frequency range from MIR (e.g. hexagonal boron nitride (hBN)[282]–[292], SiC[118], [119], [293]–[296], SiO_2 [297], and AlN[298]) to FIR (e.g., LiF[299], [300], GaN[301], GaAs[302], InP[281], and CaF2[281]). Such SPhP modes can be stimulated between the longitudinal optical (LO) and transverse optical (TO) phonon frequencies of the polar dielectrics. This spectral range is referred as the Reststrahlen (RS) band or polaritonic gap. Similar to the metal-based and graphene-based 1D PCs discussed above, SiC-based 1D PC (as a polar-based 1D PC) is also an [119]appropriate candidate for nearly-perfect light absorption and, thus, coherent thermal emission in 10.3 to 12.6 μm in the MIR range[118], [119]. This range is in fact the polaritonic gap of SiC. The schematic of this structure is depicted in Figure 2.5g that is taken from[118]. It is noteworthy that, according to Kirchhoff's law, the spectral-directional emissivity, is the same as the spectral-directional absorptivity of the system. Notice that coherent thermal emission from surface relief gratings holds promise for spectral and directional control of thermal radiation but is limited to transverse magnetic waves, which can excite surface plasmon or phonon polaritons in the patterned structures. However, for the SiC-based 1D PC, due to the support of Tamm phonons, a coherent thermal source can be realized by an unpatterned structure[118], [119]. It should be mentioned that another promising application for these IR absorbing materials is the thermal detection. Thermal detection is currently revolutionizing the IR technology and it is envisioned to expand the market for cameras. These thermal detectors are essentially micro bolometers that are fabricated using micromachining of a thermistor material. Nichrome (NiCr) is one of the most studied THz absorbing materials used in these designs[303], [304]. Considering the fact that these thermal detectors need no cryogenic cooling, they are promising options for future compact, light-weight, and potentially low-cost cameras.

Another distinguishable polar material suitable for light absorption and thermal emission purposes in the mid-IR region is hBN. As schematically shown in Figure 2.5h, hBN-based 1D PC that is composed on an unpatterned film of hBN and 1D PC separated by a spacer layer, is another candidate for nearly perfect resonant light absorption and coherent thermal emission in the MIR range[120]. Hexagonal boron nitride is a natural hyperbolic material, for

which the dielectric constants are the same in the basal plane ($\varepsilon_t \equiv \varepsilon_x = \varepsilon_y$) but have opposite signs ($\varepsilon_t \varepsilon_z < 0$) in the normal one ($\varepsilon_z$) in 6.2-7.3 μm and 12-12.82 μm wavelengths in the mid-IR region, respectively, named as RS-II and RS-I regions. RS-I and RS-II bands represent the wavelength regions at which hyperbolic phonon polaritons (HPPs) supported by hBN show type I and type II hyperbolicities, respectively. Owing to this property, finite-thickness slabs of hBN are capable of supporting sub-diffractional volume-confined polaritons and can act as multimode waveguides for the propagation of HPP collective modes for TM polarization that originate from the coupling between photons and electric dipoles in phonons[282]–[292]. It has been recently reported that, due to the support of HPPs, 1D grating of hBN is capable of supporting highly concentrated resonant absorptions[287]. In addition, because of the coupling of magnetic polaritons in metal gratings with HPPs of hBN in TM polarization, MIR perfect or nearly perfect absorption can be observed by an unpatterned film of hBN on top of a metallic grating[288]. Moreover, patterned metamaterials that are composed of graphene-hBN heterostructures are also another promising candidate for the support of tunable nearly perfect resonant absorptions[284]. However, as illustrated in Figure 2.5h, the structure under our consideration in the hBN-based 1D PC is composed of unpatterned film of hBN with thickness t and ε_{hBN}. The 1D PC is composed of alternating layers of KBr ($\varepsilon_1 = 2.25$, $d_1 = 923$ nm) and Ge ($\varepsilon_2 = 16$, $d_2 = 576$ nm) with an spacer layer of Ge of thickness d_s. Due to hybridization of surface waves of the 1D PC and HPPs of hBN, Tamm phonons can be supported by the system for both polarizations. As discussed in[120], both spectral and directional characteristics of the nearly perfect resonant absorptions of the hBN-based 1D PC can be exactly predicted by dispersion of Tamm modes supported by the structure. Consequently, evaluating Tamm modes by Eqs. (4) and (7) is a true approach for a reliable estimation of the resonant absorption supported by unpatterned lossy-based 1D PC. Moreover, mode profiles of the Tamm phonons highlights this point that, in contrast to Tamm plasmons, magnetic field is localized under the polar film for these modes[120].

As we mentioned earlier, several types of polar materials have been realized to operate in the MIR and FIR ranges. Notice that by using a similar approach, i.e. by appropriately designing unpatterned polar-based 1D PCs, it is possible to achieve nearly perfect resonant absorptions at the corresponding

wavelengths. As depicted in Figure 2.5i, multilayer graphene/hBN metamaterial (hypercrystal) is the last structure that we would like to investigate as a tunable device appropriate for coherent light absorption and thermal emission in the MIR range[122]. Through the investigation of the band structure of the metamaterial we found that, due to the coupling between the hybrid plasmon–phonon polaritons supported by each unit cell, the graphene–hBN metamaterial can support hybrid plasmon–phonon polaritons bands[305]. Moreover, the analysis of light transmission through the metamaterial revealed that this system is capable of supporting high-k propagating hybrid plasmon–phonon polaritons[305]. Owing to these optical properties, it has been recently reported that this multilayer structure can exceed blackbody thermal radiation in near-field[122] and also is capable of light absorption in the MIR region[306].

Based on this work, light perfect absorption in the whole EM spectrum (from UV to FIR) can be realized using large scale compatible, planar, lithography-free multilayer designs. For this purpose, it is necessary to find the proper material and design architecture to obtain strong light-matter interaction. Figure 6 outlines the proper materials for different parts of the EM spectrum. In the UV and Vis frequency ranges, this absorption can be obtained by semiconductors and noble metals. Moreover, it was recently proven[268] that graphene can be also a UV responsive material in a proper planar design. To extend the absorption upper edge toward longer wavelengths such as NIR range, lossy metals such as Cr, Ti, and Bi can be a good choice. In the short wavelength NIR regime, alternative plasmonic materials that show epsilon-near-zero (ENZ) characteristic (such as AZO, GZO, and ITO) can be effectively utilized for light near unity absorption[20]. In these materials, tuning the plasma frequency can provide us the opportunity to control the spectral position of the strong light-matter interaction. Perfect light absorption in longer wavelengths i.e. MIR, FIR, and THz which are inaccessible with unpatterned metal based multilayer designs, can be acquired using graphene, black phosphorus and suitable polar materials as shown in the Figure 1.1. Therefore, it can be envisioned that planar light perfect absorbers that do not require sophisticated lithography fabrication techniques, can be an excellent option for future large scale optoelectronic application. For this aim, according to the operation wavelength and the application, the proper design architecture and material should be used.

Metal based planar metamaterial absorbers can be listed in two main categories; narrowband and broadband perfect absorbers. As illustrated earlier, narrowband perfect light absorbers can be acquired using noble low loss metals such as Au and Ag. These structures can be of particular interest in color filtering, imaging, and display applications. The planar and large scale compatible nature of these multilayer designs facilitates their integration into commercialized color-CCD/cameras[224]. Different from nanostructured plasmonic designs, these Febry-Perot based resonators can operate in a wide incident light polarizations and angles that makes them suitable for practical applications. Moreover, the light absorption can be also obtained in broad/ultra-broad wavelengths. An ideal black-body absorber that suppresses incident light reflection and transmission in a broad spectral range can ensure efficient use of the solar power. One of the most studied areas of interest for these ultrabroadband perfect absorbers is thermophotovoltaics (TPV). This system harvests the incident photons in a broad spectral range and transduces them into thermal energy and then a frequency-selective emitter which is matched into the band gap of the PV cell radiates a narrowband thermal emission. Based on previous works, this system can ideally overcome the fundamental limits of conventional PV cells[307]. In a PV cell, the absorption is restricted into the photons with energies above the optical band gap of the active layer. Therefore, only a specific portion of the solar spectrum will be efficiently harvested. However, metals can retain their perfect absorption property over the entire Vis and NIR regimes. Covering the most parts of solar irradiation power can guarantee the efficient harvesting of the incident light. Therefore, the use of lossy metals in metal-insulator pair based configuration can provide near unity absorption of the light and this intense absorbed power can be directed into a PV cell using a narrowband emitter to substantiate the PV cell efficiency. The narrowband emitter can be also realized using dielectric based PC structure which makes the whole TPV system lithography-free[67]. Thus, the integration of a PC narrowband emitter with a refractory lossy metal based ultra-broadband perfect absorber can be considered as a winning strategy for the design of future highly efficient TPV systems. Another area of usage of these ultra-broadband absorbers is solar driven steam generation. Advancements in this area have proved efficiencies as high as 90% at only 4-sun intensity (4 kW m^{-2})[68]. Therefore, same as TPV, the realization of ultra-broadband light perfect absorbers can be of great interest in the steam generation.

Strong light absorption in ultrathin semiconductor based perfect absorbers can also have high potentials in PV, photodetectors and photoelectrochemical applications. Our theoretical findings revealed that spectrally broad strong light-matter interaction can be acquired in MIS cavity based designs. Therefore, the incident light is efficiently harvested in sub wavelength geometries and the ultrathin thickness of the semiconductor would minimize the transport length of photogenerated carriers that in turn maximizes their collection efficiency. However, the main challenge in these semiconductor-based metamaterials is the crystalline quality of the photoactive layer. Utilizing common deposition and growth techniques for ultrathin films, it is difficult to fabricate single crystalline semiconductor in such thicknesses. In most of these designs the active layer is made of amorphous semiconductor and therefore, their optoelectronic performance is far inferior to those of bulk crystalline counterparts. Therefore, the main challenge, that limits the replacement of conventional bulk semiconductor based optoelectronic systems with these ultrathin metamaterials, is their poor electrical properties of the photoactive layer. A recent study demonstrated a high performance MIS configuration based photodetector where the single-crystalline Ge membrane undergoes a strong light-matter interaction on a functionalized nanocavity design[79]. The use of chemical synthesis methods can be also an alternative to realize single crystalline semiconductors in such nanometer scale thicknesses. Two-dimensional (2D) TMDs are another category of semiconductors that can be employed in ultrathin optoelectronics. Transition from bulk to monolayer makes these semiconductors a direct band gap material and consequently a better absorption dynamics are emerged. However, the atomic thickness of the layer can absorb only a small portion of the light and thus, a trapping mechanism is required to provide strong light-matter interaction. As shown in the above sections, the use of MS or MIS cavity architectures could not be a good solution for light perfect absorption for 2D TMDs. These cavity designs can efficiently harvest the light in multiple layer thicknesses. To realize perfect light absorption in unpatterned monolayer of TMDs, PC configuration is the right strategy to confine the entire power in the position of the monolayer where this confined energy is harvested efficiently. A recent Perspective in the application of these van der waals materials in PV technology predicted that it is possible, in principle, to achieve power conversion efficiencies as high as 25%[308]. Introducing a tandem scheme where these 2D materials are brought to a

junction with another bulk semiconductor (such as Si) could further substantiate the cell efficiency. This bulk semiconductor can be replaced with a MIS nanocavity design to localize the absorbed power in ultrathin dimensions. Then, a PC capped 2D TMD can be grown on top of this design to make an ultrathin efficient tandem solar cell. Therefore, the findings of this study can serve as a beacon for future performance enhanced semiconductor optoelectronic devices.

As mentioned hereinabove, graphene, black phosphorus and polar materials are appropriate candidates for achieving light absorption in the MIR, FIR, and THz ranges. MIR/FIR directional light emitters are a distinguished category of light absorbers that have attracted intense interests during the previous years due to their potential application in radiative heat transfer and energy conversion systems[122], [294], [296]. A thermal light-emitting source, such as a black body or the incandescent filament of a light bulb, is often presented as a typical example of an incoherent source and is in marked contrast to a laser. Whereas a laser is highly monochromatic and very directional, a thermal source has a broad spectrum and is usually quasi-isotropic. It has been shown recently that the light absorption by polar-based 1D PCs is considerably enhanced in a directional manner compared to a bare polar film. This system, therefore, is capable of emitting radiation efficiently in well-defined directions and can act as a coherent thermal source at a fair distance. For these structures, narrow angular emission lobes similar to antenna lobes are observed and the emission spectra of the source depend on the observation angle. As mentioned earlier, the origin of the coherent emission is in the support of Tamm phonon polaritons by the above-mentioned polar-based 1D PC. The unpatterned lossy-based narrowband absorbers may also be employed as radiative coolers that are reflective in the solar spectrum and emissive in the transparency window of the atmosphere (8-13 μm). These absorbers, therefore, can be regarded as a critical component in the MIR photodetectors and imaging systems that are important in applications such as night vision and astronomy research[295], [309], [310]. MIR/FIR filtering and sensing for detecting gases as well as biological and chemical agents can be mentioned as another potential application of the narrow band light absorbers discussed in this thesis wor[311].

Chapter 3. Characterization Methods and Instrumentation

Throughout this thesis, various materials, steady state and transient optical and photoelectrochemical characterization techniques are used. In the context of this chapter, we aim to provide an overview of these characterization methods.

3.1. Material Characterizations

- .Scanning electron microscopy (SEM) for investigation of designs morphology.
- Transmission electron microscopy (TEM) for analyzing the samples morphology and crystallinity in atomic scales.
- X-ray photoelectron spectroscopy (XPS) for elemental composition and surface analysis.
- X-ray diffraction spectroscopy (XRD) for crystallinity investigations.
- Atomic force microscopy (AFM) for measuring the surface topology and the thickness of ultrathin layers.

3.2. Optical Characterizations

- .UV-Vis-NIR spectroscopy for measuring the perfect absorbers reflection and transmission response in the solar spectrum.
- Fourier-transform infrared spectroscopy (FTIR) to obtain the infrared spectrum of absorption or emission of a sample.
- Spectroscopic ellipsometry to extract the refractive index of a single layer and to measure the oblique angle response of the perfect absorber.
- Photoluminescence spectroscopy to characterize the emission response of the devices
- Time resolved photoluminescence (TRPL) to characterize the emission lifetime of the samples.
- Transient absorption spectroscopy (TA) to understand the excited state lifetime of the samples.

3.3. Photoelectrochemical Measurements

- Linear sweep voltometry (LSV) to measure current-voltage response of the water splitting cells.
- Chronoamperometry (CA) to measure current-time response of the water splitting cells
- Electrochemical impedance spectroscopy (EIS) to measure the impedance of the samples.
- Incident photon conversion efficiency (IPCE) to measure the spectral photoconversion response of the cells.

Chapter 4. LFMAs for Filtering Application

4.1. Preface

This chapter of the thesis is based on the publications:

”*Lithography-free planar bandpass refective color filter using a series connection of cavities*”, A. Ghobadi, H. Hajian, M. Soydan, B. Butun, E. Ozbay, **Scientific Reports.** 2019, 209, 1 – 11. Adapted (or “Reproduced in part”) with permission from Nature Publishing Group.

”*Bismuth-based metamaterials: from narrowband reflective color filter to extremely broadband near perfect absorber*”, A. Ghobadi, H. Hajian, M. Gokbayrak, B. Butun, E. Ozbay, **Nanophotonics.** 2018, 8, 823 – 832. Adapted (or “Reproduced in part”) with permission from De Gruyter Publishing Group.

4.2. Motivation

In a common FP resonance-based structure that is made of a metal-insulator-metal (MIM) stack, tuning the insulator layer can offer the narrowband reflection/transmission spectra in the entire visible light regime. In these FP resonators, the red-green-blue (RGB) additive colors and their complementary subtractive ones of cyan-magenta-yellow (CMY) can be obtained in transmission and reflection modes, respectively. Besides their simple, large scale compatible, and EBL free fabrication route, these structures can provide relatively high efficiency, high color purity, and low crosstalk. However, under oblique angle light incidence, the increase in optical passage length of light within the cavity imposes a blue shift in the resonance frequency of the design. This angular dependency is more pronounced in reflection mode, due to the longer optical path of the light. To mitigate this deficiency, several different

methodologies have been conducted. The angle insensitivity response of the resonance can be attained by increasing the refractive index (n) and reducing the cavity thickness. This material can be a lossless material, such as Si_3N_4[312], ZnS[205], WO_3[228], and TiO_2[204], [208], [223], [226], or a lossy material such as amorphous Silicon (a-Si)[204], [227], [229], [313]. In the case of a lossy medium such as the cavity layer, the phase acquired upon the reflection at the metal (air)-semiconductor interface can be much greater than π and, therefore, unlike the lossless layers, the FP resonance can be attained in our desired wavelength in much thinner thicknesses[143], [229]. Consequently, the optical path length difference would be negligible between normal and oblique incident lights. However, the drawback with this architecture is the fact that the cavity semiconductor layer can absorb light and reduce the efficiency of the color filter. This reduction is especially significant in the shorter wavelengths where the extinction coefficient (κ) of the semiconductor is larger. To lessen this adverse effect, a phase compensating dielectric overlay can be placed above the cavity to achieve the angle-insensitive characteristics without sacrificing the amplitude for all the primary reflective and transmissive colors[204], [226]. However, adding this overlay on top of the FP design increases the bandwidth (BW) which this, in turn, leads to reduction in the color purity. Moreover, in all of these lithography-free FP designs, the structure performs as a band-stop filter at the reflection mode that absorbs a narrow frequency range and reflects the rest of the spectrum. Therefore, the generation of RGB additive colors is not possible in these designs and they can create these colors in the transmission spectra. But due to the inherent loss of the materials, transmissive color filters are in general less efficient compared to that of reflective ones.

In this chapter, we propose three solutions to generate high efficiency RGB colors in reflection mode. Two of these solutions are based on tandem shape FP design architectures, and the third solution is based on the unique properties of Bi layer.

4.3. Lithography-Free Planar Band-Pass Reflective Color Filter Using A Series Connection of Cavities

Figure 4.1a-b schematically represent the structure of the MIMIS multilayer design. In this configuration, the structure is made of; 1) a bottom 70 nm thick metal layer that is an optically thick Al coating acting as a reflecting mirror with no transmission throughout our desired frequency range, 2) an insulating separator having a thickness of D_{IB} that tailors the spectral position of the cavity resonance, 3) a thin partially reflecting/transmitting metal layer with a thickness of D_M to make a MIM cavity, 4) a top insulator layer of D_{IT}, and 5) an ultrathin Ge semiconductor layer to create the MIS cavity resonance mode. The optimized designs have been fabricated as described in the methods section. As shown in Figure 4.1c, the proposed stack formation is confirmed by looking at its scanning electron microscope (SEM) image. During sample milling (by focused ion beam (FIB)) to create a perpendicular side wall, a thin protective Pt is coated on sample. To capture the SEM image, the FIB is used to prepare a cross section of the sample. Therefore, considering the ultrathin thickness of the Ge (in the order of couple of nanometers), it is not possible to distinguish this layer in the SEM image. To evaluate the layer roughness and top Ge layer thickness, the atomic force microscope (AFM) measurement has been carried out. As can be seen in Figure 4.1d, the coated Ge layer has a relatively smooth layer with an RMS roughness value of approx. 0.4 nm. Finally, spectroscopic ellipsometer measurement is used to extract the permittivity values of the deposited Al and Al_2O_3 layers in our desired range, see Figure 4.1e.

To begin with, it is essential to find the ideal materials for each layer of the stack. For this aim, the transfer matrix method (TMM) modeling approach is adopted to find the ideal top layer for the MIM and MIS cavities, as shown in Figure 4.2a. In this model, Al and Al_2O_3 coatings are chosen as thick bottom reflector and separator, respectively. The ideal permittivity values to get a reflection below 0.2 is obtained for four different cases of $D_I = 100$ nm, 200 nm, and $D_M = 5$ nm, 10 nm. The thickness of the bottom Al mirror is set at 100 nm to ensure that light cannot pass across the layer throughout our desired frequency range. The details of the modelling are explained in our previous

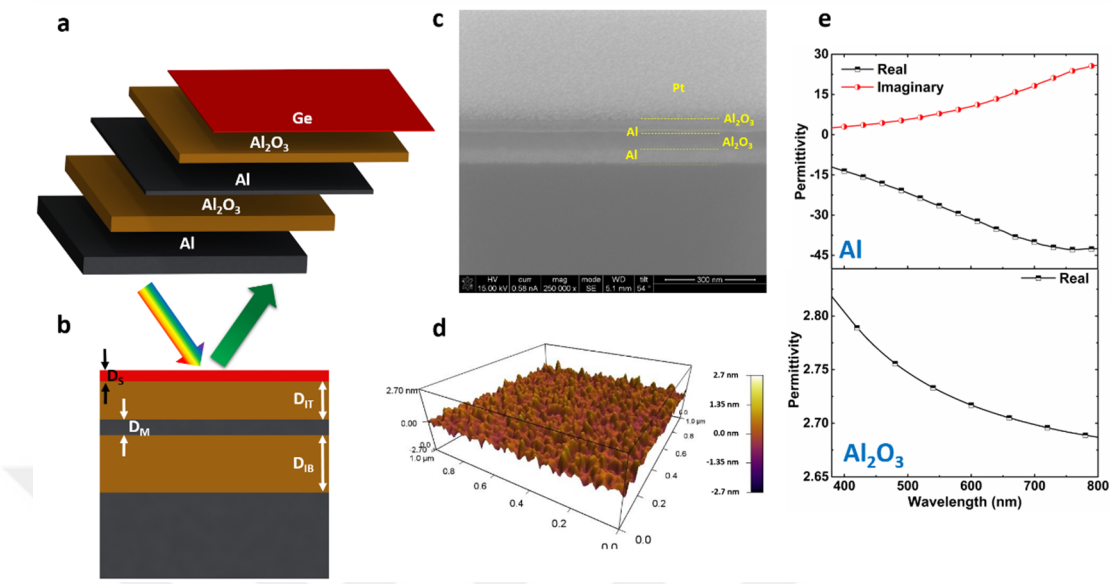


Figure 4.1 (a) The schematic representation of the MIMIS design and (b) its reflection upon excitation with a broadband light. (c) Cross sectional SEM image of the fabricated structure showing the successful formation of different layers. The proposed structure has a thick Al layer that reflects light back into the cavity, an Al_2O_3 layer that defines the spectral position of the reflection peak, a thin Al layer, a top Al_2O_3 insulator layer and top semiconductor Ge layer (d) the AFM image of the top Ge coating. The color bar spans from -2.7 nm to 2.7 nm. As we can see from this map, the top Ge layer has quite low roughness. (e) The experimentally extracted permittivity values for Al and Al_2O_3 layers in the range of 380 nm-800 nm.

study[165] and summarized in the following formulas. In this method, we suppose the MIM (or MIS) stack is surrounded with air having a permittivity of ε_A. For p-polarized light, H_y is considered as:

$$H_y(z) = \begin{cases} A_i e^{ik_A(z-D_M)} + A_r e^{-ik_A(z-D_M)}, & z > D_M \\ M_{11} e^{ik_M z} + M_{12} e^{-ik_M z}, & 0 < z < D_M \\ D_1 e^{ik_I z} + D_2 e^{-ik_I z}, & -D_I < z < 0 \\ M_{21} e^{ik_R(z+D_I)} + M_{22} e^{-ik_R(z+D_I)}, & -D_I - D_R < z < -D_I \\ S_t e^{ik_S[z+(D_I+D_R)]}, & z < -D_I - D_R \end{cases} \quad (1)$$

and by adjusting proper boundary conditions, the amount of reflected wave is calculated as $R = |F_{12}/F_{11}|^2$. Here, $F = \begin{bmatrix} F_{11} \\ F_{12} \end{bmatrix} = a^{-1} m_{11} m_{12}^{-1} d_1 d_2^{-1} m_{21} m_{22}^{-1} s$ where:

$$a=\begin{bmatrix} 1 & 1 \\ ik_A/\varepsilon_A & -ik_A/\varepsilon_A \end{bmatrix},\ s=\begin{bmatrix} 1 \\ ik_S/\varepsilon_S \end{bmatrix},\ (2a)$$

$$m_{11}=\begin{bmatrix} 1 & 1 \\ ik_M/\varepsilon_M & -ik_M/\varepsilon_M \end{bmatrix},$$

$$m_{12}=\begin{bmatrix} e^{ik_M D_M} & e^{-ik_M D_M} \\ ik_M e^{ik_M D_M}/\varepsilon_M & -ik_M e^{-ik_M D_M}/\varepsilon_M \end{bmatrix},\ (2b)$$

$$d_1=\begin{bmatrix} 1 & 1 \\ ik_I/\varepsilon_I & -ik_I/\varepsilon_I \end{bmatrix},$$

$$d_2=\begin{bmatrix} e^{ik_I D_I} & e^{-ik_I D_I} \\ ik_I e^{ik_I D_I}/\varepsilon_I & -ik_I e^{-ik_I D_I}/\varepsilon_I \end{bmatrix},\ (2c)$$

$$m_{21}=\begin{bmatrix} 1 & 1 \\ ik_R/\varepsilon_R & -ik_R/\varepsilon_R \end{bmatrix},$$

$$m_{22}=\begin{bmatrix} e^{ik_R D_R} & e^{-ik_R D_R} \\ ik_R e^{ik_R D_R}/\varepsilon_R & -ik_R e^{-ik_R D_R}/\varepsilon_R \end{bmatrix},\ (2d)$$

and $k_{i=(\mathrm{A,M,I},R,\mathrm{S})}=\sqrt{\varepsilon_i\omega^2/c^2-k_x^2}$ which c is the speed of light in vacuum. Moreover,D_I, D_M, and D_R are the insulator, thin top coating and bottom thick coatings, respectively. The brown and green highlighted areas depict the tolerable region for these four different cases, as shown in Figure 4.2. In other words, if a material's permittivity values are located inside these regions in a specific wavelength range, the cavity can absorb above 80 percent of light. As already explained in the introduction section, our ultimate goal is to design a series connection of two cavities to get light reflection in a narrow wavelength range. Therefore, these two cavities should absorb shorter and longer wavelengths. The above part is an MIS cavity that is responsible for light absorption in shorter wavelengths and should pass the longer wavelengths. The below MIM cavity should absorb the longer wavelengths and reflect the

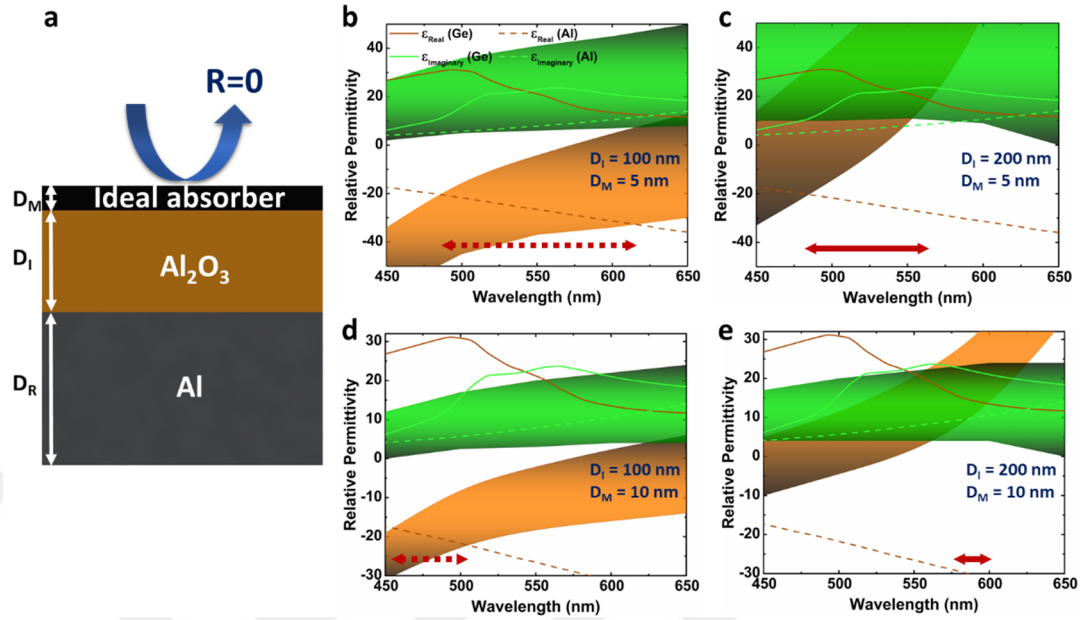


Figure 4.2 (a) The schematic representation of the cavity structure used in TMM model to find the ideal absorber case. The dimensions of the structure have been shown using vertical arrows. The bottom metal layer has a thickness of D_R= 70 nm, the spacer Al_2O_3 layer has a thickness of D_I and top ideal material has a thickness of D_M. The ideal acceptable/tolerable regimes for real and imaginary portions of the permittivity to obtain an absorption above 0.8 for four different cases of (b) D_I= 100 nm, D_M= 5 nm, (c) D_I= 200 nm, D_M= 5 nm, (d) D_I= 100 nm, D_M= 10 nm, (e) D_I= 200 nm, D_M= 10 nm and their comparison with the permittivity values of Al and Ge. In these panels, the brown and green highlighted regions depict the tolerable region for real and imaginary parts of permittivity to obtain a reflection R below 0.1. If the permittivity of a material stays inside these regions, the material can absorb above 0.9 of the incident light. The red arrows show the spectral ranges that have this matching.

shorter ones.[218], [314], [315] Therefore, the semiconductor layer should have a relatively weak absorption in the visible light region and metal layer should be a good reflector. Therefore, we have compared the permittivity values of Al and Ge layers with the ideal model. Figure 4.2b-e show the matching condition of these materials with the ideally tolerable region for four different cases. As can be clearly seen in this figure, at a thin insulator layer thickness of 100 nm, both the real and imaginary parts of Al permittivity can stay inside the region in specific wavelength ranges but there is no matching for Ge in this configuration. However, Ge shows a resonant light absorption in the case of D_I =200 nm. Moreover, based on these results, as material thickness increases from 5 nm to 10 nm, the absorption BW gets narrower and shifts to other wavelength

values. Therefore, both of these materials can act as a nearly perfect absorbers in our desired wavelength range and we only need to optimize the configuration to achieve this goal.

At the first step, we need to find the optimal design geometries for both MIM and MIS cavities. To achieve this goal, numerical simulations are conducted

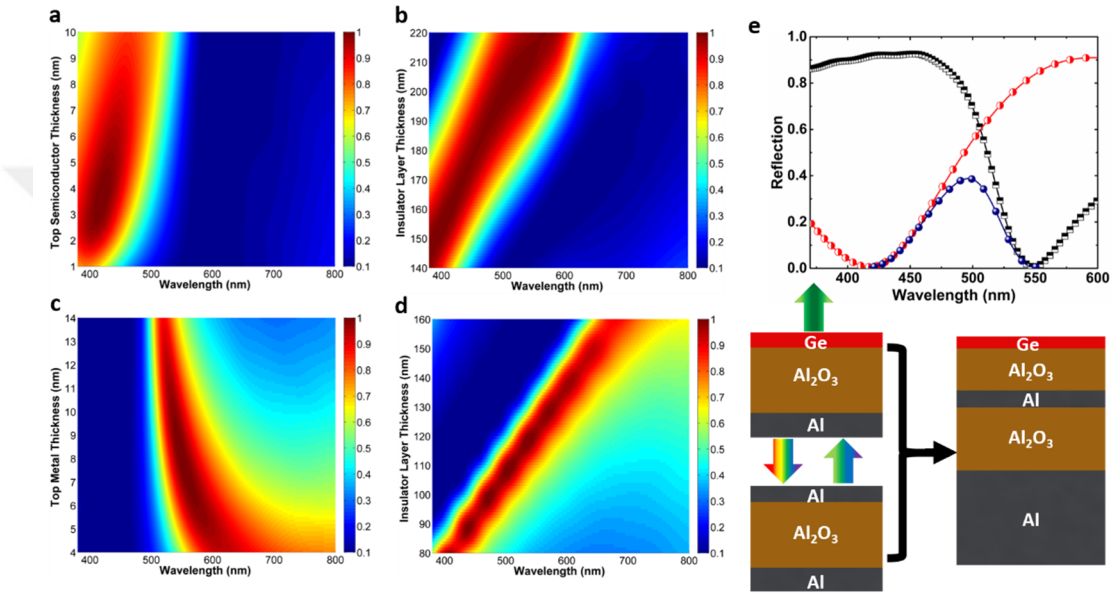


Figure 4.3 The contour plots of the absorption spectra for different (a) D_M and (b) $D_I$values in the Al-Al_2O_3-Ge MIS cavity. Increase in top insulator layer thickness (D_M) makes the absorption strength less and the bandwidth wider. The optimum value is chosen as 3 nm. In this sweep the insulator layer thickness is fixed at 160 nm. By setting the top layer thickness at 3 nm, in the second counter plot, the insulator layer thickness is varied from 140 nm to 220 nm. This plot shows that the spectral position of light perfect absorption gets a red shift as we increase the insulator layer thickness. The absorption contour plot for different (a) D_M and (b) $D_I$values in the Al-Al_2O_3-Al MIM cavity. Similar to MIS case, we first sweep top metal layer thickness while fixing the insulator layer thickness in 100 nm. Considering both absorption strength and bandwidth the optimum top layer thickness is chosen as 9 nm. As shown in the other contour plot, the perfect absorption peak can be tuned by changing the insulator layer thickness. (e) The reflection spectra of the MIM (black), MIS (red), and MIMIS (blue) samples. As we can see from the schematic, the MIM structure absorbs the longer visible wavelengths while MIS cavity harvest the shorter wavelengths. In the spectral range in between these two absorption peaks both MIM and MIS cavities are inactive and light reflection occurs. Therefore, series connection these two cavities (MIMIS) could lead to a narrow light reflection.

using Lumerical FDTD Solutions[316]. The structures are excited with a plane wave in our frequency range of interest which is 380 nm-800 nm. To record the reflection profile (R), a 2D power monitor is placed above the plane wave excitation. Moreover, the absorption spectra (A) of these samples is calculated using $A = 1 - R$ formula. For the permittivity values of Al and Al_2O_3 layers, the experimental data (as shown in Figure 4.1e) are employed. For the permittivity of the Ge layer, the Palik's dispersive material data is utilized[70]. Initially, it is required to find the proper geometries for the MIS cavity. To achieve this, first the thickness of insulating coating is set at a specific value and top material thickness is swept to get the optimum geometries for near unity light absorption (which corresponds to a reflection near zero at that wavelength). Figure. 3a shows the absorption contour plot for different D_M values in the Al-Al_2O_3-Ge MIS cavity configuration in which the thickness of insulator separator (D_I) is fixed at 160 nm. As already explained, our MIMIS color filter works based on the subtraction of two resonance modes of MIM and MIS cavities. Therefore, the absorption spectra of the structure should have a sharp and nearly perfect peak in its resonance condition. Taking this into account, the optimum case is recorded for the Ge thickness of 3 nm. To evaluate the tunability of this resonance, this time, we fixed the Ge thickness at 3 nm and applied a sweep on the insulator layer thickness. Figure 4.3b proves that the nearly perfect light absorption (an absorption above 0.9) characteristic of the MIS design is retained and shifted toward longer wavelengths as the insulator layer thickness increases. Moreover, in line with modeling estimations, the spectral BW of the absorption response gets also wider. Similar to this case, the same route is followed to find the optimized geometries of the MIM configuration where the insulator layer thickness is fixed at 100 nm. For the Al layer, the best result is attained for a thickness of 9 nm and this nearly zero reflection functionality of the cavity design is kept for the thicker insulator layers, see Figure 4.3c-d. All of the above-mentioned results demonstrate that the series connection of these two cavities can provide a reflection type color filter across the whole visible frequency range where the position of the reflection peak is located at the frequency that both of the cavities are inactive. This has been schematically shown in Figure 4.3e. When light impinges on the sample surface, the larger

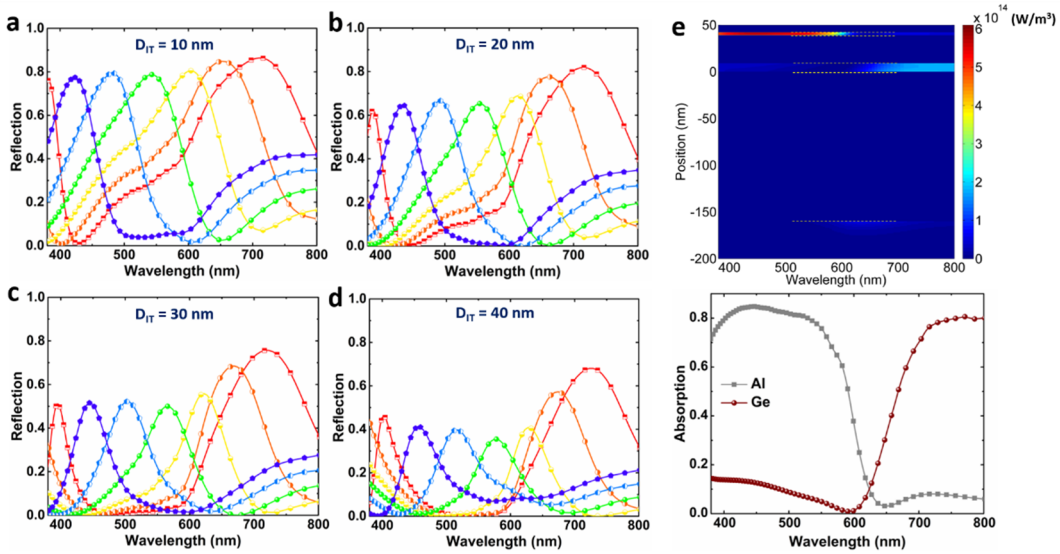


Figure 4.4 The reflection spectra of the MIMIS stack for different D_{IT} values of (a) 10 nm, (b) 20 nm, (c) 30 nm, and (d) 40 nm. In all of these cases, the thickness of bottom insulator is swept from 100 nm to 200 nm with a step size of 20 nm. In these simulations, the bottom metal layer, the middle Al layer and top Ge layer thicknesses have been fixed at optimal values of 70 nm, 9 nm, and 3 nm. (e) The contour plot showing the absorbed power across the MIMIS cavity as a function of incident light wavelength for the case of $D_{IT} = 30\,nm$ and $D_{IB} = 160\,nm$. As we can see the absorption in lower wavelengths occurs at top Ge layer while longer wavelengths are mainly harvested in the middle Al layer. The linear graph also illustrates the amount of absorbed power in the Al and Ge layers.

wavelength values are trapped inside the bottom MIM cavity. In fact, this MIM cavity acts as a partial reflecting mirror that sends back a portion of the spectral region and absorbs the rest. The reflected portion creates a cavity with the above Ge layer and this time the shorter wavelengths would be absorbed. Thus, at the final output, a narrow band-pass reflection type color filter will be made. Unlike conventional MIM and MIS designs that perform as a reflective band-stop filter, this multilayer design operates as a band-pass filter which is necessary for several applications where reflection of a specific color and rejection of rest of the band is needed.

In the next step, we need to scrutinize the role of different geometries on the absorption capability of the MIMIS stack. From the previous section, the optimal thickness values of Ge and middle Al coatings are fixed at 3 nm and 9 nm. The only geometries that can tune the spectral position and amplitude of the

reflection peak are bottom and top insulators that are called D_{IB} and D_{IT}, respectively. To gain insight on the impact of these two values on the reflection spectra of the MIMIS structure, we swept the D_{IB} values for different fixed D_{IT} amounts of 10 nm, 20 nm, 30 nm, and 40 nm. In each of these cases, the D_{IB} has been swept from 100 nm to 200 nm with a step size of 20 nm. Figure 4.4a-d illustrates the reflection spectra of the MIMIS design for different insulator layers thicknesses. As we can clearly notice, the thinner D_{IT} makes the reflection peak stronger but the full width at half maximum (FWHM) gets wider as well. As the thickness moves toward larger values, the amplitude decreases and the color purity (which is a factor effected by the peak BW) increases. Therefore, there is a trade-off between these two factors and D_{IT} is the geometry to provide an optimum condition for MIMIS design performance. Moreover, as already estimated from the modeling results, the bottom dielectric has the role to modulate the spectral position of the peak where an increase in its thickness induces a red shift in the peak position. Taking a look at the simulation results for D_{IT} values smaller than 30 nm, one can see that for the peaks resonating at orange and red frequencies, a small tail is extended toward shorter wavelengths which reduces the color purity of the design. The color purity is related to the resonance width of the reflection peak. Therefore, the optimum choice of D_{IT} thickness, which can simultaneously satisfy both color efficiency and purity, is 30 nm. To have a clear vision on the operation principle of this design, we have plotted the absorbed power profile inside this multilayer cavity as a function of incident light wavelength for the case of D_{IT}= 30 nm, and D_{IB}= 160 nm. Figure 4.4e shows that, at the shorter wavelengths, the upmost Ge layer is the active part of the MIMIS design while the middle thin Al coating gets activated at the longer wavelengths. The absorption inside Ge and Al layers have been monitored and depicted in this figure, as well.

To figure out the validity of our numerical results, we have fabricated and characterized different MIMIS samples with the obtained optimal values of 3 nm, 30 nm, and 9 nm for Ge, top insulator, and middle Al layers, respectively. The bottom insulator layer (D_{IB}) is chosen at different values to generate different colors from ultraviolet (UV) to near infrared (NIR) regime, spanning the whole visible light colors. Figure 4.5a shows the optical image of the fabricated

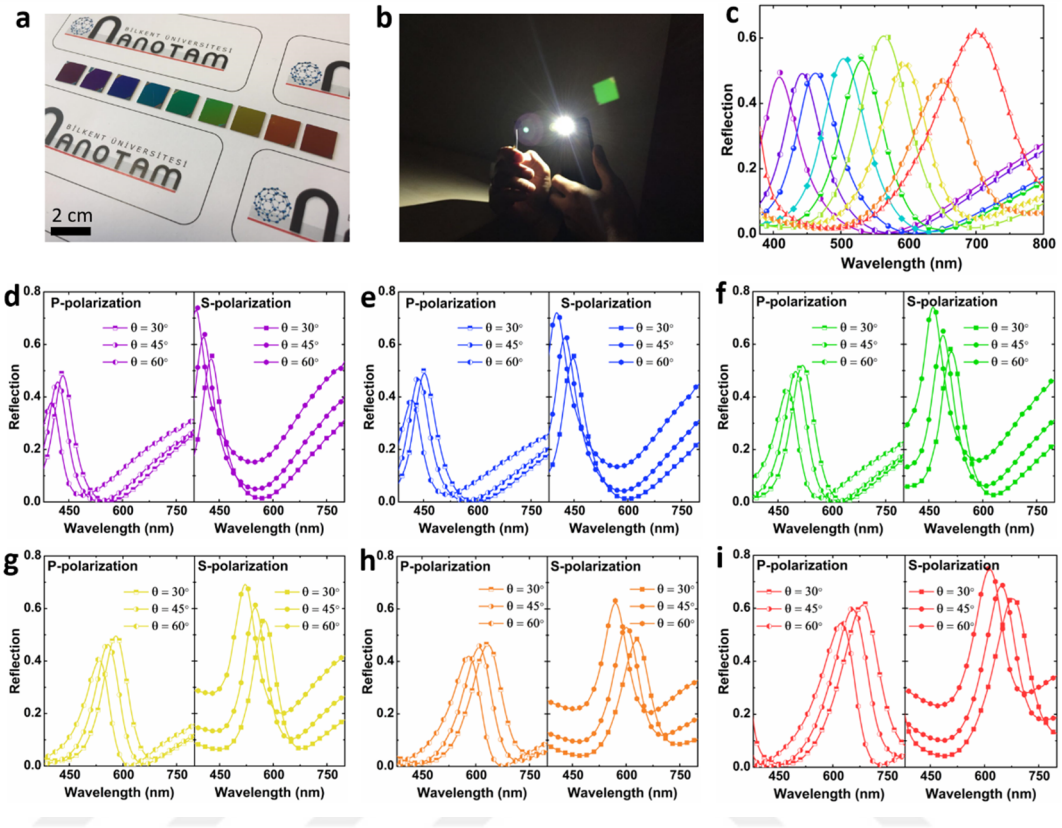


Figure 4.5 (a) The optical image of the fabricated MIMIS designs operating in different wavelengths in the visible regime. In all samples, the bottom metal layer thickness is 70 nm, the middle Al layer is 9 nm thick, the top insulator layer is 30 nm and top Ge layer is 3 nm. The bottom insulator layer thicknesses are 90 nm, 100 nm, 110 nm, 120 nm, 130 nm, 140 nm, 150 nm, 180 nm, and 195 nm. (b) The reflected green color from the fabricated sample upon excitation with white light. (c) The reflection spectra of different colored samples at normal light incidence. These data have been obtained using a reference sample of thick Al mirror as our 100% reflector. The angular response of (d) purple, (e) blue, (f) green, (g) yellow, (h) orange, and (i) red colored filters under different incidence angles (i.e. 30°, 45°, and 60°) and polarizations (S and P). In all samples, the reflection gets a blue shift as we go toward wider viewing angles.

samples. In these samples, the D_{IB} is selected as 90 nm, 100 nm, 110 nm, 120 nm, 130 nm, 140 nm, 150 nm, 180 nm, and 195 nm for all different colored samples. The proposed architecture operates as a band-pass color filter that reflects a desired wavelength range of the incident white light, see Figure 4.5b for the green light color filter that reflects green color from the white incident light. For the optical characterization of the MIMIS multilayer stack, the reflection profiles of the samples are recorded at normal light incidence using

an in-house reflection measurement setup. Figure 4.5c shows the normal incident reflection spectra of different colored MIMIS samples. These results prove that the proposed structure can perform in a good trade-off between color efficiency and purity where the reflection has retained its efficiency relatively unchanged for all of the different colors. As explained in the methods section, we have used a planar thick Al layer as the reference for 100% light reflection. These findings demonstrate that this design principle, which operates based on the series connection of two cavities with two different absorption spectral positions, can provide a simple, EBL-free and up scaling compatible approach to fabricate efficient reflective RGB color filters. In addition, unlike other reported FP based multilayer designs that absorb a narrow frequency range and reflects the rest of the spectrum, this architecture can offer a narrow band-pass filter to reflect a specific color and absorb the remaining region. Another parameter that defines the practical applicability of a color filter is its angular response under oblique light illuminations. Figure 4.5d-i show the angular response of six different colors of violet, blue, green, yellow, orange, and red for two different P and S light polarizations. The light angles of incidence have been chosen as θ =30°, 45°, 60°. As it can be clearly seen, for all the samples, the peak position experiences a blue shift for both polarizations. As the incident light angle gets wider, due to light refraction from different interfaces, the optical path of the light gets larger. Therefore, in all the cases, a blue shift is recorded for the samples upon shining them with an angled light source. Moreover, in this planar design, different Fresnel reflection coefficients for TE and TM polarizations lead to different angular responses. For instance, the blue color filter, resonating at 462 nm for normal incident light, moves its peak to 417 nm, and 401 nm (equivalent to a wavelength difference of $\Delta\lambda$= 45 nm and 61 nm) under an incident angle of 60° for p and s polarizations, respectively. The amount of this shift gets larger as we move to a red color device. For the red color (with a peak reflection at λ_0=700 nm), the amount of resonance spectral shift for p and s polarizations are 77 nm and 86 nm, respectively. To have a better qualitative comparison, the ratio of $\Delta\lambda_0 / \lambda_0$ is compared for three main colors of blue, green, and red. For p polarized incident light, these ratios are 0.09, 0.1, and 0.11 while this amount is increased to 0.13, 0.13, and 0.12 for s polarized light. Therefore, the color of the MIMIS structure is not retained in wide view angles which this, in turn, limits its applicability for practical applications.

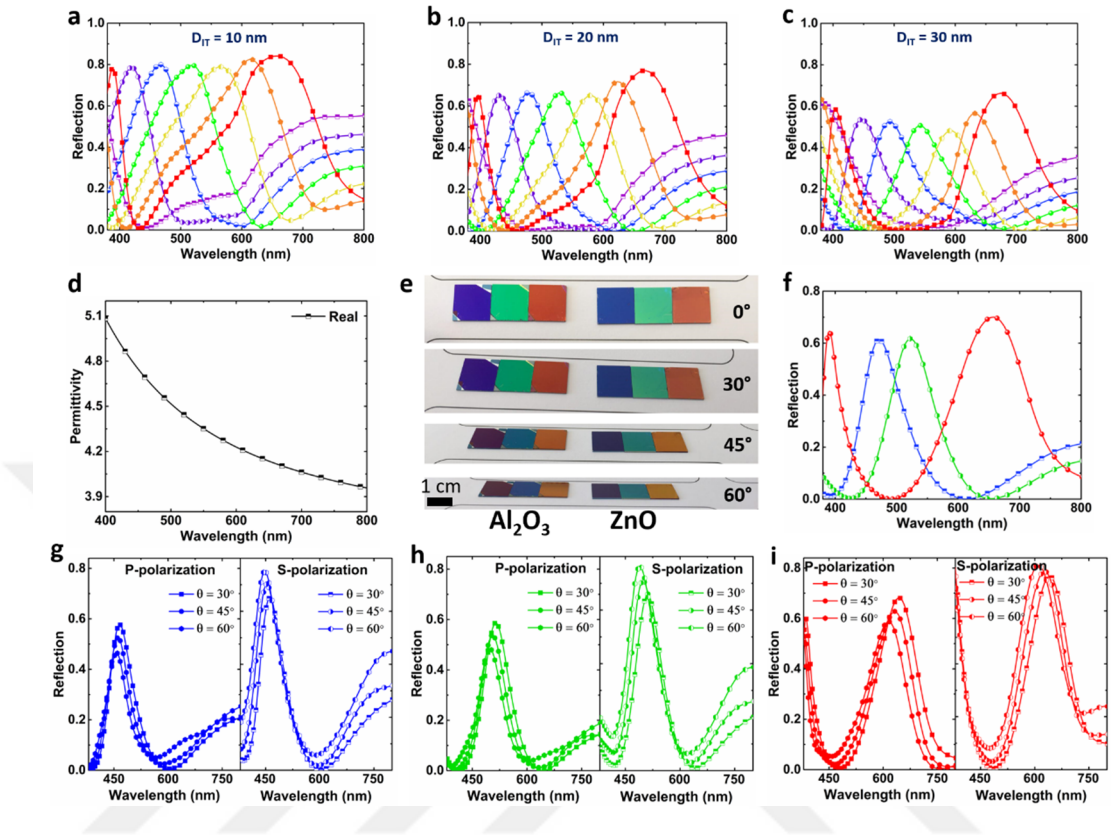


Figure 4.6 (a) The simulated reflection spectra of the ZnO based MIMIS stack for different D_{IT} values of (a) 10 nm, (b) 20 nm, (c) 30 nm. In all the simulations the bottom metal, middle metal, and Ge top layer thicknesses have been fixed at 70 nm, 9 nm, and 3nm. The bottom insulator layer thickness is swept from 55 nm to 145 nm with a step size of 15 nm. (d) The experimentally extracted permittivity values of ZnO layer. (e) The comparison of the angular reflection response of the fabricated Al_2O_3 and ZnO based MIMIS designs. For this aim, a simple white light source was used, and the images are collected at 0°, 30°, 45°, and 60°. (f) The measured reflection response of RGB color filter samples at normal light incidence. In these designs, the top insulator layer thickness is fixed at 20 nm. The bottom insulator layer is chosen as 85 nm (blue), 100 nm (green), and 145 nm (red) to obtain all three main colors. The angular response of (g) blue, (h) green, (i) red color filters under different incidence angles and polarizations. In all of the samples, going toward wider view angles, the absorption peak experiences a blue shift.

It has been demonstrated earlier that a higher refractive index material can be utilized to reduce the angular dependence of the color filters[143], [204], [205], [226] Therefore, this time, Al_2O_3 is replaced with ZnO layer that has a higher light refraction index. In the first step, similar to the previous case, the optimum geometries for top and bottom insulators should be selected. Figure 4.6a-c

illustrates the reflection of the ZnO based MIMIS design for three different D_{IT}values of 10 nm, 20 nm, and 30 nm. For each case, the bottom ZnO layer thickness is swept from 55 nm to 145 nm with a step size of 15 nm. It is worth noting that the experimentally extracted permittivity values of the ZnO layer (as shown in Figure 4.6d) have been utilized in all the simulations. According to these results, this time the optimal case can be chosen as D_{IT}= 20 nm where a fine trade-off between reflection amplitude and its FWHM can be recorded for all the colors. Moreover, the reflection values are larger compared to that of Al_2O_3. Therefore, employing a high index insulator layer can provide a higher color efficiency. To evaluate our numerical findings, the optimal MIMIS designs are fabricated and optically characterized in our desired frequency range for three main colors of red, green, and blue. The bottom insulator layer thickness is picked as 85 nm, 100 nm, and 145 nm which corresponds to blue (λ_0= 471 nm), green (λ_0= 521 nm), and red (λ_0= 657 nm) colors. It should be noted that the Ge and middle Al layers thicknesses are similar to the previous design. Figure 4.6e compares the optical image of the fabricated samples for two different cases of Al_2O_3 and ZnO based MIMIS configurations. As can be clearly realized, ZnO based samples have a much better tolerance for oblique angle light incidence where even in extreme view angles they have a slight change in their color. As explained in the previous studies[317], the variation of the resonance wavelength is inversely proportional to the refractive index of the dielectric layer in a metal-insulator pair based design. Therefore a high-index spacer layer can provide a better angular performance. In other words, as the refractive index of the insulator layer increases, based on Snell's law, the refracted light gets closer to 90° and, therefore, the path difference between different angles becomes smaller. That is why ZnO has a better angular response compared to Al_2O_3. To evaluate this property, the normal incident reflection spectra of the samples are recorded for these three cases, as shown in Figure 4.6f. This panel proves that the fabricated samples have a reflection amplitude higher than 0.6 with a relatively narrow FWHM. The angular responses of these three samples are also plotted at Figure 4.6g-i. Similar to previous measurement, these spectra have been collected for both p and s polarizations. These results prove that the use of ZnO has significantly improved the angular response of the MIMIS cavity. Under incident angle of 60° for p polarized light, the shift in the resonance wavelength are $\Delta\lambda_0$ =14 nm, 24 nm, and 43 nm for blue, green, and red colors, respectively. These values are

found to be 25 nm, 32 nm, and 49 nm for s polarization case. The resonance wavelength change ratio ($(\Delta\lambda_0) / \lambda_0$) can be also obtained for these samples to be able to have a qualitative comparison with previous samples. For the blue color, these ratios are 0.02 and 0.05 for p and s polarizations, respectively. For the red color reflecting sample, these values are found to be as 0.06 and 0.07 which are almost half of the ones obtained for the Al_2O_3 based MIMIS sample. Therefore, the utilization of a high index dielectric can simultaneously improve both efficiency and angular insensitivity of the samples. This work shows the extraordinary function of the tandem shaped cavities. As our future work, this design can be modified in a way that higher color efficiencies can be obtained. Moreover, using a simple fabrication technique, we can make spatially variant filters. In this case, sample is placed inside the chamber in a way that one part of it is close to the source and the other corner is far. By using this fabrication approach, a gradient insulator layer thickness is made. Thus, this in turn leads to monolithically integrated spatially variant color filters.

In summary, for the first time in the literature, this work presents an efficient design strategy based on an MIMIS configuration to obtain RGB band-pass color generation at the reflection mode that cannot be attained with a conventional FP resonator. For this purpose, at the initial step, the optimal materials and geometries for each of the layers are found. Then, the proposed optimal design is fabricated and characterized for different colors spanning the whole visible region. Finally, to improve the angular response of the system, the dielectric medium is replaced with a higher refractive index layer. The final results demonstrate the formation of high efficiency RGB colors with a reflection above 0.6 and a wide view angle where the color is retained almost unaltered in wide view angles. Under an incident angle of 60° for p polarized light, the shifts in the resonance wavelength are $\Delta\lambda_0$ =14 nm, 24 nm, and 43 nm for blue, green, and red. The resonance wavelength change ratio ($(\Delta\lambda_0) / \lambda_0$) for the blue color device was found to be 0.02 and 0.05 for p and s polarizations, respectively. For the red sample, these values were 0.06 and 0.07, which demonstrates the efficient operation of these samples. The overall structure is a planar and EBL-free one which can be produced by simple preparation routes. The obtained results of this paper can be extended to other type of FP resonators where a proper connection of cavities can propose functionalities that cannot be attained in the conventional single cavity designs.

4.4. Bismuth Based Metamaterials: From Narrowband Reflective Color Filter to Extremely Broadband Near Perfect Absorber

To begin with, as shown in Figure 4.7a, the ideal permittivity data is extracted for an ideal MIM and MIMI light perfect absorber. For this aim, as stated above, TMM is utilized. The details of this modeling approach have been already provided in our previous studies [318]. In this modeling, the thickness of bottom Ag meal layer is chosen as D_R, which is an optically thick mirror with no transmission and near unity reflection. The middle ideal absorber material has a thickness of D_M which is sandwiched with two symmetric insulator layers with a thickness of D_I. For this insulator layer, lithium fluoride (LiF) is chosen because it provides us the opportunity to deposit the whole structure in a single thermal evaporation step. Clearly, similar dielectrics such as Si, MgF_2, SiO_2 or TiO_2 can be also used as dielectric layer but they have generally high melting temperature and thermal evaporation is not a suitable technique for their deposition. Before analyzing the ideal condition for obtaining near perfect absorption in these designs, it is better to revisit the permittivity data of common metals and compare them with that of Bi. Figures 4.7b-c depict the real and imaginary parts of permittivity for different metals including Au, W, Ni, Ti, and Bi. For Bi, we experimentally extracted this permittivity profiles while for other metals, Palik's model is employed [70]. It can be clearly seen that, as we go toward longer wavelength values, the real permittivity data gets an exponential drop toward negative values for all different metals. However, Bi shows an extraordinary permittivity response. It stays in small negative values, in visible and short NIR ranges and becomes positive in longer wavelengths. Moreover, it has smaller imaginary parts compared to other types of metals.

The ideal permittivity data for an absorption above 0.9 is extracted for different design geometries in MIM and MIMI configurations. These ideal regions are highlighted with brown (for real part) and green (for imaginary part). For a specific wavelength, if permittivity data of a metal is located within this area, it means that structure can harvest above 90 percent of incident light. To understand the impact of different geometries in the overall absorption response of the system, we have extracted the ideal data for different D_M and D_I values. These different combinations have been extracted for MIM case and

the obtained ideal regions are compared with permittivity data of Bi, see Figures 4.7d-f. As these panels clearly show, in ultrathin absorber thicknesses of D_M = 5 nm, the matching cannot be acquired for imaginary part of epsilon. However, increasing the thickness of the layer to 20 nm, the ideal region can be perfectly matched with that of Bi permittivity data for both real and imaginary parts, up to 2.5 μm. At the same time, increasing the insulator layer thickness can be used as a parameter to tune the optical response of the system. For D_M = 20 nm, two different D_I values of 120 nm and 180 nm are studied in panels e and f. The ideal region for imaginary part is almost same for both cases but the real part experiences a red-shift, as expected. Thus, it is envisioned that the absorption upper edge cannot be altered by increasing spacer layer. On the other end of the scale, we can see that for all cases, there is a mismatch in the visible part of spectrum. The spectral position of this mismatch moves toward longer wavelengths as we increase the insulator layer thickness. In fact, this mismatch is located in the wavelength range where we have poor absorption behavior and strong reflection response. The same parametric study is conducted for MIMI case, as shown in Figures 4.7g-i. Similar behavior is recorded for the MIMI case with this difference that the ideal region is wider compared with that of MIM case. Moreover, the spectral width of notch characteristic is narrower compared to that of MIM design. Therefore, all these results tell us that MIMI case has better functionality compared to MIM cavity. To check the validity of our modeling estimations, the numerical simulations, using a commercial finite-difference time-domain (FDTD) software package (Lumerical FDTD Solutions)[316], are further employed to investigate the absorption capability of the MIM and MIMI cavity designs. In the first step, the optimum D_M dimension is found for a fixed D_I value of 140 nm. As clearly seen from Figure 4.8a, the absorption response of the MIM design is quite weak for an ultrathin top layer thickness of 5 nm. This is in accordance with our theoretical findings. The increase in the top layer thickness makes the absorption amplitude stronger and the BW wider. However, at the meantime, a broad dip in the absorption profile starts to appear in middle wavelength range (1-2 μm). To analyze these results, we have to review the theoretical findings for the ideal model in Figure 4.8. Increasing the top layer thickness, makes the bottom limit of tolerable region smaller for imaginary part of epsilon. The same behavior is recorded for

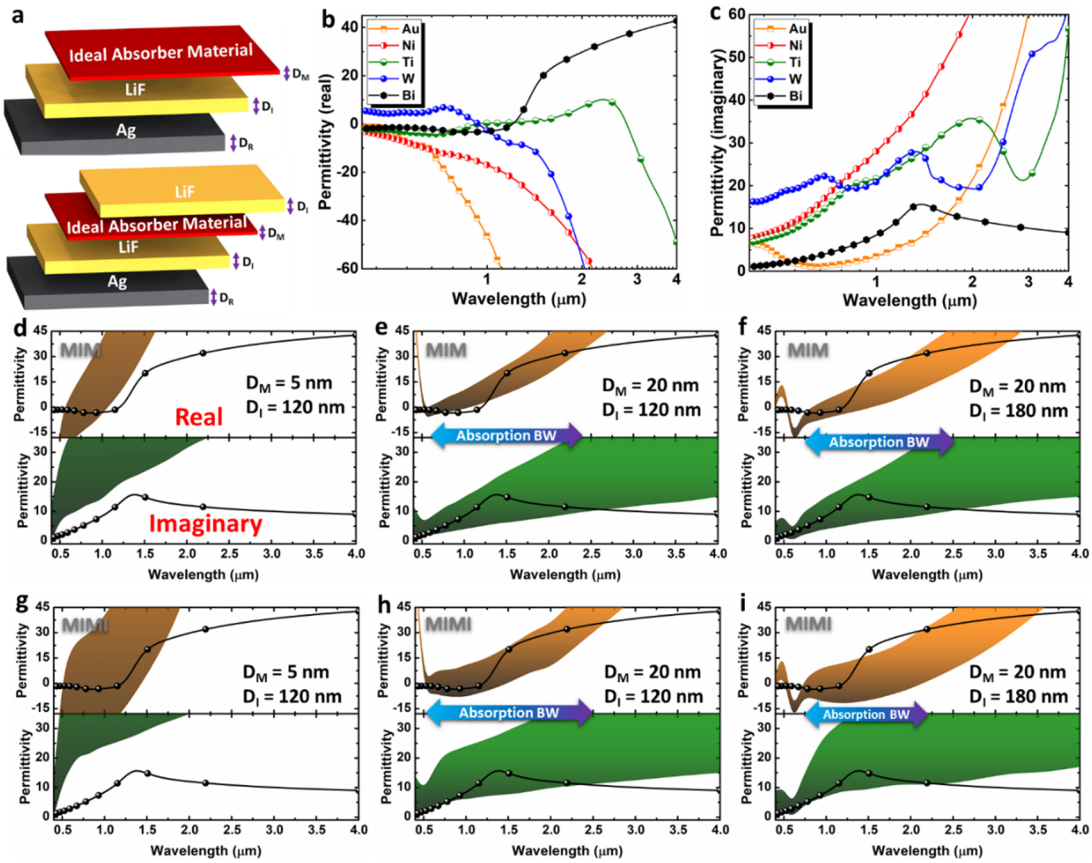


Figure 4.7 (a) The schematic representation of MIM and MIMI cavity designs. The (b) real, and (c) imaginary parts of permittivity for different type of metals including Bi. The extracted ideal absorption regions for real and imaginary parts of permittivity in a MIM cavity design for three different configurations of (d) D_M = 5 nm and D_I = 120 nm, (e) D_M = 20 nm and D_I = 120 nm, (f) D_M = 20 nm and D_I = 180 nm. The extracted ideal absorption regions for real and imaginary parts of permittivity in a MIMI cavity design for three different configurations of (g) D_M = 5 nm and D_I = 120 nm, (h) D_M = 20 nm and D_I = 120 nm, (i) D_M = 20 nm and D_I = 180 nm.

real part (compare the ideal regions in Figures 4.7d and Figure 4.7e). Thus, while overall matching for both components is extended toward longer wavelength values, a mismatch starts to appear in real part for middle wavelength values. This mismatch shows itself as a dip in absorption. Therefore, a moderate thickness value should be chosen to have strong and nearly flat light absorption in a broad wavelength range. For this aim, the optimal value for D_M is picked as 20 nm where the absorption profile stays above 0.8 throughout the whole operation regime. Fixing the top layer thickness in this optimal amount, this time, we investigate the impact of D_I thickness on

the harvesting capability of the design. The sweep on D_I thickness is conducted from 110 nm to 230 nm with a step size of 30 nm. As we see in the Figure 4.8b, moving toward thicker spacer layers, the response experiences a red-shift but the absorption stays above 0.8 in the operation BW of the design. This is also in agreement with our theoretical estimations. Similar parametric study is applied for the MIMI configuration, as shown in Figures 4.8c-d. For this case, the optimal value for D_M is found as 25 nm. However, the response in this case is stronger and the near unity absorption is satisfied in a broader wavelength range. For instance, in MIM and MIMI cases for D_M = 20 nm and D_I = 140 nm geometries, absorption stays above 0.8 throughout 0.63-2.45 μm and 0.56-2.59 μm, respectively. Moreover, the absorption profile for MIMI case is quite flat and near unity.

Another feature that should be discussed in these figures is the visible response of these configurations. As it can be clearly seen, a strong and narrow notch is appeared for both configurations and the spectral position of this notch monolithically shifts toward longer wavelength values as we increase the

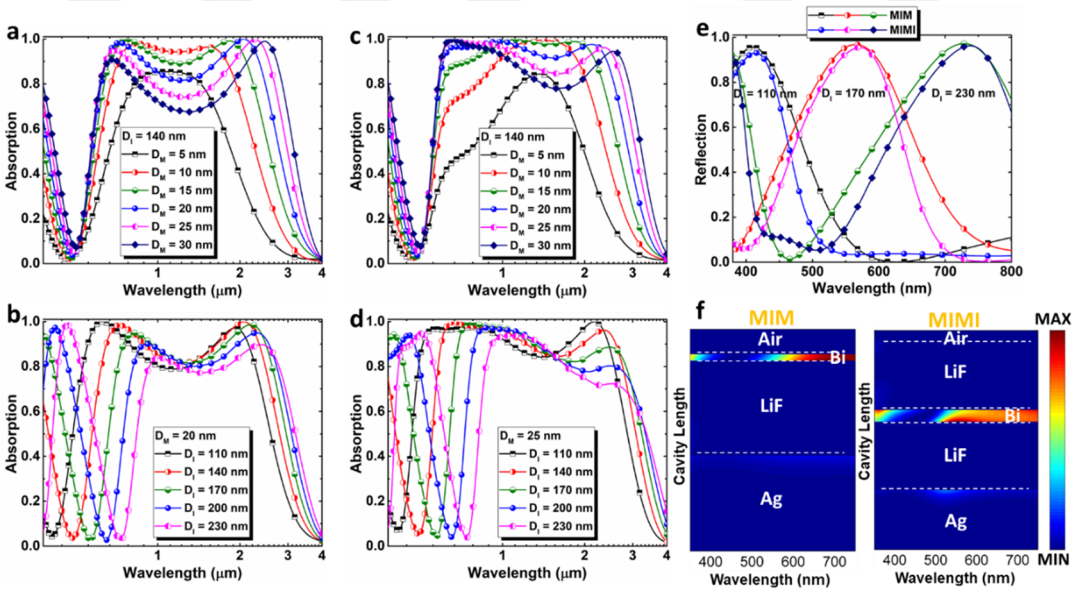


Figure 4.8 The absorption spectra of the MIM design for different (a) D_M and (b) D_I values. The absorption spectra of the MIMI cavity for different (c) D_M and (d) D_I values. (e) The reflection spectra of the MIM and MIMI designs in visible frequency range for three different D_I values of 110 nm, 170 nm, and 230 nm. (f) The absorption contour plot across the cavity for MIM and MIMI architectures for the case of D_I = 110 nm.

spacer thickness. Considering the fact that this structure has no transmission, this notch behavior in absorption profile is equivalent to a peak in reflection response of the design. Therefore, this means the structure is acting as a reflective red-green-blue (RGB) color filter. In a common planar lithography-free fabry-perot (FP) cavity design (such as MIM), the structure performs as a band-stop filter at the reflection mode that absorbs a narrow frequency range and reflects the rest of the spectrum [223], [224]. In these FP resonators, the RGB additive colors and their complementary subtractive ones of cyan-magenta-yellow (CMY) can be obtained in transmission and reflection modes, respectively. Therefore, the generation of RGB additive colors is not possible in these designs and they can create these colors in the transmission spectra. But due to the inherent loss of the materials, transmissive color filters are in general less efficient compared to that of reflective ones (generally limited to efficiencies below 0.7)[317]. However, the extraordinary optical response of Bi metal provides the opportunity to create these RGB colors in the reflection with reflection amplitudes as high as near unity. Thus, this structure will simultaneously act as ultra-broadband perfect absorber and narrowband perfect reflector. To compare the reflective behavior of the MIM and MIMI designs, we have drawn the reflection spectra for three different D_I values with the optimal D_M for each case. As we can see from Figure 4.8e, the reflection peaks for both configurations have almost same amplitude but the spectral width for the MIMI cavity is narrower. This is actually beneficiary for color filtering application of these structures where narrower peaks lead to more pure colors and less crosstalk. Hence, the MIMI cavity is not only better from absorption broadness perspective, but also it provides narrower reflection peaks. The profile of the absorbed power versus the incident light wavelength is plotted across the cavity in Figure 4.8f. As we can see from this panel, the middle Bi layer becomes transparent into the incident wave in the resonance wavelength of the reflection peak. This transparency is retained in a narrower range for the MIMI cavity design, compared to that of MIM case.

To verify our modeling and simulation results, the optimized MIMI configurations were fabricated using single thermal evaporation step. The bottom metal layer was set as Ag, the insulator layers were chosen as LiF, and the middle layer was Bi. Figure 4.9a shows the cross-sectional scanning electron microscopy (SEM) image of the fabricated design. This image shows

the successful formation of MIMI cavity structure with an optimal Bi layer thickness of 24 nm which is quite close to our intended goal. The bottom layer thickness was ~ 70 nm to act as a mirror in our operation wavelength. The LiF layer thicknesses were picked as 105 nm, 130 nm, 150 nm, 190 nm, 220 nm to generate five different visible light colors; blue, cyan, green, orange, and red. The optical image of these five different samples have been shown in Figure 4.9b. The use of proper materials as insulator and metal layers can provide us the opportunity to

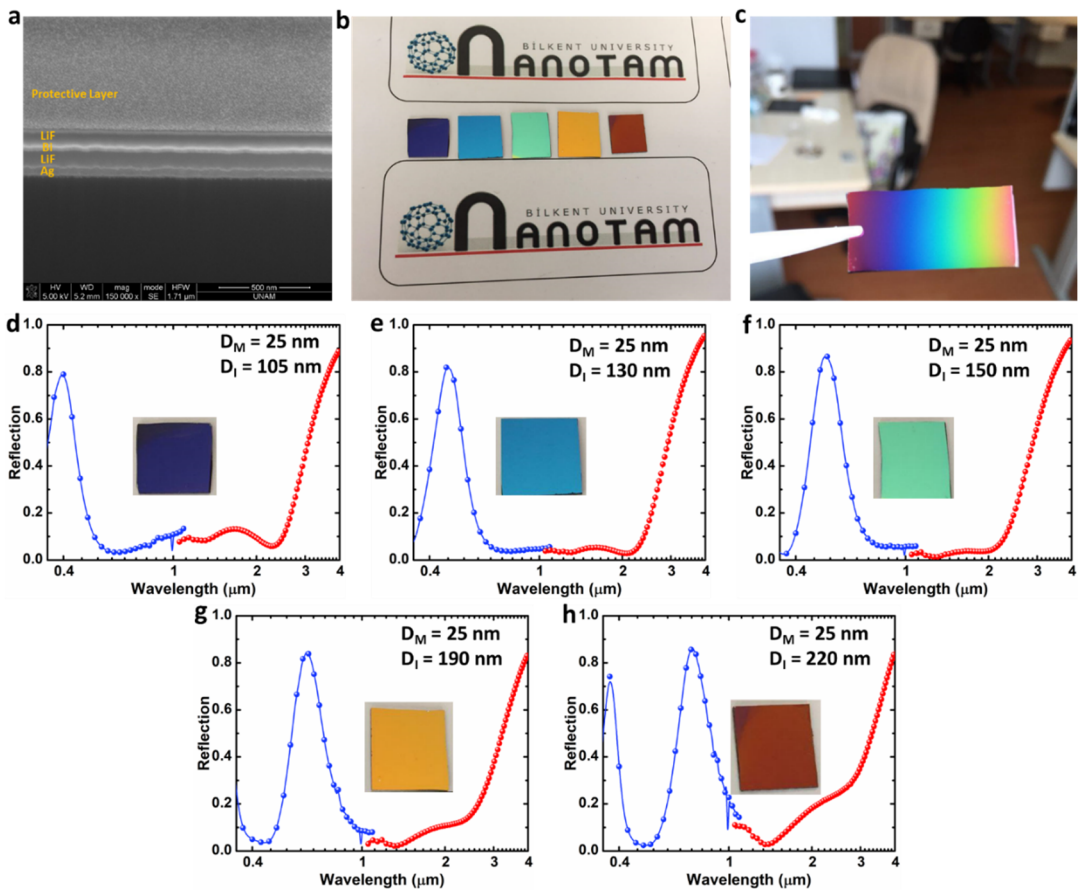


Figure 4.9 (a) The cross sectional SEM image of fabricated Ag-LiF-Bi-LiF MIMI cavity. (b) The optical image of fabricated samples with different insulator layer thicknesses of 105 nm, 130 nm, 150 nm, 190 nm, and 220 nm. Each of these thicknesses leads to generation of a specific color in reflection mode. (c) A monolithically designed spatially variant color filter by linear variation of insulator thickness across the sample, by adjusting the geometrical parameters of the deposition system. The normal incident absorption spectra of the MIMI cavity for different D_I values of (d) 105 nm (blue), (e) 130 nm (cyan), (d) 150 nm (green), (d) 190 nm (orange), and (d) 220 nm (red). In all samples, the Bi layer thickness was 25 nm which the optimal value.

fabricate a planar and spatially tunable color filter using a simple evaporation step. Getting benefit from this property, we made a thickness variant multi-color high efficiency color filter design. The distance between the evaporation source and sample corners can be adjusted in a way that the insulator layer thickness linearly increases from one end to the other. The details of this fabrication have been provided in experimental section. The normal incident reflection spectra of the MIMI designs throughout 0.35-4 μm range have been depicted in Figures 4.9d-h. The reflection spectra of the structure for D_I = 105 nm shows a reflection peak at 399 nm, corresponding to blue color. The same structure shows reflection below 0.1 (corresponding to an absorption above 0.9) across an ultra-broadband range spanning from 0.51 μm to 2.51 μm. For the case of 130 nm thick spacer layers, the reflection peak moves to 467 nm and the perfect absorption region (absorption above 0.9) spans a 0.62–2.42 μm range. The absorption BW decreases for other three colored samples while the reflection peak monolithically red shifts. These experimental results are in great agreement with our modeling and simulation findings. For all colors, the reflection peak amplitude stays above 0.8 which shows a high efficiency color generation out of a planar design. Thus, as stated above, the cavity architecture represents both ultra-broadband perfect absorption and spectrally selective narrowband perfect reflection.

To understand the angular response of the cavity, the absorption spectra of the design is measured under p and s polarized light for three different incident angles of θ=30°, 45°, and 60°. The angular reflection response of the cavity has been depicted in Figures 4.10a-e. These results have been measured in the range of 0.35-2 μm using a V-Vase ellipsometry equipment. The overall trend for all five different samples is similar. For both polarizations, the increase in incident light angle leads in a blue shift in the reflection peak of the structure. This is expected considering the fact that the optical path length of the light increases as light impugns surface in a wider view angle. This could be mitigated by the use of a higher refractive index medium as spacer[317]. Based on Snell's law, higher refractive index makes the incident light more closely to normal direction and this consequently reduces the angular dependency of the result. Moreover, the absorption strength of the design is retained high for all these wide incident angles. For p polarized excitation, the absorption amplitude becomes larger as we go toward larger angles while for s polarized light, the

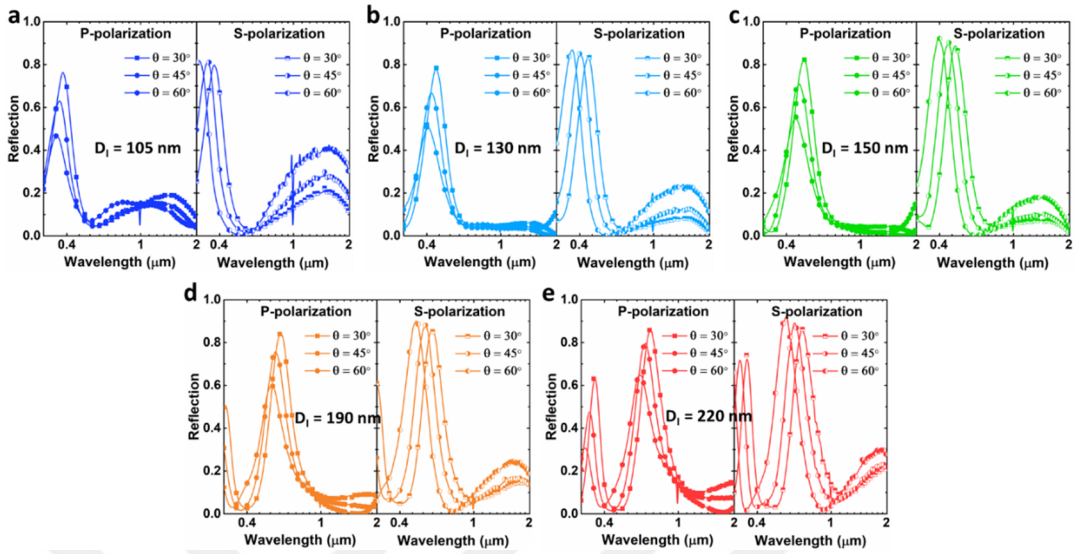


Figure 4.10 The angular response of (a) blue, (b) cyan, (c) green, (d) orange, and (e) red colored filters under different incidence angles (i.e. 30°, 45°, and 60°) and polarizations (s and p). In all samples, the reflection gets a blue shift as we go toward wider viewing angles.

perfect absorption capability gradually diminishes. This is due to different reflection coefficients seen by incident light in these two different incident light polarizations. It should be mentioned that Bi has low melting point which limits its thermal stability and its potential use in high temperature applications, such as thermal photovoltaics. However, from optical perspective, it has many advantages compared to other noble metals. As explained in the theoretical section, the absorption bandwidth in other noble metals based absorbers is much narrower and solar irradiation cannot be fully harvested. However, the broadband absorption response of Bi layer can be of great interest for energy conversion applications such as hot electron based photodetection, photovoltaics and photoelectrochemical water splitting. The temperature levels in these applications are generally much below the melting point of Bi metal. Moreover, the color reflective behavior can be employed in filtering and colorometric sensing which is again low thermal-budget applications. Moreover, Bi is a low-cost earth-abundant element, unlike other precious and rare metals such as gold. As future studies, our group is currently working on development of Bi based optoelectronic devices on abovementioned applications.In this study, we revealed extraordinary optical response of Bi metal in design of deep sub-wavelength resonant cavities. Using a modeling

approach based on TMM, we first found the ideal condition for light perfect absorption. While all other common metals can only satisfy this ideal condition in visible and short NIR range, Bi is perfectly matched to it in an ultra-broadband frequency range. Additionally, the structure was predicted to act as a narrowband perfect reflector in visible range. Thus, a same cavity can propose two distinct functionalities. Afterward, numerical simulations are employed to find the optimal geometries for achieving the best performance. The characterization results of the fabricated samples show that the MIMI cavities have both ultra-broadband near perfect absorption and narrowband perfect reflection where the spectral position of the reflection peak can be easily tuned by chaining the spacer insulator layer thickness. It was found that this planar structure can absorb above 90 percent of incident light in an extremely broadband regime spanning from 0.51-2.51 μm. To the best of our knowledge, this is the highest absorption BW reported compared to any MI pair based planar design. Moreover, the structure can create RGB colors in reflection mode with high efficiency, high purity, and low crosstalk which is generally cannot be achieved using common FP based designs. All in all, the findings of this study demonstrate a high potential for Bi metal to be used in optical devices. This paper shows the importance of the material selection for design of deep sub-wavelength optical cavity structures.

Chapter 5. LFMAs for Sensing Application

5.1. Preface

This chapter of the thesis is based on the publications:

”*Lithography-free disordered metal–insulator–metal nanoantennas for colorimetric sensing*”, Z. Eftekhari, A. Ghobadi, E. Ozbay, **Optics Letters.** 2020, 45, 6719 – 6722. Adapted (or “Reproduced in part”) with permission from OPTICA Publishing Group.

”*Lithography-Free Random Bismuth Nanostructures for Full Solar Spectrum Harvesting and Mid-Infrared Sensing*”, M. Can Soydan, A. Ghobadi, D. Umut Yildirim, E. Sarıgül Duman, A. Bek, V. Behcet Erturk, E. Ozbay, **Advanced Optical Materials.** 2020, 8, 1901203. Adapted (or “Reproduced in part”) with permission from John Wiley and Sons.

5.2. Motivation

Biosensors have revealed their tremendous potential in many applications, including medical diagnosis, food safety, and environmental monitoring. However, their main use is in the detection of analytes and bio-agents such as disease biomarkers and contaminants. Based on the detected signal, biosensors can be classified as optical (such as plasmonic biosensors), electrochemical, piezoelectric, or magnetic biosensors [319], [320]. Among -all biosensors, optical biosensors are one of the most commonly used tools for analytical biosensing due to their high sensitivity, specificity, potential for real-time sensing, and cost effectiveness [321], [322].

One the most commonly used colorimetric optical sensing schemes is based on localized surface plasmon resonances (LSPRs) and propagating surface polaritons (PSPs), since noble metal nanostructures show LSPR in the visible frequencies [51], [323]–[328]. In this configuration, upon the excitation of LSPRs, absorption and scattering cross section of noble metallic nanoparticles are greatly enhanced, and extremely intense and localized electromagnetic fields are created in “hot-spots” [329]–[332] . These high intensity spots enable these devices to track any small change in the dielectric environment surrounding these nanostructures [9]. However, this can also be considered as a drawback for these systems. The non-uniform lateral field intensity in these designs causes a limitation on their detection capability [329], [331]. For example, in a periodic design, we have high field localization in the gap between units and low enhancement at the top of the units. Therefore, depending on the location of bio-agent with respect to the unit, the field enhancement and resonance shift can change. Although a single plasmonic antenna can also be used for detection, the probability of overlapping of a molecule with this single element is quite low. That’s why they are not a viable solution for practical use. Besides this technical limitation, these plasmonic sensors are mainly high cost precious-metal based designs or their fabrication demands expensive tools such as electron beam lithography (EBL) which is not a large-scale compatible tool. It should be noted that some innovative EBL-free designs have been proposed in recent years[333], [334]. Moreover, dielectric based metasurfaces were found to be promising to replace the precious-metal based plasmonic sensors [335]–[338].

The above-mentioned scalability requirement can be solved by planar design since they do not need any lithography and pattering. Strong optical interference in metal-insulator (MI) and metal-semiconductor (MS) pair based designs can be used to achieve ultra-broadband perfect absorbers and narrowband color filters [2], [35]. The most widely used cavity design color filter is a metal-insulator-metal (MIM) configuration. In a typical MIM design, a specific wavelength is absorbed by the cavity and the rest of the spectrum gets reflected. This creates a set of subtractive colors called the CMY (cyan-magenta-yellow) model. In a recent paper, we showed that high efficiency RGB (red-green-blue) colors can be made using Bi metamaterials [339]. However, the resonance frequency of an MIM color filter is defined by the spacer layer thickness and refractive index that has no contact with

the surrounding environment. That's why these planar cavity designs have been rarely used for sensing application [340]–[342]. To be able to use them in sensing applications, nanostructuring is needed to provide an area for the interaction with the surrounding environment. However, in the meantime, the fabrication route for nanostructuring should be large scale compatible.

Similar to visible range, plasmonic narrowband absorbers in mid-infrared (MIR) range can be used for sensing application. Many different nano- pattern configurations were employed for achieving narrow- band absorbers that are highly sensitive to the changes in the dielectric properties of their surroundings.[367–380] Liu et al. designed an MIM nanodisk narrowband perfect absorber with a sensitivity of 400 nm RIU^{-1} (refractive index unit). They also developed a planar metamaterial that has cutout structures in a thin gold film as an analog of an optically bright dipole antenna and an optically dark quadrupole antenna.[367] This metamaterial sensor that is based on coupling effects experimentally yielded a sensitivity of 588 nm RIU^{-1}. Lee et al. designed gold nanoslit arrays on a glass substrate that demonstrates a sensitivity of 668 nm RIU^{-1}.[368] Di Meo et al. designed polarization insensitive cross-shaped plasmonic nanoantennas based a chemical sensor with a sensitivity of 600 nm RIU^{-1}.[369] Yong et al. theoretically proposed a unit cell with four very close cylindrical nanodisk metal–metal (MM) architectures that can operate as a refractive index sensor with a sensitivity of 885 nm RIU^{-1}.[370] Pang et al. designed a nanohole array surface plasmon resonance (SPR) biosensor that can reach 1520 nm RIU^{-1} sensitivity for certain cases.[371] Jin et al. demonstrated a highly sensitive integrated optical biosensor based on two cascaded microring resonators with a sensitivity of 1300 nm RIU^{-1}.[3722] Overall, not only is there room for improvement in the sensitivity, devices with more straightforward fabrication routes are also highly desirable. Last, but not the least, to the best of our knowledge, almost all of the designs in the literature function either as a broadband or narrowband absorber; so having each functionality in the same device remains a research problem.

5.3. Lithography-free disordered metal-insulator-metal nanoantennas for colorimetric sensing

To design and analyze this system, we first perform finite-difference-time-domain (FDTD) simulations on a planar configuration. Later, to estimate the effect of the induced randomness, the transfer matrix method (TMM) theoretical analysis is conducted. Finally, the optimized design is fabricated and characterized. To obtain a nanostructured spacer layer, the oblique angle deposition technique is used, which is a room temperature and large scale compatible approach with no material limitation. Based on the obtained optical results, visible light colors can be realized with this MIM antenna design. Upon deposition of a dielectric layer (as the modeling agent for biomarkers), the resonance frequency is red-shifted and a sensitivity as high as ~84 nm/refractive index unit (RIU) can be achieved. Moreover, the color (the position of resonance peak) of the MIM biosensor can be passively adopted by the spacer layer thickness. The proposed design strategy offers a highly sensitive, robust, and compact biomolecular diagnostics with a real-time, label-free, and early point-of-care diagnosis that can be used in various applications such as drug detection and environmental monitoring.

To gain an insight on the resonance condition of a Bi based MIM design, we initially begin our analysis using a planar design model, as shown in Figure 5.1a. The spacer layer is made of lithium fluoride (LiF) with a thickness of D_I. The bottom and top layers are Bi. The top layer thickness is D_M, while the bottom layer is an optically thick layer with no transmission in the visible range. To realize the influence of the geometrical dimensions upon the absorption response, we utilized the Lumerical (FDTD) simulation package. In the FDTD simulations, we illuminated the unit cell with a broadband plane wave at normal incidence whose electric-field is polarized in the x-direction. Prior to these simulations, the permittivity values of bulk Bi and LiF layers have been experimentally extracted using a spectroscopic ellipsometer, as explained in detail in our previous work [339]. The permittivity data of Bi has been shown in Figure 5.1b. Due to superior matching of the Bi permittivity data with that of an ideal absorber, the MIM design can absorb all of the frequencies except for the ones with constructive interference. This can be seen from the absorption contour plot shown in Figure 5.1c. As this panel implies, the

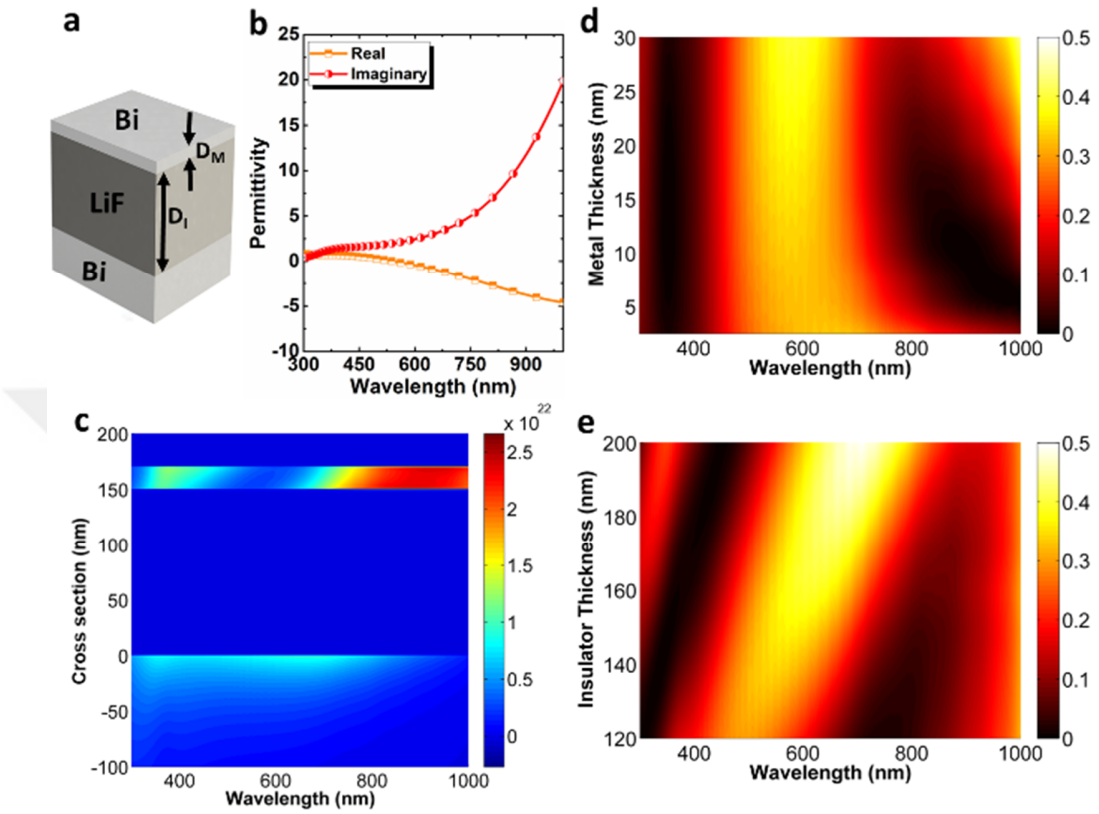


Figure 5.1 (a) Schematic representation of the proposed MIM cavity with its (b) extracted spectral permittivity of Bi (both real and imaginary) in our desired range of 300 nm-1,000 nm. (c) The two-dimensional profile of the absorbed power across the MIM cavity as a function of incident light wavelength. Sweep and optimization of reflection spectra for different geometries of (d) D_M (while the $D_I$is fixed at 150 nm) and (e) D_I (while the $D_M$is fixed at 20 nm).

incident light is dominantly absorbed in the top layer and it shows a notch in the middle of the simulated spectrum. By this design, a spectrally selective reflection peak can be achieved and a reflective RGB color filter can be realized. To optimize the color purity, we need to reduce the full-width-at-half-maximum (FWHM) of the reflection peak and broaden the absorption bands to avoid multi-color reflection. For this purpose, the top layer thickness is initially swept while the spacer layer thickness is fixed at 150 nm. Figure 5.1d shows the dependence of the reflection spectra of the MIM design to D_M. As implied from this plot, as $D_M$increases, the

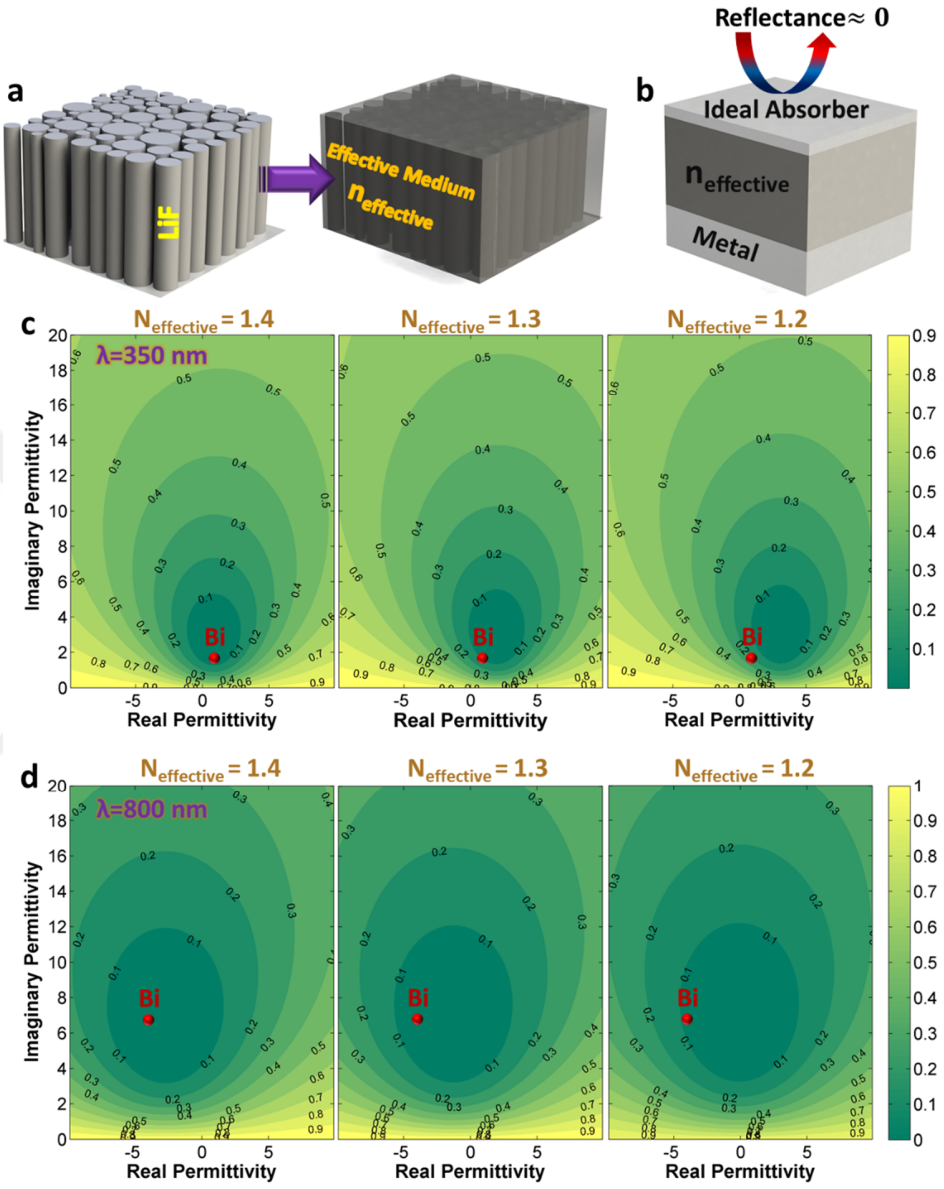


Figure 5.2 (a) Schematic illustration of the real LiF NR design and its effective medium model. (b) The MIM ideal absorber used to extract the reflection contour plots. The TMM extracted reflection contour plots for three different $N_{effective}$ of 1.4, 1.3, and 1.2 for incident light wavelengths of (c) 350 nm, and (d) 800 nm.

FWHM of reflection gradually narrows. However, at large dimensions, a new Reflection peak starts to appear in off-resonance frequencies. Therefore, a trade-off should be followed to have the best color purity, and for this, $D_M$is depicted as 20 nm. In the next step, the spacer layer influence on the reflection response of

the MIM cavity is investigated, as shown in Figure 5.1e. In this panel, the reflection peak experiences a nearly linear red shift as the thickness increases. Therefore, based on the desired color, the D_I can be modified to tune the spectral position of the reflection peak.

All of the above-mentioned results prove the RGB color generation of a planar Bi based MIM cavity. Yet, the spectral position of this MIM cavity is defined by the spacer optical thickness (both thickness and refractive index). Therefore, a change in color requires a tuning on the spacer layer. However, in a planar configuration, this layer is capped by the top metal absorber and it has no interaction with an outside dielectric region that is air. Due to this reason, it cannot be a good option for the colorimetric optical sensing of an unknown agent. To make it functional for sensing purposes, the nanostructuring should be introduced into this architecture to enhance its active surface area. In other words, the planar MIM layer should be split into sub-wavelength MIM nanoantennas with ultra-small gaps for the sensing agent diffusion. Therefore, instead of a bulk LiF layer, we need to have nanorod designs. However, the question is “can we keep the reflective color generation property of planar MIM design in a nanoantenna MIM configuration?”. Based on effective medium theory, sub-wavelength dielectric geometries can be modeled as a bulk system with an effective refractive index that is a value between air and dielectric indices, as shown in Figure 5.1a. To predict the absorption response of this effective medium MIM design, we use a modeling approach based on TMM. As explained in detail in our previous studies [2], [339] in this model, we fix the geometries ($D_I = 150$ nm and $D_M = 20$ nm), and the spacer layer material (as LiF) and look for an ideal absorber material data (with near zero reflection) for the top coating. Then, we compare this ideal material permittivity data with that of Bi. Figure 5.1b shows our model used in TMM modeling. For this design, the reflection contour plots have been extracted as a function of top material real (Re(ε)) and imaginary (Im(ε)) permittivity parts. In these panels, for instance, staying within 0.1 circle means that the MIM design is below 10% reflection at that wavelength. These contour plots have been acquired for three different spacer effective refractive indices ($N_{effective}$) of 1.4, 1.3, and 1.2 to simulate different LiF nanorods (NRs) filling fraction. The resonance wavelengths of 350 nm and 800 nm are chosen for these plots, since the light absorption of Bi top layer is maximum at

these wavelengths. For 350 nm incident light wavelength, Figure 5.2c, reducing the $N_{effective}$ causes a slight shift in the reflection circles. However, in all three conditions, Bi data stays within 0.2 circle. The same holdsfor the 800 nm excitation, as exhibited in Figure 5.2d. Therefore, nanostructuring of LiF does not ruin the absorption optical response of the MIM cavity. Specifically, in the case of high $N_{effective}$, we can have a quite similar response with the planar design. This implies that higher packing density is more favorable. On the other hand, in all panels, the ideal point (the zero reflection point) shifts toward more negative Re(ε), as the effective refractive index increases. Looking at the Bi permittivity data, we can see that as the wavelength increases, the Re(ε) moves toward negative values. This matching is quite promising from sensing the point of value. This means that as we expose these MIM nanoantennas into a biomarker adsorption, the $N_{effective}$ increases and the reflection dip shift toward longer wavelengths. All of these theoretical calculations predict the high functionality of a tightly packed MIM nanoantennas absorber in colorimetric sensing.

In the next step, we have to find a fabrication route to realize these LiF NRs in large scales. Among the various large scale compatible nanostructuring techniques, oblique angle deposition is an effective approach to fabricate nanostructures with no material restriction. Specifically, for dense high aspect ratio structures, where the EBL becomes challenging, this approach can provide a robust solution. Figure 5.3a schematically depicts the proposed MIM nanoantenna design with multiple NRs radii. Every NR is capped with a thin Bi layer. To realize this design configuration, we first deposit a 150 nm Bi layer on a diced Si substrate. This layer is coated by the thermal evaporation technique (VAKSIS tool). The deposition rate was set at ~2 Å/s and the chamber pressure was kept below 5e-6 Torr throughout the process. Afterward, oblique angle deposition is utilized to fabricate LiF NRs, as explained in detail in our previous study [339]. The deposition conditions were the same as the Bi layer, but only the rate was 5-6 Å/s to create a better nanotexturing. Finally, a 20 nm thick Bi layer is coated on top of the NRs to complete the fabrication of disordered MIM nanoantennas. It should be noted that the size of the samples are 1 cm* 1 cm. Due to the large scale compatibility of the fabrication route, this dimensions can be up scaled. To verify the formation of this hybrid design, scanning electron microscopy (SEM) imaging is utilized. Figure 5.3b

exhibits the existence of standing tightly packed LiF NRs with sub-wavelength radii. According to Figure 5.3c, the deposition of Bi thin film has not led to continuous layer formation and the surface morphology has not changed. Therefore, a biomarker analyte can diffuse within its small gaps and tune the cavity's effective index. In this way, upon adsorbent deposition, the resonance wavelength shifts and consequently the color changes. This has been graphically explained in Figure 5.3d. To demonstrate the biosensing capability of our disordered MIM

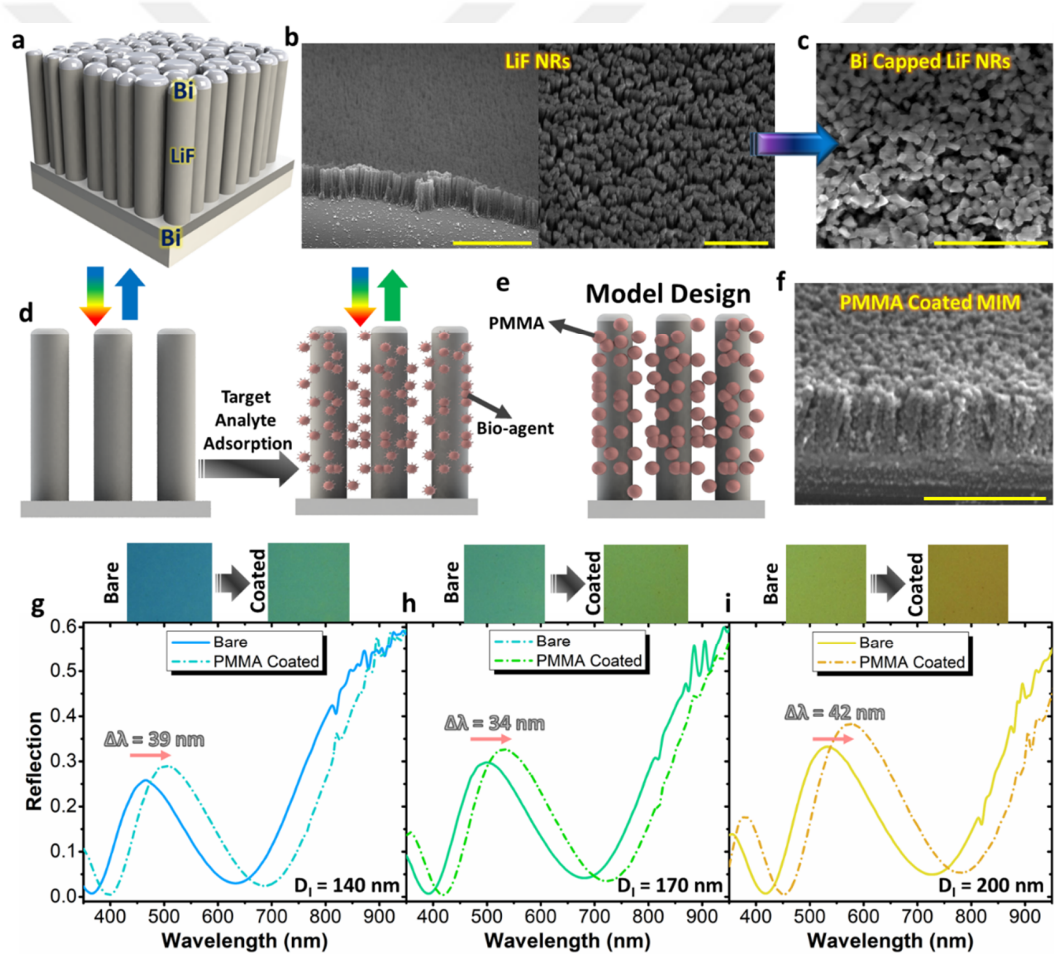


Figure 5.3 (a) Simplified schematic illustration of the disordered MIM nanoantennas design. The SEM images of the (b) bare LiF NRs and (c) the ones coated with a thin Bi layer. (d) The operation principle of our proposed biosensor. (e) The model design and (f) its cross sectional SEM image. In all of the SEM images, the bar length is 400 nm. The reflection spectra of the bare and PMMA coated MIM nanoantenna samples for three

different D_I values of (g) 140 nm, (h) 170 nm, and (i) 200 nm. At the top of this linear plots, the optical images of bare and PMMA coated samples are depicted.

nanoantenna, a model design is used, as shown in Figure 5.3e. To model these bio-agent analytes, we spin-coated the MIM cavity with 495Poly(methyl methacrylate) (495PMMA) A2 to coat the NRs surface and the gaps in between, as depicted in the SEM image in Fig 5.3f.

To evaluate the colorimetric response of this disordered MIM nanoantenna array design, the optical reflection response of the structure is evaluated for three different D_I values of 140 nm, 170 nm, and 200 nm, see Figure 5g-i. The three different thicknesses are used to generate three different colors. The reflection spectra of these MIM nanoantennas, in the range of 350 nm-950 nm, before and after PMMA coating have been measured using a homemade setup. In this setup, a halogen lamp is used as the light source, integrated with a microscope to collect the reflection data. This collected reflection data is transferred into a spectrometer (Newport Corporation; Irvine, CA, USA) (Newport OSM2). In all of the measurements, the obtained reflection values are normalized with that of a thick Al sheet. To have a better visualization, the optical image of the samples before and after coating have been shown ontop of the spectral reflection plot. For the case of D_I = 140 nm, the PMMA coating has caused a 39 nm shift in the reflection peak position. Taking the PMMA refractive index to be ~1.5 in these frequencies, the maximum experimental sensitivity of the nanosensor is recorded as S_{max} = $\Delta\lambda/\Delta n$ = 39 nm/(1.5 −1.0) = 72 nm/RIU. The same characterization has also been conducted on D_I = 170 nm, and 200 nm, where the resonance red shift was found to be 34 nm and 42 nm (corresponding to the S_{max} values of 68 nm/RIU and 84 nm/RIU).

Overall, this work demonstrates a design strategy to realize a sensitive, real-time, and label-free optical biosensing scheme. The proposed route is a large scale and extendable approach that can be adopted for other MI combinations. The detailed design, analysis, and characterization results show the unprecedented potential of this random plasmonic platform for many optoelectronic applications.

5.4. Lithography-Free Random Bismuth Nanostructures for Full Solar Spectrum Harvesting and Mid-Infrared Sensing

In an effort to scrutinize the impact of the parameters on absorbance performance and to understand the physical phe- nomena governing our device, numerical simulations were conducted for a simplified version of the fabricated sample using the commercial Lumerical FDTD Solutions software package. It is critical to mention that randomly distributed nanorods cannot be exactly modeled in the simulation region due to the random shape of the fabricated nanorods and unpre-dictable surface roughness. Therefore, we considered a simpler test device, whose schematic is shown in Figure 5.4. This device comprises nanorods of radius *R* and length *L* that are periodic in two directions with a period, *P*. In this design, the incident electromagnetic radiation interacts with metallic nanorods and, consequently, it is diffracted into the metal nanorod–air com- position and excites several modes. These are mainly the longi- tudinal resonant modes among the nanorods because metallic nanostructures elongated at one direction can support multiple longitudinal and transverse modes[34] which are mainly local-ized surface plasmon resonances (LSPRs). A nanorod in this structure can be considered as a monopole antenna where SPRs are excited at the Bi–air interface.First, we investigated the role of the height of each nanorod, L, on the absorbance spectrum, by sweeping L, while fixing R and P at 80 and 200 nm, respectively. As Figure 5.4b clearly illustrates, the proposed nanoantenna has multiple longi-tudinal modes that appear as straight lines. For L< 200 nm, only the dominant mode is excited (which is the first-order longitudinal mode) and near unity absorbance is acquired in a narrow spectral range. As the rod length becomes larger, multiple absorbance modes are supported with the design and superposition of these modes leading to a broadband near unity absorbance, which are in line with the

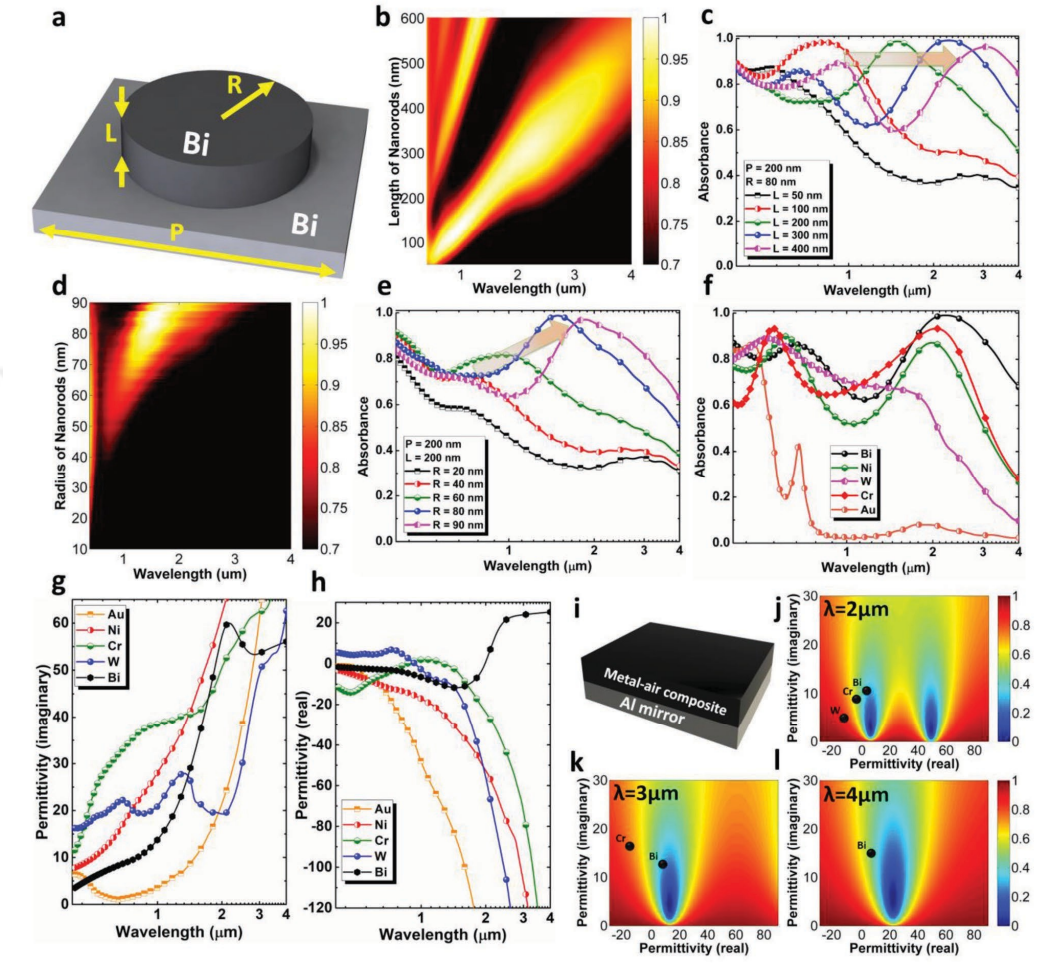


Figure 5.4 Parameter effect and modeling. a) The perspective view of the unit cell of designed two-layered structure. b) Contour plot of absorbance for the length parameter. c) Sweep and optimization of *L* from 50 to 400 nm while *P* = 200 nm and *R* = 80 nm. d) Contour plot of absorbance for radius parameter. e) Sweep and optimization of *R* from 20 to 90 nm while *P* = 200 nm and *L* = 300 nm. f) Absorbance performance comparison of Bi with Au, Cr, Ni, and W in FDTD simulation. g) Real and h) imaginary parts of the permittivity of the given materials. i) Generalized case of designed MM structure with a thick Al layer as a common reflector and an effective medium of metal nanorod–air composition. Contour plot of reflection of the structure in panel (i) and effective permittivity of the upper layer as a dot at the wavelengths of j) λ = 2 μm, k) λ = 3 μm, l) λ = 4 μm. In panels (j)–(l), f_1 was chosen as $f_1 = (\pi R^2)/P^2 = 0.503$ for *R* = 80 nm and *P* = 200 nm.

previous findings. Moreover, the absorbance strength continuously grows stronger with increasing nanorod lengths as expected because the excited

modes are mainly longitudinal modes, and new modes are excited with increased nanorod lengths. Furthermore, a slight redshift of the resonance wavelengths occurs in longer nanorods. It is clearly seen in Figure 1c that lower order modes (resonances at longer wavelengths) have weaker absorbance peaks at resonances of higher order modes (resonances at shorter wavelengths) because as the order of modes is increased, the modes get closer and the coupling between them becomes stronger. At sufficiently high values of L, the absorbance profiles of different modes overlap with each other and, therefore, absorbance approaches unity. When it is increased too much, however, their overlap decreases because of the different amount of redshift that occurs for different res-onances. Therefore, the optimal L value was chosen as 300 nm to have a fair trade-off between the absorbance amplitude and bandwidth.Another critical design parameter is the rod's transverse dimension, which is R. For this plot, L and P are each fixed at 300 and 200 nm, respectively, and R is swept. Figure 1d shows the resonance modes for different radius values. When nanorods have a small radii, absorbance performance is quite poor because of the low packing density, in other words, the large gap distances between neighboring nanorods. In fact, the response is mainly originated from the bulk absorbance of the Bi bottom plate. As the radius increases (or correspondingly the gap distances are reduced), the dominant peak becomes stronger and shifts to longer-wavelength values, which is also observed in Figure 1e. According to previous studies, the EMW confinement in deep subwavelength nanogaps can cause a spectrally narrow EMW absorption.[51] In addition, as the gap reduces, this absorption peak experiences a redshift. These are in line with our findings. When the packing density is higher, the strong field localization between the nanorods and the

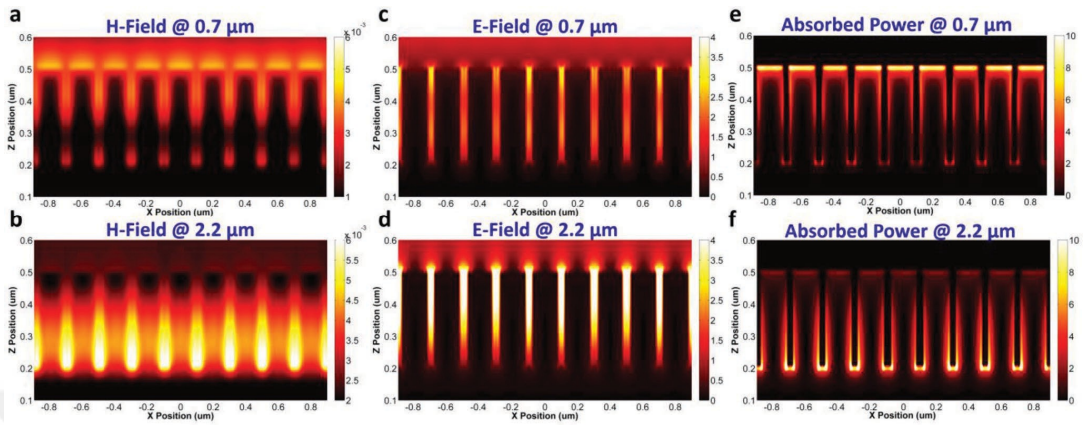


Figure 5.5 Field Profiles. H-field profiles at a) 0.7 µm and b) 2.2 µm. E-field profiles at c) 0.7 µm and d) 2.2 µm. Absorbed power profiles at e) 0.7 µm and f) 2.2 µm.

cou-pling of incident radiation to the low Q-factor LSPRs, due to the lossy nature of Bi, lead to perfect EMW harvesting in a broad-band wavelength regime, when the packing density is high.However, a disparate phenomenon is observed in the shorter wavelengths. The high packing density will turn this nanostruc-ture design into a semimirror bulky structure and, therefore, the absorbance in shorter wavelengths will be diminished. Therefore, a wise design should have multiple gap sizes to cover both spectral regions. To find an optimum size, we pre-ferred to choose the largest bandwidth with at least 0.7 absorb-ance to have satisfying absorptive properties in the Vis and NIR regions; therefore, we continued to have simulations with a radius of 80 nm.Despite the fact that it is difficult to obtain a broadband perfect absorber with an MM structure, since metals are reflective due to their high refractive indices at the Vis and infrared regimes, our results demonstrate that the proposed Bi-based MM structure has a remarkably strong absorb-ance response. Such a strong absorbance in an MM structure can then be attributed to the excellent optical properties of Bi. To prove this argument and to compare Bi with other common metals, the optimum absorbance of the MM struc-ture for each different metal was extracted by simulating them with the above-mentioned strategy. The comparison of these metals with Bi is shown in Figure 5.4f. This figure reveals the superior absorbance performance of Bi in comparison with the lossy metals, such as Cr, Ni, W, and Au (a noble metal). While these metals, except for Au, show a similar absorbance spectrum up to 2 µm,

Bi maintains its performance in the NIR and MIR regimes, although the absorbance of the other metals decreases abruptly to the levels as low as 0.3. Such an outstanding absorbance performance arises from the unique optical property (i.e., permittivity) of Bi. Although Bi and other metals share a similarity in terms of the imaginary part of their corresponding permittivities (see Figure 5.4g), the dis-persion of the real part of the permittivity of Bi is completely different than the other metals, as shown in Figure 5.4h. The real part of the complex permittivities of Bi and other metals are close to each other up to 2 μm, similar to their absorb-ance performance in Figure 5.4f. Nevertheless, the real part of the permittivities of other metals abruptly decreases to large negative values after 2 μm, whereas the real part of the permittivity of Bi assumes positive values. It is this distinctive feature of Bi that enables the Bi-based MM absorber to have a significantly better performance compared to the absorbers with other metals for wavelengths larger than 2 μm. In fact, bismuth acts as a plasmonic metal in shorter wavelengths and a lossy dielectric in longer wavelengths.

In The next step the effective permittivity of the design is extracted.The calculated effective permittivity values for all of these materials are projected as black dots onto the reflection contour plots in Figure 5.4j–l. In this figure, the blue semicircles are per-mittivity values that lead to a reflection below 0.3 (or equiva-lently an absorbance above 0.7). At a wavelength of 2 μm, Bi and Cr are located in the vicinity of this ideal circle. However, for larger wavelengths, these blue regions correspond to the areas that require large positive real permittivities. In fact, at a 4 μm incident EMW wavelength, only the effective permittivity of Bi is located in the close proximity of the perfect absorption circle. Thus, any composition of a metal other than Bi (with a permittivity that has a negative real part) and air (whose permit-tivity is 1) cannot satisfy this ideal condition. However, Bi, with a positive real permittivity, can satisfy this matching condition upon finding the proper disk dimensions. Therefore, this verifies the aforementioned uniqueness of the optical response of the Bi layer to achieving ultra-broadband EMW absorption in an MM design configuration.To better understand the nature of the excited modes and how optical radiation is confined inside the nanorods at the resonance

wavelength, electric (E-field) and magnetic (H-field) plots, and absorbed power graphs are shown in Figure5.5a–f at two different wavelengths of 0.7 and 2.2 μm that correspond to the positions of absorbance peaks. When the structure is con-sidered from a monopole antenna standpoint, multiple surface plasmon polaritons (SPPs) at different wavelengths are excited at the Bi–air interface. The excited resonant plasmon modes confine the H-field of the incident EMW mostly at the top of the nanorods at shorter wavelengths depending on the order of the modes. At the Vis region, the material properties become the dominant factor in determining the overall reflection from the structure. Near-ideal index matching between Bi nanorod–air composition and the environment (i.e., air) results in absorption at the interfaces. At longer wavelengths, small gaps between adjacent nanorods result in stronger field localiza-tion due to the interaction between metallic nanostructures.[51]Thus, incident H-field is mostly confined at the bottom of the nanorods and very small gaps, as shown in Figure 5.5a,b. E-field is mainly localized at the gaps along the nanorods, as shown in Figure 5.5c,d. From Figure 5.5e,f, it can be seen that optical energy is mostly confined and harnessed at the top edges of the nanorods at 0.7 μm while this energy is localized around the side walls at the bottom of the nanorods at 2.2 μm. The EMW confinement region is observed to shift into the bottom parts of the nanorods and become stronger with an increasing wavelength. It can be inferred from the resemblance between the H-field and absorbed power localization regions that the structure exhibits magnetic dipole characteristics.Our discussions up to this point have indicated the extraor-dinary absorbance response of Bi metal. It is demonstrated that a strong absorbance can be acquired in a periodic pattern of Bi nanostructures in an MM configuration. Sub-stantial improvement in absorbance can be accomplished by introducing a disorder into the geometries of the design. It was shown that the changes in L and R are an effective tool in manipulating the spectral position and strength of the absorbance peak. This randomness can be applied not only to the geometrical parameters but also to the orientation of nanorods. In such an architecture, multiple absorbance peaks can be superposed to achieve an overall flat, perfect absorbance throughout an ultra-broadband wavelength regime.

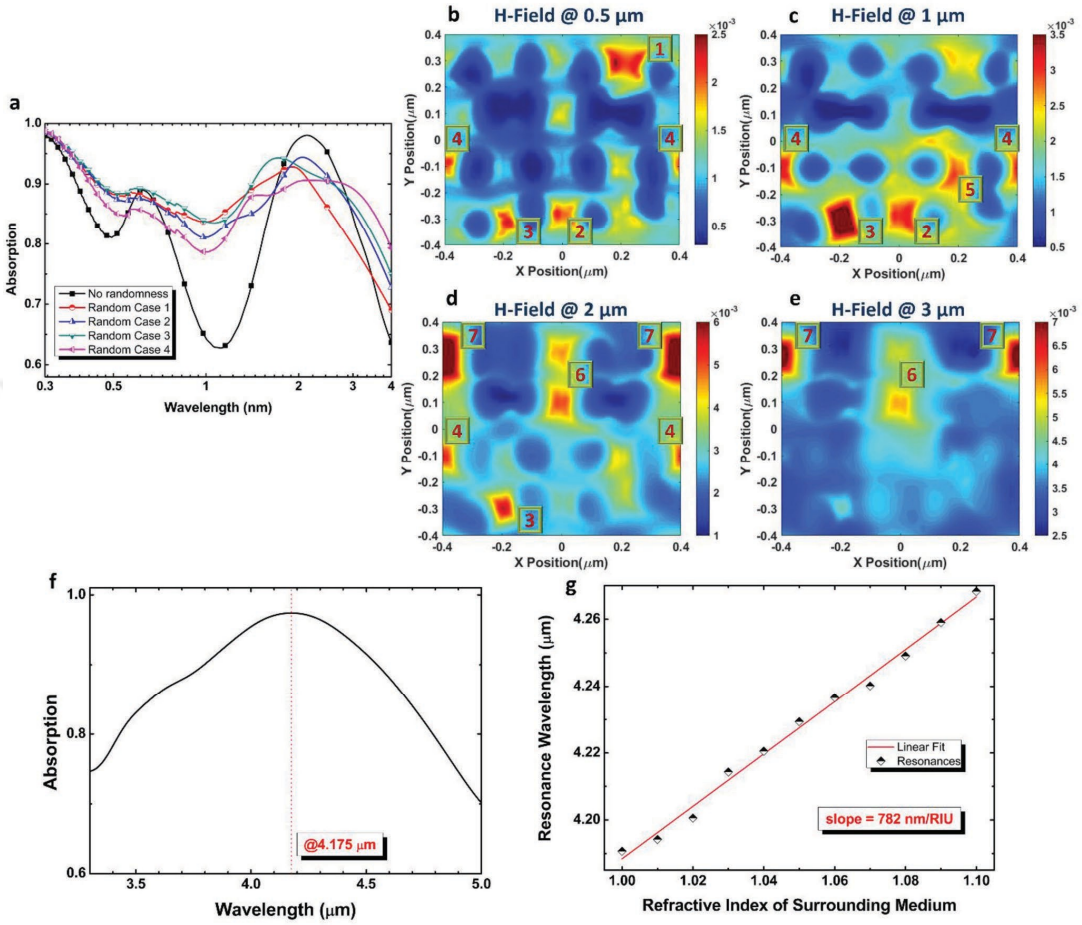


Figure 5.6 Effect of randomness on absorbance performance and EMW confinement mechanism. a) Absorbance spectra of 16 nanorod unit cell when nanorods have no orientation and different random scenarios. H-field profile of the unit cell at the middle height of the nanorods at wavelengths of b) 0.5 µm, c) 1 µm, d) 2 µm, and e) 3 µm. f) Simulated absorbance spectrum for the range of 3.2–5 µm. g) Resonance wavelengths for different surrounding medium refractive index values and linear fit in order to find the sensitivity of the sensor.

To test the validity of this, we carried out simulations by ran-domizing the nanorods. For this purpose, we designed a unit cell containing 16 nanorods with random design geometries. Using the random number generator function of the Lumer-ical software, nanorods were rotated around the x- and y-axes for a random value between −30° and 30°. We also added 10% tolerance to the radius and length of the nanorods (i.e., R can take a value between 72 and 88 while L can take a value within 270 and 330). Using this approach, the absorbance profiles of four different random combinations were compared

with a periodic design, as shown in Figure 5.6a. As this figure clearly highlights, when the structure has such random geometries, it achieves broader and stronger absorbance compared to the periodic structure. In addition, different randomness scenarios reveal distinct absorbance spectra in which the minimum value may differ for a value around 0.1 (while random case 1 has minimum absorbance around 0.68, random case 4 reveals minimum absorbance around 0.78). Although the simulated random 16 nanorod unit cell is eventually a periodic structure, the fabricated sample simultaneously includes many different combinations of randomly grown nanorods. Therefore, the simultaneous utilization of the unique optical response of Bi and the proposed randomness can lead to a flat perfect absorbance in an ultra-broadband range.To better explain this, the H-field profiles of the unit cell comprise 16 random nanorods as shown in Figure 5.6b–e, on which localized light confinement regions are numbered. It can be inferred from these panels that, at four different wave-lengths, there is a circulation of resonance regions so that at least one mode is excited in the structure. In other words, the active regions of the MM structure are interchanged in dif-ferent wavelength values. For example, incident light with 0.5 μm wavelength excites four different modes in the unit cell, where 1 is the strongest light confinement region. At 1 μm, res-onant mode at 1 vanishes and a new mode is excited at 5 while the light is mostly confined at region 3, as shown in Figure 5.6c. At 2 μm, the new resonant modes are excited at regions 6 and 7 instead of modes at regions 2 and 5. It can be concluded from these field profiles that the proposed random structure can sup-port multiple modes in different wavelength values. Thus, there are always excited resonance modes in the structure; and this in turn leads to a broadband absorbance of the incident light.In addition to the broadband absorbance profile of the proposed design in Vis and NIR, the MIR response of the periodic Bi nanorods was analyzed, and numerical analysis yielded a narrow resonance peak was also noted at 4.175 μm, as shown in Figure 5.6f. In plasmonic narrowband absorbers, where the absorption is achieved via excitation of SPR in the metal–dielectric interface, the change in the index of the sur-rounding medium can cause a shift in the absorption peak. This redshift of the resonance, induced by an increase in the refractive index of the dielectric environment, is widely utilized for sensing applications. The

sensing capability of a design is usually described by the term of sensitivity, which is defined as $S=\Delta n/\Delta\lambda$ where S, $\Delta\lambda$, and Δn are sensitivity, shift in resonance wavelength, and change in refractive index of the surrounding medium on the surface, respectively. To demonstrate the sensing performance of this design, the refractive index of the environment was varied from 1 to 1.10 with a step interval of 0.01, and the corresponding new resonance wavelengths are shown in Figure 3g, where a notable redshift of resonance is observed. The sensitivity is measured from the slope of the line that is attained by linearly fitting the peak spectral positions of the resonances. It is calculated as 782 nm RIU^{-1}, which is on par with the other reported values.

Chapter 6. LFMAs for Enhancement and Engineering of Light Emission

6.1. Preface

This chapter of the thesis is based on the publications:

”*Strong light emission from a defective hexagonal boron nitride monolayer coupled to near-touching random plasmonic nanounits*”, Z. Eftekhari, A. Ghobadi, M. Can Soydan, D. Umut Yildirim, N. Cinel, E. Ozbay, **Optics Letters.** 2021, 46, 1664 – 1667. Adapted (or “Reproduced in part”) with permission from OPTICA Publishing Group.

”*Disordered and Densely Packed ITO Nanorods as an Excellent Lithography-Free Optical Solar Reflector Metasurface*”, D. Umut Yildirim, A. Ghobadi, M. Can Soydan, O. Atesal, A. Toprak, M. Deniz Caliskan, E. Ozbay, **Acs Photonics.** 2021, 6, 1812-1822. Adapted (or “Reproduced in part”) with permission from American Chemical Society.

6.2. Motivation

In this chapter, we will discuss the application LFMAs in light emission enhancement and enginerring. For this aim, these LFMAs will be used in two main optical regime; i) visible light where quantum dot emitters are the main sources,ii) MIR range where the erath black body radiation is located on. In the visible range, LFMAs will be used to intensdify the light emission from quantum emitters. In the MIR range, LFMAs will be used for radiative cooling, security labeling, and thermal camouflage application.

Coupling of quantum emitters with plasmonic nanostructures has received a great deal of attention as constituents of quantum plasmonic circuits. These hybrid

systems confer the chance to study the light-matter interaction at the nanoscale and manipulate the nature of quantum light[343]–[349]. To this extent, bright and stable quantum emitters together with well-engineered plasmonic nanoantennas are essential components. Recently, hexagonal boron nitride (hBN), a two dimensional (2D) semiconductor with a wide bandgap of ~ 6 eV, has emerged, that hosts isolated defect centers which are optically active at room temperature[350]–[355]. The quantum emitters embedded in hBN have great potential to be integrated with plasmonic cavities, making them promising elements for future quantum technologies[356]. Therefore, it is appealing to investigate their Purcell enhancement through plasmonic resonators.

The hBN defect centers can be activated through electron irradiation, high-temperature annealing or substrate-engineering[357]–[359]. The latter technique provides an intriguing route to merge the emitters with plasmonic devices. The approach to combine quantum emitters with plasmonic structures is achieved by hybrid systems where the emitters are assembled into the confined plasmonic optical fields. Recent demonstrations that introduced coupling of periodic plasmonic array fabricated by e-beam lithography (EBL) technique, with hBN quantum emitters [360], [361] showed a direct comparison before and after coupling, enabled them to determine the effects of absorption and emission enhancement of the emitters. Another approach used atomic force microscope (AFM) to directly realize the coupling of hBN emitters with plasmonic resonators[362]. Unlike quantum dots, as the building blocks of emissive systems, the emission in hBN originates from the defect centers and it has a broad spectral response. Therefore, their emission peak, bandwidth, and strength are essentially governed by plasmonic design.

In this work, we demonstrate a hybrid design that provides strong light-matter interaction in an ultra-broadband frequency range. The coupling of defect centers in chemical vapor deposition (CVD) monolayer of hBN to a random lithography-free gold nanostructure significantly enhances the photoluminescence (PL) strength of the quantum emitters. We employ a disordered and densely packed gold nanorod (NR) scaffold design to optically activate defect centers nested in hBN. The disordered structure is fabricated by employing oblique-angle deposition

technique[9], [87], which offers a large-scale compatible route that can flexibly and cost-effectively merge these plasmonic structures with quantum emitters. Moreover, due to the atomic scale shadowing effect, near-touching plasmonic particles can be achieved. In this deep sub-wavelength gaps, strong light confinement in the electromagnetic hotspots can be probed. Owing to the broadband emission of defect centers of monolayer hBN [350], the spectral matching between quantum emitter and optical mode can occur efficiently. Therefore, strong and spectrally broad PL can be accomplished.

In the other side, we used these LFMAs for engineering thermal emission from a hot object. Temperature stabilization and its uniform distribution are vital for spacecraft and satellites because most of their components become less reliable when operated outside of their acceptable temperature range. Propellant freezing, thermal cycling damage to the equipment, and instrument/ antenna/camera misalignment are additional issues to be avoided during all of the mission phases. The coating system called Optical Solar Reflectors (OSRs), which are secondary-surface mirrors, therefore, play a crucial role for the optimum performance of spacecraft and satellites and success of their missions. OSRs simultaneously minimize the direct and indirect solar energy input to the spacecraft while passively emitting the thermal energy generated on the board. OSRs are then required to have a small solar absorptance (α_s) over the blackbody radiation spectrum of sun at 5778 K, corresponding to the ultraviolet (UV), visible (VIS), and near-infrared (NIR) parts of the electromagnetic spectrum. Concurrently, OSRs should have a large thermal emissivity (ϵ_{IR}) in the mid-infrared (MIR) and far-infrared (FIR) parts of the spectrum (thermalinfrared) related to the blackbody radiation at room temperature, 300 K. OSRs can be regarded as spectrally selective filters, that is, they are broadband mirrors in the solar spectrum, but perfect absorbers in the thermal infrared. A Figure of Merit (FoM) for an OSR can, therefore, be defined as ϵ_{IR}/α_s. Another critical consideration for an OSR is the stability over the course of the mission. This is because an OSR is affected during their missions by contamination, highvacuum, UV radiation, and charged particles. The general result is an increase in αs, with a negligible effect on ϵ_{IR}. There are different strategies and material choices to design an OSR, and they can be classified under two categories: conventional methods of using white paint, second-surface mirrors

using quartz or Teflon; and metamaterial-based solutions. Under the category of conventional methods, white color is often painted on the exterior surfaces and radiators of a spacecraft due to having a large ϵ_{IR}/α_s ratio. However, these paintings are very prone to environmental degradation due to UV radiation that darkens the pigments. Second-surface reflectors based on silver (Ag)- or aluminum (Al)-backed quartz films combine the high reflection of the metal layer with the strong absorption/emission of quartz in the thermal infrared to achieve very high ϵ_{IR}/α_s. In addition, quartz is highly insensitive to UV radiation and darkening, so it has very stable thermo-optical properties. Nevertheless, having large emissivity in the thermal infrared range requires using thick tiles of quartz ranging from 250 μm to a few cm. Moreover, the rigid and brittle tiles are prone to breaking while handling and are inflexible. This adds significant weight and, consequently, launch and assembly costs for the spacecraft. The other type of secondary-surface mirrors replace quartz with fluorinated ethylene propylene (FEP) Teflon film. The resultant Ag/FEP and Al/FEP materials provide flexibility and an excellent beginning-of-life ϵ_{IR}/α_s ratio. However, FEP is highly susceptible to degradation during its lifespan, primarily due to charged-particle damage and atomic oxygen. This makes the lifespan of Ag/FEP and Al/FEP materials shorter compared to quartz tiles. Thus, the conventional methods cannot simultaneously offer high performance, low weight, and the associated costs at the same time. Recently, transparent conductive oxides (TCOs), such as indium tin oxide (ITO), Aluminum-doped ZnO (AZO) and gallium-doped ZnO (GZO) emerged as strong candidates for infrared plasmonics, while being highly transparent in the solar spectrum. Their relatively high loss in thermal infrared promises plasmonic resonances with low quality factors and a broad absorption spectrum. Conversely, their low-loss dielectric response in the visible range would not contribute significantly to absorption. This means high ϵ_{IR}, but low α_s are simultaneously achievable. In the present work, we use disordered and densely packed Indium Tin Oxide (ITO) nanorod forests as the top layer of a metal−insulator-oxide cavity. The outstanding light trapping capability of the scaffold increased the residing time of thermal radiation in the device. This trapped light is then harvested by the hybrid system of ITO and SiO_2. As a result, perfect broadband absorption over the entire thermal-infrared, ranging from 2.5 to 25 μm is achieved and the experimental ϵ_{IR} reached as high as 0.968. At the same time, solar absorptance, α_s, is also

minimized to an experimental value of 0.168, owing to the lowloss dielectric characteristic of ITO in this spectral range. In fabricating the nanorod forests, we exploited the inherent line of-sight type coating of PVD systems, such as thermal evaporator and sputtering, to eliminate the need for lithography. In the method, which is known as oblique-angle deposition, the substrate is placed at an angle to the source, enabling the creation of quasi-3D structures with drastically different properties. The work is organized as follows: In the first part of this paper, we utilize the finite-difference-time-domain (FDTD) method to numerically investigate broadband light absorption in thermalinfrared and broadband reflection in solar spectrum, in a metasurface comprised of periodic nanodiscs. We scrutinize the effects of the geometrical dimensions of a single nanodisc, and cavity thicknesses on absorption spectrum, ϵ_{IR}, α_s, and FoM, to shed light on optimizing the actual device. In the second part, we demonstrate our oblique-angle deposition strategy in detail and present the experimental results for the optimized OSR. Overall, our robust, large-area compatible and ultrahigh performance OSR holds great promise in not only space missions, but also in radiative cooling and thermal imaging.

6.3. Strong Quantum Emission from Defective Hexagonal Boron Nitride Monolayer Coupled to Near-Touching Random Plasmonic Nanounits

The PL enhancement arises from both optical field enhancement and spontaneous emission enhancement. We separately simulated the local enhancement of electromagnetic field and the radiative enhancement of quantum emitter due to Purcell effect at the presence of plasmonic nanorods. Initially, we started modeling the plasmonic structure as a one that consists of simple periodic nanodisc with radius *R* and height *H* and period of *P* in x- and y- directions, as in Figure 6.1a. To realize the influence of the geometrical dimensions upon field enhancement, we calculated the electric field intensity of gold nanodiscs for different *R* and *H*. For this, we utilize finite-difference-time-domain (FDTD) simulations. In the FDTD simulations, we illuminated the unit cell with a broadband plane wave at normal incidence whose electric-field is polarized in the x-direction. In the x- and y-directions of the simulation region, we used periodic boundary conditions, while in

the z-direction perfectly matched layers (PML) are adopted and they are placed four wavelengths away from the structure.

The normally-incident plane wave interacts with the nano discs and excites localized surface plasmon resonances (LSPRs)[363]. Extreme enhancement and confinement of near-electromagnetic fields during the excitation of LSPRs modifies the photonic density of states significantly and the dynamics of light–matter interactions can be extensively improved. We first fixed the height of the disc at 20 nm with period of 100 nm and swept the radius. When NRs have small radius, the field enhancement is quite low due to the large gap distances between neighbouring rods, and their decreased “interconnectedness” consequently decreases the coupling of dipole oscillations. In contrast, as the radius is increasing and the NRs become more densely packed, the electromagnetic field confinement boosts and gives rise to large field enhancement. These two arguments are also observable as shown in Figure 6.1c. To investigate the effect of height of rods on field enhancement, we did R sweeping for 50 nm thick rods as well and the results delineate that the largest radius again outweigh others, however, the enhancement of EM field of 20 nm rods dominates in a broadband wavelength regime, as can be seen by comparing Figures 6.1b-c. The near-field electric field profile, in the proposed view plane of Figure 6.1d, of 20 nm thick discs with radii of 25 nm, 35 nm and 45 nm is shown at their resonance wavelengths, in Figures 6.1e-g, respectively. The localized plasmonic fields (hot spots) are most intense near the edge of metal surface, as shown in the optical field intensity profile. Thus, all in all, the highest field enhancement is acquired in thin near-touching plasmonic design.

In addition to field enhancement, plasmonic resonances provide Purcell effect and consequent spontaneous emission enhancement. When quantum emitters of hBN are collocated with high intensity optical field, Purcell enhancement result in a bright emission of the quantum emitter. To model this effect we have used numerical simulations. For this aim, we model the defect centre with a dipole emitter (DE), as shown in Figure 6.1h. In the periodic design, we demonstrated that changing R and H is an effective tool to manipulate light-matter interaction and strengthen the field localization. In this simulation, we also introduce randomness

to our design and the disorder can be adopted to the geometrical parameters as well as the orientation of the NRs. The disordered and densely packed design is comprised of NRs which their size, radius, orientation and their spacing are defined randomly during the initial phases of the fabrication. The random number generator function of the Lumerical FDTD software package is utilized to introduce the disorder to the design as NRs were tilted around the x- and y-axes for a random value between −10° and 20°. We also added 5% tolerance to the radius and length of the nanorods (i.e., R can take a value between 38 nm and 42 nm, while L can take a value within 19 nm and 21nm). The spontaneous emission rate within surface plasmons can dominate the radiative and non-radiative rates (γ_{rad} and γ_{nrd}, respectively), which gives rise to strong coupling to surface plasmons and enhancement of the total decay rate (γ_{total}) with respect to that of an emitter in vacuum (γ_0). This enhancement can be identified by a Purcell factor, $PF = \gamma_{total}/\gamma_0$. To estimate the emission enhancement, we calculated the Purcell factor of the design using an electrical dipole emitter (DE) source placed at the spacing of rods where the field localization is in its highest intensity. Since the hBN is laid on the top of disarray, we located the dipole a few nanometer above the structure. The results of three separate simulations of the dipole oriented along the x, y and z axes were combined incoherently. The theoretical calculation of PF for three thicknesses of 20 nm, 50 nm and 100 nm NR disc array, represented in Figure 6.1i, shows that the maximum coupling between quantum emitter and NRs is achieved for the 20 nm thickness. So far, we demonstrated that the PL intensity of a hypothetical DE is governed by its excitation rate (that is, near-field intensity enhancement) and its emission efficiency (that is, Purcell factor)[349],[364]. The periodic nanorods structure was employed to scrutinize the near field enhancement and corresponding electromagnetic hotspots. The upmost compact rods of height 20 nm illustrated the highest field enhancement and the consequent excitation rate enhancement as $\gamma_{exc} \sim |\mathbf{E}|^2$. In addition, the emission rate enhancement of the random structure with the highest fill factor were

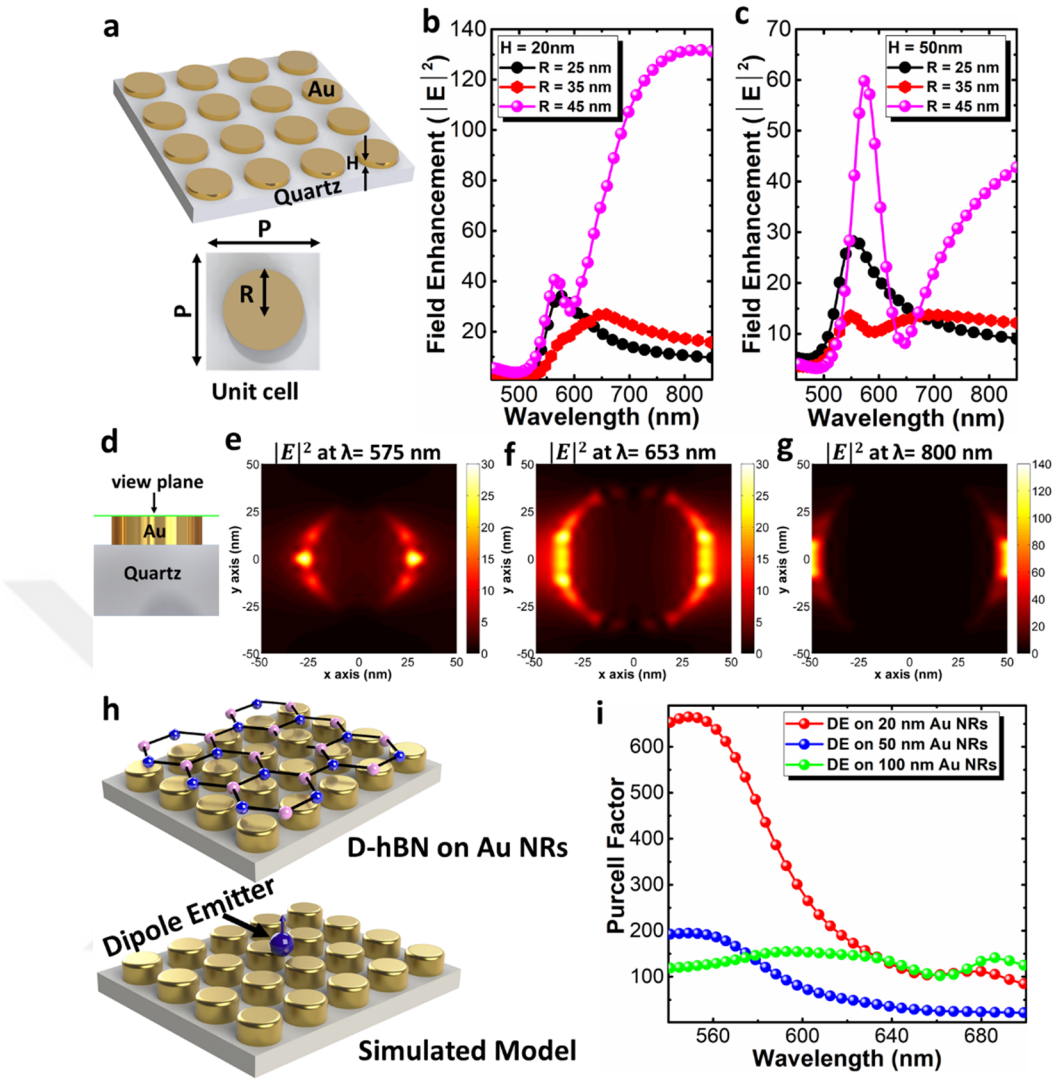


Figure 6.1 (a) Schematic of modeled gold nanodiscs on quartz substrate. inset, the schematic illustration of the unit cell. Sweep and optimization of *R* for two heights of (b) H= 20 nm and (c) H= 50 nm while P = 100 nm. (d) Schematic of the unit cell with illustration of electric field profile view plane. $|E|^2$ profiles of (e) R=25 nm, (f) R= 35 nm and (g) R=45 nm at their resonances. (h) The real device and its model for numerical simulations. (i) The Purcell factor of a DE placed at three different disc heights plasmonic design.

considered via calculation of Purcell factor for different heights of rods which the 20 nm thick rods result in the highest PF and it confirms the correlation of emission enhancement with the strong field intensity localization.

Thus, from numerical simulations, the coupling of hBN monolayer with near-touching plasmonic design will provide us the strongest light-matter interaction.

However, from the fabrication perspective, realization of such narrow gaps (< 10 nm) using electron beam lithography (EBL) or nanoimprint lithography (NIL) is a quite challenging task. The complexity of these fabrication methods also hinders the large-scale compatibility, reproducibility and mass-production of these devices. Therefore, lithography-free methods are highly sought as they allow the fabrication of a design with ultra-narrow gap features while still enabling high-throughput and upscaling features. Moreover, in the case of a broadband emitter (as in hBN monolayer), we need to ensure field enhancement in a broad spectral range to have a full bandwidth emission enhancement. All the above mentioned requirements can be achieved using a multi-dimension/multi-spacing nanounit plasmonic design. In other words, a disordered and densely packed design is the ideal scheme for hBN monolayer emitter. In our experiment, we employed oblique-angle deposition approach to construct densely packed and disordered NRs by thermal evaporation. As fabricated samples in Figure 6.2b illustrates the NRs with length of 20 nm and 100 nm respectively. The proposed method provides a compact disordered structure with high throughput and the length of NRs can be controlled by regulation of the deposition time. However, looking at these images, one can find the fact that the spacing between nanounits is larger for thicker layer. As explained above, the oblique angle deposition operates based on atomic scale shadowing. This process is a competitive approach in which the larger parts eliminate the smaller counterparts. In essence, in the initial parts of the deposition, the evaporated gold flux induced random, multi-sized nucleation sites all over the substrate. As the deposition continues, due to the oblique angle of the sample and consequent shadowing effect, only the main nucleation spots were elongated, while they prevent growing small nano particles and result in a disordered porous structure, with only the main nucleating spots becoming dominant. In thicker layers, the density of nanorods reduces and their gap distance increases. Therefore, realization of ultra-narrow gaps is much probable in thinner layer and this thickness regime causes stronger light-matter interaction. This can be seen from atomic force microscopy (AFM) images. Based on these plots, the nano islands are tightly packed with heights from 16 nm to 25 nm.

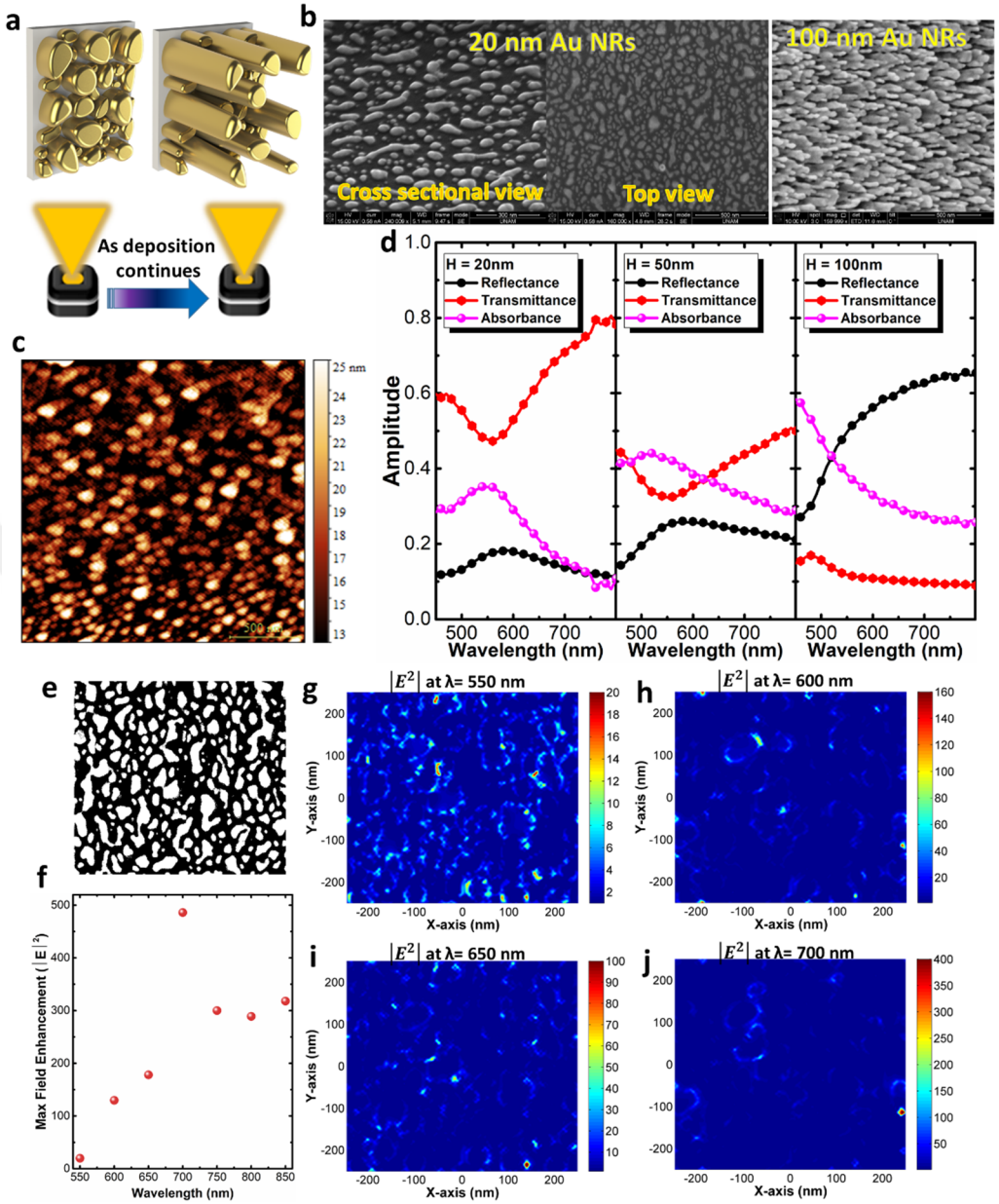


Figure 6.2 (a) Schematic illustration of oblique-angle deposition and the formation of nanorods. (b), SEM images of 20 nm and 100 nm NRs. (c), AFM image of 20 nm NRs showing the surface roughness measurement. (d), reflectance, transmittance and absorbance spectra of NRs with heights H= 20 nm, 50 nm and 100 nm by ellipsometry. (e) The binary image of the 20 nm NRs converted from the top-view SEM image. (f), The simulated maximum field enhancement at different wavelengths. The contour plots of electric field amplitude profile of the 20 nm NRs at wavelengths of (g), 550 nm, (h), 600 nm, (i), 650 nm, and (j), 700 nm.

To scrutinize the light-matter interaction in plasmonic NRs, we fabricated three samples consisting NRs with lengths of 20 nm, 50 nm and 100 nm and performed ellipsometry measurements. The resulting transmission, reflection and absorption spectra of all samples are shown in Figure 6.2d. It is evident from Figure 6.2d that the absorption cross section of 20 nm- thick NRs overlaps well with the emission spectrum of the monolayer hBN emitter, therefore, it is expected to obtain the largest PL enhancement for this particular sample.

For further physical understanding and numerical analysis, we converted the top-view SEM image of 20 nm gold nanorods into a binary image and imported into the FDTD simulation, see Figure 6.2e. Maximum field enhancement at different excitation wavelengths is calculated showing in Figure 6.2f. The electric field profiles of the random design at different wavelength values, Figures 6.2g-j, exhibit large number of hotspots compared to others and it confirms that this design meets the necessary requirement for coupling the plasmonic structure to the hBN defects, because of the tight light confinement covering the emission range of hBN. Moreover, comparing with periodic design (Figure 6.1b), the filed enhancement is even larger in our proposed structure. Also, the randomness of the design makes the number of hot spots larger compared to a periodic ordered structure. Based on these results, placing a quantum emitter in these hot spot positions could lead to order of magnitudes emission enhancement. After design, and analysis of the plasmonic design platform, hBN emitter is transferred. The hBN exploited in the experiment was a CVD grown monolayer hBN on copper foil. First, the hBN on Cu samples were spin coated by poly(methyl methacrylate) (PMMA) at 2500 RPM for 1 min. After baking the samples at 180℃ for 90 seconds, the copper foil was removed in a bath of 0.5 M ammonium persulfate solution and rinsed with DI water several times. The resultant films were placed on samples of 20 nm, 50 nm and 100 nm thick Au NRs and one bare quartz substrate for pristine hBN as reference. Then the samples were heated at 90℃ for 90 s for adhesion of hBN to the substrates and placed in aceton bath to remove the PMMA. In the next step, the as-prepared samples were annealed at 400 °C with Ar/H flow (100 sccm) for 2 h in a vacuum tube furnace.

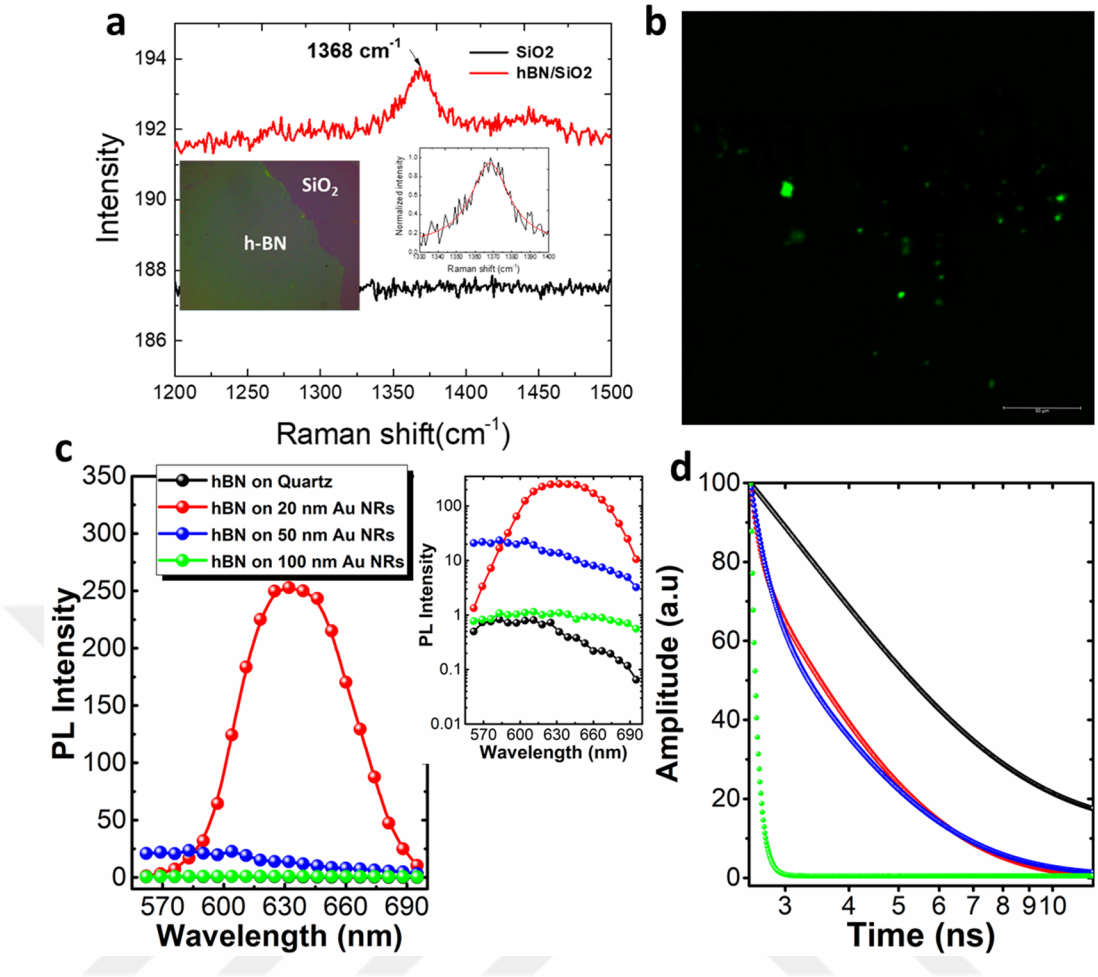


Figure 6.3 (a), Raman scattering spectrum of monolayer hBN and corresponding Lorentzian fit to the experimental data.inset, optical image of transferred monolayer hBN on the silicon dioxide substrate. (b), Scanning confocal map of a mmonolayer hBN sample illustrating bright illuminate defect centers. (c), Room-temperature PL spectra of defect centre in pristine monolayer hBN and coupled hBN with Au NRs. Inset shows the data in logarithmic scale. (d) The decay lifetime of different samples.

We performed optical characterization of each configuration (pristine hBN, hBN on 20 nm, 50 nm and 100 nm NRs) using confocal microscopy and investigated PL of the single defects in hBN film. The Raman spectrum of monolayer hBN with Raman shift at 1368 cm^{-1} is illustrated in Figure 6.3a, while the insets show an optical image of transferred hBN on a silicon dioxide substrate and the Lorentzian fit to the experimental data. The PL confocal map of monolayer hBN on 20 nm NRs under 514 nm continuous-wave excitation, shown in Figure 6.3b, exhibits the bright luminescent spots due to the presence of strong coupling between embedded defects in hBN and hot spots formed in plasmonic gaps. In

the ideal case, the brightest spot is achieved when the defect is exactly located in the hot spot place.

PL spectra of the brightest spots in monolayer hBN on bare quartz substrate and plasmonic NRs with different heights are recorded at room temperature, see Figure 6.3c. For better visualization, this data has been also shown in logarithmic scale, see inset. As this graph implies, the strongest PL is achieved for 20 nm thick Au NR sample, with above two orders of magnitude enhancement. While the PL intensity is reduced for thicker layers, all plasmonic designs have higher PL values compared to bare hBN monolayer. All these findings are in line with our simulation and expectations. Moreover, the PL decay lifetime measurement shows the shortening of the lifetime in plasmonic designs.

6.4. Disordered and Densely Packed ITO Nanorods as an Excellent Lithography-Free Optical Solar Reflector Metasurface

Our proposed device in Figure 6.4a is designed to obtain the required spectral response of an OSR, that is, broadband reflection in the solar spectrum, while achieving broadband absorption in the thermal-infrared, due to its highly diffracting/scattering and electromagnetic wave (EMW) trapping nature. This proposed structure, which we call Device 1, consists of a metal−insulator-oxide (MIO) cavity, where a thick metal back-reflector, aluminum (Al), is used to redirect the otherwise transmitted EMWs back into the cavity. The spacer, SiO_2, is used to create the necessary phase accumulation to redirect the EMWs mostly to the top absorbing layer of our MIO cavity, which makes use of ITO nanorods. We also outlined the reasons of picking these materials in more detail in the Supporting Information. ITO is a plasmonic material in the thermal-infrared, so the nanorods can be used to excite localized surface plasmon resonances (LSPRs). LSPRs define the nonpropagating excitations of the conduction electrons that are coupled to the incident electromagnetic radiation. When the nanoparticle dimensions become comparable to wavelength, the plasmons are confined to the surface of

nanoparticles and the collective harmonic oscillations result in a dipolar response with a specific resonance wavelength. The resonance wavelength and its Qfactor are highly related to the morphology (size, shape, spacing, and density) of the nanostructures.88 Therefore, in understanding the operation of Device 1, it is pivotal to first grasp how individual nanorod dimensions and the cavity thickness affect the spectral response as well as the OSR parameters, ϵ_{IR}, α_s and ϵ_{IR}/α_s. To understand how the performance is affected by the geometrical parameters, we initially scrutinized the LSPRs supported by nanodiscs/nanorods of radius r, thickness h, that are periodic in two directions with a period of P, when the spacer thickness is chosen as t_{SiO2}. We name this testing device as Device 2, whose schematic is shown in Figure 6.4b, and its unit-cell from the top view is shown in Figure 6.4c. To clarify the difference between Devices 1 and 2, Device 1 is the device that will be fabricated and characterized in the upcoming parts of this paper. It has nanorods whose size, shape, radii, and spacing are defined randomly during the fabrication, while h is controlled by deposition rate and time. On the other hand, Device 2 has periodic nanodiscs with precise radii and spacing, which can be controlled by EBL. It is defined to compare the optical performance of a patterned top layer to that of Device 1. In the numerical analysis of Device 2, we utilize finitedifference-time-domain (FDTD) simulations. Details of the simulation setup are outlined in the Experimental Section. With the aid of FDTD method, we calculated the spectral absorption, A(λ,T), of Device 2. Based on the calculated absorption data and the spectral radiance B(λ,T), the ϵIR and αs values are calculated.

We first fixed t_{Al} at 125 nm (throughout this paper), P at 1100 nm, h at 50 nm, t_{SiO2} at 2000 nm, and swept r. Our primary purpose in these set of simulations is to find out the effect of the density or fill factor of the nanodics in the absorption spectrum and the OSR parameters. In Figure 6.4d we show the spectral response of Device 2 for different values of r. First, it is seen that the high-loss plasmonic optical nature of ITO in thermal infrared results in a broad absorption spectrum, while in the solar spectrum, the oscillations in absorption corresponds to response of a Fabry-Perot cavity,´ due to ITO's low-loss dielectric nature. Figure 6.4e shows how OSR parameters respond to changes in r. In the thermalinfrared, it is evident that, as the nanodiscs get closer to each other with decreasing r, in other words, as the discs become denser, their

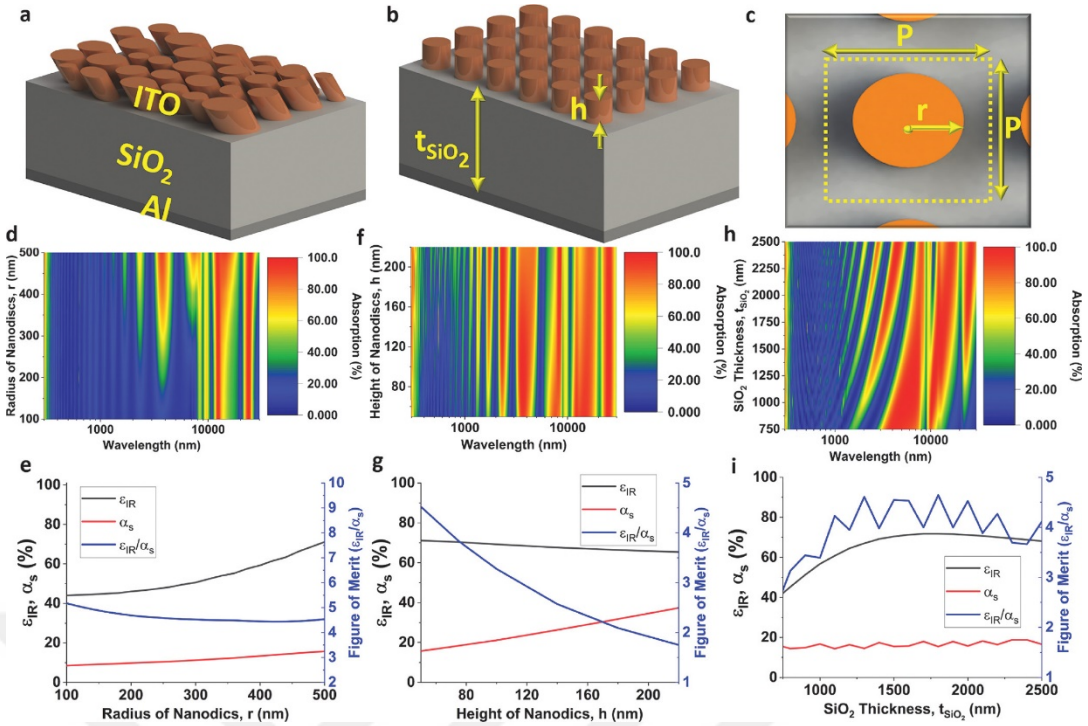


Figure 6.4 Schematics of Devices 1 and 2 and the parameter sweeps on the geometrical dimensions of Device 2. (a) Device 1 to achieve broadband absorption in thermal-infrared and broadband reflection in solar spectrum. (b) Device 2 to test the effect of geometrical dimensions of a nanodisc on absorption spectrum, thermal emissivity, and solar absorptivity. (c) Top-view of Device 2, showing the geometrical parameters in detail. Absorption spectrum of Device 2 under varying (d) nanodisc radius, r, (f) thickness of nanodiscs, h, and (h) thickness of the SiO_2 spacer, t_{SiO2} . OSR parameters Device 2 when (e) r, (g) h, and (i) t_{SiO2} are changed.

"interconnectedness" increases and the coupling of dipole oscillations become stronger,89 and broad LSPRs can be supported. In the solar spectrum, an increase in r corresponds to a larger fill factor of ITO compared to vacuum, so the dielectric losses increase. The increase in the αs, nevertheless, outweighs the increase in ϵIR, so the FoM, ϵ_{IR}/α_s is essentially larger for the more isolated nanodiscs. We also varied the periodicity, P, of the unit cell with a fixed h of 50 nm, t_{SiO2} of 2000 nm and r of 200 nm. Next, we investigated the role of height of each nanodisc in the absorption spectrum and the OSR parameters. For this purpose, we kept P at 1100 nm, r at 500 nm, t_{SiO2} at 2000 nm, and swept h. We preferred to keep the nanodiscs densely packed as it imitates our proposed densely packed nanorods better. The absorption spectrum for different values of Figure 6.4f shows that, in the solar spectrum, the height causes an increase in the absorption because the EMWs interact more with ITO before reaching

the cavity. In thermal-infrared though, longer nanodiscs caused a decrease in the absorption strength, as the strength of EMWs reaching to the cavity is now reduced, and reflection due to ITO is increased.56 The OSR parameters based on our findings is plotted in Figure 6.4g, which clearly shows that a thin layer of ITO is beneficial for both ϵ_{IR} and α_s, consequently, for the figure of merit as well. The cavity thickness, t_{SiO2} is of fundamental importance in an MIM cavity configuration. For our design, we used a Salisbury screen configuration,90 with a thickness of λ /4n 0 SiO_2 , where n_{SiO2} is the real part of the complex refractive index of SiO_2. Due to transmission-line theory91 and the quarterwavelength separation of the aluminum ground plane from the ITO layer, the former acts an open circuit at the position of the latter. It is in this way that matching the impedance of ITO layer to free-space is sufficient to achieve perfect absorption. This strong dispersion in n_{SiO2} means t = λ /4n_{SiO2} will be a greatly varying value in the thermal-infrared. Moreover, the resultant Reststrahlen bands show an increased reflectivity in the thermal-infrared, which is detrimental to ϵIR. To optimize the cavity thickness based on these considerations, we kept P at 1100 nm, h at 50 nm, r at 500 nm, and swept t_{SiO2} . Absorption spectrum in Figure 6.4h clearly shows

that the cavity resonances evolve to larger wavelengths as we increased tSiO2 . While smaller cavity thicknesses (750−1250 nm) supported the resonances in the 5−10 μm range, the thicker cavities (1500−2500 nm) supported LSPRs in the 20− 30 μm range. Resonances around 10−15 μm are supported for all of these thicknesses. To find the optimum cavity thickness, the spectral overlap of A(λ,T) with the thermal-radiation spectrum, which peaks around 10 μm, is of most importance. The calculation results for the OSR parameters are outlined in Figure 6.4i. In Figure 6.4i, it can be observed that ϵIR is almost constant for a wide range of 1.5−2 μm, while the fringes in αs is again related to the Fabry-Perot cavity. As a result, the FoM′ also has fringes. Another important consideration for an OSR in space missions is its spectral response under obliquely incident radiation. Overall, this numerical analysis of Device 2 shows that it can support broad LSPRs in the thermal-infrared and reach a moderate FoM of 4.5 at the cost of requiring a throughputlimiting lithography step. Moreover, Figure 6.4d, f, and h all demonstrate the main limiting factor associated with Device 2 in achieving larger FoM. Device 2 has a highly ordered ITO pattern, so its diffracting/scattering and EMW trapping features are poor.

This causes a significant portion of the EMWs to be reflected by SiO2 at the Reststrahlen bands. These back-reflected EMWs cannot be efficiently retrapped by the ITO layer and, consequently, they leave the device without being harnessed. In these spectral regions, the EMW-ITO interaction is inherently limited and most of the absorption is due to absorption of the EMWs in the SiO2 layer. This will be analyzed in further detail in the next part of the paper. As a result, better trapping and harvesting of this reflected radiation, while not increasing the solar absorption, is pivotal to achieve an FoM that is competitive to existing OSR solutions. Fabrication and Characterization of the Metasurface OSR with Disordered and Densely Packed ITO Nanoforests as the Top Layer. The results of the previous subsection show that there is significant room for increasing ϵIR above 0.8, while keeping αs at a low value. This can be achieved by using a

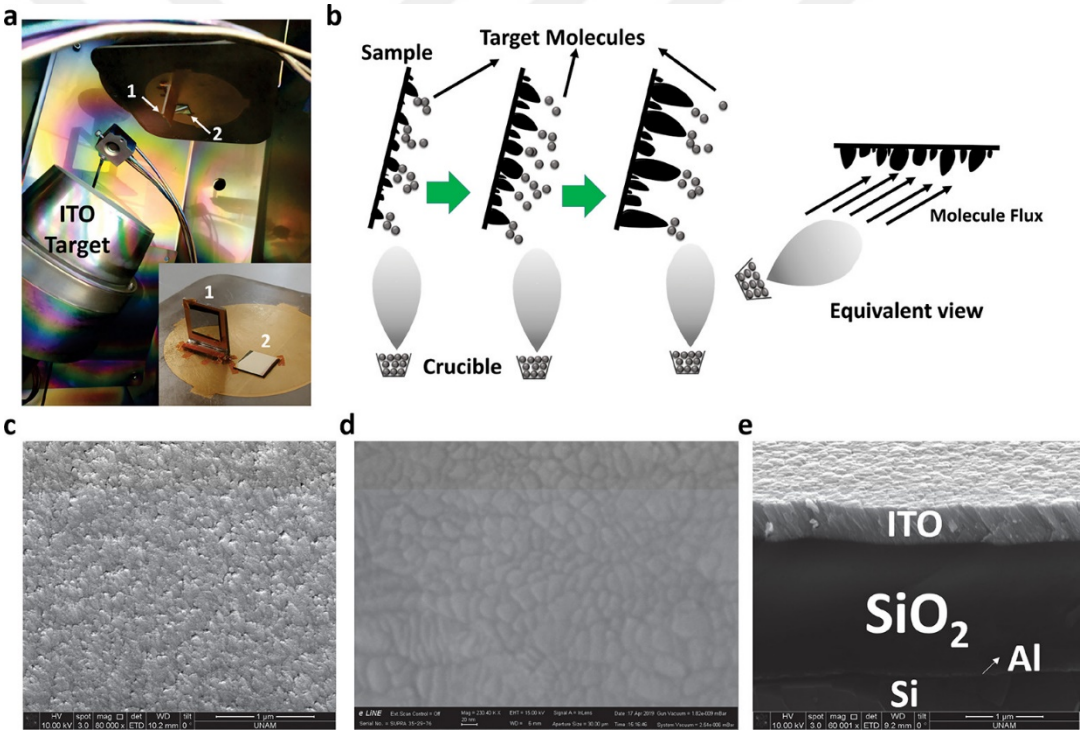


Figure 6.5 Fabrication of the metasurface OSR and the formation of ITO nanoforests. (a) Placement of samples in the sputtering chamber before coating of ITO. (b) Schematic illustration of line-of-sight coating in a sputtering system and the formation of tilted nanowires. (c) Low and (d) high resolution top-view SEM micrographs of one of the fabricated devices. (e) Cross-sectional SEM image of a sample metasurface OSR.

thin layer of disordered and densely packed ITO nanorod forests. For this aim, we fabricated Device 1 with the procedure outlined in the Experimental Section. The fabrication step with the most significance is realizing the top-ITO layer. To achieve it, we utilized a sputtering system but placed our samples at an oblique-angle to the ITO target. Such a deposition scheme is known as oblique-angle deposition, and it combines the inherent line-ofsight coating of PVD systems with shadowing to achieve quasi3D nanosized columnar fills with an intrinsic tilt and porosity. Figure 6.5a shows placement of two samples in the sputtering system. While sample 1 is placed at an oblique angle to the ITO target, sample 2 is placed in an ordinary manner for planar deposition, which is used for comparison purposes and for extracting the dielectric permittivity of ITO. The inset of Figure 6.5a shows the placement of samples in the sample holder plate and the special FR-4 apparatus that we designed to place the oblique-angled sample. In the oblique-angle deposition, a standard planar thin-film deposition, as in Sample 2, is transformed into a preferential deposition of random nucleation sites, formed during the initial stages of deposition. Continued deposition results in the deposition on these nucleation sites, while no deposition takes place in the shadowed regions. Consequently, disordered and densely packed nanocolumns emerge and they are intrinsically tilted toward the source. Such a process flow, along with an equivalent picture, is illustrated schematically in Figure 6.5b. The formation of such nanorod forests is verified by using planar and cross-sectional scanning electron microscopy (SEM) micrographs, as presented in Figure 6.5c, d, and e, respectively. The device in these figures has a 400 nm coating of ITO (which is larger than the devices to be mentioned later in this paper) in order to better demonstrate the details of the nanoforests, as well as the tilting of nanowires toward the source. In finding the reflection spectrum of the fabricated devices, measurements in the UV/VIS/NIR ranges are carried out in a total reflection spectrophotometer. In the thermal-infrared, the Fourier Transform Infrared Spectroscopy (FTIR) technique is utilized, and the details for optical characterization are given in the Experimental Section. The absorption spectra for the fabricated devices are then found by $A = 1 - R$. In our initial set of fabrication and experiments, we fabricated Device 1 with the thickness of the ITO layer as 50 nm and the SiO_2 thickness as 2 μm. The experimental absorption spectrum of this device, in comparison to the FDTD simulations of Device 2 using periodic discs of 50 nm thickness, is presented in Figure 6.6a. In the FDTD simulations, the periodicity

of the discs is set as 1100 nm and its diameter is 1 μm. The result in Figure 6.6a demonstrates a remarkable enhancement of light−matter interaction in Device 1 compared to Device 2 and, consequently, ultrabroadbandabsorption in the thermal-infrared, resulting in an outstanding ϵ_{IR} of 0.962. From the space missions perspective, it is equally important to keep αs within acceptable limits while increasing ϵIR. It is critical to mention that our designed scaffold with high diffraction/scattering and light trapping also means solar radiation interacts more with the low-loss dielectric ITO, which may result in higher αs. To alleviate this, a thin ITO layer is needed to simultaneously provide a large ϵ_{IR}, while not emphasizing losses in the solar spectrum. In Figure 6.6a, it is seen that Devices 1 and 2 produce similar absorption profiles in the solar spectrum below the bandgap of ITO, where the losses due to ITO are not significant. However, below 400 nm, interband transitions of ITO become a prominent loss mechanism, and strong light−matter interactions in the Device 1 produce more absorption than Device 2. Nevertheless, using only 50 nm ITO thickness allowed us to keep αs at 0.168. The FoM reached a record-high value of 5.73. Another important observation from Figure 6.6a is that the spectral positions of the peaks and dips in the absorption spectrum have great agreement between the FDTD simulations of Device 2 and the experimental result of Device 1. This is because these peaks and dips are determined by the phase accumulation during the round-trip in the SiO2 cavity and the added phases due to reflections at ITO−SiO_2 and SiO_2−Al boundaries, as given in eq S3. In an attempt to further improve the FoM, it is more important to decrease αs rather than increasing ϵIR, as the former is already very close to unity in Device 1, with h = 50 nm and tSiO2 = 2 μm. Moreover, the numerical results for Device 2 show that thicker layers of ITO accentuate αs more than ϵ_{IR}, so FoM is deteriorated. Therefore, in our second set of experiments, thicker layers of ITO are not investigated, and we reduced the thickness of the ITO layer to 30 nm. The experimental absorption spectrum of this device is shown in Figure 6.6b, along with the spectrum for Device 2, while the other geometrical parameters are the same as before. In the solar spectrum, the intention of decreasing αs is accomplished, as it decreased to 0.161 due to the smaller thickness of ITO. In the thermal-infrared, however, Device 1, with h = 30 nm, has worse absorption when compared to the h = 50 nm case, due to the poorer light-trapping capability of the scaffold. Similar to the h = 50 nm case, Device 1 still outperforms Device 2 in the h = 30 nm case, as ϵ_{IR} reached 0.884 and the FoM is 5.49. We also

compared Device 1 with another lithography-free design that utilizes a planar ITO layer to further represent the power of the designed ITO nanoforests as a light-trapping scaffold. The experimental result for the planar device with h = 50 nm and t_{SiO2} = 2 μm is first shown in Figure 6.6c, as well as the FDTD simulations for this device. In Figure 6.6d, we compare the experimental results for Device 1 and the planar design with the h = 50 nm and tSiO2 = 2 μm parameters. While the planar design achieves an αs of 0.151, its ϵIR is only 0.697, so the FoM is limited to 4.61. The planar design gives the worst ϵIR, because it lacks both the light-trapping capability of Device 1 and the LSPRs supported in Devices 1 and 2. However, it does not suffer from diffraction/scattering and the resultant excited guided-modes of the structure.92 Overall, the ITO nanoforest design still outweighs the planar design. Our proposed device is experimentally confirmed to provide an excellent scaffold for ultrabroadband thermal-infrared absorption and provides far superior ϵIR

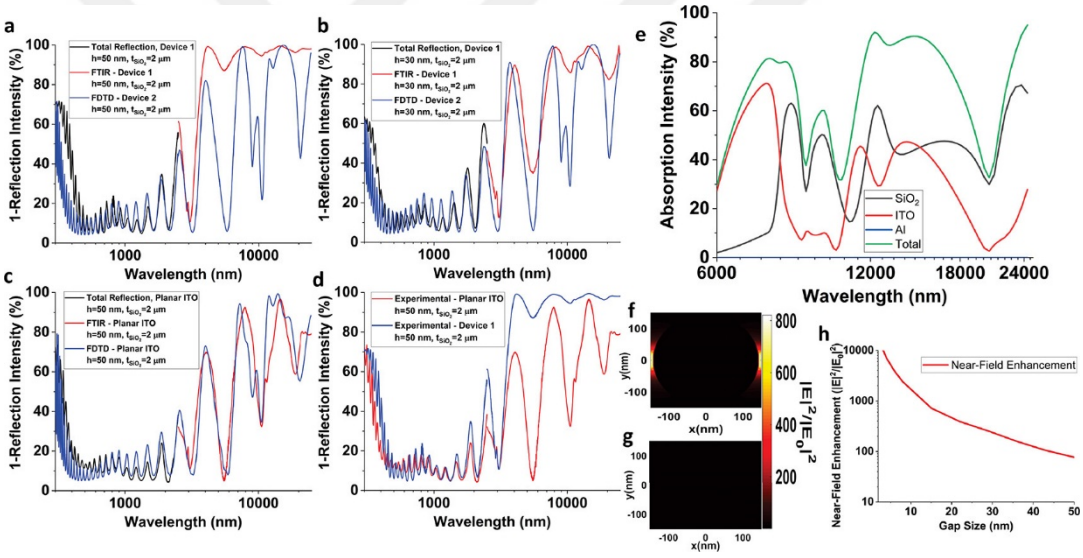


Figure 6.6 Optical characterization of the fabricated devices with disordered ITO nanorods, comparisons to numerical simulations of Device 2 and experimental results of a planar design, and physical explanations on ϵIR enhancement in the proposed device. (a) Experimental absorption results for Device 1 with h = 50 nm and tSiO2 = 2 μm compared to the numerical simulations of Device 2 with the same h and tSiO2 . (b) Experimental absorption result for Device 1 with h = 30 nm and tSiO2 = 2 μm compared to the numerical simulation Device 2 with the same h and tSiO2 . (c) Experimental absorption result for a planar device with h = 50 nm and tSiO2 = 2 μm compared to numerical simulations for the same device. (d) Comparison of the absorption spectra of the planar device and Device 1 with h = 50 nm and tSiO2 = 2 μm. (e) Contribution of each layer to the absorption in thermal-infrared. (f) Localization and enhancement

of electric-field between nanodiscs of P = 300 nm, r = 142.5 nm. (g) |E| 2 /|E0| 2 value recorded at a planar ITO layer. (h) Near-field enhancement, |E| 2 /|E0| 2 values as a function of gap size between nanodiscs. In (f), (g), and (h), the |E| 2 /|E0| 2 values are recorded at 15 μm and at the midgap position.

compared to Device 2. There are five underlying physical reasons for this. First and foremost, the strong dispersion and phonon reflection of SiO2 at the Reststrahlen bands was the primary reason for limiting ϵIR of Device 2 under 0.8. In those regions, incident radiation is back-reflected, and a significantly smaller portion of the radiation is trapped and harvested in the device. To make matters worse, the back-reflected EMWs cannot be efficiently retrapped in Device 2 by the periodic ITO nanodiscs, due to their poor diffraction/scattering and trapping features. Therefore, these back-reflected EMWs are not harnessed in Device 2, and light-ITO interaction is limited in these areas. This is analyzed in more detail and verified numerically by placing three three-dimensional (3D) monitors on the Al, SiO2, and ITO layers and calculating the contribution of each layer to absorption in the thermal infrared. The absorption spectrum in Figure 6.6e clearly shows that in the phonon reflection bands (around 10 and 20 μm) of the SiO2 absorption of the transmitted light in the cavity is the main driver behind the absorption spectrum. However, this strong reflection is mitigated in Device 1, which is clearly visible upon comparing the absorption spectra of Devices 1 and 2 around 10 and 20 μm in Figure 6.6a. This is a direct result of the rough and highly diffracting/scattering top-layer ITO scaffold. While the thermal radiation is reflected in Device 2 at Reststrahlen bands, in Device 1, the scaffold traps this thermal radiation (or, in other words, the residing time of thermal radiation in the structure is improved) and it is absorbed by the hybrid system of broad plasmonic resonances supported by ITO and phonon bands of SiO2. The fact that thinner ITO layers suffer more from reflection losses (by comparing Figure 6.6a and b) also supports the argument that increasing the residing time of EMWs in Device 1 and coupling them to the ITO/SiO2 hybrid is the main driver in enhanced absorption. Second, ITO offers a plasmonic response with relatively high losses,so the excited LSPRs inherently have a large line width. Third, the randomness in the morphology of the nanorods, as confirmed in the SEM images in Figure 6.5d,e, results in multiple adjacent LSPRs of different strength, spectral position, and line width. Since our fabrication route generates random geometries, the superposition of the excited LSRPS then contribute to a flat, perfect absorption

over an ultrabroad bandwidth. Fourth, the gap distances between the tilted nanorods is found to be very small and not uniform. It is shown in the literature that extremely small gaps between plasmonic nanostructures result in the extreme enhancement and localization of optical fields. We show the near-field enhancement of optical fields between the ITO nanodiscs, due to the dipolar LSPRs in Figure 6.6f, as an exemplary case from Device 2. The optical field inside the ITO layer of a planar device is also calculated, and the result is shown in Figure 6.6g. Comparison of Figure 6.6f-g demonstrates that the plasmonic resonance and the corresponding electromagnetic hotspots between the nanodiscs do not exist in the planar case. This is the reason why the planar design had the poorest ϵIR. In Figure 6.6h, we indicate that further decreasing the gap distance between the nanodiscs results in higher enhancement of optical fields. This extreme localization results in larger optical losses. Thus, the formation of deep subwavelength gaps between the nanowires, as demonstrated in Figure 6.5d-e, triggers the existence of intense local fields, and these hotspots lead to strong light absorption in the thermal infrared. Moreover, when the distance between the nanostructures become very small, the position of plasmon resonances is determined by the gap size, rather than the individual dimensions of the nanostructures. The randomness in the porosity of the deposited film, as shown in Figure 6.5c, is then a contributor to the perfect absorption. Lastly, the random nanorods in Device 1 diffract light in more directions, compared to the periodic discs of Device 2. Therefore, Device 1 may be aiding the coupling of a larger portion of incident radiation to the surface-plasmon polaritons (SPPs) in the SiO_2−Al interface. Large-Scale Fabrication of the Proposed Device and Optical Characterization. Oblique-angle deposition not only offers a substantial enhancement to the OSR performance, it also enables a facile route for large-scale fabrication, which is of paramount importance to establish a competitive OSR technology to the planar conventional devices. As a proof-of-concept, Device 1 with h = 50 nm and t_{SiO2} = 2 μm is fabricated on a 4-in. silicon wafer. The wafer is placed in the sputtering chamber at an angle to the source, similar to Figure 6.5a. To do that, the plate is removed, and the wafer is directly fixed in the sample holder, as shown in Figure 6.7a, which shows the attachment of wafer from the back side. The same apparatus used for small area samples is also used to put the wafer at an oblique angle, and two strips are adhered to the sides of wafer for additional support. The wafer is characterized from nine different areas, which are shown

in Figure 6.7b to indicate the adaptation of oblique-angle deposition technique to large-scale fabrication, and also examine the uniformity of the coating. The experimental results are shown in Figure 6.7c. The solar absorption is measured only from area 5 and αs is calculated as 0.167, which is almost identical to the small-area fabrication. On the other hand, spectral response in thermalinfrared is measured from all nine areas. To further discern the variations in the absorption spectra between different areas, we zoomed into 3 μm to 25 μm region. It is seen that the regions further away from the source has slightly lower absorption, which is attributed to the minor nonuniformity in ITO thickness within the wafer. Nevertheless, the smallest ϵIR is found to be 0.957, while its highest value reached 0.97, so the variations within the wafer are not significant. Experimental results up to now have demonstrated the optimized optical performance of the metasurface OSRs. Nevertheless, decreasing the thickness of SiO2 is still desirable to decrease the launch and assembly costs and the weight of the OSRs when they are used to coat a spacecraft. The numerical results of Device 2 has shown that several different cavity thicknesses can result in almost equal FoM. It can be seen in Figure 6.4i that a cavity thickness between 1.5 and 1.6 μm gives the peak FoM, while also being the most tolerant area to thickness inaccuracies. Device 1 with h = 50 nm and tSiO2 = 1.55 μm is fabricated on a 4-in. wafer and is characterized in the same way as before. Experimental result for this device and numerical result for Device 2 with the same h and tSiO2 are shown in Figure 6.7d. The experimental results show similar characteristics to Figure 6.7c, and the physical reasoning outlined until now applies to this sample. The maximum ϵIR is calculated as 0.968, while its minimum value is 0.952. αs is found to be 0.169. Therefore, almost identical performance to the ITOD50CAV2000 device is achieved with a smaller thickness of SiO_2. Spectral response of Device 1 with h = 50 nm and $tSiO_2$ = 1.55 μm under obliquely incident radiation is measured experimentally in the thermal-infrared, from 3 to 25 μm, by utilizing ellipsometry method. The results at 30° and 45° incidence angles are shown in Figure 6.7e and f, respectively, for both p- and s-polarized incident radiations. The blue-shifting of the spectral response as well as increased absorption behavior are observed in these results. In this paper, up to this point, we have demonstrated that the outstanding performance of our proposed device fulfills the key functionality of an OSR, that is, a very high ϵIR, a small αs, large-scale compatibility, and uniformity. Our proposed device has a thickness around 2

μm, which is at least 2 orders of magnitude smaller than that of the conventional OSRs. Nevertheless, application of these devices to the radiative cooling of spacecraft in real-time necessitates further studies in scrutinizing the heat transfer and finding the cooling rates. In addition to these, the ongoing studies will focus on applying these ideas to flexible substrates and tests involving the mechanical, thermal, UV, and radiation resistance of the proposed devices. The perfect absorption in the thermalinfrared range and the experimentally obtained ϵIR of 0.968 are also very promising in the areas of thermal-imaging cameras with labeled security. As a proof-of-concept, a mask with drilled holes to create the labeling word “NANOTAM” is placed on the wafer before sputtering. After fabricating Device 1 with h = 50 nm and tSiO2 = 1.55 μm, the wafer is observed with a thermal camera. Lithography is not preferred to create the label in order not to sacrifice from large-scale compatibility. The view of the wafer with the naked eye is given in Figure 6.7g, and the “NANOTAM” label is barely

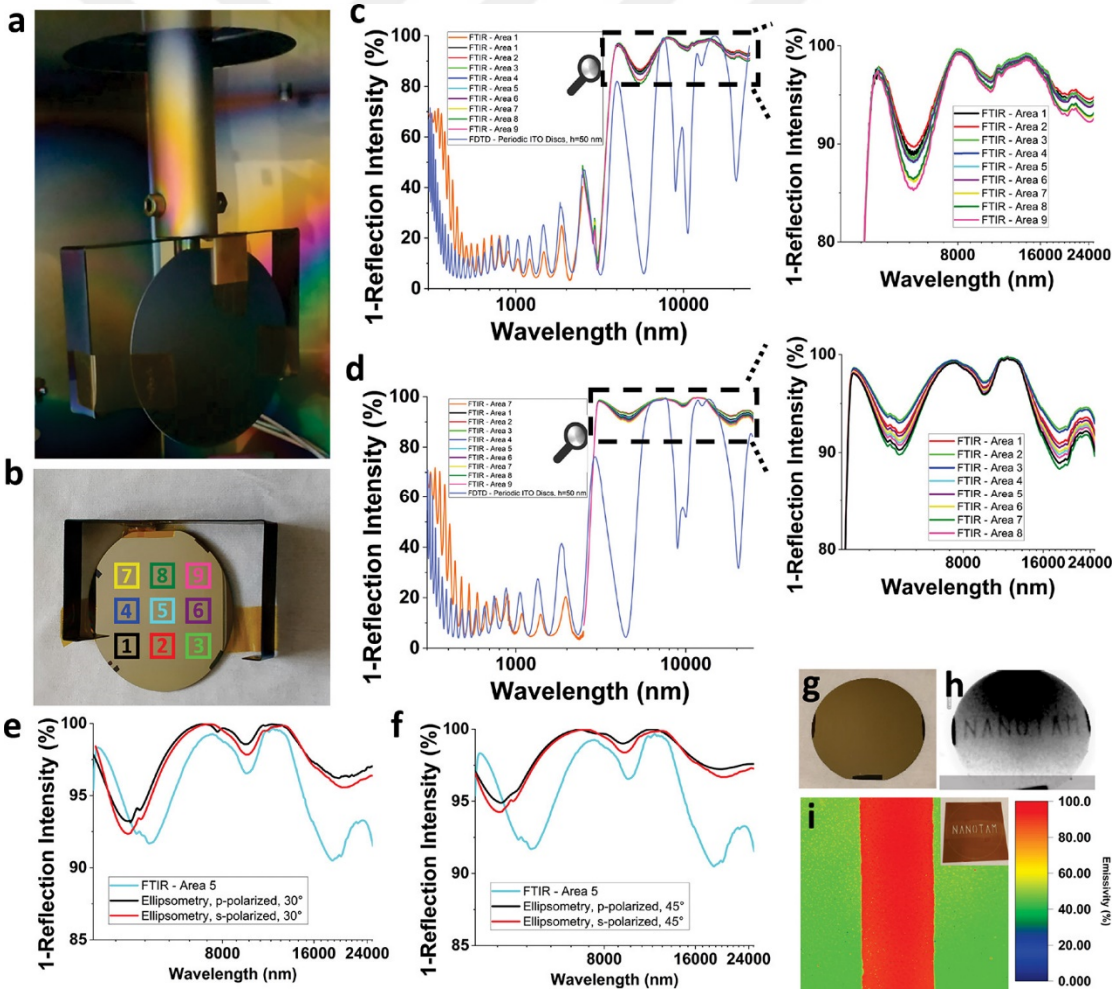


Figure 6.7 Large-scale fabrication and optical characterization of the proposed device. (a) Positioning of the wafer in the sample holder as seen from the back view. (b) Measurement areas in the fabricated wafers. Experimental absorption result for Device 1 with h = 50 nm and (c) tSiO2 = 2 μm and (d) tSiO2 = 1.55 μm, when fabricated on a wafer. Absorption spectrum under obliquely incident radiation at an incidence angle of (e) 30° and (g) 45°. Device 1, as seen with the (g) naked eye and by (h) thermal camera. (i) Thermal microscope image of Device 1. The ellipsometry measurements are taken from area 5.

recognizable. However, when this wafer is inspected under a thermal camera, the large emissivity difference between the ITO-coated versus noncoated areas makes the label clearly discernible, as shown in Figure 6.7h. In Figure 6.7i, we show a thermal microscope micrograph from one of the areas. The sharp contrast between the ITO-coated areas (appear red due to very high thermalemissivity) versus the noncoated areas is clearly distinguishable. It is also important to note from Figure 6.7i that the areas with only SiO2 coating still have an ϵIR of 0.5. This further supports our argument that the perfect absorption in the proposed devices are a result of the hybrid system of ITO and SiO2. Last but not least, the very high performance of our proposed devices can also find applications in daytime radiative coolers. However, the overall flat absorption over the entire thermal-infrared should be adapted to the atmospheric absorption lines, which is an ongoing study at this time.

In conclusion, metasurfaces utilizing disordered, densely packed, and titled ITO nanorod forests as the top absorbing layer are experimentally analyzed in this paper and the attainment of a record-high thermal-emissivity of 0.968, and Figure of Merit of 5.73 are verified. The top ITO scaffold of our metasurfaces enabled the very efficient harvesting of thermal-radiation to have an ultrabroadband absorption in the thermal-infrared range, while their small thickness did not accentuate the dielectric losses in the solar spectrum. The utilization of oblique-angle deposition with the line-of-sight coating of PVD systems allowed not only the realization of such ITO nanoforests, but also large-scale and high-throughput fabrication. The experimental results of the proposed devices are compared to the numerical simulations of periodic ITO discs and the experimental results of the planar ITO thin-film as the top absorbing layer. These comparisons further proved the absorption enhancement by the ITO nanoforests, which is mainly due to relieving the strong phonon reflection bands of SiO2 in thermal-infrared. Overall, our

ultrahigh performance, yet large-scale compatible devices hold great promise for the radiative cooling of spacecraft during their space missions, and it is also highly applicable to many areas such as terrestrial radiative coolers and thermal imaging for labeled security purposes.

Chapter 7. LFMAs for Photodetection Application

7.1. Preface

This chapter of the thesis is based on the publications:

”*Spectrally Selective Ultrathin Photodetectors Using Strong Interference in Nanocavity Design*”, A. Ghobadi, Y. Demirag, H. Hajian, A. Toprak, B. Butun, E. Ozbay, **Electron Device Letters.** 2019, 40, 925 – 928. Adapted (or “Reproduced in part”) with permission from IEEE.

7.2. Motivation

The collective oscillation of conduction electrons, so-called localized surface plasmon resonances (LSPRs), and inter-band transitions are the main responsible mechanisms for light absorption in nanometals. The large wave-vectors of surface plasmons triggers the confinement of EM fields into dimensions much smaller than the wavelength and these local hot spots provide the opportunity to manipulate light below the diffraction limits. The non-radiative decay of LSPR can generate “hot carriers”[365], [366]. The non-radiative decay pertains to the formation of hot-carriers and then energetic carriers can transfer to a neighboring semiconductor with a proper band alignment[367], [368]. While, in recent years, plasmonics found promising applications as single molecule level probing[369], [370], sensing[371], guiding[372], lasing[373], and color generation[374], the hot electron based photoconversion systems including photovoltaics (PV)[375], photodetector (PD)[376], and photoelectrochemical (PEC) cells[377] have triggered much attention. In spite of years of intensive studies to find an alternative plasmonic material[26], [27], [55], [378], [379], gold (Au) plasmonics keep and strengthen

its dominance in this field mainly owing to its high LSPR quality factor, energetic and relatively long-lived hot electron generation, and high chemical stability. However, in spite of intensive attempts, the hot electron technology has reached to a performance plateau with a weak up-scaling capacity. However, the relaxation of hot electrons in plasmonic nanounits with a dominant electron-electron scattering mechanism, called Landau damping, occurs in a few tens of femtosecond timescale and, therefore, only highly energetic carriers have the chance to traverse the Schottky barrier[53]. The hot electron photoemission efficiency is much less in planar and large particle sizes[54] where the absorption mechanism is mainly due to non-resonant inter-band transitions rather than the excitation of LSPRs. In fact, it was theoretically proved that LSPR decay can generate higher density of hot electrons with a narrow spectral distribution[380], [381]. But, even in this case, the inherent short carrier lifetime is the main performance limiting factor, and design/geometrical manipulation can partly ameliorate it. In recent years, the search for alternative low-cost and high-performance material platforms encompassed a vast variety of elements and compounds, including earth-abundant metallic elements (such as Al)[55]–[57], conductive oxides[27], [58], [59], transition metal nitrides/carbides (such as TiN)[60], [61], and doped semiconductors[62]–[64]. However, the hot electron extraction efficiency of the systems made of all these materials is still much lower than desired. One of the prime applications of hot electrons is realization of sub band gap detection via CMOS-compatible near infrared (NIR) PD to be potentially employed in the telecommunications band[382]–[384], avoiding the need to use InGaAs and Ge PDs. In hot electron-driven PDs, plasmonic nanoantennas based systems were limited with a photoresponsivity lower than 100 mA/W[376], [385]. Thus, an alternative pathway was chosen by scientists, where rather than material, a hybrid configuration, named as “antenna-collector”, was employed[386]. Antenna produces electron, and a two dimensional (2D), high mobility material such as graphene[387], [388], or molybdenum disulfide (MoS_2)[389] is utilized as carrier collector. This hybrid system has led to a responsivity on the orders of A/W (5.2 A/W at 1070 nm)[389]. However, in spite of its large photoresponsivity, its response time was slow. Recently, the concept of free-carrier absorption (FCA) in highly doped semiconductors was demonstrated for hot electron based PDs[390]. In this system the “collector” is not only there for collection but also it contributes to the overall efficiency of the system, via generation of hot free carriers. Although

combination of hot carrier and FCA in highly doped semiconductors can boost the photoresponse, such design is not a robust one and has material and design limitations. Similar to hot electron emission over a metal-semiconductor interface, the injection of hot electrons to anti-bonding orbitals of an adsorbent can also drive chemical reactions[391], [392]. On nanometals, hot-carrier mediated photocatalysis provides new possibilities for converting thermally-driven catalytic processes into light-driven processes with substantially lower operating temperatures. Killer applications of hot electron based photocatalysis encompass water splitting[393], H_2 production from alcohol[394], gas phase oxidation reactions[395], and hydrocarbon conversion[396]. Similar to PD/PV technology, hot electron based photochemistry was subjected into intensive material-geometry-composition explorations, but, due to the same obstacles, its efficiency is still low[377]. Different from PD/PV, plasmonic particles (rather than gold) can undergo severe corrosion and this, in turn, can restrict their long-term stability. Moreover, strongly plasmonic particles (noble metals) are generally a weak catalyst, and strongly catalyst particles (transition metals) have poor plasmonic dynamics. Colloidal suspension and thin film designs are two main platforms in this application. The former shows lower benchmarks and suffers from a lack of proper mechanism for the spatial separation of reduced/oxidized products. However, applying an external bias into a thin film platform allows us to separate the energetics and kinetics constraints by using two/three electrode systems to drive the oxygen and hydrogen evolution. The state-of-the-art hot electron based photoconversion devices employ hybrid architectures to exploit synergetic effects. In PD and PV, “antenna-collector”[389] created a new benchmark for hot electron based technology. Similarly, in PEC, “antenna-reactor” complexes[397], [398], where the antenna is a plasmonic hot electron generator, and the reactor is a catalyst host, seems to be a promising approach. However, all these hybrid designs’ efficiency is still limited by inherent poor excited state dynamics of the materials. This is essentially due to existence of multiple loss channels in hot electron-driven systems including resistive dissipation, ultra-short excited state lifetime (~10s of femtoseconds), low carrier mobility, interface trapping, and electron-momentum conservation[386]. Therefore, the first step is to find new materials with strong photo-electronic response. Moreover, the possible future up-scaling of these designs to industrial levels requires well-developed, reliable, and large scale compatible routes. This thesis work aims to unveil the unprecedented

photo-electronic response from a new class of materials, called p-block semimetals and their compounds.

Similar to metals, LFMAs can be also realized in semiconductor based designs. These LFMAs can also be realized in planar semiconductor based metasurfaces and they can go beyond the Yablonovitch limit [71], [153], [399]–[403]. These metal-semiconductor (MS) designs could be of particular interest in the vast variety of optoelectronic applications. In a recent Perspective [318], we showed that strong light absorption can be realized using lithography-free planar semiconductor based metamaterials, in a broad or narrow frequency range, upon the proper choice of material and configuration. Our theoretical findings reveal that the use of a metal-insulator-semiconductor (MIS) configuration (instead of MS design) adds a new degree of freedom to improve the design response. By tuning the spacer layer thickness, it is possible to tune the operation wavelength [79] and bandwidth (BW) of the design [404]. Therefore, PLA can be acquired in dimensions much smaller than the carriers' diffusion length. Considering the fact that semiconductors in such thin thicknesses are amorphous and have a short diffusion length [252], the total absorption of light in nanometer scale dimensions can significantly increase the carriers' collection efficiency. Therefore, the concept of photodetectors with cavity enhancement have been the subject of several studies[79], [405]–[407].

In ths thesis, a spectrally selective visible blind ultraviolet (UV) photodetector is fabricated using a 4 nm thick a-Si layer in an MIS architecture. The proposed cavity design is designed in a way that the ultrathin semiconductor layer undergoes a strong light-matter interaction in the UV range while it is transparent into the incident visible light. The resonant mode in the cavity is adjusted with both spacer and top layer thicknesses to optimize the detector UV response. The optimized design has above 70 percent absorption in UV and only 2 percent in the visible range. This leads to an approx. two orders of magnitude difference in the photoresponsivity of the design between these two spectral regions. The design shows responsivity values of 120 mA/W and 2.5 mA/W in the UV (λ=350 nm) and visible (λ=500 nm) regions, respectively. It is envisioned that the use of other semiconductors in proper cavity geometries could lead to spectrally selective photodetectors.

7.3. Spectrally Selective Ultrathin Photodetectors Using Strong Interference in Nanocavity Design

To begin with, a theoretical method based on the transfer matrix method (TMM) is adopted to find the ideal permittivity data for light perfect absorption in a MIS configuration [318], as depicted in Figure 7.1a. In this model, the bottom layer is thick aluminium (Al) mirror, the spacer is aluminum oxide (Al_2O_3) with a thickness of D_I. The top ideal material has been extracted for a D_S thick layer. The reflection contour plots at different wavelengths have been extracted for two different D_M thicknesses of 3 nm, and 10 nm, as shown in Figure 7.1b-c. As these contour plots show, the reflection near zero regions (the bluish circles) are much wider for the thinner top layer. Thus, the probability that a

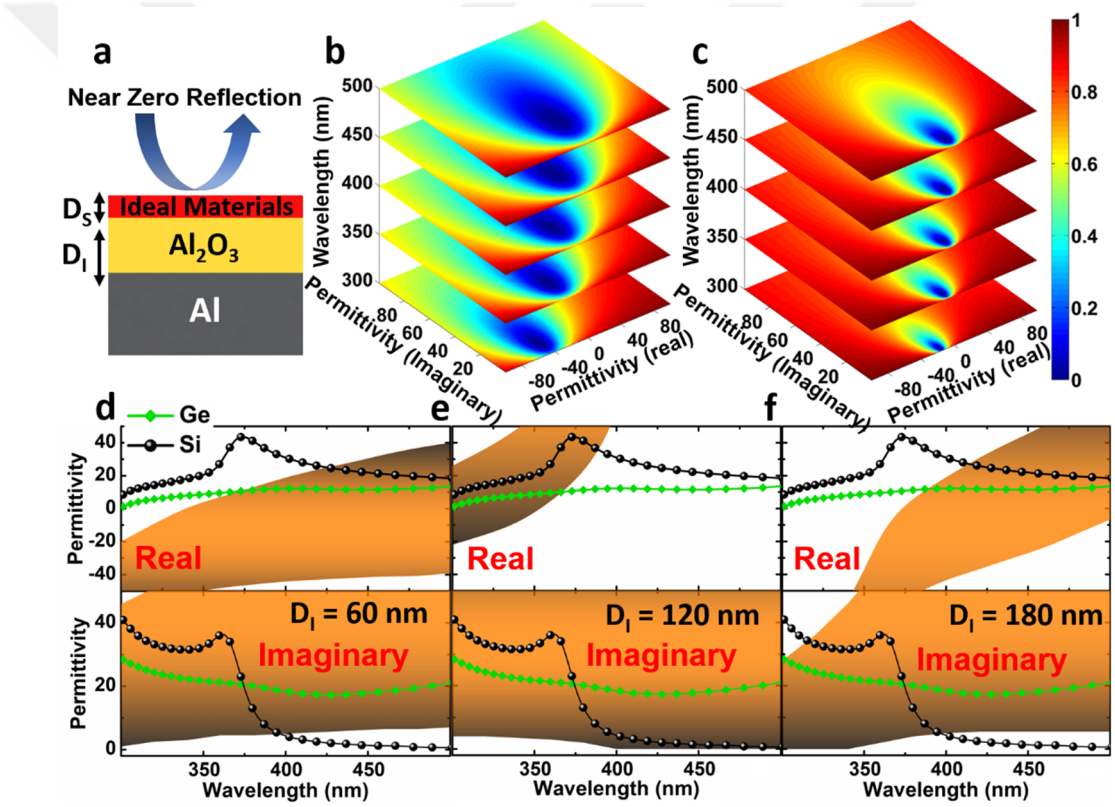


Figure 7.1 (a) The schematic representation of MIS cavity design and its geometries. (b) The reflection contour plots as a function of real and imaginary parts of permittivity in different wavelength values for (b) D_S=3 nm, (c) D_S=10 nm. The insulator is fixed at 60 nm. The extracted ideal regions and their matching with the permittivity data of Si and Ge for three different D_I values of (d) 60 nm, (e) 120 nm, (f) 180 nm.

semiconductor permittivity locates inside the ideal perfect absorption region is higher for thinner top layers. Therefore, the D_S is fixed at 3 nm and this time the impact of D_I is investigated. For this aim, the tolerable real (ε_{real}) and imaginary ($\varepsilon_{imaginary}$) parts of permittivity for a reflection below 0.2 (corresponding to an absorption above 0.8) is extracted for D_I = 60 nm, 120 nm, and180 nm, as shown in Figures 7.1d-f. In other words, the highlighted region shows the borders of blue circles for ε_{real} and $\varepsilon_{imaginary}$ where the reflection is below 0.2. These ideal regions are compared with the permittivity data for Si and Germanium (Ge). For the case of Si, the matching of $\varepsilon_{imaginary}$ is only met for the shorter wavelengths while the real part matching is tuned as we change the D_I. At the specific dimension of D_I = 120nm, we have matching in both parts. However, for Ge, the imaginary part matching is obtained in the whole range Taking this theoretical estimations into account, numerical simulations, using a commercial finite-difference time-domain (FDTD) software package[316], are further employed to investigate the absorption capability of the MIS design. Based on our theoretical calculations, we will focus on the design of a silicon metasurface based visible blind UV photodetector. To further optimize our MIS design, we need to find the amount of the absorbed power inside the ultrathin Si coating to maximize the UV absorption while minimizing the visible response. For this purpose, three D_S values of 1 nm, 4 nm, and 10 nm are selected. Fig. 2(a)-(c) depict the absorbed power data inside the Si layer. To have a better qualitative comparison, the average UV (300 nm-400 nm) and visible (400 nm-500 nm) light absorptions have been calculated and exhibited in Figure 7.2d. The 1 nm thick case has quite negligible visible absorption while the UV absorption is high. The UV response becomes stronger while the visible light absorption is still quite small for 4 nm thick Si layer. This behaviour is diminished in the case of 10 nm thick top layer. and the matching of real part experiences a red shift as we go to thicker spacer layers (see Figure 7.1e-f). Therefore, while Si acts as an UV absorber, Ge can reveal spectrally selective visible perfect absorption by tuning the D_I, which is in line with previous studies[79].

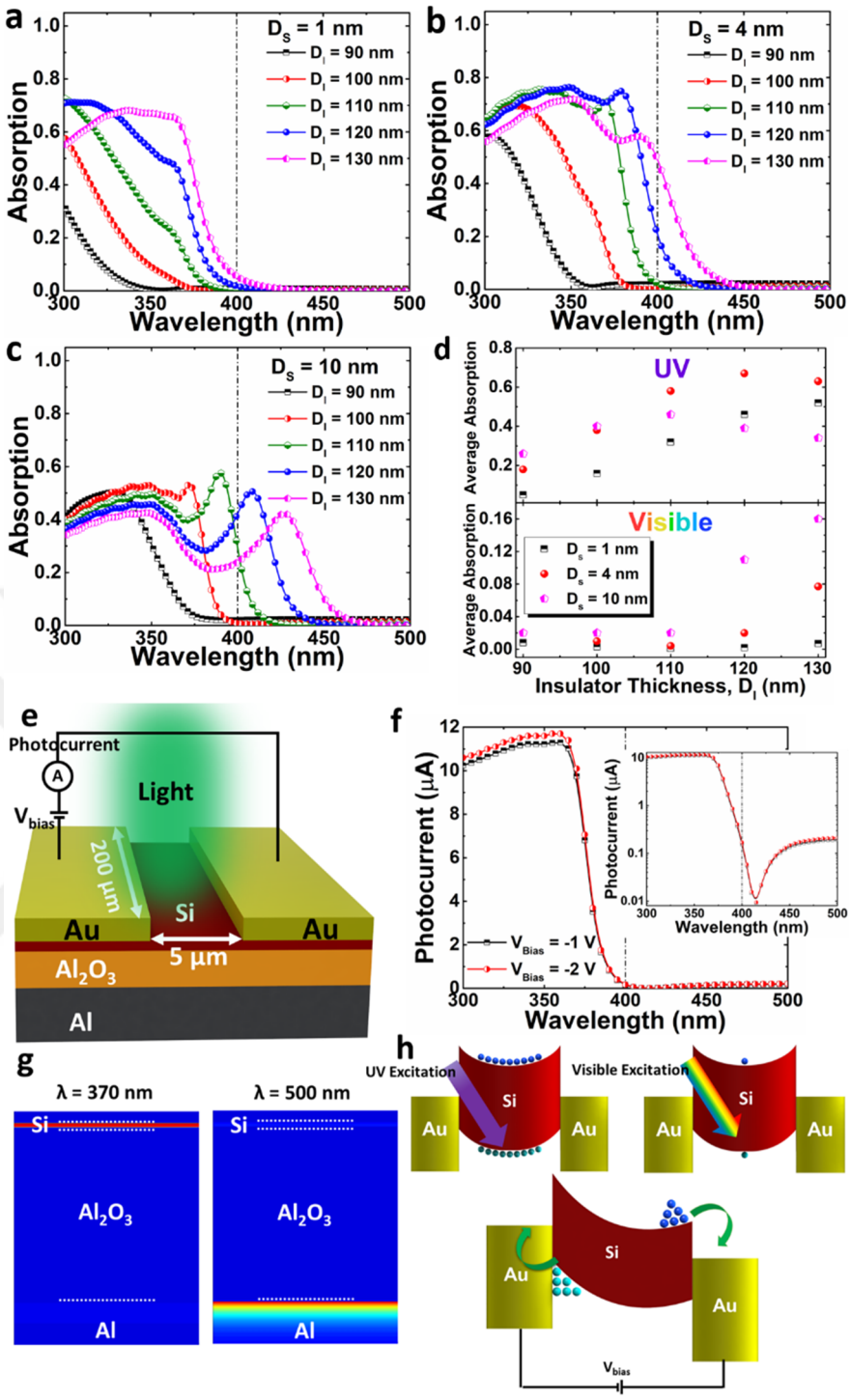


Figure 7.2 The absorbed power within Si slab for different D_S values of (a) 1 nm, (b) 4 nm, and (c) 10 nm. (d) Average light absorption in UV and visible regimes for different design geometries. (e) The proposed MSM photodetector made on MIS cavity, (f) simulated photocurrent values of the design as a function of light wavelength, (g) light absorption across the cavity in two wavelengths of λ=370 nm, and 500 nm, and (h) representation of device operation under UV and visible light irradiation.

Looking at the average absorption values, it can be understood that the optimized response belongs to D_S= 4 nm, D_I= 120 nm where UV absorption is above 0.7 while it is just 0.02 for visible light. In order to numerically analyze the electrical response of the detector, COMSOL Multiphysics finite element method solver is utilized. For the optimal design and mentioned geometries in Figure 7.2e, the photocurrent response of the cavity in the UV region is about two order of magnitude higher compared to that of visible light, see Figure 7.2f. Inset shows data in the logarithmic scale. This response could be further explained by looking at the absorption profile of the MIS design in two different wavelengths of 370 nm and 500 nm, as plotted in Figure 7.2g. While for the UV excitation (370 nm), most of the light is harvested in the ultrathin Si layer, this layer is transparent to visible incident light. Therefore, the formation of a symmetric metal-semiconductor-metal (MSM) junction (Au-Si-Au) at the top surface led to the formation of a visible blind UV detector. The band alignment and operation principle of this photodetector is illustrated in Figure 7.2h.

To verify our numerical results, the proposed optimal structure is fabricated and characterized. The structure is an MIS cavity made of Al (100 nm)-Al_2O_3 (120 nm)-Si (4 nm). Afterward, inter-digitated Au electrodes are deposited on top of the cavity to from MSM junction. Figure 7.3a shows cross sectional scanning electron microscope (SEM) image of the MIS structure and its top view showing the Au electrodes. Al and Si layers are deposited using thermal evaporation with an approximate rate of ~ 1A°/sec. Al_2O_3 layer is formed using atomic layer deposition similar to our previous study [408]. To minimize the formation of native oxide layer between the Au and a-Si, both layers have been deposited in the same deposition process without breaking the chamber vacuum. Finally, standard photolithography and etching (using Au etchant) processes are conducted on the sample to form inter-digitated electrodes. To characterize the structure, first, the permittivity data of Al and Al_2O_3 layers are extracted using an elipsometry device [408]. These permittivity data are employed in our simulations. To characterize the photocurrent response of the system, IV characteristic of the structure is measured for dark and 370 nm illuminated light conditions. As we can see from Figure 7.3b, the photocurrent is about two order of magnitude larger compared to dark one. As seen in this panel, the dark current minimum does not locate in the 0 V bias. This could be due to the

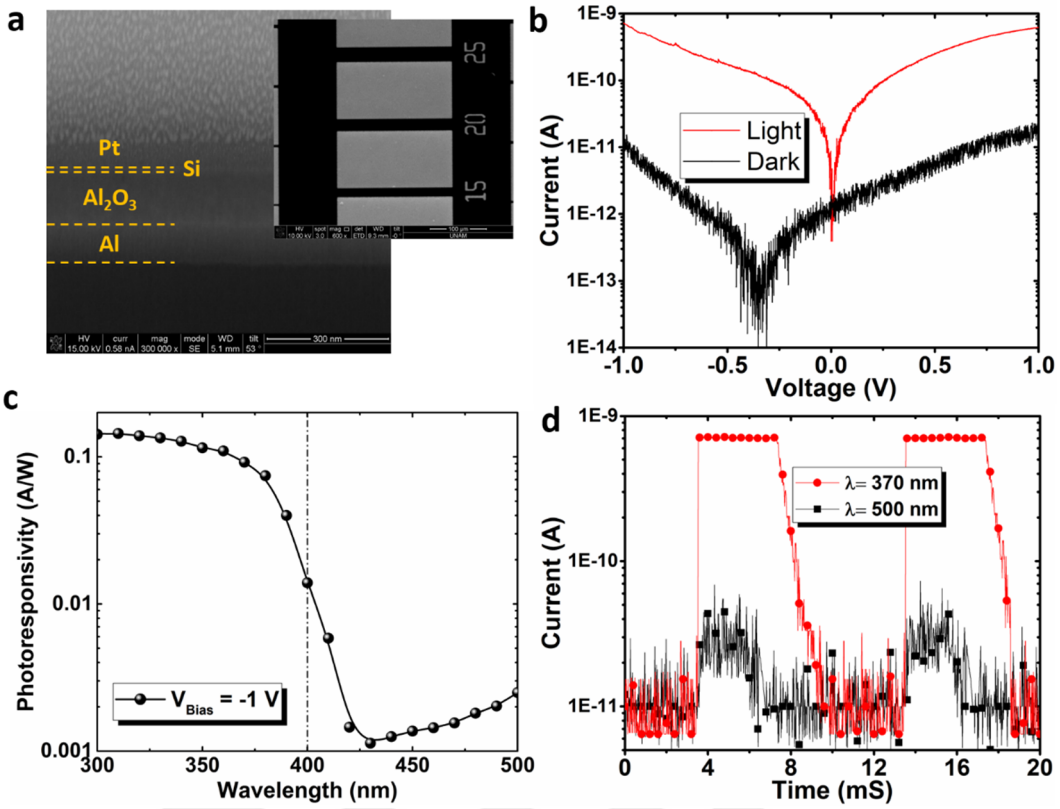


Figure 7.3 (a) Cross-sectional and top SEM images of the photodetector, (b) I-V characteristic, (c) photoresponsivity, and (d) I-t response of the photodetector for different dark and light conditions.

existence of electron trapping-de-trapping in metal-semiconductor interface which is Au-Si in our case. As previously explained, in equilibrium condition, electrons are trapped in interface defects. When a negative voltage is applied, the trapped electrons can be de-trapped and contribute to the overall current [409]. To have a better qualitative comparison, the photoresponsivity of the photodetector is measured from 300 nm to 500 nm under a bias voltage of V=-1V. The measurement setup was similar to the one used in our previous study[410]. The cavity design exhibits a photoresponsivity of 120 mA/W at λ=350 nm while it drops to significantly smaller values of 2.5 mA/W for λ=500 nm, see Figure 7.3c. Therefore, the structure shows a high responsivity ratio of about 50 for UV and visible lights. These results further confirm our simulations that this cavity acts as a high performance visible blind UV detector. The speed of this UV detector has been also investigated by analyzing its transient response under a bias voltage of -1V for two incident light wavelengths of 370 nm (UV) and 500 nm (Visible), Figure 7.3d. While the structure shows a weak

visible light response, the UV activity of the MIS cavity has relatively short rise and fall times. Taking all of these results into consideration, the proposed sub-wavelength MIS cavity-based design has high UV detection performance. The proposed cavity has not only application in photodetectors and photovoltaics, but also it can be utilized for emission applications. It is known that reducing the size of a semiconductor nanoparticle down to its exitonic Bohr radius can intensify its emission property[411], [412]. In the other side, as demonstrated in this paper, the strong light-matter interaction in a semiconductor based cavity occurs in nanometer scale thicknesses. Therefore, it is envisioned that introduction of a thin layer of semiconductor nanoparticles into this cavity can significantly enhance its emission property. Thus, this strategy can serve as a beacon for design of efficient, ultrathin optoelectronic devices.

In this WORK, we demonstrated a visible blind UV photodetector using a MIS cavity configuration. The proposed configuration shows responsivities of 120 mA/W and 2.5 mA/W in the UV and visible regions, respectively. This work demonstrates the functionality of strong interference in semiconductor based cavity designs to obtain spectrally engineered, ultrathin optical devices.

7.4. Spectrally Selective Bismuth Based Photodetectors: Preliminary Results

The first objective of this project proposal is to scrutinize the photo-electron dynamics of selected group VA semimetals and their VA-VIA compounds, as highlighted in Figure 7.4a. Optical, an ideal blackbody absorber: The prime example of these elements is Bismuth (Bi). Decades ago, it was the subject of many studies due to its superior physical properties, including its giant magnetoresistance and diamagnetism, long electron mean-free path length, and quantum confinement effects in ultrathin planar and nanostructured geometries. While the UV plasmonics was predicted for Bi, back in 1995, it was recently proved by experiments that Bi can support both LSPR and inter-band transitions to achieve light absorption in all spectral range of solar irradiation. In a recent study by my team, we showed that Bi has an extraordinary permittivity response that exactly follows the ideal absorber model, as obtained by the transfer matrix method. Figure 7.4b compares the permittivity data of our targeted elements and compounds. Unlike common noble and lossy metals,

these materials all show small negative values in the visible (Vis) and NIR ranges and positive real permittivities in the longer wavelengths. Therefore, it can be expected that nano Bi can support LSPRs in the UV-Vis-short NIR range, and Mie resonances in the longer ranges. Electrical, a topological insulator with large electron mobility: Very recently, it was unveiled that Bi is a "higher-order topological insulator", where it can theoretically conduct electricity without any dissipation. Bi also shows small carrier density (10^{17} cm^{-3}) with a superior high electron mobility (106 $cm^2 s^{-1}$ V^{-1}), even in the polycrystalline phase. Moreover, the electron mean free path for Bi is an order of magnitude larger (~1-4 μm) compared to all common lossy and noble metals (~< 50 nm). Photoexcited carrier dynamics, energetic hot carriers with nanosecond scale lifetime: Although these group of materials unveil superior light harvesting and electronic transport capability, what inspired me to write this proposal was their stunning excited state dynamics, as the femtosecond-scale hot electron relaxation in noble metals is the prominent limiting factor in hot electron systems. To explore the excited states dynamics, I conducted transient absorption (TA) spectroscopy on thin (10 nm) Bi and antimony (Sb) films, using a 500 nm pump and multiple probe wavelengths, see Figure 7.4c. Based on these spectra, both of these semimetals have excited state lifetimes in the nanosecond scales, orders of magnitude larger compared to that of Au. Considering the fact that a planar design does not excite LSPRs, the obtained excited state decay dynamics belongs to the inter-band transition mediated hot electrons. Besides prolonged excited state lifetime, we need energetic (with respect to Fermi level) hot carriers to overcome the Schottky barrier. Ab Initio calculations are performed to predict the most probable excitation paths for these materials. As depicted in Figure 7.4d, excitations wavelengths in the vicinity of solar irradiance peak generates both energetic hot electrons and hot holes. This unconventional character might be a key factor in the photoconversion performance of Bi. Previous studies demonstrated the photocatalytic performance of nano Bi, although the activity of those works was low, with a photocurrent density in the orders of μA cm-2. A recent report demonstrated an ultra-broadband PD with responsivity values as high as 250 mA/W in a simple planar bulk Bi layer, where inter-band transitions are the only active mechanism (no LSPR). Different from PEC, where hot carriers undergo a fast oxidation/reduction upon excitation, in a PD, the photogenerated electron/hole pair's separation and collection are the processes that define the

overall efficiency. Thus, Bi has an inherent charge separation mechanism. Therefore, based on all these experimental findings, theoretical models, and predictions, VA semimetals and their VA-VIA alloys are an uncharted territory in the hot electron industry.

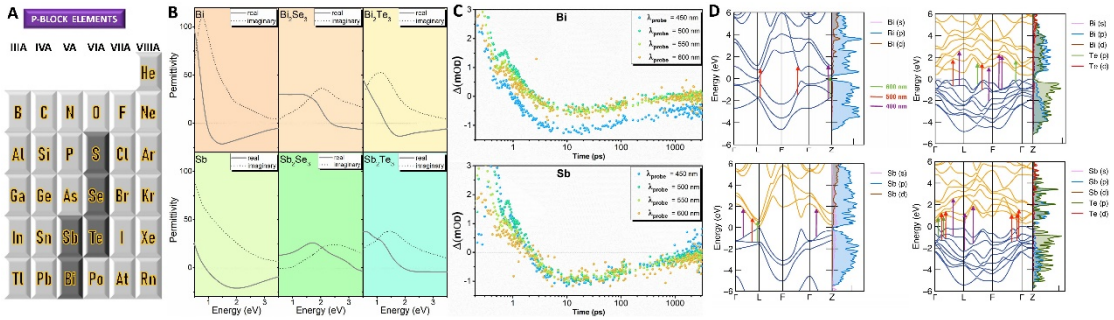


Figure 7.4 (A) P-block elements, and (B) the permittivity values of the targeted elements and compounds. (C) The TA decay profiles for different probe signals for Bi, and Sb thin films. (D) The Ab Initio quantum calculations showing the possible electron excitation routes in four different materials of Bi, Sb, Bi2Te3, Sb2Te3

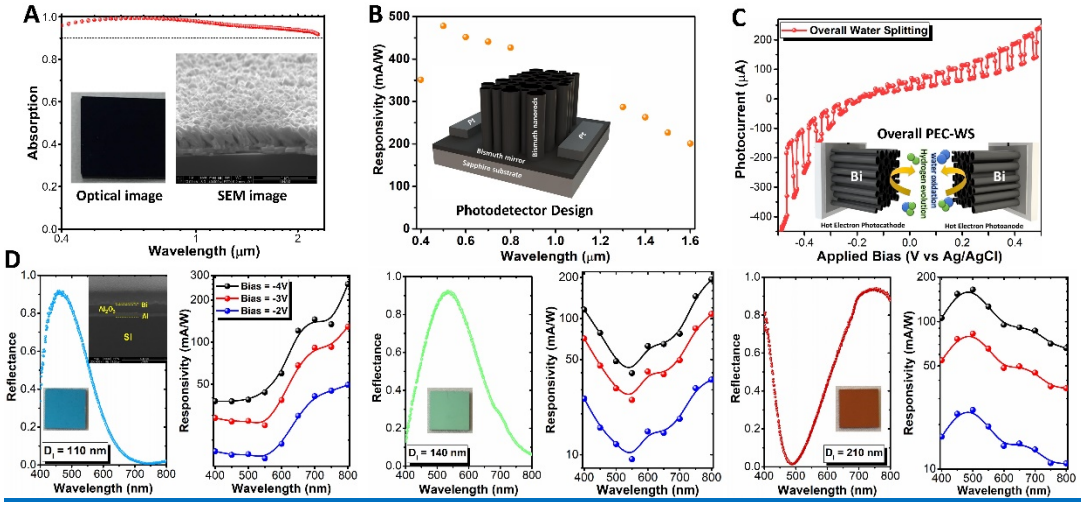


Figure 7.5 (A) The absorption response of Bi nanorod metaabsorber (the inset shows the optical and the scanning electron microscopy (SEM) image of fabricated sample), (B) the responsivity values for the ultrabroadband Bi PD (inset: device configuration). (C) Anodic and cathodic chopped photocurrent-voltage characteristic of the sample (inset: setup). (D) MIM based color PD for different insulator layer thicknesses of D_I.

All the above mentioned findings shows unprecedented potential of these p-block components for hot electron based photoconversion devices. To achieve

the preliminary results, Bi is chosen and some killer applications are explored. For this purpose, I made planar nanocavity and nanorod based (using oblique angle deposition approach) designs and scrutinized its photocurrent and responsivity as a PD, and PEC cell. As depicted in Fig. 7.5a, the obtained Bi nanorods can undergo strong light-matter interaction in a broad wavelength regime (0.4-2.4 μm) covering the whole solar spectrum. The simple PD, made of these nanorods, shows an ultra-broadband responsivity with a maximum of around 500 mA/W, Fig 7.5b. This value is substantially higher than common hot electron devices. The same configuration is used for the PEC water splitting (PEC-WS), wherein the Bi nanostructure revealed an extraordinary response by efficient operation in both anodic (water oxidation) and cathodic scans (hydrogen evolution), Figure 7.5c. The selective isolation of hot electrons/holes in bulk-surface interface of Bi could be the origin of this response, but further theoretical and ultra-fast analyses are required. Moreover, the performance of planar layer in design of spectrally selective PDs is also studied, using a simple metal-insulator-metal (MIM) nanocavity, where the top layer is Bi. As illustrated in Figure 7.5d, Bi nanocavity could provide low cost and high performance color PDs, simply tuned by the spacer layer thickness.

Chapter 8. LFMAs for Photoelectrochemical Water Splitting Application

8.1. Preface

This chapter of the thesis is based on the publication ”*Strong Light–Matter Interactions in Au Plasmonic Nanoantennas Coupled with Prussian Blue Catalyst on $BiVO_4$ for Photoelectrochemical Water Splitting*”, A. Ghobadi, T. G. Ulusoy Ghobadi, M. Soydan, M. Barzegar Vishlaghi, S. Kaya, F. Karadas, E. Ozbay, **ChemSusChem**, 2020, 13, 2577 – 2588. Adapted (or “Reproduced in part”) with permission from John Wiley and Sons.

8.2. Motivation

Conversion of sunlight into electricity and chemical energy are the major paths to produce green energy. Unlike semiconductors, which only harvest photon energies above their bandgap, nanometals exhibit resonant light absorption in the whole electromagnetic spectrum, via the excitation of localized surface plasmon resonances (LSPRs) and inter-band transitions. Thus, plasmonic photoelectrochemical water splitting (PEC-WS) offers a promising approach to convert sunlight into chemical energy, which has recently received intense research.[65], [413]–[418] Plasmonic nanometals can contribute in semiconductor activity enhancement via two main pathways; i) radiative (scattering, optical near field coupling) and ii) non-radiative energy transfer (hot electron injection, plasmon resonant energy transfer).[65] In the former mechanism, the plasmonic nanoantenna can improve light absorption for above bandgap photons, while the later one can provide sub-bandgap light harvesting.

Although one of the most successful semiconductors - for plasmonic PEC-WS - is titanium dioxide (TiO_2), mainly due to its chemical stability, earth

abundance, and cost effectiveness,[419]–[427] it suffers from poor absorption response that only covers the ultraviolet (UV) portion of the solar spectrum. Therefore, in recent years, extensive attempts were made for the design and realization of plasmonic coupled low bandgap metal oxides for driving water oxidation and reduction reactions.[416], [428]–[447] By decorating plasmonic deep sub-wavelength nanoparticles on a semiconductor, near field effects[429], [442], [444] and hot electron injection[423], [444] can simultaneously contribute in the overall activity of the cell. Strong light-matter interaction, in the plasmonic-semiconductor interface, can trigger the formation of intense localized fields.[448] These confined fields increase the density of photogenerated carriers in the vicinity of the surface, and facilitate the charge separation.[449], [450] However, larger noble metal particles cannot support LSPRs and have a negligible hot electron injection yield. In this platform, these particles act as a mirror that reflect/scatter light. The formation of Fabry-Perot (FP) resonance modes in metal-semiconductor nanocavity is the main mechanism in these architectures to harvest solar irradiation. Some recent works have proposed innovative hybrid schemes that take advantage of using both FP resonances (supported by Au reflector in a nanocavity) and LSPRs (through the use of plasmonic nanoparticles) to achieve the high performance photoanode in PEC-WS systems.[445], [446]

Besides the superior absorption characteristics of these plasmonic-narrow bandgap semiconductor designs, their electrical performance is also a prominent factor. The main bottlenecks of low bandgap semiconductors (compared to wide bandgap ones) are their shorter diffusion length and higher recombination rate. Therefore, just a portion of carriers in the vicinity of their surface can participate in a water oxidation reaction. This drawback can be intensified in the presence of plasmonic nanometals. These metallic nanoparticles act as an electron trapping center that captures the photocarriers and hamper their collection efficiency. That is why, an optimum metal loading is required to make a right trade-off for performance improvement.[450]–[452] Another approach could be the use of a proper catalyst for the selective isolation of photogenerated carriers to enhance their lifetime.[443], [446] Therefore, in an ideal scheme, a low bandgap semiconductor loaded by a plasmonic-catalyst heterostructure with a selective decoration can reveal superior opto-electronic and catalytic properties. Moreover, the simultaneous

formation of small and large particles could excite both FP and LSPR modes to achieve both semiconductor light absorption enhancement and plasmonic hot electron injection. In recent studies,[424], [453], [454] we developed a facial route based on oblique angle deposition to synthesize plasmonic nanostructures in large scales. Moreover, we demonstrated that cyanide chemistry, so-called CoFe-PBA is a strong and robust water oxidation catalyst (WOC), when connected to an organic chromophore.[455], [456] Inspiring with these studies, herein, we adopt an extendable platform for the realization of catalyst-plasmonic architecture to improve the performance of semiconductor photoanodes with a facial and large scale compatible design in PEC-WS.

For this purpose, in the first study, bismuth vanadate ($BiVO_4$) nanostructures are capped with Au particles using a shadowing effect of an oblique angle deposition. In this method, the dimension and shape of Au capping are defined by the shape of $BiVO_4$ and, therefore, it leads to the formation of multi sized/shape particles. The larger particles enhance light absorption within the semiconductor bulk, via light scattering and FP resonance modes. The small ones provide sub-bandgap absorption and contribute in photocurrent via LSPR induced hot electron injection. Finally, to optimize the electron dynamics, PBA, as a WOC, is decorated on the surface of the photoanode. As a result of these modification, the photocurrent value at 1.23 V (vs RHE) is enhanced by an order of magnitude compared to that of bare $BiVO_4$ (from 190 μA cm^{-2} to 1,800 μA cm^{-2}).

In the second study, a large scale compatible sub-wavelength densely-packed disordered semiconductor metasurface design is developed for PEC hydrogen generation. In the proposed design, oblique angle deposition is employed to fabricate random chromium (Cr) nanorods. Afterward, thermal oxidation is applied to transform these metallic units into a p-type chromium oxide (CrO_X) semiconductor. It is shown that, at an optimal annealing time, enhancement in the photocurrent values near an order of magnitude can be detected. Numerical simulations show that these CrO_X nanounits can ideally support multiple electrical and magnetic modes. Moreover, from these simulations, the ultra-small gap regions can trigger the formation of localized hot spots. These hot spots not only intensify light absorption in near surface regions, but also facilitate charge separation and reduce charge transfer

resistance in the semiconductor-electrolyte interface. In addition to these superior optical and electrical responses, the fabricated CrO_X metafilms reveal promising excited state electron dynamics. Femtosecond transient absorption (TA) spectroscopy demonstrate a nanosecond scale excited state lifetime for the excited carriers. Moreover, this photocathode design revealed stable operation, upon long-term light irradiation. Finally, to substantiate the photocurrent response, a heterostructure made of CrO_X-NiO_X is introduced. In this core-crown configuration, the NiO_X layer acts as a hydrogen evolution catalyst. The proposed heterodesign shows a photocurrent as large as 50 μA cm^{-2}. Furthermore, the incident photon conversion efficiency (IPCE) of the design is extended up to 500 nm. The proposed design methodology can be used as a toolbox to design and fabricate scalable photo-electronic devices.

8.3. Strong Light-matter Interaction in Au Plasmonic Nanoantennas Coupled with Prussian Blue Catalyst on $BiVO_4$ for Photoelectrochemical Water Splitting

To For the preparation of a plasmonically modified $BiVO_4$ electrode (Au-$BiVO_4$), an oblique angle physical vapor deposition procedure was adapted to selectively coat Au on the tip of the photoanode, represented schematically at Figure 8.1a. Oblique deposition, sometimes referred as glancing angle deposition, is a physical vapor deposition technique that is used to form a nanostructured film with adjustable density and columnar grain growth in the vapor flux direction.[9] In this approach, a sample is placed in a position that is oblique to evaporated atoms. When the evaporated flux reaches to the substrate, an additional factor is introduced into the growth process, which can result in nanostructures instead of continuous layer. It is widely accepted that the mechanistic factor controlling the nanostructural evolution of the films is an atomic-scale “shadowing effect”, which prevents the deposition of particles in regions situated behind initially formed nuclei (i.e. shadowed regions). Inspired from this technique, we have developed the proposed design. In our case, the previously grown nanostructures are exposed into the gold vapor. Due to the shadowing effect of $BiVO_4$ nanostructures, only their tip is coated. The tip size and its direction define the size and shape of gold caps. As depicted in this

Figure 1a, the sample is placed on the holder with an incident angle as wide as 80-85°. Since the gold vapor cannot reach the bulk of the $BiVO_4$ nanostructure due to this shadowing effect, only the tip of photoanodes are coated. From the top view of the SEM images for bare $BiVO_4$ and Au-$BiVO_4$ (Figure 8.1b-c), it is obvious that the gold capping has not changed the morphology of the bare sample. The magnified image in Figure 8.1c inset, clearly reveals the expected formation of Au decoration on $BiVO_4$ photoanode. Further analysis on the

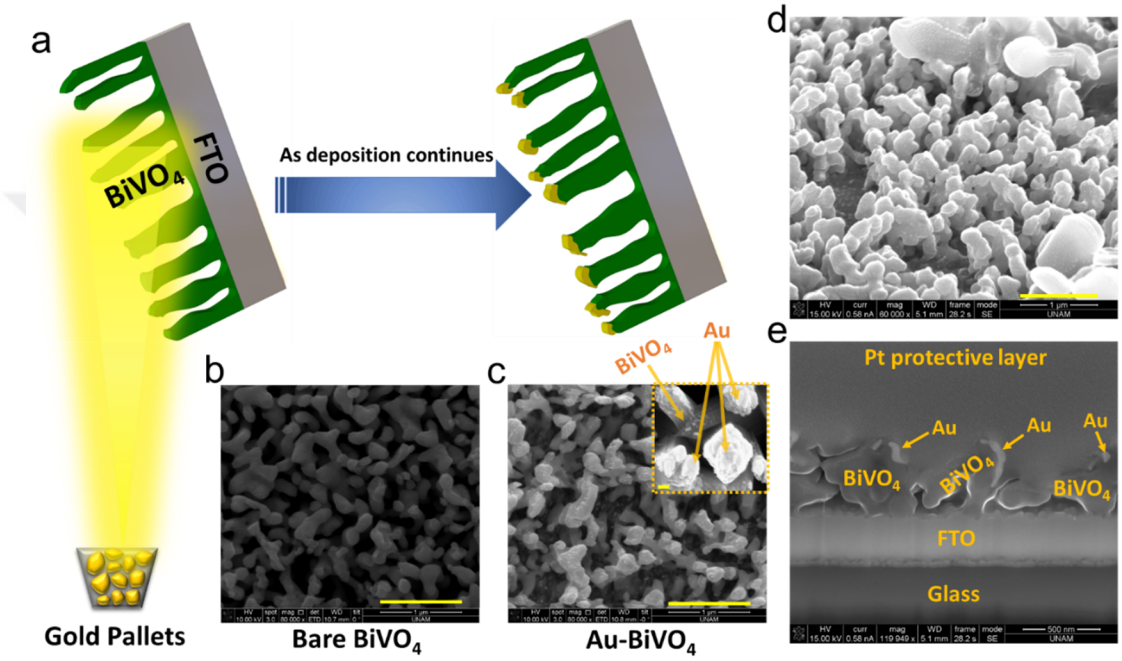


Figure 8.1 (a) Schematic representation of fabrication route for preparing gold capped $BiVO_4$ photoanode by using oblique angle physical vapor deposition. The position of electrodes (with an 80-85° angle) resulted in Au nanoisland formation, yielding Au-$BiVO_4$ plasmonic photoanode. A top-view of the SEM images of the (b) bare $BiVO_4$ and (c) Au-$BiVO_4$ photoanodes, scale bar: 1 μm and the inset shows the high magnified image of the SEM, scale bar: 20 nm. (d) Cross sectional SEM images of the Au-$BiVO_4$ photoanode, illustrating the morphology of the nanostructure photoanode. (e) Cross sectional FIB image of the Au-$BiVO_4$ sample, showing the formation of multi sized/shape Au nano capping islands.

photoanodes morphology and the gold cap can be acquired by cross sectional SEM images, shown in Figure 8.1d-e. As labelled in panel d, a thin layer of Au is coated on the tip of $BiVO_4$, in which the shape and size of the Au nanoislands are defined by the morphological character of the $BiVO_4$ host and,

therefore, an inherent randomness is present on the geometries of Au tips. We will later discuss that; this randomness will trigger a strong light-matter interaction throughout an ultra-broadband wavelength range, via the excitation of LSPR and FP modes. After the successful fabrication of plasmonic photoanode, the structural characterizations have been applied. Raman spectroscopy features shown in Figure 8.2a are in agreement with monoclinic $BiVO_4$.[457], [458] The most intense Raman band at about 826 cm^{-1} is assigned to the symmetric (v_s) V–O stretching mode (A_g symmetry), the weak shoulder at about 710 cm^{-1} is assigned to asymmetric (v_{as}) V–O stretch (B_g symmetry). The symmetric (A_g) and anti-symmetric (B_g) bending modes appear at 366 cm^{-1} and about 325 cm^{-1}, respectively. The peaks at 209 and 124 cm^{-1} are originated from external modes (rotation/translation). Additional peaks that could be originated from Bi_2O_3 (at 315 and 448 cm^{-1}), V_2O_5 (at 440 and 980 cm^{-1}), or any other Bi-rich phase were not detected.[458] Furthermore, XRD analysis was performed to identify the crystalline structure of the $BiVO_4$ sample. The XRD pattern (Figure 8.2b) clearly reveals that the diffraction peaks of the bare $BiVO_4$ sample are in agreement with the standard diffraction patterns of monoclinic $BiVO_4$ (JCPDS 01−075−1866) confirmed by the prominent (110) and (011) planes at about the characteristic splitting peak of 2θ = 18.5°.[459] No diffraction peaks from any other impurities are detected. To determine the specific surface composition and chemical state of the $BiVO_4$ and Au-$BiVO_4$, XPS measurement is employed. The high resolution XPS spectra of Bi4f and V2p are shown in Figure 8.2c-d, respectively**.** The two strong peaks at 164.03 eV and 158.73 eV with the orbital splitting of 5.3 eV, corresponding to $Bi4f_{5/2}$ and $Bi4f_{7/2}$, are the characteristics of Bi^{3+} species for the as-prepared $BiVO_4$ film.[460], [461] The 1/2 and 3/2 spin-orbit doublet components of the V^{5+} of the same electrode are located at 523.7 eV and 516.25 eV, respectively (see Figure 8.2d).[462], [463] After the deposition of Au nanoislands, V2p and Bi4f peaks have slightly blue shifted (~0.1 eV) compared to the bare $BiVO_4$, suggesting an electron transfer from Au to $BiVO_4$, which could be attributed to relatively high electronegativity of Au (see Figures 8.2c-d).[463]–[466] The XPS measurement is not only used to provide

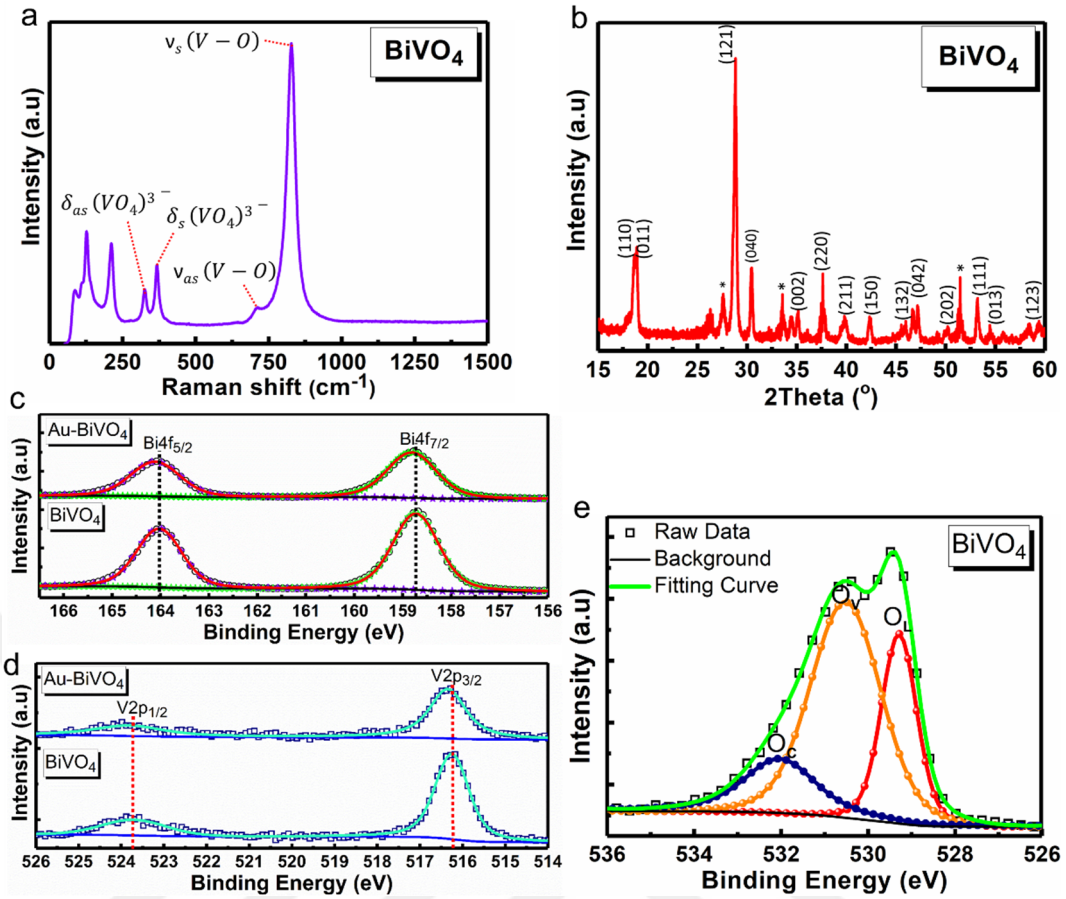


Figure 8.2 (a) RAMAN spectrum and (b) XRD patterns with diffraction patterns of pristine $BiVO_4$ film conforming to its monoclinic phase, "∗" indicates crystal planes of FTO substrate. High resolution XPS spectra of (c) Bi4f and (d) V2p spectra for the as-prepared $BiVO_4$ and Au-$BiVO_4$ electrodes. (e) The O1s spectrum of pristine $BiVO_4$ film which is deconvoluted into three different peaks indicating the presence of three types of oxygen: lattice oxygen (O_L), oxygen vacancy (O_V), and chemisorbed oxygen (O_C).

information about the surface composition of the sample, but it can also be employed to study the surface properties of the layer and the electronic band structure of the design. For the investigation on the existence of surface defects, the O1s spectra of the samples have been analyzed. The core-level O1s spectrum of as-prepared $BiVO_4$ is deconvoluted into three Gaussian peaks, as explained in our previous study.[467] The major O1s peak at around 529.30 eV is attributed to the lattice oxygen atoms (O_L) in the metal oxide. This low-binding peak is attributed to O^{2-} coordinated with the V^{5+} and Bi^{3+} ions in the bulk $BiVO_4$. The other two Gaussian components with center binding energies of 530.53 eV and 532.06 eV are assigned to oxygen vacancy or defects (O_V) and chemisorbed oxygen species (O_C), respectively. Due to water

adsorption and dissociation at the surface, hydroxyl groups can be coordinated to the metal ions (M-O bonds) in the oxygen deficient region (O_V).[468] These oxide ions could be described as low-coordinated oxygen ions, O-species, having lower electron densities than the lattice oxygen atoms. The surface dissociated oxygen or OH species can also be loosely attached to the surface (O_C) such as dangling oxo-bonds.[461], [464], [469]–[472] These loosely surface-adsorbed oxygen or OH species increase the hydroxyl concentration on the electrode surface.[468] As this graph clearly implies, in the case of bare $BiVO_4$, the nanoporous sample has a relatively large density of the O_V and O_C component. These oxygen defects in the metal-oxide surface can trap the charge carriers at the surface and result in interfacial charge recombination also found in previous articles.[473], [474] A similar profile is detected for Au-$BiVO_4$ which is expected, considering the fact that the gold capping layer has been physically evaporated on the surface, rather than being chemically bonded. Overall, the $BiVO_4$ photoanode is an oxygen defect rich sample and, therefore, its PEC-WS performance is poor. The effect of oxygen vacancies in $BiVO_4$ PEC performance is still under debate in literature. Recent works indicate that oxygen vacancy can have multiple roles on the PEC-WS performance of metal oxides[470], [475]–[481]. From the positive side, it was commonly accepted that oxygen vacancies inside the bulk medium improves the free carrier concentration and consequently leads to a better charge carrier transport.[481] Moreover, some authors highlight the electro-catalytic function of these trap states, if they are located on the surface.[481] However, it should be noted that not all types of trap states can provide this beneficial impact. Essentially, traps can be categorized into two main groups; 1) shallow traps and 2) deep traps.[482], [483] Shallow traps that are energetically close to the conduction band of metal oxide can be excited into the conduction band by thermal activation and thus, they can improve the overall bulk conductivity. However, electrons or holes in the deep trap states cannot be de-trapped, which act as charge recombination centers to reduce the transport efficiency. Moreover, it has been shown that the carriers in deep hole trap states are energetically unable to drive water oxidation.[480] Although abovementioned discussion implies that trap states could introduce bulk conductivity and surface electro-catalytic performance, they have a major detrimental impact in the interfacial charge transfer where they mediate electron-hole recombination.[481] Due to this trade-off, the density of these oxygen vacancies is a crucial factor to

determine their effect on PEC-WS process. In our sample, the large density of oxygen vacancies can be detected from XPS. Although this reduces the charge transport resistance within the bulk (as it will be shown from EIS analysis in the upcoming section), it induces high interfacial charge recombination. Thus, in an ideal senario, bulk vacancy level is needed to improve the bulk conductvity, and should suppress the surface trap states to minimize interfacial charge recombination. Gaining an insight on the chemical composition and surface states of the photoanodes, the band alignment between Au and $BiVO_4$ should be extracted. For this aim, the energetic level of valance band maximum (VBM) (i. e. E_F-E_{VBM}, where the Fermi level energy (E_f) is the zero point) is estimated using XPS measurement of the valance band (VB) spectra. As illustrated in Figure 8.3a-b, E_{VBM}-E_f for $BiVO_4$ is found to be 1.52 eV. The VB spectra for the Au-$BiVO_4$ sample, however, has a dominant response arisen from the top capping of gold. For the sample with Au nanoislands, a 5d-band edge lies at 1.08 eV relative to its E_F, while the lower energy tail is attributed to 6sp electrons.[484] In equilibrium, the Fermi levels of $BiVO_4$ and Au will be aligned. Therefore, in this study, the aligned E_F in Au-$BiVO_4$ interface is assumed to be located at the original E_F of $BiVO_4$. To find the band diagram, we also need to know the bandgap of $BiVO_4$. For this purpose, the absorption behaviors of the photoanodes were investigated at a wavelength range of 320 nm to 550 nm. As shown in Figure 8.3c, UV−Visible spectrum of $BiVO_4$ photoanode has an absorption tail extend up to 490 nm. The optical bandgap of $BiVO_4$ is estimated from Tauc plot, as shown in Figure 8.3c inset.[412] This indirect bandgap value of about 2.5 eV is quite matched with the absorption threshold of $BiVO_4$, which is close to the reported value of the monoclinic phase.[485] This is in line with RAMAN, and XRD findings implying the formation of monoclinic phase of $BiVO_4$. It should also be noted that, in the same panel, the absorption spectrum for Au-$BiVO_4$ suggests that the introduction of Au on top of the $BiVO_4$ nanostructure has caused light absorption improvement in both the below and above bandgap regimes. In the following sections, this will be scrutinized in detail, using numerical simulations. Bringing all of the above results together, the band alignment between different interfaces for the plasmonic Au-$BiVO_4$ photoanode is schematically illustrated

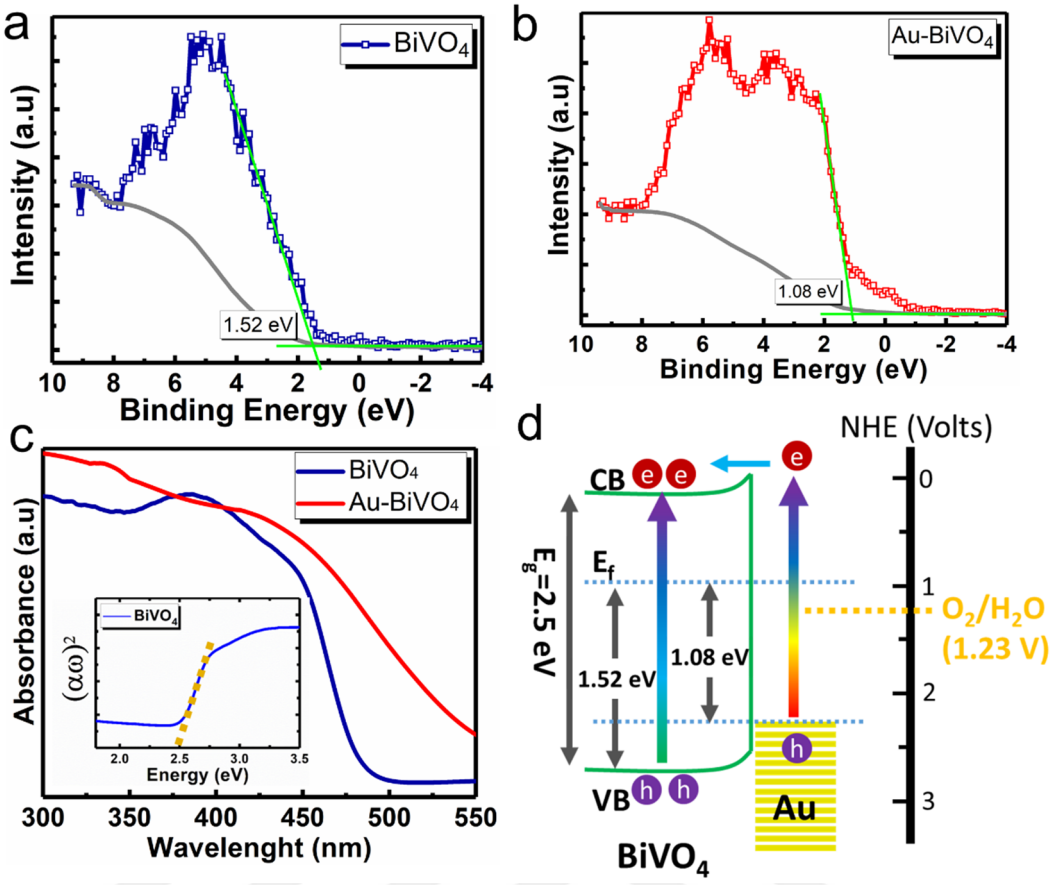


Figure 8.3 XPS valence band spectra of (a) $BiVO_4$ and (b) Au-$BiVO_4$. Green lines show the linear extrapolation of the curves for deriving the valance band edge position of $BiVO_4$ samples, i. e. E_f-E_{VBM}. The grey lines also show the background signal. (c) Absorption profiles for both $BiVO_4$ and Au-$BiVO_4$ photoanodes at the wavelength range of 300–550 nm. The inset shows the Tauc Plot used for the estimation of the optical bandgap (2.5 eV) of the $BiVO_4$. (d) Schematic energy band diagram of Au-$BiVO_4$ showing the band alignments and the involved water oxidation electron transfer processes.

in Figure 8.3d. According to the extracted energy diagram, the photoexcited hot electrons with energies above the Schottky barrier height, will be injected into $BiVO_4$ and the corresponding hot holes will participate in water oxidation reaction. Given the aforementioned structural analysis, we further sought the PEC-WS performance of the photoanodes. The PEC water oxidation measurements were performed with a three-electrode cell using as-prepared $BiVO_4$ and Au-$BiVO_4$ as working electrodes (see cell configuration in Figure 8.4a). As illustrated in Figure 8.4b, the linear sweep voltammograms (LSVs)

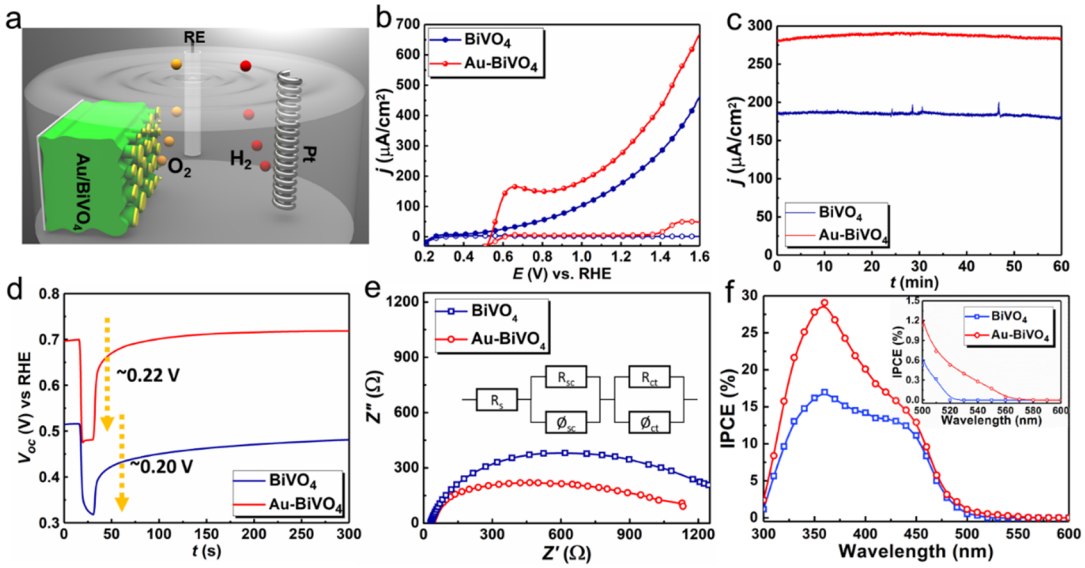


Figure 8.4 (a) Illustrative representations of a 3D schematic of the PEC-WS system consisting of Au-$BiVO_4$ coated FTO electrode (1 cm^2), as a working electrode. (b) LSV measurements, *j-V* curves, of the working electrodes under light illumination (Solid symbols), under dark (empty symbols) with a white-light source. Anodic scan rate: 50 mVs^{-1}, Electrolyte: N_2-saturated 0.1 M PBS pH 7, Light intensity: 100 mW cm^{-2}. (c) Chronoamperogram for 1 hours of illumination at 1.23 V (vs. RHE) bias. (d) OCVD measurement as a function of time for a duration of 300 s. (e) EIS Nyquist plots at a bias of 1.23 V (vs. RHE) in the frequency range 100 kHz to 0.1 Hz under solar irradiation. The inset shows the circuit model used for fitting. (f) IPCE spectra of the PECs with a 1.23 V (vs. RHE) external bias. The wavelength was scanned from 300 to 600 nm with a step size of 10 nm.

exhibit that Au nanotips in Au-$BiVO_4$ enhanced the photocurrent response of bare $BiVO_4$ from 190 μA cm^{-2} to 295 μA cm^{-2} at 1.23 V (vs. RHE). Therefore, the decoration of photoanode with Au nanoantennas has effectively improved the photoactivity of the structure. Moreover, Au-$BiVO_4$ photoanode exhibits a plateau at around 0.7 V vs. RHE, which could be due to the catalytic effect induced by Au nano-islands.[486], [487] As depicted in Figure 8.3d, the gold Fermi level is located between the conduction band of $BiVO_4$ and the water oxidation level. Thus, the gold nano-islands can act as a catalyst for the selective transfer of photogenerated holes to the electrolyte, thereby reducing the recombination rate and improving the interfacial kinetics. The cathodic shift in the onset overpotential under light illumination also supports this thesis. The photogenerated holes in $BiVO_4$ valance band and hot holes formed in the gold nanounits are, thus, responsible for this photocurrent enhancement. As the

applied bias increases, the electron dynamics are improved and the current increases exponentially, similar to that of bare $BiVO_4$ LSV profile. Overall, gold nanoislands introduce three main functions: i) enhancing the light absorption in $BiVO_4$ photoanode, ii) generating hot holes for the direct oxidation of water, and iii) acting as a co-catalyst that mediates the electron transfer from $BiVO_4$ valence band to the electrolyte. To test the long-term stability of the photoanode, transient photocurrent measurement by the chronoamperometry (CA) technique is conducted on Au-$BiVO_4$ for a duration of 60 minutes at 1.23 V (vs. RHE). As seen in Figure 8.4c, bare and plasmonic samples have stable operation over this period of time, confirms the stability of both electrodes. From the previous section findings, the as-prepared $BiVO_4$ samples are oxygen deficient and so these oxygen vacancy levels act as shallow/deep trap states that capture the photogenerated carriers. While some reports claim the positive impact of these surface traps in water oxidation reaction, their existence in the bulk or vicinity of the surface may hamper charge transport and increase their recombination probability.[488] Here, this is likely the main reason behind the poor photoactivity of the bare $BiVO_4$ photoanode. Open circuit voltage decay (OCVD) measurement can provide us with a qualitative comparison of this issue. In this technique, the sample is left upon light illumination, and then the voltage decay profile is probed after light cut-off. The difference between open circuit potential in dark and light conditions is called photovoltage and it is a direct measure of photoactivity of the photoanode. As Figure 8.4d implies, the photovoltage is slightly larger for the Au-$BiVO_4$ sample (~0.22 V), compared to that of the bare sample (~0.20 V). This enhancement originates from stronger light-matter interaction in plasmonic sample that leads to the larger density of photogenerated carriers. A more visible difference can be found in the temporal decay profiles of OCVDs. The decay traces for both samples has been fitted by a biexponential function having time constants of τ_1 and τ_2.[489], [490] These constants for the bare sample were 2.7 s and 92.7 s, while those for the plasmonic photoanode are 1.9 s and 44.6 s. The shorter lifetime could be attributed to band-to-band recombination since similar constants were obtained for both samples. The origin of the longer component is, however, different. For the bare sample, there is a single semiconductor layer and no charge separation mechanism is involved, which implies that the prolonged decay profile is due to the existence of bulk and surface traps. The shallow and deep trap sites capture the carriers and thereby prolong their recombination times.

On the other hand, in plasmonic Au-$BiVO_4$ sample, the gold particles mediate the recombination between electrons and holes facilitating their recombination. This claim can be further confirmed by electrochemical impedance spectroscopy (EIS). From the EIS profiles, shown in Figure 8.4e, the radius of the impedance circle has reduced upon Au plasmonic sensitization. The obtained profiles are fitted to the circuit model shown in the inset of Figure 8.4e. In this model, R_S represents the series resistance of the cell (including the FTO, electrolyte layers), R_{CT} corresponds to the charge transfer resistance in the semiconductor/electrolyte interface, R_{SC} models the resistance within the semiconductor bulk. Moreover, a constant phase element (Ø) is employed to model the imperfect capacitance because a pure capacitance is an inaccurate choice for describing the semiconductor/electrolyte solution in an actual electrochemical process. According to these fittings, the most notable change in the resistance values relates to the R_{CT}, which is expected since our modification is in the semiconductors' surface. The addition of gold nanotips has reduced the R_{CT} from 1280.1 Ω to 873.6 Ω, compared to the bare sample. This is in line with XPS and OCVD findings. Thus, the gold nanoislands act as a catalyst layer and reduce the interfacial charge transfer resistance, a feature that has previously been observed in the LSV profiles as well. Therefore, the Au cap not only substantiates the optical response of the photoanode, but also improves the electron dynamics. A direct evidence for this claim can be acquired by the assessment of incident photon-to-current conversion efficiency (IPCE) of the photoanodes. Figure 8.4f shows the IPCE profiles for bare $BiVO_4$ and Au-$BiVO_4$ photoanodes at an applied bias of 1.23 V vs RHE. As revealed in this figure, the above bandgap IPCE values (λ<520 nm) have been enhanced for plasmonic sample, which is mainly due to the strengthening of the light-matter interaction in the formed metal-semiconductor nanocavities. Moreover, sub-bandgap IPCE values are also present for the Au-$BiVO_4$ photoanodes, as depicted in the inset. This data confirms the existence of hot electron injection from optically excited gold islands into the $BiVO_4$ semiconductor. Therefore, the Au capping not only improves the optical and electrical response of the semiconductor as a photoanode, but also acts as a secondary source for photocurrent generation by the injection of hot electrons.

To gain an insight into the impact of Au nanoislands in the optical absorption of $BiVO_4$ photoanode, numerical simulations are carried out by a commercial

finite-difference time-domain (FDTD) software package (Lumerical FDTD Solutions).[316] The FDTD is a state-of-the-art method for solving Maxwell's equations in complex designs. Being a direct time and space solution, it is a useful method to solve problems related to electromagnetics and photonics. FDTD also offers the frequency solution by utilizing the Fourier transforms, therefore a vast variety of quantities including the complex Poynting vector, transmission, and reflection of incident light can be calculated. For this aim, three-dimensional (3D) simulations are employed. A plane-wave excitation in the desired wavelength range (350–600 nm) is employed. The boundary conditions in the lateral directions (x and y) are set as periodic while a perfectly matched layer (PML) is assigned for the z direction. Two monitors are placed to collect the reflected (R) and transmitted (T) lights. The reflection monitor is placed above the plane-wave and the transmission monitor is placed in the bottom side of the unit cell. The absorbed (A) data is calculated using the following formula A=1−R−T. As explained, in this simulation, we suppose the structure is periodic with a unit cell shown in Figure 8.5a. Although this assumption is not realistic (looking at the SEM images of the

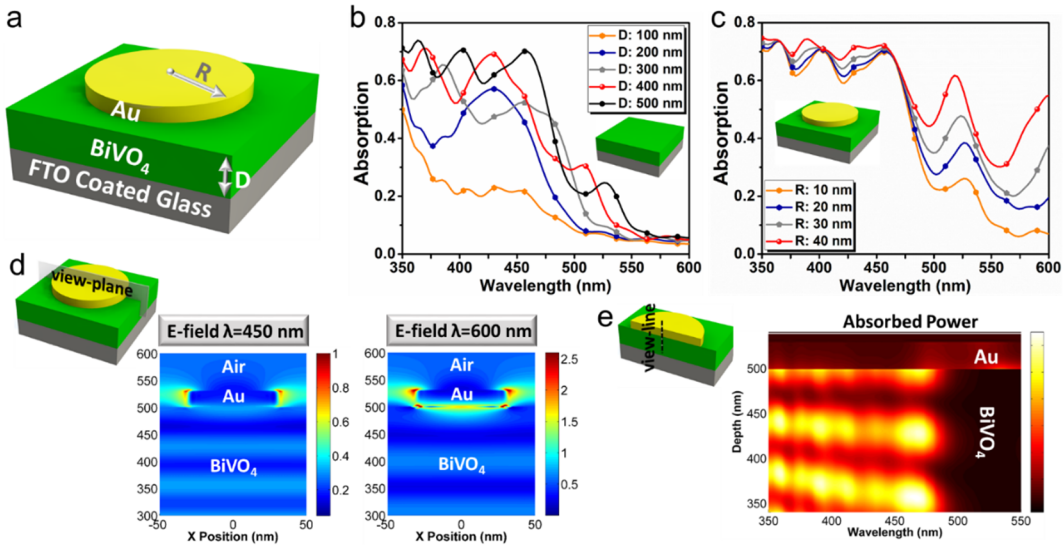


Figure 8.5 (a) The simulation unit cell. The normalized absorption as a function of (b) $BiVO_4$ length (D), and (c) Au capping radius (R). (d) The E-field distribution across the design at 450 nm where $BiVO_4$ is optically absorptive, and 600 nm, in which $BiVO_4$ is transparent to incoming photons. (e) The absorbed power profile across the view line as a function of incoming wavelength.

samples), it provides us an overall understanding of the effect of different geometries on the device optical response. As the initial step, the absorption profile of a simple planar $BiVO_4$ is studied. As deduced from Figure 8.5b, increasing the thickness of active semiconductor layer improves the absorption property of the design. However, due to the surface reflection and weak extinction coefficient of the material in longer wavelengths (which leads to light transmission through the layer), the absorption reaches a saturation level far from the unity ideal absorption. It should be noted that the existence of ripples in the absorption spectrum arises from the multiple reflection/transmission in different interfaces. Introducing a top resonant nano gold disc, however; substantiate the response. The gold layer thickness is chosen as 30 nm that is obtained also from experimental data (SEM images in Figure 8.1e). This value has been chosen considering the skin depth of the gold layer (which is around ~4 nm in 500 nm wavelength). The thicknesses above this depth will have minor impact on the absorption response of the structure. The absorption enhancement is more pronounced in longer wavelengths (near band edge absorption), where the inherent extinction of the layer is weak, see Figure 8.5c. Moving from R = 10 nm to R = 40 nm, while the periodicity of the unit cell is 100 nm, the absorption amplitude is increased. To address the mechanisms responsible for this improvement, the electric field (E-field) distribution is probed across the different layers, as schematically illustrated in Figure 8.5d. At the λ = 450 nm, where the $BiVO_4$ is optically active, the field profile shows the formation of FP resonances within the $BiVO_4$. In addition, dipole-like field distribution is seen at the location of Au disc that likely stems from the excitation of LSPRs in the Au/$BiVO_4$ interface. At a wavelength of 600 nm, in which the $BiVO_4$ is optically transparent, the same mechanisms are present, but different from a shorter wavelength response, a hot spot is created just below the Au nanounit. This strongly localized field triggers the excitation of hot electrons within the gold resonator and the generated hot electrons are injected into the semiconductor layer. Consequently, charge separation is achieved, and hot holes participate in a water oxidation reaction. To verify these estimations, the absorbed power has been calculated along an observation line, as shown in Figure 8.5e. As implied by this panel, the absorption for above bandgap photons occurs dominantly inside the $BiVO_4$ layer, while the gold nanounit harvests incoming light in the longer wavelength ranges. All of the above-mentioned results prove the superior optical response of the Au-$BiVO_4$ sample.

However, the $BiVO_4$ suffers from the large density of oxygen vacancies that inhibit carrier transportation and diminish the overall photoactivity of the layer. To expedite the electron dynamics in the photoanode/electrolyte interface, a WOC could be employed. Recently, many groups explored the integration of Prussian Blue assembly with semiconductor and molecular chromophores.[455], [491], [492] Overall, it was demonstrated that the addition of CoFe-PBA as a WOC can significantly improve the carrier dynamics of the electrode, via mediating water oxidation reaction. To understand the impact of this WOC on the surface properties of $BiVO_4$, the XPS analysis is employed. While the Bi4f and V2p spectra were similar to those of bare the $BiVO_4$ sample, the O1s profile was significantly altered. Based on the fitting results in **Figure 8.6a**, the ratio of O_V/O_L has reduced, compared to that of bare $BiVO_4$. Thus, PBA has dominantly attached into the oxygen vacancy positions and effectively passivated the surface traps. This, in turn, leads to an enhancement in the carrier concentration and the conductivity of the sample. This superior impact can be confirmed by elucidating the VB XPS spectra of the $BiVO_4$/[CoFe] and Au-$BiVO_4$/[CoFe] photoanodes. For $BiVO_4$/[CoFe], E_{VBM}-E_f is found to be 1.69 eV, which is increased by 0.17 eV, compared to that of bare $BiVO_4$. The shifting of the Fermi level toward the conduction band (CB) originates from the enhancement in the carrier concentration of the $BiVO_4$ photoanode. Moreover, another signal is in the lower binding energies that we can assign to the energetic location of CoFe-PBA with an energetic position of 0.53 eV (Figure 8.6b). The difference in the Au and equilibrium Fermi level of the Au-$BiVO_4$/[CoFe] is also found to be 1.24 eV, as shown in Figure 8.6c. Based on these findings, the Au Fermi level is located at 0.45 eV (1.69–1.24eV) above the $BiVO_4$ VBM, expectedly similar to the band alignment in Au-$BiVO_4$. The CoFe-PBA energetic location is 1.16 eV above the $BiVO_4$ VBM. According to the extracted energy diagram summarized in Figure 8.6d, proper alignment is achieved between the $BiVO_4$ VB and Au Fermi level as well as the CoFe-PBA water oxidation level**.** Upon light illumination, the photons with energies above the optical bandgap excites the electrons from the valance to the conduction band of $BiVO_4$. The photo induced holes move into catalytic sites and participate in a water oxidation reaction. On the other hand, light absorption in the nano Au unit leads to the generation of hot electrons (with sub bandgap energies). The generated hot electrons, capable of passing the Schottky barrier, are injected into the semiconductor and the left hot holes to oxidize

water It is noteworthy that in achieving an excellent interfacial carrier dynamic, the loading of catalyst should be optimized as well. Considering the insulating nature of the catalyst layers, making them too thick will reduce the activity of the overall system. Therefore, in an optimum condition, the catalyst should terminate all trap states, without further unnecessary growth. This can be deduced from Figure 8.6e, as the sequential dip-coating increases, the photocurrent increases to a point where it is almost saturated. From that point, the photocurrent value in the lower applied biases (where the bias is not enough to trigger the passage of electron through the insulator layer) starts to decline and so the optimum number of dip coating cycles is defined as 10 cycles. As a next step, a gold capping layer is introduced to the PBA thickness optimized sample. The Au- $BiVO_4$/[CoFe] plasmonic photoanode was fabricated using the same oblique angle deposition. The LSV profiles have been compared for $BiVO_4$/[CoFe] and Au-$BiVO_4$/[CoFe] photoanodes in Figure 8.6f. As shown in this panel, the introduction of gold capping has further substantiated the performance of the catalyst loaded sample. At 1.23 V (vs RHE), the photocurrent is raised from 1330 μAcm^{-2} (for $BiVO_4$/[CoFe]) to a value as high as 1,800 μAcm^{-2} (for Au-$BiVO_4$/[CoFe]). Compared to the bare $BiVO_4$, where the photocurrent was probed as 190 μAcm^{-2}, the proper use of catalyst-plasmonic combination has improved the activity of photoanode by six-fold. This prominent enhancement is essentially caused by facilitating the electron dynamics via PBA catalyst. EIS findings demonstrate that the charge transfer resistance (which corresponds to semi-circle radius) has effectively reduced by CoFe-PBA and a substantial decrease was attained through plasmonic integration, see Figure 6g. Same circuit model has been employed to find the charge transfer resistances. The fitted values have been summarized in Table S1. Based on these results, The R_{CT} is further decreased to 691.2 Ω and 553.8 Ω for $BiVO_4$/[CoFe] and Au-$BiVO_4$/[CoFe] photoanodes, respectively. Moreover, the OCVD reveals a photovoltage of 0.65 V for $BiVO_4$/[CoFe], which is significantly larger than that of the bare $BiVO_4$ sample with much faster photovoltage decay (Figure 8.4d), as shown in Figure 8.6h. This essentially originates from the photogeneration of a larger density of electrons upon excitation and could be attributed to the passivation of surface traps through WOC, as expected by the XPS results. The decay time constants for this sample is found to be 2.4 s and 61.3 s, which is slightly larger compared to those of Au-$BiVO_4$ photoanode. This enhanced lifetime is due to the selective

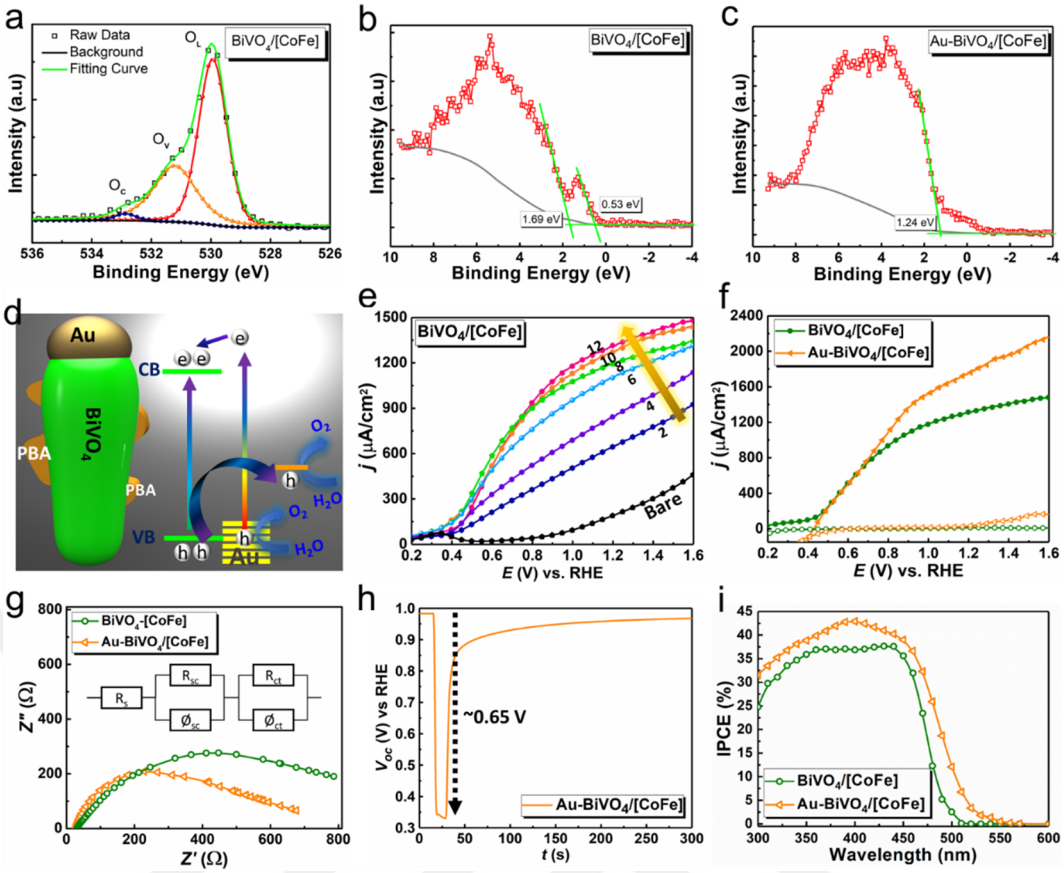


Figure 8.6 High resolution XPS spectra of (a) O2p and (b) VB spectra for ($BiVO_4$/[CoFe]), (c) VB spectra for Au-$BiVO_4$/[CoFe]. (d) Illustrative representations of the Prussian blue modified Au-$BiVO_4$ coated FTO electrode (1 cm^2), as a working electrode for photoelectrochemical water oxidation process. (e) LSV measurements under light illumination, *j-V* curves, of the bare $BiVO_4$ and 2-12 times CoFe-PBA modified $BiVO_4$ electrodes. (f) LSV curves for $BiVO_4$/[CoFe] and Au-$BiVO_4$/[CoFe] under light illumination (Solid symbols), and dark (empty symbols) with a white-light source. Anodic scan rate: 50 mV s^{-1}, Electrolyte: N_2-saturated 0.1 M PBS pH 7, Light intensity: 100 mW cm^{-2}. (g) EIS Nyquist plots at a bias of 0.8 V (vs. RHE) in the frequency range 100 kHz to 0.1 Hz under solar irradiation for both electrodes. The inset shows the circuit model. (h) OCVD temporal response throughout a 300 s duration. (i) IPCE spectra of the photoanodes with a 1.23 V (vs. RHE) external bias. The wavelength was scanned from 300 to 600 nm with a step size of 10 nm.

separation of carriers through the extraction of photogenerated holes in semiconductor-WOC interface. Finally, IPCE measurements are carried out to understand the contribution of near field effects and hot electron injection. As shown in Figure 8.6i, the photoconversion efficiency of the design has been improved in the all incident wavelengths, with a maximum as high as 37% for $BiVO_4$/[CoFe], and 43% for Au-$BiVO_4$/[CoFe] sample. In comparing the obtained results for pristine $BiVO_4$ photoanode, the introduction of PBA WOC has improved IPCE for all incoming photon energies. This is essentially stemming from the efficient interfacial electron dynamics through the WOC. For the Au-$BiVO_4$/[CoFe], the coupling of light into FP and LSPR modes has intensified light absorption and consequently the number of photogenerated carriers. By means of WOC, these excess photogenerated electrons participate in a water oxidation reaction and the IPCE increases. Moreover, the enhancement is stronger in longer ranges, i.e. near bandgap photons. This is because of the weak absorption response of $BiVO_4$ for the near band edge photons and, therefore, proposed trapping schemes is more efficient in this spectral range. The enhancement in the λ>520 nm spectral range is essentially caused by hot electrons' injection from the plasmonic nanoislands. All the above mentioned results have important implications for developing feasible plasmonic-catalytic design on the semiconductor for the solar water splitting. At the end, it should be noted that the theoretical limit of $BiVO_4$ is around 7.5 mA cm^{-2} at 1.23 V (vs RHE).[493] Although many studies have tried to reach this limit, the reported maximum current densities are 6.1 mA cm^{-2} at 1.23 V (vs RHE),[494] and 6.7 mA cm^{-2} at 1.23 V (vs RHE).[495] This proof-of-concept study provides an alternative approach to enhance the PEC performance of a semiconductor layer through the combinational use of a WOC and plasmonic particles with proper arrangement. The proposed fabrication route can be easily extended into other plasmonic hetero-junction designs with no material restriction. Thus, it can be used in a wide variety of materials for future performance enhanced PEC-WS cells.

In this work, we have developed a facial, and large scale compatible approach to fabricate plasmonic photoanode for hot electron driven water oxidation utilizing a cyanide-based catalyst assembly. First, the proposed structure, Au-$BiVO_4$ shows a superior optical response with a broadband absorption in the visible part of the spectrum. The multi size/shape nature of the formed Au nanoislands triggers the excitation of FP trapping modes and LSPRs. FP modes are effective trapping schemes at λ<520 nm (above bandgap photons), while LSPRs reveal their contribution for sub-bandgap photons (λ>520 nm)

through hot electron injection. Then, the superior absorption capability of the plasmonic Au-$BiVO_4$ design has been coupled with a WOC, called CoFe-PBA, to maximize the PEC-WS performance of $BiVO_4$. As a result of this improvement, near an order of magnitude improvement is observed in Au-$BiVO_4$/[CoFe], compared to that of bare $BiVO_4$. A maximum of 43% above-bandgap IPCE and 1,800 μAcm^{-2} (at 1.23 V vs. RHE). Moreover, the <5% IPCE of sub-bandgap photons proves the fact that, this structure benefits from the hot electron injection of plasmonic gold. This study, which presents one of the first examples of a plasmonic enhanced photoelectrode coupled with a WOC assembly, indicates that unifying the strengths of WOCs and plasmonic structures can be a viable approach to increase the performance of photoelectrodes in the visible region. The large scale compatible synthesis route for the plasmonic and WOC components has no material restriction and can be extended into other efficient metal-semiconductor heterostructures.

8.4. Sub-wavelength Densely-packed Disordered Semiconductor Metasurface Units for Photoelectrochemical Hydrogen Generation

Figure. 8.7a schematically represents the setup used for the oblique angle deposition of Cr nanorods. In this approach, the sample is placed in a position oblique to the evaporated ad-atoms, with an angle of $\alpha \sim 80^0$, with respect to the normal incidence line. When the evaporated flux reaches to the substrate, an additional factor is introduced into the growth process, which can result in the formation of nanoislands, instead of a continuous layer. It is generally accepted that the mechanistic factor controlling the nanostructural evolution of the films is a “shadowing effect”, which prevents the deposition of particles in regions behind initially formed nuclei (i.e. shadowed regions), as shown in Figure 8.7b. As deposition continues, the larger nuclei get larger and form three dimensional (3D) nanorods.

As shown in Figure 8.7c, the resultant morphology is a multi-length/multi-spacing disordered nanounits. The length of these nanostructures can be controlled with the deposition duration. This random geometry provides the opportunity to achieve strong light-matter interaction in a broadband wavelength range. This will be explained, in detail, in upcoming sections. Finally, to transform these metallic nanorods into p-type semiconductors, air annealing at 600ºC in a tube furnace is conducted to form densely packed p-

type CrO_X nanorods, as shown in Figure 8.7d. It should be noted that CrO_X shows p-type behavior, due to the existence of metal deficient sites.[496] The structural morphology of the fabricated designs has been evaluated using Scanning electron microscopy (SEM). SEM images of Cr and CrO_X nanostructures are depicted in Figures 8.7e-f, respectively. As these panels imply, upon annealing, the morphology and the surface area of the design do not alter. Therefore, using this simple and scalable fabrication route, we have

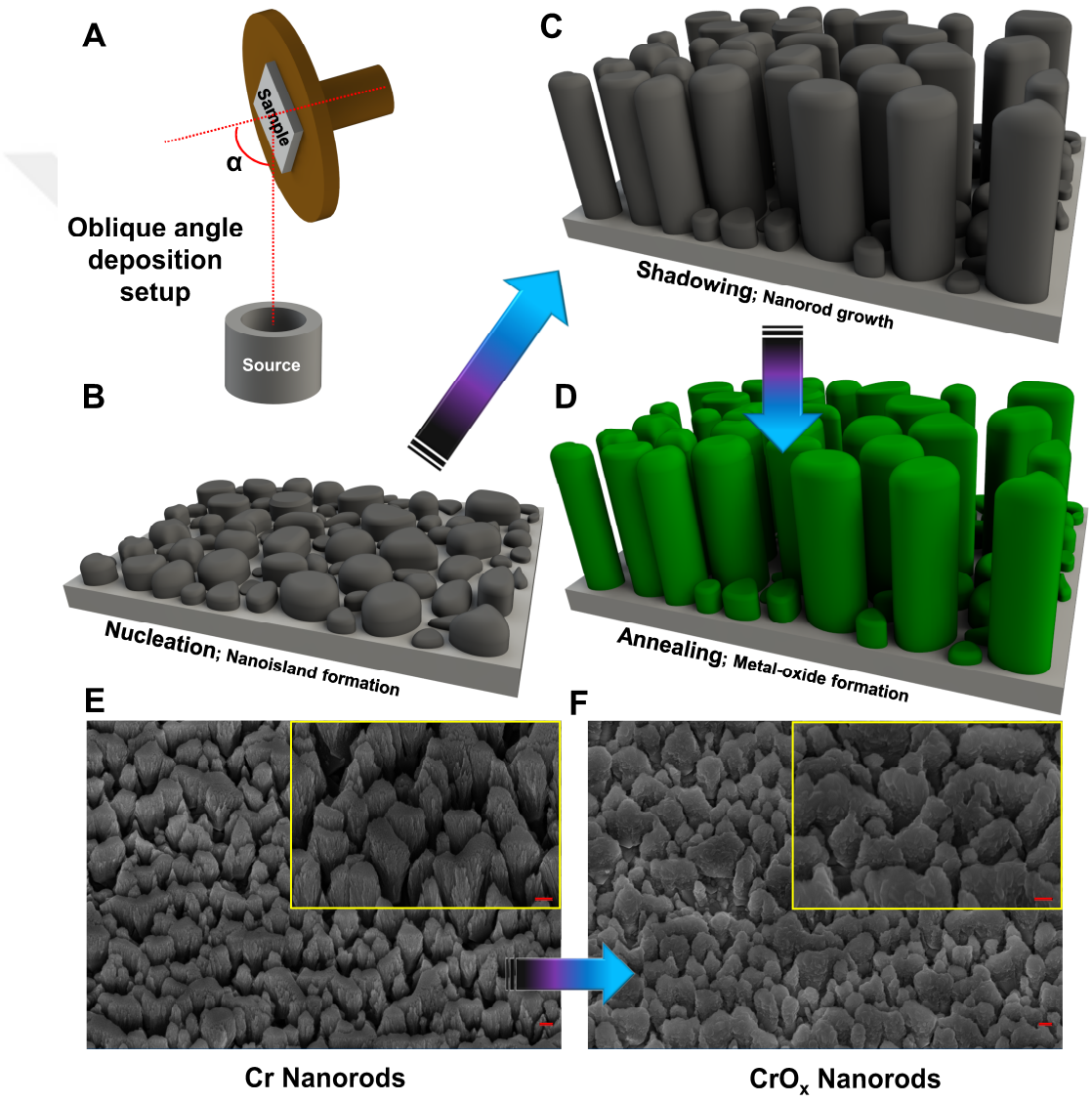


Figure 8.7 (A) The schematic representation of the setup used for the oblique angle deposition of Cr nanounits. (B) The formation of nanoislands, (C) their transformation into the random 3D nanorods due to atomic shadowing effect, and (D) annealing induced CrO_X semiconductor nanostructures. The SEM images of the resultant (E) Cr and (F) CrO_X nanostructures.

made a strong absorbing semiconductor metasurface design that can be potentially employed for PEC hydrogen generation. As experimentally proven in our previous studies, disorder in the geometrics of the produced nanounits can provide strong light-matter interaction in an ultra-broadband wavelength range.[87] It was shown that multidimensional plasmonic nanoantennas can support multiple modes and the superposition of these modes can lead to an ultra-broadband light absorption. However, in the present case, the building block material is a semiconductor with relatively high refractive index. It is theoretically demonstrated that the electric field (E-field) distribution in the vicinity of a plasmonic unit can be mimicked non-plasmonically by a high refractive index dielectric nanoparticle.[497] To understand the mechanism responsible for light absorption in this semiconductor based metasurface, numerical simulations, using the Lumerical finite-difference-time-domain (FDTD) package,[316] are utilized. Although the output structure is a random design, the periodic model is employed to understand the impact of every geometry on the overall absorption response of the structure. As shown in Figure 8.8a, three main dimensions are studied in these simulations; i) the periodicity (P) of the design, ii) the gap (G) between adjacent nanorods, and iii) the height (H) of nanorods. Keeping the H and G parameters at 200 nm, and 50 nm values, the impact of periodicity on overall response of the design is investigated. As shown in Figure 8.8b, in ultra-violet (UV) region (λ<350 nm), a constant near 0.8 absorption is existed in all samples, which originates from above band gap light absorption of the CrO_X semiconductor. In addition, the nanorod design imposes a resonant light absorption in the visible range, a feature that is absent in planar design. As we can see from this panel, the peak response is made of two partially-overlapping resonance modes (annotated as λ_1, and λ_2). As periodicity increases, the spectral separation between these modes reduces and, at P=500 nm, the response becomes a single peak resonance. Moreover, a weaker higher mode resonance is also seen in lower wavelength values, i.e. 455 nm. Besides these features, sweeping the P values from 300 nm to 500 nm causes a steady red-shift in the peak resonance wavelength. Therefore, it can be envisioned that a semi-periodic (with multiple equivalent Ps) design can provide enhanced light absorption in a large portion

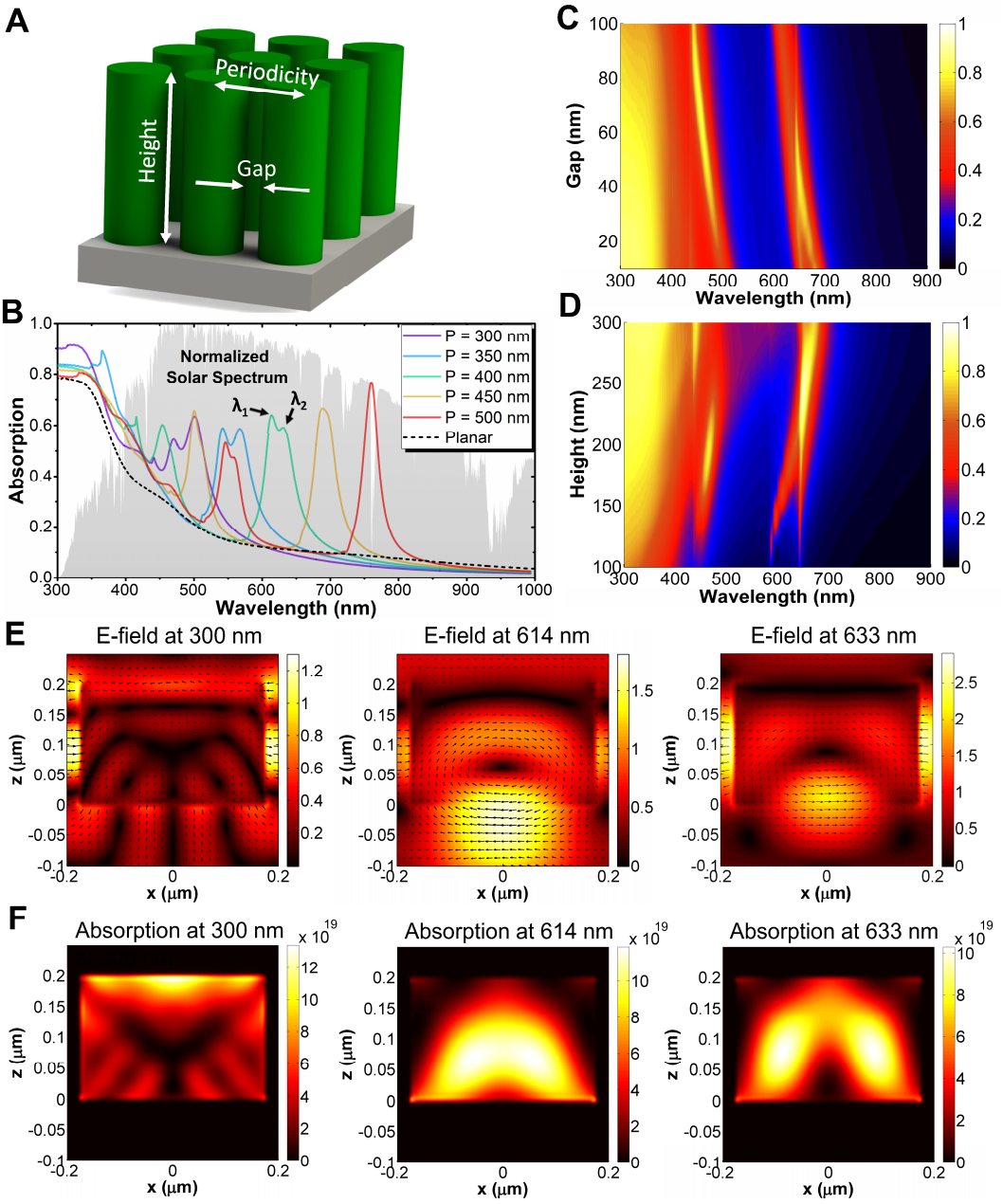


Figure 8.8 (A) The proposed periodic model for numerical simulations. (B) The dependence of absorption spectra on the periodicity of the metasurface (the background depicts the normalized solar spectrum). 2D absorption contour plots showing the effect of (C) gap, and (D) height of nanorods. (E) The E-field distributions and (F) absorption power density profiles across the metasurface design at three resonant wavelengths of 300 nm, 614 nm, and 633 nm.

of the solar spectrum. A more realistic parameter is the gap (G) between the nanorods. This time, P and H are fixed at 400 nm and 200 nm, and G is swept in the 10-100 nm range. To have a better visualization, the spectra are brought into 2D contour plots, see Figure 8.8c. As this plot implies, the double resonance peaks in the visible range is present in all G values. However, the

spectral position of these peaks gradually shifts toward longer wavelengths as the gap size reduces. Therefore, the same as periodicity, the randomness in the distance between the nanorods can tune the absorption peak positions and the superposition of these peaks can lead to ultra-broadband light absorption. Similar behavior can be seen in the H geometry, as shown in Figure 8.8d. Taking all into consideration, compared to a planar bulk design, a metasurface made of tightly-packed CrO_X nanorods can add up resonant light absorption in the visible range. However, the origin of these resonance peaks, their absorption profile, and E-field distribution across the metasurface are important factors, defining the photocarriers generation, separation, and collection. Generally, near surface absorption is desired to maximize the collection efficiency of the carriers. Figure 8.8e exhibits the field distribution and vector profiles throughout a normal plane crossing the metasurface, at three different wavelengths of 300 nm, λ_1=614 nm, and λ_2=633 nm. Moreover, at the same wavelength values, the absorption power density across the design has been also plotted, as depicted in Figure 8.8f. At 300 nm, where photons have energies above the CrO_X band gap, the bulk absorption, mainly due to the formation of Fabry-Perot (FP) modes, is the dominant mechanism. Besides that, the field distribution in the gap region shows the excitation of an electric quadrupole (EQ) mode. This EQ mode triggers the formation of hot spots in the gap region and these spots efficiently couple the incident light into the semiconductor layer and provide strong light absorption for above band gap photons. This can be observed from the absorption profile, shown in Figure 8.8f. Light absorption mostly occurred in the vicinity of the top surface and the nanorod walls, which is a desired profile for the efficient collection of photogenerated carriers. Therefore, in the UV region, both FP and EQ modes are responsible for light absorption. However, in the visible range, the story is different. As we can see in Figure 8.8e, for both resonance wavelengths of λ_1, and λ_2, the profile is a circulating field within the bulk region and represents the excitation of a magnetic dipole (MD) mode. Moreover, for both cases, the field profile in the gap region also represents the excitation of electric dipole (ED), in which the electric field is to a large extent oriented parallel to the incident field. However, for the λ_1 the dominant field enhancement is within the particle bulk while for λ_2 the hot spots, in the gap region, have the highest field intensities. Therefore, the first resonance is dominantly an MD, and the second resonance is an ED. The absorption profiles, at these two resonance wavelengths, are also similar except a higher absorption density near the walls, for the second resonance mode. When considering the random arrangement of the fabricated

designs, it is expected that the formation of hot spots in the gap region is the main responsible mechanism for the device performance enhancement.

Gaining an initial insight on the optical response of tightly packed CrO_X nanorods, in the next step, we moved to device fabrication. As already stated, in our fabrication route to synthesize the CrO_X semiconductor layer, annealing at 600ºC is applied on the deposited metallic Cr layer. However, the elemental composition (the atomic ratio between Cr and O), that essentially defines the semiconductor optical and electrical response, can be controlled with the deposition duration. To examine this, we fabricated three planar films; i) a metallic Cr thin film, and semiconducting CrO_X thin films obtained via annealing for durations of ii) 30 min. (annotated as CrO_X-30), and iii) 90 min. (annotated as CrO_X-90). Afterward, spectroscopic ellipsometry measurements are utilized to extract the refractive index data for these three thin films. The extracted data is depicted in Figure 8.9a. While CrO_X-90 shows a typical optical response of a metal oxide, the CrO_X-30 shows the formation of an intermediate metal/oxide state. The CrO_X-90 sample has an absorption edge at ~410 nm, while this value is extended up to 560 nm for the CrO_X-30. Moreover, the CrO_X-30 has larger extinction coefficient values compared to CrO_X-90. To further confirm the formation of a mixed state in the 30 min. annealed sample, X-ray photoelectron spectroscopy (XPS) is performed on the CrO_X-30 and CrO_X-90 samples. Figure 8.9b represents the depth profiling of the chemical composition of two samples. The atomic percentages near the surface is similar for both cases, but as we move toward the bulk region, the Cr/O ratio increases for CrO_X-30, while it is almost constant for CrO_X-90 case. Therefore, while 90 min. annealing at 600ºC fully transforms metal to its stable oxide form, a 30 min. duration partially oxidizes it and consequently, an intermediate state results. This can also be confirmed from the Cr3p spectra of the samples. It is known that binding energies of Cr3p peak are located at 42.4eV for metallic Cr, 43.0 eV for Cr2O3, and 48.3eV for CrO3. In our case, the peak binding energies are 42.95 eV, and 46.45 eV, for CrO_X-30 and CrO_X-90 samples, respectively. Therefore, the CrO_X-30 has a binding energy in between those of pure Cr and Cr_2O_3 thin films, which is in line with our expectations from previous data. All in all, from the above data, the CrO_X-30 has a better optical performance compared to that of CrO_X-90. This has also been investigated using FDTD simulations. For this purpose, the absorption response of the proposed periodic design, shown in Figure 8.8a, is calculated using the CrO_X-30 and CrO_X-90 refractive index data. As Figure 3D implies, the nanorod design made of CrO_X-30 has a broader and stronger absorption response in the visible range, making it a better choice for

photoconversion applications. These findings were further supported by characterization findings. The diffuse reflectance spectra for bare Cr, CrO_X-30,

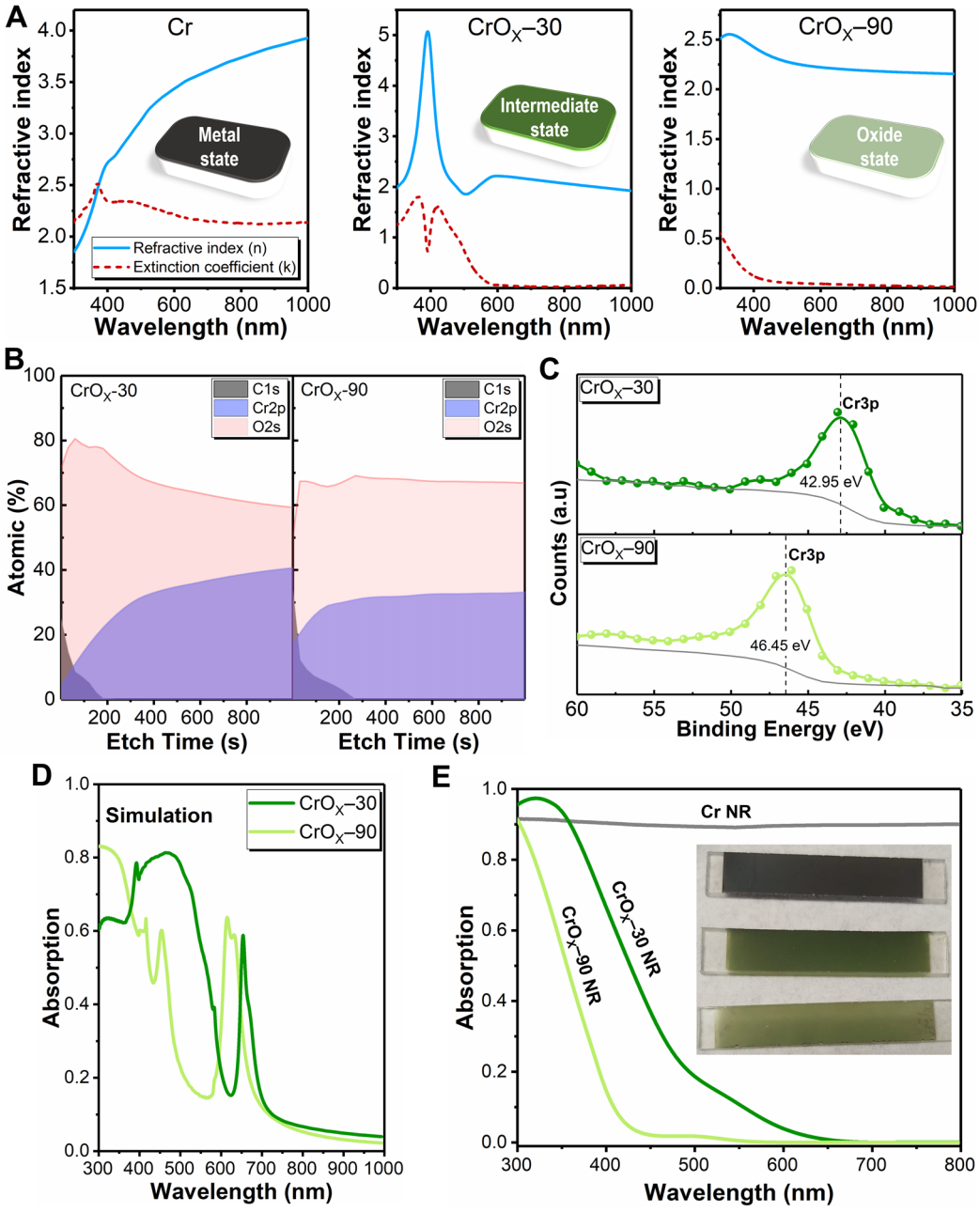


Figure 8.9 (A) The extracted refractive index data for planar Cr, CrO_X-30, and CrO_X-90 thin films. While 90 min. annealing fully transforms Cr into its oxide counterpart, the 30 min. annealing leads to a mixed state. This has been shown in the inset. (B) Atomic percentage of C, Cr, and O elements in the CrO_X-30, and CrO_X-90 thin films. Total etching time of 1000 seconds. (C) The XPS Cr3p profiles for CrO_X-30, and CrO_X-90 planar thin films. (D) Numerical simulation absorption results of the optimal periodic design, using two different refractive index values of CrO_X-30, and CrO_X-90. (E) The diffuse reflectance values of the fabricated Cr, CrO_X-30, and CrO_X-90 nanorod designs. The inset shows the optical image of the samples.

and CrO_X-90 nanorod designs are depicted in Figure 8.9e. As shown in this panel, the Cr nanorod is a broadband absorber with a flat near 0.9 absorption values. The CrO_X-30 sample shows near unity absorption in the UV region and its tail is expanded toward the visible range (~650 nm). CrO_X-90 nanorod film has an absorption peak of 0.9 at 300 nm and linearly decays to values below 0.1, with a weak absorption in the visible range. This response closely follows the extracted n-k data, as shown in Figure 8.9a. Therefore, CrO_X-30 is a better absorber and this could be seen from their optical image, as shown in the inset. While Cr sample is a black absorber and CrO_X-90 has a light green appearance, the CrO_X-30 one has a dark green color. Taking everything into account, from the optical perspective, among all of the CrO_X-30 samples is the most promising sample for photoconversion application. Moreover, regarding the optical response, the electrical character of the sample is also a prominent factor. Hall effect measurements have been performed on this sample to find out the doping type and carrier concentrations. From this characterization, it was found that both CrO_X-30 and CrO_X-90 samples are p-type semiconductors with carrier concentrations of $3.12 \times 10^{12}$and 2.31×10^{12}cm^{-3}, and hole mobility values of 2.18 and 2.38 cm^2 v^{-1} s^{-1}, respectively. Therefore, from the electrical perspective, both samples have similar responses, unlike their optical property.

Besides steady state optical and electrical characteristics of a sample, another factor that defines the efficiency of a semiconductor in photoconversion applications is its excited state lifetime. The absorption dynamics in semiconductors are in ns-fs time scales and, therefore, ultrafast pump-probe spectroscopy should be utilized to resolve them. For this aim, femtosecond transient absorption (TA) spectroscopy is employed. As shown in Figure 8.10a, the CrO_X-30 sample is pumped with a 400 nm light and a broadband probe signal (430-750 nm) is sent with different time delays spanning from 100 fs to 3 ns. Upon pumping, electrons are excited into the conduction band. If excited electrons stay on the conduction band, the probe signal further excites them to upper levels and this shows itself as a positive signal with so-called excited state absorption (ESA). If these excited electrons quickly deactivate into defects induced trap states, the TA spectra shows itself as a negative response called ground state bleaching (GSB). Figure 4B plots the TA spectra of the sample in different time delays. As we can see from this graph, in short delay times, the spectra are dominantly a broadband GSB signal. This means, in these delay scales, the excited electrons are mainly trapped in the defect sites that are energetically located inside the band gap. Moreover, the broadband response shows the wide energetic distribution of these defects inside the gap region.

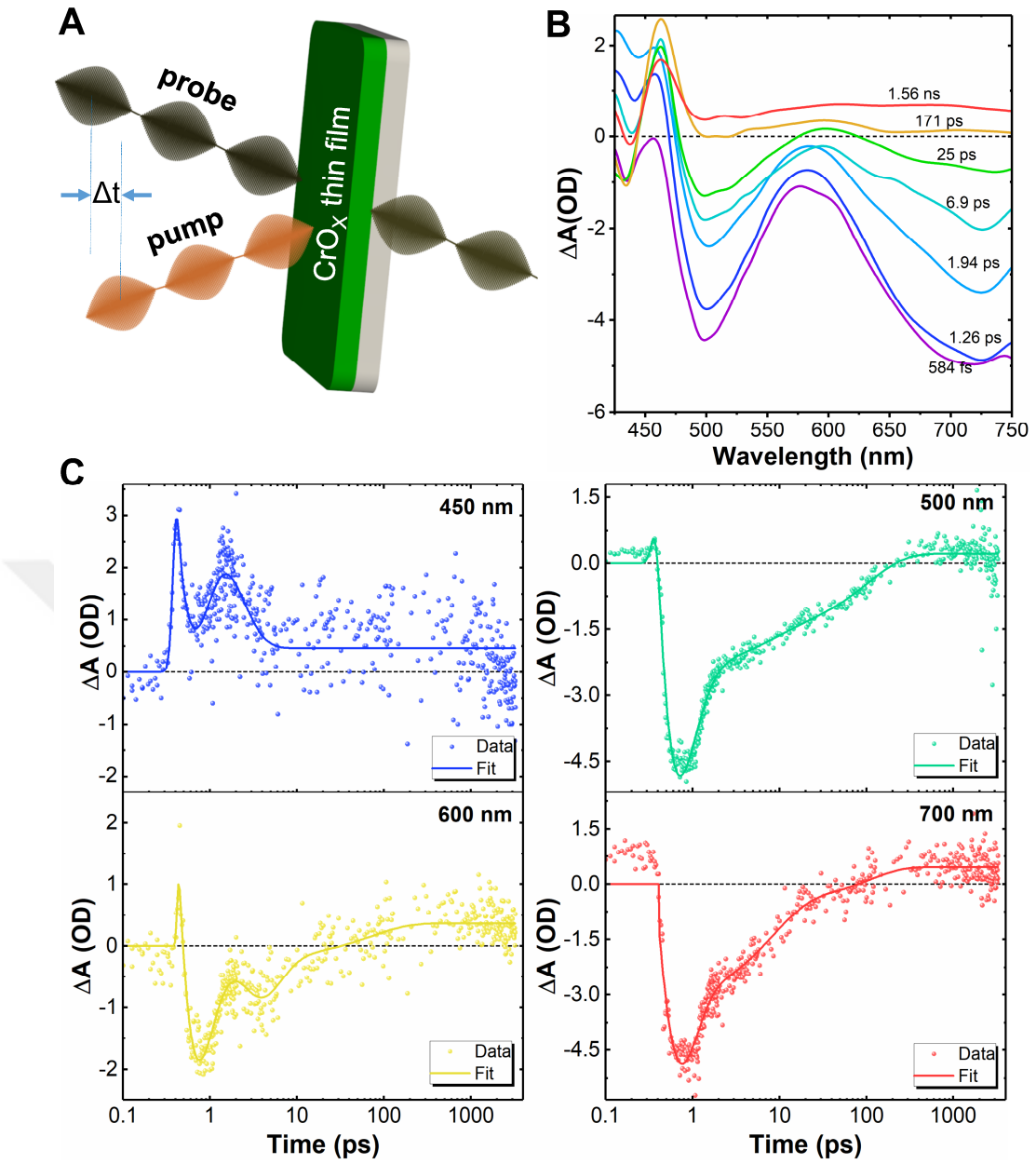


Figure 8.10 (A) The setup configuration of pump-probe TA spectroscopy. (B) The TA spectra of the CrO_X-30 film in different delay times. (C) The temporal decay profiles of the TA signal at four different probe wavelengths of 450 nm, 500 nm, 600 nm, and 700 nm.

This is expected, considering the fact that the p-type behavior of CrO_X originates from the defects, specifically metal vacancies. As the delay increases, the broadband GSB signal turn into a broadband ESA signal. This implies that the trapped electrons are immediately thermalized into the ground state, while a portion of excited carriers stay on the conduction band and this portion generates a broadband ESA signal. In summary, from these TA data, a major portion of excited electrons immediately fall back to the ground state through the trap states. However, the rest of the carriers stay in the conduction

band with lifetimes in the nanosecond scales. This portion is actually the active carriers in photoconversion process. To have a better qualitative comparison, the temporal decay profiles have been extracted for four probe wavelengths of 450 nm, 500 nm, 600 nm, and 700 nm. At all wavelengths, for delays above 100 ps, the signal is a positive ESA signal. Therefore, the CrO_X-30 sample not only has a broadband light harvesting property, but its excited state lifetimes are also long enough to provide the participation of these photogenerated carriers in HER.

To examine the PEC performance of these semiconductor metasurfaces, measurements were performed in a standard three-electrode cell configuration with CrO_X nanorod samples as photocathode with an exposed area of 1 cm^2, Pt mesh as counter electrode, and Ag|AgCl|KCl(sat) as the reference electrode. The proposed configuration is schematically represented in Figure 8.11a. Using this setup, chopped linear sweep voltammetry (LSV) measurement is performed under neutral conditions, pH 7. As expected, disorder nanorod designs have a much stronger photocurrent response compared to planar design. Moreover, the best performance belongs to CrO_X-30 sample, see Figure 5B. As highlighted in the inset, at -0.1 V_{RHE}, the difference between dark and photocurrents is found to be 1.7 $\mu A.cm^{-2}$, 13.9 $\mu A.cm^{-2}$, and 21.3 μAcm^{-2} for planar, CrO_X-30, and CrO_X-90 photocathodes, respectively. This is an 30 sample. However, in photoconversion applications such as PEC hydrogen generation, besides light harvesting capacity, the charge separation of the carriers is also an important factor that defines the overall activity of the photocathode. In an ideal case, the generated electron-hole pairs should be effectively separated and participate in HER before they recombine within the bulk medium. To explore this factor, electrochemical impedance spectroscopy (EIS) analysis is measurement for the CrO_X-30 sample, under light irradiation, at a bias voltage of -0.1V_{RHE} performed on all three photocathodes. The EIS Nyquist plots, at a bias of -0.1 V (vs. RHE) in the frequency range of 100 kHz-0.1 Hz under solar irradiation, are shown in Figure 8.11c. The radius of this semicircle shows the charge transfer resistance through the semiconductor-electrolyte interface. Therefore, a smaller radius shows better charge separation dynamics. As anticipated, the radius of impedance semicircle exactly follows the photoactivity order of the three samples. Photocathode with higher activity has smaller semicircle radius. This difference is rather pronounced between the planar and nanorod designs. This could originate from the near-field induced charge separation in the tightly-packed nanorods. As shown in Figure 8.8e, the formation of ED and EQ modes in the semiconductor metasurface triggers the

formation of strong electric fields in the gap region (between nanorods). While these hot spots lead to the generation of high density of photocarriers, in the meantime, they facilitate carrier's separation to direct the electrons toward the surface, where HER occurs. This has been schematically shown in Figure 5D. This could be further supported by the incident photon conversion efficiency (IPCE) profiles of the samples. As can be seen in Figure 8.11e, the CrO_X-30 photocathode has the highest efficiencies in both UV Nyguist plot at -0.1 V (vs. RHE), and (F) IPCE response of the CrOx-NiOx photocathode, and its comparison with that of CrOx-30. and visible ranges. Moreover, the IPCE tail is extended toward longer wavelengths for CrO_X-30 (compared to that of CrO_X-90), which is in line with the optical properties of the materials shown in Figure 8.9a. Moreover, the activity of the photocathodes, their stability under light irradiation is also another prominent factor, defining the long-term operation of the photocathode. To measure this, chronoamperometry (CA) characterization is performed on CrO_X-30 sample for an exposure duration of 9 hours. As shown in Figure 8.11f, the photocathode retains its photocurrent response over this period, even after the light turn off-on cycle. Therefore, all in all, this large-scale compatible semiconductor metasurface has a stable and efficient operation for PEC hydrogen generation.

To further substantiate the PEC hydrogen evolution activity of these nanorods, a proper catalyst could be utilized. The most common catalysts for this purpose are Pt [498] and Ru. However, both of these metals are precious, rare, and high cost elements. A more practical choice could be metal oxides with a conduction band just above the hydrogen evolution potential. For this aim, NiO_X is selected as the catalyst layer. There are multiple reasons behind this selection. First, NiO_X is a high band gap visible transparent material and, therefore, it does not lead to parasitic absorption and transmit the incoming light toward the active NiO_X layer. Second is its proper conduction band position, which is placed between CrOx conduction band and hydrogen evolution potential[499]. Finally, NiO_X can be easily made by thermal oxidation and, therefore, it can be finely adopted to the CrOx fabrication. The synthesis route of the proposed CrOx-NiOx is schematically shown in Figure 8.12a. Initially, Cr nanorods are generated using oblique angle deposition. Then, normal angle is utilized to deposit Ni nanoislands on the tip of the Cr nanorods. Finally, the design is annealed at 600ºC for a duration of 30 min. As can be clearly seen from the elemental mapping of transmission electron microscopy (TEM)

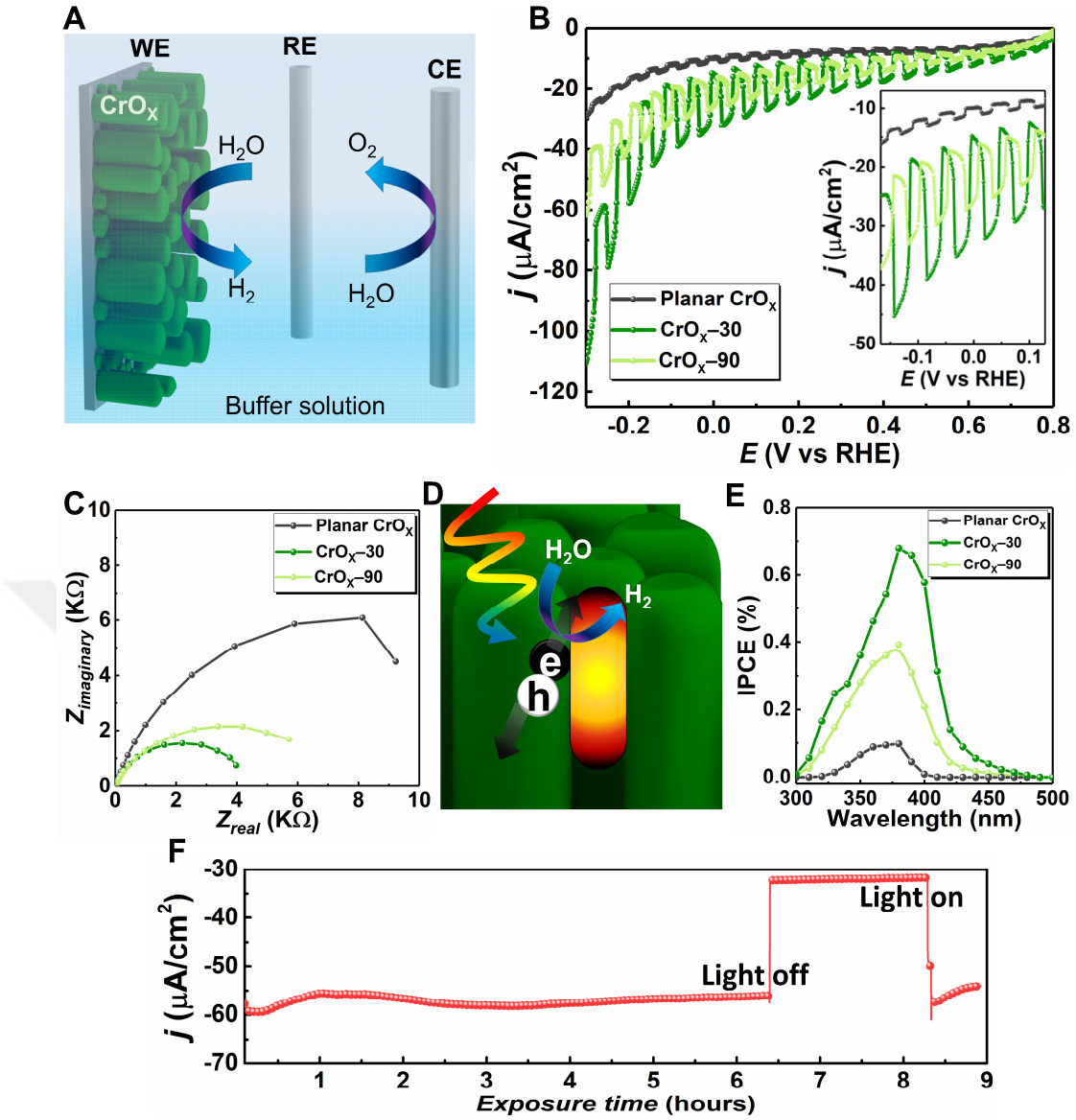


Figure 8.11 (A) Schematic representation of the three-electrode setup used for PEC experiments. (B) The chopped LSV profiles of the planar CrO_X, and nanorod based CrO_X-30, and CrO_X-90 photocathodes. (C) Nyquist plots obtained by EIS characterizations for all three samples at a bias of -0.1V_{RHE} and a frequency range of 100 kHz-0.1 Hz under AM1.5 solar irradiation. (D) Schematic representation of field induced charge separation in the near surface region in a nanorod design. (E) The IPCE values of all three samples at the bias voltage of -0.1V_{RHE}. (F) The long-term CA expected response, considering the stronger absorption response of the CrO_X-

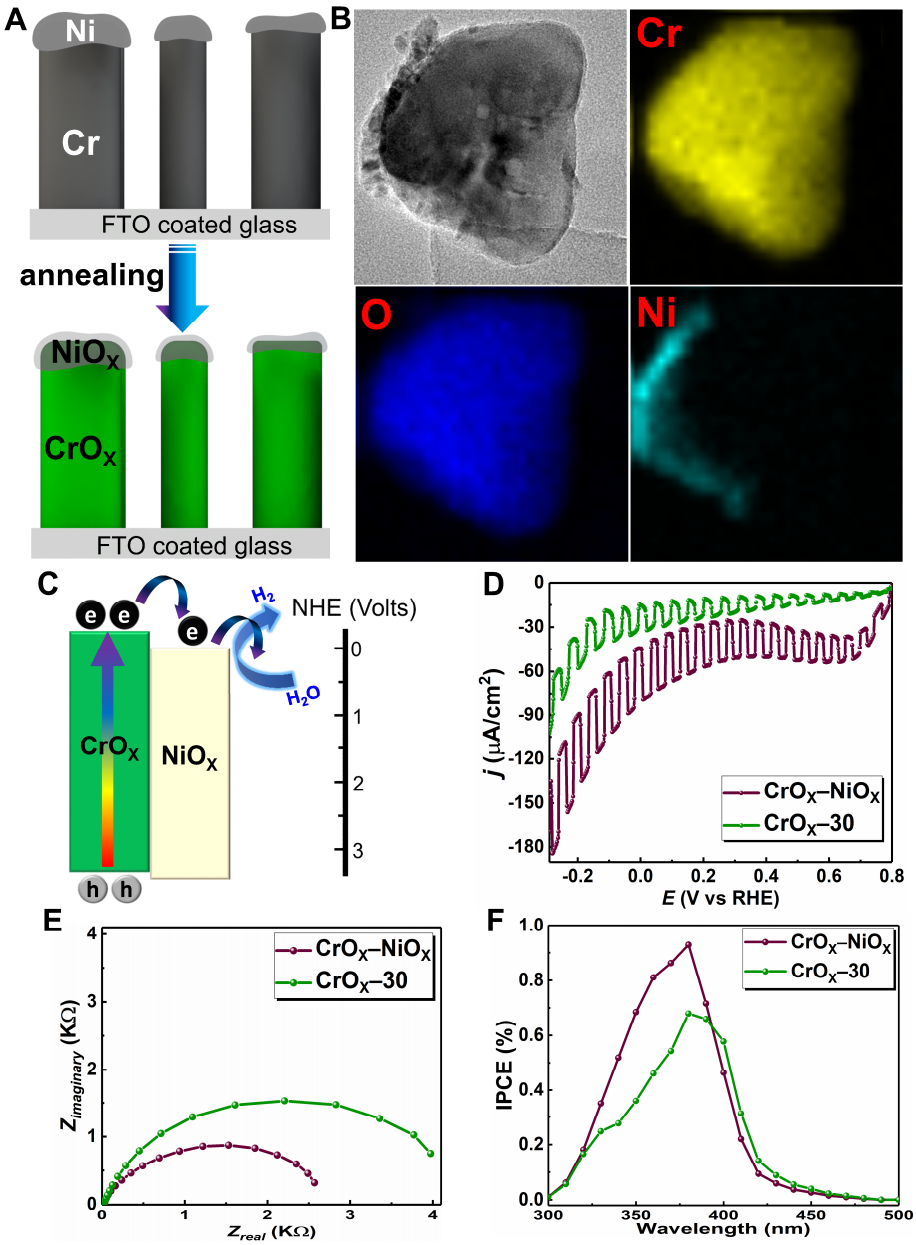


Figure 8.12 (A) The fabrication route of CrOx-NiOx heterostructure. (B) High resolution TEM elemental mapping of an individual CrOx-NiOx nanounit. These mapping data shows the formation of a core-crown configuration in this heterodesign. (C) The band alignment between CrOx and NiOx layers extracted using XPS characterizations, as explained by detail in SI. (D) The chopped LSV profile, (E)

images, the final architecture is a core-crown shape CrOx-NiOx heterostructure, as seen in Figure 8.12b. To act as a hydrogen evolution catalyst, NiO_X should have a proper band alignment with CrOx. As depicted in Figure 6C, the conduction band of NiO_X is located slightly below that of CrOx[499]. Therefore, upon light excitation, the electron-hole pairs are generated inside the CrOx bulk and the excited electrons are immediately injected into the conduction band of NiO_X. It is in this way that an efficient charge

separation happens and electrons will be directed toward the surface where the HER takes place. As a consequence of this modification, the photocurrent values of the photocathode have also been boosted. As depicted in Figure 6D, at -0.1 V_{RHE}, the photo-dark currents difference reaches a value as high as 54.7 $\mu A.cm^{-2}$, which is nearly 2.5 times larger compared to a bare CrO_X-30 photocathode. Therefore, NiO_X has indeed catalyzed the HER via the selective isolation of carriers in semiconductor-electrolyte interface. This can be confirmed in the reduced charge transfer resistance, as depicted in Figure 6E. Moreover, the IPCE data also shows enhancement in the conversion efficiencies for the CrOx-NiOx heterostructure.

As a conclusion, this work proposes an extendable toolbox to fabricate perfect absorber metasurface sub-wavelength designs for photoconversion applications in large scales. Utilizing various steady state optical, electrical, and transient techniques, it was found that in an intermediate metal/oxide state, chromium oxide nanounits achieve the best performance. In this condition, the material shows a larger absorption bandwidth and strength, harvesting a big portion of the UV range with an extended response in the visible spectrum. Moreover, TA findings showed that the synthesized material has nanosecond scale lifetime. This superior material properties have been brought together with densely-packed random geometries to achieve a high performance PEC photocathode. Finally, to further improve the photocurrent response, NiO_X crown is introduced to catalyze the HER. As a consequence of these modifications, the photocurrent response was enhanced with nearly two orders of magnitude compared to that of a planar design. The proposed design and methodology could be extended for the fabrication of high performance photo-electronic designs.

Chapter 9.Conclusions

Based on this thesis study, light perfect absorption in the whole EM spectrum (from UV to FIR) can be realized using large scale compatible, planar, lithography-free multilayer designs. For this purpose, it is necessary to find the proper material and design architecture to obtain strong light-matter interaction. Figure 1.1 outlines the proper materials for different parts of the EM spectrum. In the UV and Vis frequency ranges, this absorption can be obtained by semiconductors and noble metals. Moreover, it was recently proven[268] that graphene can be also a UV responsive material in a proper planar design. To extend the absorption upper edge toward longer wavelengths such as NIR range, lossy metals such as Cr, Ti, and Bi can be a good choice. In the short wavelength NIR regime, alternative plasmonic materials that show epsilon-near-zero (ENZ) characteristic (such as AZO, GZO, and ITO) can be effectively utilized for light near unity absorption[20]. In these materials, tuning the plasma frequency can provide us the opportunity to control the spectral position of the strong light-matter interaction. Perfect light absorption in longer wavelengths i.e. MIR, FIR, and THz which are inaccessible with unpatterned metal based multilayer designs, can be acquired using graphene, black phosphorus and suitable polar materials as shown in the Figure 1.1. Therefore, it can be envisioned that planar light perfect absorbers that do not require sophisticated lithography fabrication techniques, can be an excellent option for future large scale optoelectronic application. For this aim, according to the operation wavelength and the application, the proper design architecture and material should be used.

Metal based planar metamaterial absorbers can be listed in two main categories; narrowband and broadband perfect absorbers. As illustrated earlier, narrowband perfect light absorbers can be acquired using noble low loss metals such as Au and Ag. These structures can be of particular interest in color filtering, imaging, and display applications. The planar and large scale compatible nature of these multilayer designs facilitates their integration into commercialized color-CCD/cameras[224]. Different from nanostructured plasmonic designs, these Febry-Perot based resonators can operate in a wide incident light polarizations and angles that makes them suitable for practical applications. Moreover, the light absorption can be also obtained in broad/ultra-broad wavelengths. An ideal black-body absorber that suppresses incident light reflection and transmission in a broad spectral range can ensure efficient use

of the solar power. One of the most studied areas of interest for these ultrabroadband perfect absorbers is thermophotovoltaics (TPV). This system harvests the incident photons in a broad spectral range and transduces them into thermal energy and then a frequency-selective emitter which is matched into the band gap of the PV cell radiates a narrowband thermal emission. Based on previous works, this system can ideally overcome the fundamental limits of conventional PV cells[307]. In a PV cell, the absorption is restricted into the photons with energies above the optical band gap of the active layer. Therefore, only a specific portion of the solar spectrum will be efficiently harvested. However, metals can retain their perfect absorption property over the entire Vis and NIR regimes. Covering the most parts of solar irradiation power can guarantee the efficient harvesting of the incident light. Therefore, the use of lossy metals in metal-insulator pair based configuration can provide near unity absorption of the light and this intense absorbed power can be directed into a PV cell using a narrowband emitter to substantiate the PV cell efficiency. The narrowband emitter can be also realized using dielectric based PC structure which makes the whole TPV system lithography-free[67]. Thus, the integration of a PC narrowband emitter with a refractory lossy metal based ultra-broadband perfect absorber can be considered as a winning strategy for the design of future highly efficient TPV systems. Another area of usage of these ultra-broadband absorbers is solar driven steam generation. Advancements in this area have proved efficiencies as high as 90% at only 4-sun intensity (4 kW m^{-2})[68]. Therefore, same as TPV, the realization of ultra-broadband light perfect absorbers can be of great interest in the steam generation.

Strong light absorption in ultrathin semiconductor based perfect absorbers can also have high potentials in PV, photodetectors and photoelectrochemical applications. Our theoretical findings revealed that spectrally broad strong light-matter interaction can be acquired in MIS cavity based designs. Therefore, the incident light is efficiently harvested in sub wavelength geometries and the ultrathin thickness of the semiconductor would minimize the transport length of photogenerated carriers that in turn maximizes their collection efficiency. However, the main challenge in these semiconductor-based metamaterials is the crystalline quality of the photoactive layer. Utilizing common deposition and growth techniques for ultrathin films, it is difficult to fabricate single crystalline semiconductor in such thicknesses. In most of these designs the active layer is made of amorphous semiconductor and therefore, their optoelectronic performance is far inferior to those of bulk crystalline counterparts. Therefore, the main challenge, that limits the replacement of conventional bulk

semiconductor based optoelectronic systems with these ultrathin metamaterials, is their poor electrical properties of the photoactive layer. A recent study demonstrated a high performance MIS configuration based photodetector where the single-crystalline Ge membrane undergoes a strong light-matter interaction on a functionalized nanocavity design[79]. The use of chemical synthesis methods can be also an alternative to realize single crystalline semiconductors in such nanometer scale thicknesses. Two-dimensional (2D) TMDs are another category of semiconductors that can be employed in ultrathin optoelectronics. Transition from bulk to monolayer makes these semiconductors a direct band gap material and consequently a better absorption dynamics are emerged. However, the atomic thickness of the layer can absorb only a small portion of the light and thus, a trapping mechanism is required to provide strong light-matter interaction. As shown in the above sections, the use of MS or MIS cavity architectures could not be a good solution for light perfect absorption for 2D TMDs. These cavity designs can efficiently harvest the light in multiple layer thicknesses. To realize perfect light absorption in unpatterned monolayer of TMDs, PC configuration is the right strategy to confine the entire power in the position of the monolayer where this confined energy is harvested efficiently. A recent Perspective in the application of these van der waals materials in PV technology predicted that it is possible, in principle, to achieve power conversion efficiencies as high as 25%[308]. Introducing a tandem scheme where these 2D materials are brought to a junction with another bulk semiconductor (such as Si) could further substantiate the cell efficiency. This bulk semiconductor can be replaced with a MIS nanocavity design to localize the absorbed power in ultrathin dimensions. Then, a PC capped 2D TMD can be grown on top of this design to make an ultrathin efficient tandem solar cell. Therefore, the findings of this study can serve as a beacon for future performance enhanced semiconductor optoelectronic devices.

As mentioned hereinabove, graphene, black phosphorus and polar materials are appropriate candidates for achieving light absorption in the MIR, FIR, and THz ranges. MIR/FIR directional light emitters are a distinguished category of light absorbers that have attracted intense interests during the previous years due to their potential application in radiative heat transfer and energy conversion systems[122], [294], [296]. A thermal light-emitting source, such as a black body or the incandescent filament of a light bulb, is often presented as a typical example of an incoherent source and is in marked contrast to a laser. Whereas a laser is highly monochromatic and very directional, a thermal source

has a broad spectrum and is usually quasi-isotropic. It has been shown recently that the light absorption by polar-based 1D PCs is considerably enhanced in a directional manner compared to a bare polar film. This system, therefore, is capable of emitting radiation efficiently in well-defined directions and can act as a coherent thermal source at a fair distance. For these structures, narrow angular emission lobes similar to antenna lobes are observed and the emission spectra of the source depend on the observation angle. As mentioned earlier, the origin of the coherent emission is in the support of Tamm phonon polaritons by the above-mentioned polar-based 1D PC. The unpatterned lossy-based narrowband absorbers may also be employed as radiative coolers that are reflective in the solar spectrum and emissive in the transparency window of the atmosphere (8-13 μm). These absorbers, therefore, can be regarded as a critical component in the MIR photodetectors and imaging systems that are important in applications such as night vision and astronomy research[295], [309], [310]. MIR/FIR filtering and sensing for detecting gases as well as biological and chemical agents can be mentioned as another potential application of the narrow band light absorbers discussed in this thesis study[311].

In summary, besides the development of low-cost, facile, and extendable routes, material exploration is an essential key to realizing cm-scale high-performance LFMAs. The integration of the right elements with large-scale compatible nanofabrication routes will put this technology one step closer to industrialization. In photoconversion, a deep understanding of hot electron dynamics, exploring new materials with a long hot electron lifetime, synthesis of ultrathin high mobility crystalline semiconductors, and the development of designer heterojunctions are some of the key goals to be followed. Spectrally-selective thermal emitters are another area of high interest, due to the lack of cost-effective, narrow-band light sources in the MWIR and LWIR. TPV technology and steam generation could also widen the opportunities for the use of these LFMAs in the green energy industry. The integration of these large-scale compatible designs with microfluidic channels can offer a real-time and label-free detection platform for bio-agents with high sensitivity and reliability.

Chapter 10. BIBLIOGRAPHY

[1] E. Ozbay, “Plasmonics : Merging Photonics and Electronics at Nanoscale Dimensions,” *Science (80-.).*, vol. 311, pp. 189–194, 2006.

[2] A. Ghobadi, H. Hajian, B. Butun, and E. Ozbay, “Strong Light-Matter Interaction in Lithography-Free Planar Metamaterial Perfect Absorbers,” *ACS Photonics*, vol. 5, no. 11, pp. 4203–4221, 2018.

[3] J. Toudert, “Spectrally Tailored Light-Matter Interaction in Lithography-Free Functional Nanomaterials,” *Phys. Status Solidi Appl. Mater. Sci.*, vol. 217, no. 6, pp. 1–13, 2020.

[4] Z. Liu *et al.*, “Automatically Acquired Broadband Plasmonic-Metamaterial Black Absorber during the Metallic Film-Formation,” *ACS Appl. Mater. Interfaces*, vol. 7, pp. 4962–4968, 2015.

[5] S. Wang *et al.*, “Large-Area Low-Cost Dielectric Perfect Absorber by One-Step Sputtering,” *Adv. Opt. Mater.*, vol. 7, no. 9, pp. 1–8, 2019.

[6] A. Ghobadi, S. A. Dereshgi, H. Hajian, B. Bozok, B. Butun, and E. Ozbay, “Ultra-broadband , wide angle absorber utilizing metal insulator multilayers stack with a multi-thickness metal surface texture,” *Sci. Rep.*, vol. 7, p. 4755, 2017.

[7] A. Ghobadi, H. Hajian, S. A. Dereshgi, B. Bozok, B. Butun, and E. Ozbay, “Disordered Nanohole Patterns in Metal-Insulator Multilayer for Ultra-broadband Light Absorption: Atomic Layer Deposition for Lithography Free Highly repeatable Large Scale Multilayer Growth,” *Sci. Rep.*, vol. 7, no. 15079, pp. 1–10, 2017.

[8] A. Ghobadi, H. Hajian, A. R. Rashed, B. Butun, and E. Ozbay, “Tuning the metal filling fraction in metal-insulator-metal ultra-broadband perfect absorbers to maximize the absorption bandwidth,” *Photonics Res.*, vol. 6, no. 3, pp. 168–176, 2018.

[9] A. Barranco, A. Borras, A. R. Gonzalez-Elipe, and A. Palmero, “Perspectives on oblique angle deposition of thin films: From fundamentals to devices,” *Prog. Mater. Sci.*, vol. 76, pp. 59–153, Mar. 2016.

[10] Y. He, J. Fu, and Y. Zhao, “Oblique angle deposition and its applications in plasmonics,” *Front. Phys.*, vol. 9, no. 1, pp. 47–59, 2014.

[11] D. U. Yildirim *et al.*, “Disordered and Densely Packed ITO Nanorods as an Excellent Lithography-Free Optical Solar Reflector Metasurface,” *ACS Photonics*, vol. 6, no. 7, pp. 1812–1822, 2019.

[12] Z. Eftekhari, A. Ghobadi, and E. Ozbay, “Lithography-free disordered metal–insulator–metal nanoantennas for colorimetric sensing,” *Opt. Lett.*, vol. 45, no. 24, p. 6719, 2020.

[13] Z. Eftekhari, A. Ghobadi, M. C. Soydan, D. U. Yildirim, N. Cinel, and E. Ozbay, “Strong light emission from a defective hexagonal boron nitride monolayer coupled to near-touching random plasmonic nanounits,” *Opt. Lett.*, vol. 46, no. 7, p. 1664, 2021.

[14] M. C. Soydan, A. Ghobadi, D. U. Yildirim, V. B. Erturk, and E. Ozbay, “Deep Subwavelength Light Confinement in Disordered Bismuth Nanorods as a Linearly Thermal-Tunable Metamaterial,” *Phys. Status Solidi - Rapid Res. Lett.*, vol. 2000066, pp. 1–6, 2020.

[15] J. E. Melzer and E. McLeod, “3D Nanophotonic device fabrication using discrete components,” *Nanophotonics*, vol. 9, no. 6, pp. 1373–1390, 2020.

[16] L. Shen *et al.*, “Nanostructured Silicon Photocathodes for Solar Water Splitting Patterned by the Self-Assembly of Lamellar Block Copolymers,” *ACS Appl. Mater. Interfaces*, vol. 7, no. 47, pp. 26043–26049, 2015.

[17] X. Ruan *et al.*, “Ultrathin, broadband, omnidirectional, and polarization-independent infrared absorber using all-dielectric refractory materials,” *Nanophotonics*, vol. 10, no. 6, pp. 1683–1690, 2021.

[18] H. Robatjazi, S. M. Bahauddin, L. H. Macfarlan, S. Fu, and I. Thomann, “Ultrathin AAO Membrane as a Generic Template for Sub-100 nm Nanostructure Fabrication,” *Chem. Mater.*, vol. 28, no. 13, pp. 4546–4553, 2016.

[19] U. T. D. Thuy, N. T. Thuy, N. T. Tung, E. Janssens, and N. Q. Liem, “Large-area cost-effective lithography-free infrared metasurface absorbers for molecular detection,” *APL Mater.*, vol. 7, no. 7, 2019.

[20] J. Rensberg *et al.*, “Epsilon-Near-Zero Substrate Engineering for Ultrathin-Film Perfect Absorbers,” *Phys. Rev. Lett.*, no. 8, p. 014009, 2017.

[21] J. W. Cleary, N. Nader, K. D. Leedy, and R. Soref, “Tunable short- to mid-infrared perfectly absorbing thin films utilizing conductive zinc oxide on metal,” *Opt. Mater. Express*, vol. 5, no. 9, p. 1898, 2015.

[22] M. Sakamoto *et al.*, “Clear and transparent nanocrystals for infrared-responsive carrier transfer,” *Nat. Commun.*, vol. 10, no. 1, pp. 1–7, 2019.

[23] A. Cleri *et al.*, “Mid-wave to near-IR optoelectronic properties and epsilon-near-zero behavior in indium-doped cadmium oxide,” *Phys. Rev. Mater.*, vol. 5, no. 3, p. 35202, 2021.

[24] K. P. Kelley *et al.*, “Multiple Epsilon-Near-Zero Resonances in Multilayered Cadmium Oxide: Designing Metamaterial-Like Optical Properties in Monolithic Materials,” *ACS Photonics*, vol. 6, no. 5, pp. 1139–1145, 2019.

[25] E. L. Runnerstrom *et al.*, “Defect Engineering in Plasmonic Metal Oxide Nanocrystals,” *Nano Lett.*, vol. 16, no. 5, pp. 3390–3398, 2016.

[26] G. V Naik, V. M. Shalaev, and A. Boltasseva, “Alternative Plasmonic Materials : Beyond Gold and Silver,” *Adv. Mater.*, vol. 25, pp. 3264–3294, 2013.

[27] G. V Naik, J. Kim, and A. Boltasseva, “Oxides and nitrides as alternative plasmonic materials in the optical range [Invited],” *Opt. Mater. Express*, vol. 1, no. 6, pp. 1090–1099, 2011.

[28] A. Shabani, M. Tsegay Korsa, S. Petersen, M. Khazaei Nezhad, Y. Kumar Mishra, and J. Adam, “Zirconium Nitride: Optical Properties of an Emerging Intermetallic for Plasmonic Applications,” *Adv. Photonics Res.*, vol. 2, no. 11, p. 2100178, 2021.

[29] P. K. B. Palomaki, E. M. Miller, and N. R. Neale, “Control of plasmonic and interband transitions in colloidal indium nitride nanocrystals,” *J. Am. Chem. Soc.*, vol. 135, no. 38, pp. 14142–14150, 2013.

[30] H. Shen, L. Yang, Y. Jin, and S. He, “Perfect mid-infrared dual-band optical absorption realized by a simple lithography-free polar dielectric/metal double-layer nanostructure,” *Opt. Express*, vol. 28, no. 21, p. 31414, 2020.

[31] T. Taliercio and P. Biagioni, “Semiconductor infrared plasmonics,” *Nanophotonics*, vol.

8, no. 6, pp. 949–990, 2019.

[32] R. Zhou *et al.*, “Recent advances in graphene and black phosphorus nonlinear plasmonics,” *Nanophotonics*, vol. 9, no. 7, pp. 1695–1715, 2020.

[33] A. N. Grigorenko, M. Polini, and K. S. Novoselov, “Graphene plasmonics,” *Nat. Photonics*, vol. 6, no. 749–758, 2012.

[34] Y. Zhong, S. D. Malagari, T. Hamilton, and D. Wasserman, “Review of mid-infrared plasmonic materials,” *J. Nanophotonics*, vol. 9, no. 1, p. 093791, 2015.

[35] C. Ji, K. T. Lee, T. Xu, J. Zhou, H. J. Park, and L. J. Guo, “Engineering Light at the Nanoscale: Structural Color Filters and Broadband Perfect Absorbers,” *Adv. Opt. Mater.*, vol. 5, no. 20, pp. 1–22, 2017.

[36] A. C. Kosger, A. Ghobadi, A. R. Rashed, H. Caglayan, and E. Ozbay, “Generation of additive colors with near unity amplitude using a multilayer tandem Fabry–Perot cavity,” *Opt. Lett.*, vol. 46, no. 14, p. 3464, 2021.

[37] A. Ghobadi, H. Hajian, M. Gokbayrak, B. Butun, and E. Ozbay, “Bismuth-based metamaterials: From narrowband reflective color filter to extremely broadband near perfect absorber,” *Nanophotonics*, vol. 8, no. 5, pp. 823–832, 2019.

[38] Z. Yang *et al.*, “Reflective Color Filters and Monolithic Color Printing Based on Asymmetric Fabry–Perot Cavities Using Nickel as a Broadband Absorber,” *Adv. Opt. Mater.*, vol. 4, no. 8, pp. 1196–1202, 2016.

[39] S. Daqiqeh Rezaei, J. Ho, T. Wang, J. K. W. Yang, and S. Ramakrishna, “Direct Color Printing with an Electron Beam,” *Nano Lett.*, vol. 20, no. 6, pp. 4422–4429, 2020.

[40] J. Lee, J. Kim, and M. Lee, “High-purity reflective color filters based on thin film cavities embedded with an ultrathin Ge2Sb2Te5absorption layer,” *Nanoscale Adv.*, vol. 2, no. 10, pp. 4930–4937, 2020.

[41] F. Liu *et al.*, “ Tunable reflective color filters based on asymmetric Fabry–Perot cavities employing ultrathin Ge 2 Sb 2 Te 5 as a broadband absorber ,” *Appl. Opt.*, vol. 57, no. 30, p. 9040, 2018.

[42] Q. He, N. Youngblood, Z. Cheng, X. Miao, and H. Bhaskaran, “Dynamically tunable transmissive color filters using ultra-thin phase change materials,” *Opt. Express*, vol. 28, no. 26, p. 39841, 2020.

[43] F. Z. Shu *et al.*, “Dynamic Plasmonic Color Generation Based on Phase Transition of Vanadium Dioxide,” *Adv. Opt. Mater.*, vol. 6, no. 7, pp. 1–10, 2018.

[44] H. Liu *et al.*, “Rewritable color nanoprints in antimony trisulfide films,” *Sci. Adv.*, vol. 6, no. 51, pp. 1–8, 2020.

[45] Z. Cheng *et al.*, “Antimony thin films demonstrate programmable optical nonlinearity,” *Sci. Adv.*, vol. 7, no. 1, pp. 1–10, 2021.

[46] T. J. Palinski *et al.*, “Vibrant reflective sensors with percolation film Fabry-Pérot nanocavities,” *Opt. Express*, vol. 29, no. 16, p. 25000, 2021.

[47] J. Zhang *et al.*, “Grayscale-patterned metal-hydrogel-metal microscavity for dynamic multi-color display,” *Nanophotonics*, vol. 6021, pp. 1–7, 2021.

[48] S. Chervinskii *et al.*, “Humidity- and Temperature-Tunable Metal–Hydrogel–Metal Reflective Filters,” *ACS Appl. Mater. Interfaces*, vol. 13, no. 42, pp. 50564–50572, 2021.

[49] M. Serhatlioglu, S. Ayas, N. Biyikli, A. Dana, and M. E. Solmaz, “Perfectly absorbing ultra thin interference coatings for hydrogen sensing,” *Opt. Lett.*, vol. 41, no. 8, p. 1724, 2016.

[50] S. Ayas, G. Bakan, E. Ozgur, K. Celebi, G. Torunoglu, and A. Dana, “Colorimetric detection of ultrathin dielectrics on strong interference coatings,” *Opt. Lett.*, vol. 43, no. 6, p. 1379, 2018.

[51] G. Qiu, Z. Gai, Y. Tao, J. Schmitt, G. A. Kullak-Ublick, and J. Wang, “Dual-Functional Plasmonic Photothermal Biosensors for Highly Accurate Severe Acute Respiratory Syndrome Coronavirus 2 Detection,” *ACS Nano*, vol. 14, no. 5, pp. 5268–5277, 2020.

[52] K. Yao, R. Toole, P. Basnet, and Y. Zhao, “Highly sensitive double-layered nanorod array gas sensors prepared by oblique angle deposition,” *Appl. Phys. Lett.*, vol. 104, no. 7, 2014.

[53] X. Li, D. Xiao, and Z. Zhang, “Landau damping of quantum plasmons in metal nanostructures,” *New J. Phys.*, vol. 15, pp. 023011–023025, 2013.

[54] T. P. White and K. R. Catchpole, “Plasmon-enhanced internal photoemission for photovoltaics: Theoretical efficiency limits,” *Appl. Phys. Lett.*, vol. 101, p. 073905, 2012.

[55] M. W. Knight, N. S. King, L. Liu, H. O. Everitt, P. Nordlander, and N. J. Halas, “Aluminum for plasmonics,” *ACS Nano*, vol. 8, no. 1, pp. 834–840, 2014.

[56] L. Zhou *et al.*, “Aluminum Nanocrystals as a Plasmonic Photocatalyst for Hydrogen Dissociation,” *Nano Lett.*, vol. 16, no. 2, pp. 1478–1484, 2016.

[57] M. J. McClain *et al.*, “Aluminum Nanocrystals,” *Nano Lett.*, vol. 15, no. 4, pp. 2751–2755, 2015.

[58] M. A. Noginov *et al.*, “Transparent conductive oxides: Plasmonic materials for telecom wavelengths,” *Appl. Phys. Lett.*, vol. 99, no. 2, pp. 1–4, 2011.

[59] A. Calzolari, A. Ruini, and A. Catellani, “Transparent Conductive Oxides as Near-IR Plasmonic Materials: The Case of Al-Doped ZnO Derivatives,” *ACS Photonics*, vol. 1, no. 8, pp. 703–709, 2014.

[60] A. Habib, F. Florio, and R. Sundararaman, “Hot carrier dynamics in plasmonic transition metal nitrides,” *J. Opt.*, vol. 20, p. 064001, 2018.

[61] U. Guler, V. M. Shalaev, and A. Boltasseva, “Nanoparticle plasmonics: Going practical with transition metal nitrides,” *Mater. Today*, vol. 18, no. 4, pp. 227–237, 2015.

[62] F. Scotognella *et al.*, “Plasmonics in heavily-doped semiconductor nanocrystals,” *Eur. Phys. J. B*, vol. 86, no. 154, pp. 1–13, 2013.

[63] F. B. Barho *et al.*, “Highly doped semiconductor plasmonic nanoantenna arrays for polarization selective broadband surface-enhanced infrared absorption spectroscopy of vanillin,” *Nanophotonics*, vol. 7, no. 2, pp. 507–516, 2017.

[64] I. Kriegel, F. Scotognella, and L. Manna, “Plasmonic doped semiconductor nanocrystals: Properties, fabrication, applications and perspectives,” *Phys. Rep.*, vol. 674, pp. 1–52, 2017.

[65] T. G. U. Ghobadi, A. Ghobadi, E. Ozbay, and F. Karadas, “Strategies for Plasmonic Hot-Electron-Driven Photoelectrochemical Water Splitting,” *ChemPhotoChem*, vol. 2, pp. 161–182, 2018.

[66] E. Rephaeli and S. Fan, “Absorber and emitter for solar thermo-photovoltaic systems to achieve efficiency exceeding the Shockley-Queisser limit,” *Opt. Express*, vol. 17, no. 17, pp. 15145–15159, 2009.

[67] S. M. Fu, Y. K. Zhong, M. H. Tu, B. R. Chen, and A. Lin, “A fully functionalized metamaterial perfect absorber with simple design and implementation,” *Sci. Rep.*, vol. 6, p. 36244, 2016.

[68] L. Zhou *et al.*, “Self-assembly of highly efficient, broadband plasmonic absorbers for solar steam generation,” *Sci. Adv.*, vol. 2, no. 4, pp. e1501227–e1501227, 2016.

[69] A. Ghobadi, T. G. Ulusoy Ghobadi, F. Karadas, and E. Ozbay, “Semiconductor Thin Film Based Metasurfaces and Metamaterials for Photovoltaic and Photoelectrochemical Water Splitting Applications,” *Adv. Opt. Mater.*, vol. 7, no. 14, 2019.

[70] Palik, “E. D. Handbook of optical constants of solids. Vol. 3 (Academic, 1998).”

[71] M. A. Kats, R. Blanchard, P. Genevet, and F. Capasso, “Nanometre optical coatings based on strong interference effects in highly absorbing media,” *Nat. Mater.*, vol. 12, no. 1, pp. 20–24, 2012.

[72] S. Fan and X. Zheng, “High-Performance Ultrathin BiVO4 Photoanode on Textured Polydimethylsiloxane Substrates for Solar Water Splitting,” *ACS Energy Lett.*, vol. 1, pp. 68–75, 2016.

[73] M. Rebello, S. Dias, C. Gong, Z. A. Benson, and M. S. Leite, “Lithography-Free, Omnidirectional, CMOS-Compatible AlCu Alloys for Thin-Film Superabsorbers,” *Adv. Opt. Mater.*, vol. 6, p. 1700830, 2018.

[74] D. Liu, H. Yu, Z. Yang, and Y. Duan, “Ultrathin planar broadband absorber through effective medium design,” *Nano Res.*, vol. 9, no. 8, pp. 2354–2363, 2016.

[75] Q. Li *et al.*, “Transmission enhancement based on strong interference in metal-semiconductor layered film for energy harvesting,” *Sci. Rep.*, vol. 6, p. 29195, 2016.

[76] D. Liu, H. Yu, Y. Duan, Q. Li, and Y. Xuan, “New Insight into the Angle Insensitivity of Ultrathin Planar Optical Absorbers for Broadband Solar Energy Harvesting,” *Sci. Rep.*, vol. 6, p. 32515, 2016.

[77] H. Dotan *et al.*, “Resonant light trapping in ultrathin films for water splitting,” *Nat. Mater.*, vol. 12, no. 2, pp. 158–164, 2012.

[78] V. Steenhoff, M. Theuring, M. Vehse, and K. Von Maydell, “Ultrathin Resonant-Cavity-Enhanced Solar Cells with Amorphous Germanium Absorbers,” *Adv. Opt. Mater.*, vol. 3, pp. 182–186, 2015.

[79] Z. Xia *et al.*, “Single-crystalline germanium nanomembrane photodetectors on foreign nanocavities,” *Sci. Adv.*, vol. 3, no. 7, pp. 1–9, 2017.

[80] I. A. Digdaya, B. J. Trześniewski, G. W. P. Adhyaksa, E. C. Garnett, and W. A. Smith, “General Considerations for Improving Photovoltage in Metal − Insulator − Semiconductor Photoanodes,” *J. Phys. Chem. C*, vol. 122, pp. 5462–5471, 2018.

[81] J. Zheng, R. A. Barton, and D. Englund, “Broadband Coherent Absorption in Chirped-Planar-Dielectric Cavities for 2D-Material-Based Photovoltaics and Photodetectors,” *ACS Photonics*, vol. 1, pp. 768–774, 2014.

[82] H. Lu, X. Gan, D. Mao, Y. Fan, D. Yang, and J. Zhao, “Nearly perfect absorption of light in monolayer molybdenum disulfide supported by multilayer structures,” *Opt. Express*, vol. 25, no. 18, pp. 21630–21636, 2017.

[83] J. D. Ryckman, “Random Coherent Perfect Absorption with 2D Atomic Materials Mediated by Anderson Localization,” *ACS Photonics*, vol. 5, pp. 574–580, 2017.

[84] A. Kay *et al.*, “Film Flip and Transfer Process to Enhance Light Harvesting in Ultrathin Absorber Films on Specular Back-Reflectors,” *Adv. Mater.*, vol. 30, no. 1802781, pp. 1–7, 2018.

[85] Y. Piekner *et al.*, “Implementing Strong Interference in Ultrathin Film Top Absorbers for Tandem Solar Cells,” *ACS Photonics*, vol. 5, no. 12, pp. 5068–5078, 2018.

[86] J. Toudert, R. Serna, M. G. Pardo, N. Ramos, R. J. Peláez, and B. Maté, “Mid-to-far infrared tunable perfect absorption by a sub - λ/100 nanofilm in a fractal phasor resonant cavity,” *Opt. Express*, vol. 26, no. 26, p. 34043, 2018.

[87] M. C. Soydan *et al.*, “Lithography-Free Random Bismuth Nanostructures for Full Solar Spectrum Harvesting and Mid-Infrared Sensing,” *Adv. Opt. Mater.*, vol. 8, no. 4, pp. 1–11, 2020.

[88] H. Peng *et al.*, “Broadband and highly absorbing multilayer structure in mid-infrared,” *Appl. Opt.*, vol. 55, no. 31, pp. 8833–8837, 2016.

[89] X. Liu *et al.*, “Large-area, lithography-free, narrow-band and highly directional thermal emitter,” *Nanoscale*, vol. 11, no. 42, pp. 19742–19750, 2019.

[90] M. Li, D. Liu, H. Cheng, L. Peng, and M. Zu, “Manipulating metals for adaptive thermal camouflage,” *Sci. Adv.*, vol. 6, no. 22, pp. 1–11, 2020.

[91] L. Peng, D. Liu, H. Cheng, S. Zhou, and M. Zu, “A Multilayer Film Based Selective Thermal Emitter for Infrared Stealth Technology,” *Adv. Opt. Mater.*, vol. 6, no. 23, pp. 1–8, 2018.

[92] R. Hu *et al.*, “Thermal camouflaging metamaterials,” *Mater. Today*, vol. 45, no. May, pp. 120–141, 2021.

[93] H. Zhu *et al.*, “Multispectral camouflage for infrared, visible, lasers and microwave with radiative cooling,” *Nat. Commun.*, vol. 12, no. 1, pp. 1–8, 2021.

[94] E. Buhara, A. Ghobadi, B. Khalichi, H. Kocer, and E. Ozbay, “Mid-infrared adaptive thermal camouflage using a phase-change material coupled dielectric nanoantenna,” *J. Phys. D. Appl. Phys.*, vol. 54, no. 26, 2021.

[95] A. Kalantari Osgouei, A. Ghobadi, B. Khalichi, and E. Ozbay, “A spectrally selective gap surface-plasmon-based nanoantenna emitter compatible with multiple thermal infrared applications,” *J. Opt.*, 2021.

[96] A. Kalantari Osgouei, H. Hajian, B. Khalichi, A. E. Serebryannikov, A. Ghobadi, and E. Ozbay, “Active Tuning from Narrowband to Broadband Absorbers Using a Sub-wavelength VO2 Embedded Layer,” *Plasmonics*, vol. 16, no. 1013, p. 1021, 2021.

[97] B. Khalichi, A. Ghobadi, A. Kalantari Osgouei, and E. Ozbay, “Diode like high-contrast asymmetric transmission of linearly polarized waves based on plasmon-tunneling effect coupling to electromagnetic radiation modes,” *J. Phys. D. Appl. Phys.*, vol. 54, no. 36, p. 365102, 2021.

[98] B. Khalichi, A. Ghobadi, A. K. Osgouei, H. Kocer, and E. Ozbay, “A Transparent All-Dielectric Multifunctional Nanoantenna Emitter Compatible with Thermal Infrared and Cooling Scenarios,” *IEEE Access*, vol. 9, pp. 98590–98602, 2021.

[99] Y. Qu *et al.*, “Thermal camouflage based on the phase-changing material GST,” *Light Sci. Appl.*, vol. 7, no. 1, pp. 1–10, 2018.

[100] A. Tittl *et al.*, “A Switchable Mid-Infrared Plasmonic Perfect Absorber with Multispectral Thermal Imaging Capability,” *Adv. Mater.*, vol. 27, pp. 4597–4603, 2015.

[101] J. K. Behera, K. Liu, M. Lian, and T. Cao, “A reconfigurable hyperbolic metamaterial perfect absorber,” *Nanoscale Adv.*, vol. 3, no. 6, pp. 1758–1766, 2021.

[102] W. J. M. Kort-Kamp, S. Kramadhati, A. K. Azad, M. T. Reiten, and D. A. R. Dalvit, “Passive Radiative ‘thermostat’ Enabled by Phase-Change Photonic Nanostructures,” *ACS Photonics*, vol. 5, no. 11, pp. 4554–4560, 2018.

[103] S. Campione *et al.*, “Directional and monochromatic thermal emitter from epsilon-near-zero conditions in semiconductor hyperbolic metamaterials,” *Sci. Rep.*, vol. 6, no. June, pp. 1–9, 2016.

[104] M. Desouky, A. M. Mahmoud, and M. A. Swillam, “Silicon based mid-IR super absorber using hyperbolic metamaterial,” *Sci. Rep.*, vol. 8, no. 1, pp. 8–15, 2018.

[105] E. Azmoudeh and S. Farazi, “Ultrafast and low power all-optical switching in the mid-infrared region based on nonlinear highly doped semiconductor hyperbolic metamaterials,” *Opt. Express*, vol. 29, no. 9, p. 13504, 2021.

[106] K. Sun *et al.*, “Metasurface Optical Solar Reflectors Using AZO Transparent Conducting Oxides for Radiative Cooling of Spacecraft,” *ACS Photonics*, vol. 5, no. 2, pp. 495–501, 2018.

[107] K. S. Novoselov *et al.*, “Electric Field Effect in Atomically Thin Carbon Films,” *Science (80-.).*, vol. 306, pp. 666–670, 2004.

[108] T. Low and P. Avouris, “Graphene Plasmonics for Terahertz to Mid-Infrared Applications,” *ACS Nano*, vol. 8, no. 2, pp. 1086–1101, 2014.

[109] X. Wang, X. Jiang, Q. You, J. Guo, X. Dai, and Y. Xiang, “Tunable and multichannel terahertz perfect absorber due to Tamm surface plasmons with graphene,” *Photonic Res.*, vol. 5, no. 6, pp. 536–542, 2017.

[110] Y. Chang *et al.*, “Realization of mid-infrared graphene hyperbolic metamaterials,” *Nat. Commun.*, vol. 7, p. 10568, 2016.

[111] M. A. K. Othman, C. Guclu, and F. Capolino, “Graphene-based tunable hyperbolic metamaterials and enhanced near-field absorption,” *Opt. Express*, vol. 21, no. 6, pp. 7614–7632, 2013.

[112] R. Ning, S. Liu, H. Zhang, B. Bian, and X. Kong, “Tunable absorption in graphene-based hyperbolic metamaterials for mid-infrared range,” *Phys. B*, vol. 457, pp. 144–148, 2015.

[113] D. Dong *et al.*, “Designing a nearly perfect infrared absorber in monolayer black phosphorus,” *Appl. Opt.*, vol. 58, no. 14, p. 3862, 2019.

[114] X. Yu *et al.*, “Narrow bandgap oxide nanoparticles coupled with graphene for high performance mid-infrared photodetection,” *Nat. Commun.*, vol. 9, no. 1, pp. 1–8, 2018.

[115] C. Lan, Z. Shi, R. Cao, C. Li, and H. Zhang, “2D materials beyond graphene toward Si integrated infrared optoelectronic devices,” *Nanoscale*, vol. 12, no. 22, pp. 11784–11807, 2020.

[116] N. S. Azar, J. Bullock, S. Balendhran, H. Kim, A. Javey, and K. B. Crozier, “Light-Matter Interaction Enhancement in Anisotropic 2D Black Phosphorus via Polarization-Tailoring Nano-Optics,” *ACS Photonics*, vol. 8, no. 4, pp. 1120–1128, 2021.

[117] C. Chen *et al.*, “Widely tunable mid-infrared light emission in thin-film black phosphorus,” *Sci. Adv.*, vol. 6, no. 7, pp. 1–8, 2020.

[118] B. J. Lee, C. J. Fu, and Z. M. Zhang, “Coherent thermal emission from one-dimensional photonic crystals,” *Appl. Phys. Lett.*, vol. 87, p. 071904, 2005.

[119] B. J. Lee and Z. M. Zhang, “Coherent Thermal Emission From Modified Periodic Multilayer Structures,” *J. Heat Transfer*, vol. 129, pp. 17–26, 2007.

[120] H. Hajian, A. Ghobadi, B. Butun, and E. Ozbay, “Nearly perfect resonant absorption and coherent thermal emission by hBN-based photonic crystals,” *Opt. Express*, vol. 25, no. 25, 2017.

[121] S. Abedini Dereshgi *et al.*, “ Tuning of Optical Phonons in α-MoO 3 –VO 2 Multilayers ,” *ACS Appl. Mater. Interfaces*, vol. 13, no. 41, pp. 48981–48987, 2021.

[122] K. Shi, F. Bao, and S. He, “Enhanced Near-Field Thermal Radiation Based on Multilayer Graphene-hBN Heterostructures,” *ACS Photonics*, vol. 4, pp. 971–978, 2017.

[123] S. Abedini Dereshgi *et al.*, “Lithography-free IR polarization converters via orthogonal in-plane phonons in α-MoO3 flakes,” *Nat. Commun.*, vol. 11, no. 1, pp. 1–9, 2020.

[124] D. R. Smith, J. B. Pendry, and M. C. K. Wiltshire, “Metamaterials and Negative Refractive Index,” *Science (80-.).*, vol. 305, pp. 788–793, 2004.

[125] J. Yao *et al.*, “Optical Negative Refraction in Bulk Metamaterials of Nanowires,” *Science (80-.).*, vol. 321, p. 930, 2008.

[126] A. J. Hoffman *et al.*, “Negative refraction in semiconductor metamaterials,” *Nat. Mater.*, vol. 6, pp. 946–950, 2007.

[127] M. Lapine, I. V Shadrivov, D. A. Powell, and Y. S. Kivshar, “Magnetoelastic metamaterials,” *Nat. Mater.*, vol. 11, no. 1, pp. 30–33, 2011.

[128] D. Fleischman, A. Davoyan, P. Yeh, and H. A. Atwater, “Optical magnetism in planar metamaterial heterostructures,” *Nat. Commun.*, vol. 9, p. 296, 2018.

[129] C. Menzel *et al.*, “Asymmetric transmission of linearly polarized light at optical metamaterials,” *Phys. Rev. Lett.*, vol. 104, no. 25, p. 253902, 2010.

[130] Z. Li, M. Mutlu, and E. Ozbay, “Chiral metamaterials : from optical activity and negative refractive index to asymmetric transmission,” *J. Opt.*, vol. 15, p. 023001, 2013.

[131] A. Fang, T. Koschny, and C. M. Soukoulis, “Lasing in metamaterial nanostructures,” *J. Opt.*, vol. 12, p. 024013, 2010.

[132] E. Plum, V. A. Fedotov, P. Kuo, D. P. Tsai, and N. I. Zheludev, “Towards the lasing spaser : controlling metamaterial optical response with semiconductor quantum dots,” *Opt. Express*, vol. 17, no. 10, pp. 11–14, 2009.

[133] D. Schurig *et al.*, “Metamaterial Electromagnetic Cloak at Microwave Frequencies,” *Science (80-.).*, vol. 314, pp. 977–981, 2006.

[134] J. Valentine, J. Li, T. Zentgraf, G. Bartal, and X. Zhang, “An optical cloak made of dielectrics,” *Nat. Mater.*, vol. 8, no. 7, pp. 568–571, 2009.

[135] T. Ergin, N. Stenger, P. Brenner, J. B. Pendry, and M. Wegener, “Three-dimensional invisibility cloak at optical wavelengths,” *Science (80-.).*, vol. 328, no. 5976, pp. 337–339, 2010.

[136] N. I. Landy, S. Sajuyigbe, J. J. Mock, D. R. Smith, and W. J. Padilla, “Perfect Metamaterial Absorber,” *Phys. Rev. Lett.*, vol. 100, p. 207402, 2008.

[137] M. E. Stewart *et al.*, “Nanostructured Plasmonic Sensors,” *Chem. Rev.*, vol. 108, pp. 494–521, 2008.

[138] P. Offermans, M. C. Schaafsma, S. R. K. Rodriguez, Y. Zhang, and M. Crego-calama, “Universal Scaling of the Figure of Merit of Plasmonic Sensors,” *ACS Nano*, vol. 5, no. 6, pp. 5151–5157, 2011.

[139] T. Xu, Y.-K. Wu, X. Luo, and L. J. Guo, “Plasmonic nanoresonators for high-resolution colour filtering and spectral imaging,” *Nat. Commun.*, vol. 1, p. 59, 2010.

[140] N. I. Landy, C. M. Bingham, T. Tyler, N. Jokerst, D. R. Smith, and W. J. Padilla, “Design, theory, and measurement of a polarization-insensitive absorber for terahertz imaging,” *Phys. Rev. B - Condens. Matter Mater. Phys.*, vol. 79, no. 12, pp. 1–6, 2009.

[141] T. Ellenbogen, K. Seo, and K. B. Crozier, “Chromatic Plasmonic Polarizers for Active Visible Color Filtering and Polarimetry,” *Nano Lett.*, vol. 12, pp. 1026–1031, 2012.

[142] S. Yokogawa, S. P. Burgos, and H. A. Atwater, “Plasmonic color filters for CMOS image sensor applications,” *Nano Lett.*, vol. 12, no. 8, pp. 4349–4354, 2012.

[143] C. Ji, K. T. Lee, T. Xu, J. Zhou, H. J. Park, and L. J. Guo, “Engineering Light at the Nanoscale: Structural Color Filters and Broadband Perfect Absorbers,” *Adv. Opt. Mater.*, vol. 5, no. 20, p. 1700368, 2017.

[144] J. K. Tong, W. Hsu, Y. Huang, S. V Boriskina, and G. Chen, “Thin-film ‘ Thermal Well ’ Emitters and Absorbers for High-Efficiency Thermophotovoltaics,” *Sci. Rep.*, vol. 5, p. 10661, 2015.

[145] C. Wu *et al.*, “Metamaterial-based integrated plasmonic absorber / emitter for solar thermo-photovoltaic systems,” *J. Opt.*, vol. 14, p. 024005, 2012.

[146] T. I. A. N. J. I. L. Iu and J. U. T. Akahara, “Ultrabroadband absorber based on single-sized embedded metal-dielectric-metal structures and application of radiative cooling,” *Opt. Express*, vol. 25, no. 12, pp. 1443–1447, 2017.

[147] D. Wu *et al.*, “The design of ultra-broadband selective near-perfect absorber based on photonic structures to achieve near-ideal daytime radiative cooling,” *Mater. Des.*, vol. 139, pp. 104–111, 2018.

[148] E. Rephaeli, A. Raman, and S. Fan, “Ultrabroadband Photonic Structures To Achieve High-Performance Daytime Radiative Cooling,” *Nano Lett.*, vol. 13, pp. 1457–1461, 2013.

[149] F. P. G. de Arquer, A. Mihi, and G. Konstantatos, “Large-Area Plasmonic-Crystal−Hot-Electron-Based Photodetectors,” *ACS Photonics*, vol. 2, pp. 950–957, 2015.

[150] W. Li and J. Valentine, “Metamaterial Perfect Absorber Based Hot Electron Photodetection,” *Nano Lett.*, vol. 14, pp. 3510–3514, 2014.

[151] J. Fang *et al.*, “Ag/diatomite for highly efficient solar vapor generation under one-sun irradiation,” *J. Mater. Chem. A*, vol. 5, pp. 17817–17821, 2017.

[152] K. Bae, G. Kang, S. K. Cho, W. Park, W. J. Padilla, and K. Kim, “Flexible thin-film black gold membranes with ultrabroadband plasmonic nanofocusing for efficient solar vapour generation,” *Nat. Commun.*, vol. 6, pp. 1–9, 2015.

[153] J. Park *et al.*, “Omnidirectional Near-Unity Absorption in an Ultrathin Planar Semiconductor Layer on a Metal Substrate,” *ACS Photonics*, vol. 1, pp. 812–821, 2014.

[154] C. Hägglund and S. P. Apell, “Plasmonic Near-Field Absorbers for Ultrathin Solar Cells,” *Phys. Chem. Lett.*, vol. 3, pp. 1275–1285, 2012.

[155] P. Detectors, M. Entezari, and M. Zavvari, “Application of Hyperbolic Metamaterials for Responsivity Enhancement of Thin Film Photo-Conductive Detectors,” *IEEE Sens. J.*, vol. 16, no. 24, pp. 8916–8920, 2016.

[156] W. Wang, A. Klots, D. Prasai, Y. Yang, K. I. Bolotin, and J. Valentine, “Hot Electron-Based Near-Infrared Photodetection Using Bilayer MoS 2,” *Nano Lett.*, vol. 15, pp. 7440–7444, 2015.

[157] V. E. Ferry *et al.*, “Light trapping in ultrathin plasmonic solar cells,” *Opt. Express*, vol. 18, pp. 237–245, 2010.

[158] O. Lopez-Sanchez, E. Alarcon Llado, V. Koman, A. Fontcuberta I Morral, A. Radenovic, and A. Kis, “Light generation and harvesting in a van der waals heterostructure,” *ACS Nano*, vol. 8, no. 3, pp. 3042–3048, 2014.

[159] P. Spinelli *et al.*, “Plasmonic light trapping in thin-film Si solar cells,” *J. Opt.*, vol. 14, p. 024002, 2012.

[160] Y. Wang, T. Sun, T. Paudel, Y. Zhang, Z. Ren, and K. Kempa, “Metamaterial-Plasmonic Absorber Structure for High Efficiency Amorphous Silicon Solar Cells,” *Nano Lett.*, vol. 12, pp. 440–445, 2012.

[161] M. A. Green and S. Pillai, “Harnessing plasmonics for solar cells,” *Nat. Photonics*, vol. 6, pp. 130–132, 2012.

[162] N. Vandamme, N. Bardou, and C. Dupuis, “Metal Nanogrid for Broadband Multiresonant Light-Harvesting in Ultrathin GaAs Layers,” *ACS Photonics*, vol. 1, pp. 878–884, 2014.

[163] C. F. Guo, T. Sun, F. Cao, Q. Liu, and Z. Ren, “Metallic nanostructures for light trapping in energy-harvesting devices,” *Light Sci. Appl.*, vol. 42, pp. 1–12, 2014.

[164] A. Ahmadivand, M. Karabiyik, and N. Pala, *6. Plasmonic photodetectors*. Elsevier Ltd, 2016.

[165] A. Ghobadi, H. Hajian, A. R. Rashed, B. Butun, and E. Ozbay, “Tuning the metal filling fraction in absorbers to maximize the absorption bandwidth,” *Photonics Reseach*, vol. 6, no. 3, pp. 168–176, 2018.

[166] M. Steslicka, R. Kucharczyk, A. Akjouj, B. Djafari-rouhani, L. Dobrzynski, and S. G. Davison, “Localised electronic states in semiconductor superlattices,” *Surf. Sci. Rep.*, vol. 47, pp. 93–196, 2002.

[167] H. Hajian, A. Soltani-vala, and M. Kalafi, “Optimizing terahertz surface plasmons of a monolayer graphene and a graphene parallel plate waveguide using one-dimensional photonic crystal,” *J. Appl. Phys.*, vol. 114, p. 033102, 2013.

[168] S. Ogawa and M. Kimata, “Metal-Insulator-Metal-Based Plasmonic Metamaterial Absorbers at Visible and Infrared Wavelengths: A Review,” *Materials (Basel).*, vol. 11, no. 458, pp. 1–18, 2018.

[169] N. Liu, M. Mesch, T. Weiss, M. Hentschel, and H. Giessen, “Infrared perfect absorber and its application as plasmonic sensor,” *Nano Lett.*, vol. 10, no. 7, pp. 2342–2348, 2010.

[170] K. Aydin, V. E. Ferry, R. M. Briggs, and H. a. Atwater, “Broadband polarization-independent resonant light absorption using ultrathin plasmonic super absorbers,” *Nat. Commun.*, vol. 2, no. 517, pp. 1–7, 2011.

[171] J. Hao, J. Wang, X. Liu, W. J. Padilla, L. Zhou, and M. Qiu, “High performance optical absorber based on a plasmonic metamaterial,” *Appl. Phys. Lett.*, vol. 96, p. 251104, 2010.

[172] M. K. Hedayati *et al.*, “Design of a perfect black absorber at visible frequencies using plasmonic metamaterials,” *Adv. Mater.*, vol. 23, no. 45, pp. 5410–5414, 2011.

[173] J. Hao, L. Zhou, and M. Qiu, “Nearly total absorption of light and heat generation by plasmonic metamaterials,” *Phys. Rev. B*, vol. 83, p. 165107, 2011.

[174] C. M. Watts, X. Liu, and W. J. Padilla, “Metamaterial Electromagnetic Wave Absorbers,” *Adv. Opt. Mater.*, vol. 24, pp. OP98–OP120, 2012.

[175] Q. Wen, Y. Xie, H. Zhang, Q. Yang, and Y. Li, “Transmission line model and fields analysis of metamaterial absorber in the terahertz band,” *Opt. Express*, vol. 17, no. 22, pp. 20256–20265, 2009.

[176] M. Yan, “Metal-insulator-metal light absorber: a continuous structure,” *J. Opt.*, vol. 15, no. 2, pp. 25006(1–8), 2013.

[177] H. Tao *et al.*, “A dual band terahertz metamaterial absorber,” *J. Phys. D. Appl. Phys.*, vol. 43, p. 225102, 2010.

[178] Z. Yong, S. Zhang, C. Gong, and S. He, “Narrow band perfect absorber for maximum localized magnetic and electric field enhancement and sensing applications,” *Sci. Rep.*, vol. 6, p. 24063, 2016.

[179] P. Mandal, “plasmonic metamaterial perfect absorber at visible frequency : design rule,” *J. Nanophotonics*, vol. 11, no. 3, p. 036003, 2017.

[180] B. Wang, W.-Q. Huang, and L.-L. Wang, “Ultra-narrow terahertz perfect light absorber based on surface lattice resonance of a sandwich resonator for sensing applications,” *RSC Adv.*, vol. 7, pp. 42956–42963, 2017.

[181] D. Wu *et al.*, “Infrared Perfect Ultra-narrow Band Absorber as Plasmonic Sensor,” *Nanoscale Res. Lett.*, vol. 11, no. 1, p. 483, 2016.

[182] J. Kim, K. Han, and J. W. Hahn, “Selective dual-band metamaterial perfect absorber for infrared stealth technology,” *Sci. Rep.*, vol. 7, p. 6740, 2017.

[183] S. Shu, Z. Li, and Y. Y. Li, “Triple-layer Fabry-Perot absorber with near- perfect absorption in visible and near-infrared regime,” *Opt. Express*, vol. 21, no. 21, pp. 4795–4801, 2013.

[184] Y. S. Do and K. C. Choi, “Poly-periodic hole arrays for angle-invariant plasmonic filters,” *Opt. Lett.*, vol. 40, no. 16, pp. 3873–3876, 2015.

[185] A. Moreau *et al.*, “Controlled-reflectance surfaces with film-coupled colloidal nanoantennas,” *Nature*, vol. 492, pp. 86–90, 2012.

[186] A. Cattoni, P. Ghenuche, D. Decanini, J. Chen, and J. Pelouard, “λ3/1000 Plasmonic Nanocavities for Biosensing Fabricated by Soft UV Nanoimprint Lithography,” *Nano Lett.*, vol. 11, pp. 3557–3563, 2011.

[187] N. Zhang *et al.*, “Reversibly tunable coupled and decoupled super absorbing structures,”

Appl. Phys. Lett., vol. 108, p. 091105, 2016.

[188] W. Chang, J. Won, L. S. Slaughter, and S. Link, “Plasmonic nanorod absorbers as orientation sensors,” *PNAS*, vol. 107, no. 7, pp. 2781–2786, 2010.

[189] Y. Avitzour, Y. A. Urzhumov, and G. Shvets, “Wide-angle infrared absorber based on a negative-index plasmonic metamaterial,” *Phys. Rev. B*, vol. 79, no. 4, pp. 1–5, 2009.

[190] X. Liu, T. Starr, A. F. Starr, and W. J. Padilla, “Infrared Spatial and Frequency Selective Metamaterial with Near-Unity Absorbance,” *Phys. Rev. Lett.*, vol. 104, p. 207403, 2010.

[191] H. Wang and L. Wang, “Perfect selective metamaterial solar absorbers,” *Opt. Express*, vol. 21, no. S6, pp. 13311–13319, 2013.

[192] M. G. Nielsen, A. Pors, O. Albrektsen, and S. I. Bozhevolnyi, “Efficient absorption of visible radiation by gap plasmon resonators,” *Opt. Express*, vol. 20, no. 12, pp. 13311–13319, 2012.

[193] X. Ming and Q. Tan, “Design Method of a Broadband Wide-Angle Plasmonic Absorber in the Visible Range,” *Plasmonics*, vol. 12, no. 1, pp. 14–17, 2017.

[194] M. Kenney, J. Grant, Y. D. Shah, I. Escorcia-carranza, M. Humphreys, and D. R. S. Cumming, “Octave-Spanning Broadband Absorption of Terahertz Light Using Metasurface Fractal-Cross Absorbers,” *ACS Photonics*, vol. 4, pp. 2604–2612, 2017.

[195] X. Duan, S. Chen, W. Liu, H. Cheng, and Z. Li, “Polarization-insensitive and wide-angle broadband nearly perfect absorber by tunable planar metamaterials in the visible regime,” *J. Opt.*, vol. 16, p. 125107, 2014.

[196] A. K. Azad *et al.*, “Metasurface Broadband Solar Absorber,” *Sci. Rep.*, vol. 6, p. 20347, 2016.

[197] R. Mudachathi and T. Tanaka, “Broadband plasmonic perfect light absorber in the visible spectrum for solar cell applications,” *Adv. Nat. Sci. Nanosci. Nanotechnol.*, vol. 9, p. 015010, 2018.

[198] Y. Lu, W. Dong, Z. Chen, A. Pors, Z. Wang, and S. I. Bozhevolnyi, “Gap-plasmon based broadband absorbers for enhanced hot- electron and photocurrent generation,” *Sci. Rep.*, vol. 6, p. 30650, 2016.

[199] G. Tagliabue, H. Eghlidi, and D. Poulikakos, “Facile multifunctional plasmonic sunlight harvesting with tapered triangle nanopatterning of thin films.,” *Nanoscale*, vol. 5, no. 20, pp. 9957–62, 2013.

[200] A. Ghobadi *et al.*, “Visible light nearly perfect absorber: an optimum unit cell arrangement for near absolute polarization insensitivity,” *Opt. Express*, vol. 25, no. 22, p. 27624, 2017.

[201] T. Ji, Y. Wang, Y. Cui, Y. Lin, Y. Hao, and D. Li, “Flexible broadband plasmonic absorber on moth-eye substrate,” *Mater. Today Energy*, vol. 5, pp. 181–186, 2017.

[202] J. A. Bossard, L. Lin, S. Yun, L. Liu, D. H. Werner, and T. S. Mayer, “Near-Ideal Optical Metamaterial Absorbers with Super-Octave Bandwidth,” *ACS Nano*, vol. 8, no. 2, pp. 1517–1524, 2014.

[203] F. Ding, J. Dai, Y. Chen, J. Zhu, Y. Jin, and S. I. Bozhevolnyi, “Broadband near-infrared metamaterial absorbers utilizing highly lossy metals,” *Sci. Rep.*, vol. 6, p. 39445, 2016.

[204] C. Yang *et al.*, “Compact multilayer film structure for angle insensitive color filtering,”

Sci. Rep., vol. 5, p. 9285, 2015.

[205] K. T. Lee, S. Y. Han, and H. J. Park, “Omnidirectional Flexible Transmissive Structural Colors with High-Color-Purity and High-Efficiency Exploiting Multicavity Resonances,” *Adv. Opt. Mater.*, vol. 5, no. 14, p. 1700284, 2017.

[206] Z. Li, S. Butun, and K. Aydin, “Lithography-free transmission fi lters at ultraviolet frequencies using ultra-thin aluminum films,” *J. Opt.*, vol. 18, p. 065006, 2016.

[207] Y. Zhao *et al.*, “Artificial structural color pixels: A review,” *Materials (Basel).*, vol. 10, p. 944, 2017.

[208] Y.-T. Yoon and S.-S. Lee, “Transmission type color filter incorporating a silver film based etalon.,” *Opt. Express*, vol. 18, no. 5, pp. 5344–5349, 2010.

[209] D. Zhao *et al.*, “Ultra-narrow-band light dissipation by a stack of lamellar silver and alumina,” *Appl. Phys. Lett.*, vol. 104, p. 221107, 2014.

[210] J. Y. Lee, K. T. Lee, S. Seo, and L. J. Guo, “Decorative power generating panels creating angle insensitive transmissive colors,” *Sci. Rep.*, vol. 4, p. 4192, 2014.

[211] S. S. Mirshafieyan and D. A. Gregory, “Electrically tunable perfect light absorbers as color filters and modulators,” *Sci. Rep.*, no. January, pp. 1–9, 2018.

[212] H. A. O. P. Eng, Y. I. L. Uo, X. I. Y. Ing, Y. P. U. Ang, Y. A. J. Iang, and J. X. U. Immy, “Broadband and highly absorbing multilayer structure in mid-infrared,” *Appl. Opt.*, vol. 55, no. 31, pp. 8833–8838, 2016.

[213] Z. Li, E. Palacios, S. Butun, H. Kocer, and K. Aydin, “Omnidirectional, broadband light absorption using large-area, ultrathin lossy metallic film coatings,” *Sci. Rep.*, vol. 5, no. 15137, pp. 1–22, 2015.

[214] A. Ghobadi, S. A. Dereshgi, B. Butun, and E. Ozbay, “Ultra-broadband Asymmetric Light Transmission and Absorption Through The Use of Metal Free Multilayer Capped Dielectric Microsphere Resonator,” *Sci. Rep.*, vol. 7, p. 14538, 2017.

[215] N. Mattiucci, M. J. Bloemer, N. Akozbek, and G. D’Aguanno, “Impedance matched thin metamaterials make metals absorbing,” *Sci. Rep.*, vol. 3, no. 3203, pp. 1–11, 2013.

[216] M. Chirumamilla *et al.*, “Multilayer tungsten-alumina-based broadband light absorbers for high-temperature applications,” *Opt. Mater. Express*, vol. 6, no. 8, p. 2704, 2016.

[217] H. Deng, Z. Li, L. Stan, D. Rosenmann, and D. Czaplewski, “Broadband perfect absorber based on one ultrathin layer of refractory metal,” *Opt. Lett.*, vol. 40, no. 11, pp. 2592–2595, 2015.

[218] G. Kajtár, M. Kafesaki, E. N. Economou, and C. M. Soukoulis, “Theoretical model of homogeneous metal–insulator–metal perfect multi-band absorbers for the visible spectrum,” *J. Phys. D. Appl. Phys.*, vol. 49, no. 5, p. 055104, 2016.

[219] F. Ding *et al.*, “Lithography-free, broadband, omnidirectional, and polarization-insensitive thin optical absorber,” *Appl. Phys. Lett.*, vol. 106, p. 061108, 2015.

[220] Y. K. Zhong *et al.*, “Omnidirectional, polarization-independent, ultra-broadband metamaterial perfect absorber using field-penetration and reflected-wave-cancellation,” *Opt. Express*, vol. 24, no. 10, p. A832, 2016.

[221] Y. K. Zhong *et al.*, “Fully Planarized Perfect Metamaterial Absorbers With No Photonic Nanostructures,” *IEEE Photonics J.*, vol. 8, no. 1, p. 2200109, 2016.

[222] S. Abedini Dereshgi, A. Ghobadi, H. Hajian, B. Butun, and E. Ozbay, “Ultra-Broadband, Lithography-Free, and Large-Scale Compatible Perfect Absorbers: The Optimum Choice of Metal layers in Metal-Insulator Multilayer Stacks,” *Sci. Rep.*, vol. 7, no. 1, 2017.

[223] C. S. Park, V. R. Shrestha, S. S. Lee, and D. Y. Choi, “Trans-Reflective Color Filters Based on a Phase Compensated Etalon Enabling Adjustable Color Saturation,” *Sci. Rep.*, vol. 6, p. 25496, 2016.

[224] Z. Li, S. Butun, and K. Aydin, “Large-area, Lithography-free super absorbers and color filters at visible frequencies using ultrathin metallic films,” *ACS Photonics*, vol. 2, no. 2, pp. 183–188, 2015.

[225] K. Mao *et al.*, “Angle insensitive color filters in transmission covering the visible region,” *Sci. Rep.*, vol. 6, p. 19289, 2016.

[226] C. S. Park, V. R. Shrestha, S. S. Lee, E. S. Kim, and D. Y. Choi, “Omnidirectional color filters capitalizing on a nano-resonator of Ag-TiO2 -Ag integrated with a phase compensating dielectric overlay,” *Sci. Rep.*, vol. 5, p. 8467, 2015.

[227] K.-T. Lee, S. Seo, J. Y. Lee, and L. J. Guo, “Strong resonance effect in a lossy medium-based optical cavity for angle robust spectrum filters.,” *Adv. Mater.*, vol. 26, no. 36, pp. 6324–6328, 2014.

[228] J. H. Han, D.-Y. Kim, D. Kim, and K. C. Choi, “Highly conductive and flexible color filter electrode using multilayer film structure,” *Sci. Rep.*, vol. 6, p. 29341, 2016.

[229] K. T. Lee, S. Seo, J. Yong Lee, and L. Jay Guo, “Ultrathin metal-semiconductor-metal resonator for angle invariant visible band transmission filters,” *Appl. Phys. Lett.*, vol. 104, p. 231112, 2014.

[230] J. Toudert *et al.*, “Unveiling the Far Infrared-to-Ultraviolet Optical Properties of Bismuth for Applications in Plasmonics and Nanophotonics,” *J. Phys. Chem. C*, vol. 121, no. 6, pp. 3511–3521, 2017.

[231] Y. Lin and W. Chen, “Perfect meta-absorber by using pod-like nanostructures with ultra-broadband, omnidirectional, and polarization-independent characteristics,” *Sci. Rep.*, vol. 8, p. 7150, 2018.

[232] C. Yang *et al.*, “Compact Multilayer Film Structures for Ultrabroadband, Omnidirectional, and Efficient Absorption,” *ACS Photonics*, vol. 3, no. 4, pp. 590–596, 2016.

[233] S. He, F. Ding, L. Mo, and F. Bao, “Light Absorber with an Ultra-Broad Flat Band Based on Multi-Sized Slow-Wave Hyperbolic Metamaterial Thin-Films,” *Prog. Electromagn. Res.*, vol. 147, pp. 69–79, 2014.

[234] D. Ji *et al.*, “Broadband absorption engineering of hyperbolic metafilm patterns,” *Sci. Rep.*, vol. 4, no. 1, p. 4498, 2014.

[235] H. U. D. Eng, C. H. J. M. Athai, S. H. G. Angopadhyay, J. Ie, G. Ao, and X. I. Y. Ang, “Ultra-broadband infrared absorption by tapered hyperbolic multilayer waveguides,” *Opt. Express*, vol. 26, no. 5, pp. 6360–6370, 2018.

[236] Y. Cui *et al.*, “Ultrabroadband light absorption by a sawtooth anisotropic metamaterial slab,” *Nano Lett.*, vol. 12, no. 3, pp. 1443–1447, 2012.

[237] W. Xue, X. Chen, Y. Peng, and R. Yang, “Grating-type mid-infrared light absorber based on silicon carbide material,” *Opt. Express*, vol. 24, no. 20, pp. 22596–22605, 2016.

[238] F. Ding, Y. Jin, B. Li, H. Cheng, L. Mo, and S. He, “Ultrabroadband strong light

absorption based on thin multilayered metamaterials," *Laser Photonics Rev.*, vol. 8, no. 6, pp. 946–953, 2014.

[239] J. Wu, "Broadband light absorption by tapered metal-dielectric multilayered grating structures," *Opt. Commun.*, vol. 365, pp. 93–98, 2016.

[240] J. Zhou, A. F. Kaplan, L. Chen, and L. J. Guo, "Experiment and Theory of the Broadband Absorption by a Tapered Hyperbolic Metamaterial Array," *ACS Photonics*, vol. 1, pp. 618–624, 2014.

[241] A. Ghobadi *et al.*, "97 Percent Light Absorption in an Ultrabroadband Frequency Range Utilizing an Ultrathin Metal Layer: Randomly Oriented, Densely Packed Dielectric Nanowires As an Excellent Light Trapping Scaffold," *Nanoscale*, vol. 9, no. 43, pp. 16652–16660, 2017.

[242] A. Lin *et al.*, "Lithography-free thin-titanium-nanocone metamaterial perfect absorbers using ZnO nanostructures," *Opt. Mater. Express*, vol. 7, no. 10, pp. 3608–3617, 2017.

[243] R. D. M. John Joannopoulos, Joshua N. Winn, Steven G. Johnson, *photonic crystals molding the flow of light*. 1995.

[244] E. Yablonovitch, "Inhibited Spontaneous Emission in Solid-State Physics and Electronics," *Phys. Rev. Lett.*, vol. 58, no. 20, pp. 2059–2062, 1987.

[245] R. Badugu and J. R. Lakowicz, "Tamm State-Coupled Emission: Effect of Probe Location and Emission Wavelength," *Phys. Chem. C*, vol. 118, pp. 21558–21571, 2014.

[246] S. A. Maier, *PLASMONICS : FUNDAMENTALS AND APPLICATIONS*. 2007.

[247] P. Yeh, A. Yariv, C. Hong, and I. Introduction, "Electromagnetic propagation in periodic stratified media. I. General theory," *J. Opt. Soc. Am.*, vol. 67, no. 4, pp. 423–438, 1977.

[248] Y. Chen *et al.*, "Back focal plane imaging of Tamm plasmons and their coupled emission," *Laser Photonics Rev.*, vol. 8, no. 6, pp. 933–940, 2014.

[249] Y. Chen *et al.*, "Effect of metal film thickness on Tamm plasmon-coupled emission," *Phys. Chem. Chem. Phys.*, vol. 16, pp. 25523–25530, 2014.

[250] S. D. Choudhury, R. Badugu, and J. R. Lakowicz, "Directing Fluorescence with Plasmonic and Photonic Structures," *Acc. Chem. Res.*, vol. 48, pp. 2171–2180, 2015.

[251] M. Kaliteevski *et al.*, "Tamm plasmon-polaritons: Possible electromagnetic states at the interface of a metal and a dielectric Bragg mirror," *Phys. Rev. B*, vol. 76, p. 165415, 2007.

[252] S. Pizzini, *Advanced Silicon Materials for Photovoltaic Applications*. 2012.

[253] M. A. Green, Y. Hishikawa, A. W. Y. H. Baillie, E. D. Dunlop, and D. H. Levi, "Solar cell efficiency tables (version 51)," *Prog Photovolt Res Appl*, vol. 26, pp. 3–12, 2018.

[254] J. Liu *et al.*, "Two-Dimensional CH 3 NH 3 Pbl 3 Perovskite: Synthesis and Optoelectronic Application," *ACS Nano*, vol. 10, pp. 3536–3542, 2016.

[255] L. Zhu *et al.*, "Synthesis of ultrathin two-dimensional organic – inorganic hybrid perovskite nanosheets for polymer field-effect transistors," *J. Mater. Chem. C*, vol. 6, pp. 3945–3950, 2018.

[256] S. Yang *et al.*, "Ultrathin Two-Dimensional Organic – Inorganic Hybrid Perovskite Nanosheets with Bright , Tunable Photoluminescence and High Stability," *Angew.*

Chemie, vol. 129, pp. 4316–4319, 2017.

[257] D. Ma, Y. Fu, L. Dang, J. Zhai, I. A. Guzei, and S. Jin, “Single-crystal microplates of two-dimensional organic – inorganic lead halide layered perovskites for optoelectronics,” *Nano Res.*, vol. 10, no. 6, pp. 2117–2129, 2017.

[258] Y. Zhang *et al.*, “Ultrathin polarization-insensitive wide-angle broadband near-perfect absorber in the visible regime based on few-layer MoS 2 films,” *Appl. Phys. Lett.*, vol. 111, p. 111109, 2017.

[259] D. Jariwala, A. R. Davoyan, G. Tagliabue, M. C. Sherrott, J. Wong, and H. A. Atwater, “Near-Unity Absorption in van der Waals Semiconductors for Ultrathin Optoelectronics,” *Nano Lett.*, vol. 16, no. 9, pp. 5482–5487, 2016.

[260] J. R. Piper and S. Fan, “Broadband Absorption Enhancement in Solar Cells with an Atomically Thin Active Layer,” *ACS Photonics*, vol. 3, pp. 571–577, 2016.

[261] F. Bouhjar, B. Bessaïs, and B. Marí, “Ultrathin-layer α -Fe 2 O 3 deposited under hematite for solar water splitting,” *J. Solid State Electrochem.*, 2018.

[262] Y. Wang, J. Han, X. Gu, S. Dimitrijev, Y. Hou, and S. Zhang, “Ultrathin Fe2O3 nanoflakes using smart chemical stripping for high performance lithium storage,” *J. Mater. Chem. A*, vol. 5, no. 001, pp. 18737–18743, 2017.

[263] C. Zhu, J. Li, Y. Yang, J. Huang, Y. Lu, and X. Zhao, “SiO 2 / bi-layer GZO / Ag structures for near-infrared broadband wide-angle,” *J. Phys. D Appl. Phys. Pap.*, vol. 49, p. 425106, 2016.

[264] J. Yoon, M. Zhou, A. Badsha, T. Y. Kim, and Y. C. Jun, “Broadband Epsilon-Near-Zero Perfect Absorption in the Near-Infrared,” *Sci. Rep.*, vol. 5, p. 12788, 2015.

[265] H. Zheng *et al.*, “Optical Properties of Al-Doped ZnO Films in the Infrared Region and Their Absorption Applications,” *Nanoscale Res. Lett.*, vol. 13, no. 149, 2018.

[266] Y. Zhang, T. Wei, W. Dong, C. Huang, K. Zhang, and Y. Sun, “Near-perfect infrared absorption from dielectric multilayer of plasmonic aluminum-doped zinc oxide,” *Appl. Phys. Lett.*, vol. 102, p. 213117, 2013.

[267] J. Liu *et al.*, “Optical absorption of hyperbolic metamaterial with stochastic surfaces,” *Opt. Express*, vol. 22, no. 8, pp. 8834–8838, 2014.

[268] J. Zhu, S. Yan, N. Feng, L. Ye, J. Ou, and Q. H. Liu, “Near unity ultraviolet absorption in graphene without patterning,” *Appl. Phys. Lett.*, vol. 112, p. 153106, 2018.

[269] S. Thongrattanasiri, F. H. L. Koppens, and F. J. Garcı, “Complete Optical Absorption in Periodically Patterned Graphene,” *Phys. Rev. Lett.*, vol. 108, p. 047401, 2012.

[270] P. Q. Liu, F. Valmorra, C. Maissen, and J. Faist, “Electrically tunable graphene anti-dot array terahertz plasmonic crystals exhibiting multi-band resonances,” *Optica*, vol. 2, no. 2, pp. 135–140, 2015.

[271] B. Deng *et al.*, “Coupling-Enhanced Broadband Mid-infrared Light Absorption in Graphene Plasmonic Nanostructures,” *ACS Nano*, vol. 10, pp. 11172–11178, 2016.

[272] T. Low *et al.*, “Tunable optical properties of multilayer black phosphorus thin films,” *Phys. Rev. B*, vol. 90, p. 075434, 2014.

[273] A. Nemilentsau, T. Low, and G. Hanson, “Anisotropic 2D Materials for Tunable Hyperbolic Plasmonics,” *Phys. Rev. Lett.*, vol. 116, p. 066804, 2016.

[274] S. Ali, H. Gangaraj, S. Member, T. Low, A. Nemilentsau, and G. W. Hanson, “Directive Surface Plasmons on Tunable Two-Dimensional Hyperbolic Metasurfaces and Black Phosphorus : Green ’ s Function and Complex Plane Analysis,” *IEEE Trans. Antennas Propag.*, vol. 65, no. 3, pp. 1174–1186, 2017.

[275] Z. Liu and K. Aydin, “Localized Surface Plasmons in Nanostructured Monolayer Black Phosphorus,” *Nano Lett.*, vol. 16, pp. 3457–3462, 2016.

[276] J. Wang and Y. Jiang, “Infrared absorber based on sandwiched two- dimensional black phosphorus metamaterials,” *Opt. Express*, vol. 25, no. 5, pp. 5206–5216, 2017.

[277] J. Wang, Y. Jiang, and Z. Hu, “Dual-band and polarization-independent infrared absorber based on two-dimensional black phosphorus metamaterials,” *Opt. Express*, vol. 25, no. 18, pp. 226–232, 2017.

[278] X. Song, Z. Liu, Y. Xiang, and K. Aydin, “Biaxial hyperbolic metamaterials using anisotropic few-layer black phosphorus,” *Opt. Express*, vol. 26, no. 5, pp. 971–978, 2018.

[279] Y. Zhang *et al.*, “Fabrication and electric-field-dependent transport measurements of mesoscopic graphite devices,” *Appl. Phys. Lett.*, vol. 86, p. 073104, 2005.

[280] K. S. Novoselov *et al.*, “Two-dimensional gas of massless Dirac fermions in graphene,” *Nature*, vol. 438, pp. 197–200, 2005.

[281] J. D. Caldwell *et al.*, “Low-loss , infrared and terahertz nanophotonics using surface phonon polaritons,” *Nanophotonics*, pp. 1–26, 2014.

[282] H. Hajian, A. Ghobadi, S. A. Dereshgi, B. Butun, and E. Ozbay, “Hybrid plasmon-phonon polariton bands in graphene-hexagonal boron nitride metamaterials [Invited],” *J. Opt. Soc. Am. B Opt. Phys.*, vol. 34, no. 7, 2017.

[283] S. Dai *et al.*, “Tunable Phonon Polaritons in Atomically Thin van der Waals Crystals of Boron Nitride,” *Science (80-.).*, vol. 343, pp. 1125–1130, 2014.

[284] H. Hajian, A. Ghobadi, B. Butun, and E. Ozbay, “Tunable , omnidirectional , and nearly perfect resonant absorptions by a graphene-hBN- based hole array metamaterial,” *Opt Express*, vol. 26, no. 13, pp. 16940–16954, 2018.

[285] A. Kumar, T. Low, K. H. Fung, P. Avouris, and N. X. Fang, “Tunable Light − Matter Interaction and the Role of Hyperbolicity in Graphene − hBN System,” *Nano Lett.*, vol. 15, pp. 3172–3180, 2015.

[286] S. Dai *et al.*, “Graphene on hexagonal boron nitride as a tunable hyperbolic metamaterial,” *Nat. Nanotechnol.*, vol. 10, pp. 682–687, 2015.

[287] B. Zhao and Z. M. Zhang, “Resonance perfect absorption by exciting hyperbolic phonon polaritons in 1D hBN gratings,” *Opt. Express*, vol. 25, no. 7, pp. 7791–7796, 2017.

[288] B. Zhao and Z. M. Zhang, “Perfect mid-infrared absorption by hybrid phonon-plasmon polaritons in hBN / metal-grating anisotropic structures,” *Int. J. Heat Mass Transf.*, vol. 106, pp. 1025–1034, 2017.

[289] P. Li, I. Dolado, F. Casanova, L. E. Hueso, and R. Hillenbrand, “Optical Nanoimaging of Hyperbolic Surface Polaritons at the Edges of van der Waals Materials,” *Nano Lett.*, vol. 17, pp. 228–235, 2017.

[290] F. J. Alfaro-Mozaz *et al.*, “Nanoimaging of resonating hyperbolic polaritons in linear boron nitride antennas,” *Nat. Commun.*, vol. 8, p. 15624, 2017.

[291] E. Yoxall *et al.*, “Direct observation of ultraslow hyperbolic polariton propagation with negative phase velocity,” *Nat. Photonics*, vol. 9, pp. 674–679, 2015.

[292] P. Li *et al.*, “Infrared hyperbolic metasurface based on nanostructured van der Waals materials,” *Science (80-.).*, vol. 359, pp. 892–896, 2018.

[293] and F. K. R. Hillenbrand, T. Taubner, “Phonon-enhanced light–matter interaction at the nanometre scale,” *Nature*, vol. 418, pp. 159–162, 2002.

[294] Â. Carminati and K. Joulain, “Coherent emission of light by thermal sources,” *Nature*, vol. 416, pp. 61–64, 2002.

[295] T. Taubner, D. Korobkin, Y. Urzhumov, G. Shvets, and R. Hillenbrand, “Near-Field Microscopy Through a SiC Superlens,” *Science (80-.).*, vol. 313, p. 1595, 2006.

[296] J. A. Schuller, T. Taubner, and M. L. Brongersma, “Optical antenna thermal emitters,” *Nat. Photonics*, vol. 3, no. 11, pp. 658–661, 2009.

[297] D. J. Shelton, D. W. Peters, M. B. Sinclair, I. Brener, L. K. Warne, and L. I. Basilio, “Effect of thin silicon dioxide layers on resonant frequency in infrared metamaterials,” *Opt. Express*, vol. 18, no. 2, pp. 1085–1090, 2010.

[298] S. S. Ng, Z. Hassan, and H. A. Hassan, “Experimental and theoretical studies of surface phonon polariton of AlN thin film,” *Appl. Phys. Lett.*, vol. 90, p. 081902, 2007.

[299] M. Kafesaki, A. A. Basharin, E. N. Economou, and C. M. Soukoulis, “THz metamaterials made of phonon-polariton materials,” *Photonics Nanostructures – Fundam. Appl.*, vol. 12, pp. 376–386, 2014.

[300] A. E. Serebryannikov, E. Ozbay, and S. Nojima, “Asymmetric transmission of terahertz waves using polar dielectrics,” *Opt. Express*, vol. 22, no. 3, pp. 3075–3088, 2014.

[301] K. Feng *et al.*, “Localized surface phonon polariton resonances in polar gallium nitride,” *Appl. Phys. Lett.*, vol. 107, p. 081108, 2015.

[302] A. E. Serebryannikov, S. Nojima, K. B. Alici, and E. Ozbay, “photonic crystals made of polar dielectrics Effect of in-material losses on terahertz absorption , transmission , and reflection in photonic crystals made of polar dielectrics,” *Appl. Phys. Lett.*, vol. 118, p. 133101, 2015.

[303] J. Y. Jung *et al.*, “Infrared broadband metasurface absorber for reducing the thermal mass of a microbolometer,” *Sci. Rep.*, vol. 7, no. 1, pp. 1–8, 2017.

[304] J. Gou, J. Wang, W. Li, H. Tai, D. Gu, and Y. Jiang, “Terahertz absorption characteristics of NiCr film and enhanced absorption by reactive ion etching in a microbolometer focal plane array,” *J. Infrared, Millimeter, Terahertz Waves*, vol. 34, no. 7–8, pp. 431–436, 2013.

[305] H. Hajian, A. Ghobadi, S. A. Dereshgi, B. Butun, and E. Ozbay, “Hybrid plasmon – phonon polariton bands in graphene – hexagonal boron nitride metamaterials [Invited],” *J. Opt. Soc. Am. B*, vol. 34, no. 7, pp. D29–D35, 2017.

[306] J. Wu, L. Jiang, J. Guo, X. Dai, Y. Xiang, and S. Wen, “Tunable perfect absorption at infrared frequencies by a graphene-hBN hyper crystal,” *Opt. Express*, vol. 24, no. 15, pp. 17103–17114, 2016.

[307] M. Farhat, T.-C. Cheng, K. Q. Le, M. M.-C. Cheng, H. Bağcı, and P.-Y. Chen, “Mirror-backed Dark Alumina: A Nearly Perfect Absorber for Thermoelectronics and Thermophotovotaics.,” *Sci. Rep.*, vol. 6, p. 19984, 2016.

[308] D. Jariwala, A. R. Davoyan, J. Wong, and H. A. Atwater, “Van der Waals Materials for Atomically-Thin Photovoltaics: Promise and Outlook,” *ACS Photonics*, vol. 4, pp. 2962–2970, 2017.

[309] P. Li *et al.*, “Hyperbolic phonon-polaritons in boron nitride for near-field optical imaging and focusing,” *Nat. Commun.*, vol. 6, p. 7507, 2015.

[310] Z. Yu *et al.*, “Design of midinfrared photodetectors enhanced by surface plasmons on grating structures Design of midinfrared photodetectors enhanced by surface plasmons,” *Appl. Phys. Lett.*, vol. 89, p. 151116, 2010.

[311] A. Lochbaum, Y. Fedoryshyn, A. Dorodnyy, U. Koch, and C. Hafner, “On-Chip Narrowband Thermal Emitter for Mid-IR Optical Gas Sensing,” *ACS Photonics*, vol. 4, pp. 1371–1380, 2017.

[312] K. T. Lee, C. Ji, D. Banerjee, and L. J. Guo, “Angular- and polarization-independent structural colors based on 1D photonic crystals,” *Laser Photonics Rev.*, vol. 9, no. 3, pp. 354–362, 2015.

[313] V. R. Shrestha, S. S. Lee, E. S. Kim, and D. Y. Choi, “Non-iridescent transmissive structural color filter featuring highly efficient transmission and high excitation purity,” *Sci. Rep.*, vol. 4, p. 4921, 2014.

[314] C. Williams, G. Rughoobur, A. J. Flewitt, and T. D. Wilkinson, “Nanostructured plasmonic metapixels,” *Sci. Rep.*, vol. 7, no. 1, p. 7745, 2017.

[315] G. Kenanakis *et al.*, “Perfect absorbers based on metal–insulator–metal structures in the visible region: a simple approach for practical applications,” *Appl. Phys. A*, vol. 123, no. 1, p. 77, 2017.

[316] “Lumerical Solut. Inc. http://www.lumerical.com/tcad-products/fdtd/.,” in *Lumerical Solut. Inc. http://www.lumerical.com/tcad-products/fdtd/.*

[317] C. Ji, K. Lee, T. Xu, J. Zhou, H. J. Park, and L. J. Guo, “Engineering Light at the Nanoscale : Structural Color Filters and Broadband Perfect Absorbers,” *Adv. Opt. Mater.*, vol. 5, no. 20, p. 1700368, 2017.

[318] A. Ghobadi, H. Hajian, B. Butun, and E. Ozbay, “Strong Light − Matter Interaction in Lithography-free Planar Metamaterial Perfect Absorbers,” *ACS Photonics*, vol. 5, no. 11, pp. 4203–4221, 2018.

[319] C. I. L. Justino, A. C. Duarte, and T. A. P. Rocha-Santos, “Recent progress in biosensors for environmental monitoring: A review,” *Sensors*, vol. 17, no. 12, 2017.

[320] R. Samson, G. R. Navale, and M. S. Dharne, “Biosensors: frontiers in rapid detection of COVID-19,” *3 Biotech*, vol. 10, no. 9, pp. 1–9, 2020.

[321] J. Liu, M. Jalali, S. Mahshid, and S. Wachsmann-Hogiu, “Are plasmonic optical biosensors ready for use in point-of-need applications?,” *Analyst*, vol. 145, no. 2, pp. 364–384, 2020.

[322] C. Chen and J. Wang, “Optical biosensors: An exhaustive and comprehensive review,” *Analyst*, vol. 145, no. 5, pp. 1605–1628, 2020.

[323] J. Homola, “Surface plasmon resonance sensors for detection of chemical and biological species,” *Chem. Rev.*, vol. 108, no. 2, pp. 462–493, 2008.

[324] L. Chen, L. Chan, X. Fu, and W. Lu, “Highly sensitive and selective colorimetric sensing of Hg2+ based on the morphology transition of silver nanoprisms,” *ACS Appl. Mater. Interfaces*, vol. 5, no. 2, pp. 284–290, 2013.

[325] K. Saha, S. S. Agasti, C. Kim, X. Li, and V. M. Rotello, “Gold nanoparticles in chemical and biological sensing,” *Chem. Rev.*, vol. 112, no. 5, pp. 2739–2779, 2012.

[326] P. D. Howes, S. Rana, and M. M. Stevens, “Plasmonic nanomaterials for biodiagnostics,” *Chem. Soc. Rev.*, vol. 43, no. 11, pp. 3835–3853, 2014.

[327] L. Tang and J. Li, “Plasmon-based colorimetric nanosensors for ultrasensitive molecular diagnostics,” *ACS Sensors*, vol. 2, no. 7, pp. 857–875, 2017.

[328] X. Han, K. Liu, and C. Sun, “Plasmonics for biosensing,” *Materials (Basel).*, vol. 12, no. 9, pp. 1–24, 2019.

[329] J. Jiang *et al.*, “Plasmonic nano-arrays for ultrasensitive bio-sensing,” *Nanophotonics*, vol. 7, no. 9, pp. 1517–1531, 2018.

[330] N. Kongsuwan *et al.*, “Quantum Plasmonic Immunoassay Sensing,” *Nano Lett.*, vol. 19, no. 9, pp. 5853–5861, 2019.

[331] D. Radziuk and H. Moehwald, “Prospects for plasmonic hot spots in single molecule SERS towards the chemical imaging of live cells,” *Phys. Chem. Chem. Phys.*, vol. 17, no. 33, pp. 21072–21093, 2015.

[332] H. Wei, S. M. Hossein Abtahi, and P. J. Vikesland, “Plasmonic colorimetric and SERS sensors for environmental analysis,” *Environ. Sci. Nano*, vol. 2, no. 2, pp. 120–135, 2015.

[333] C. Q. Nguyen *et al.*, “Longitudinal Monitoring of Biofilm Formation via Robust Surface-Enhanced Raman Scattering Quantification of Pseudomonas aeruginosa -Produced Metabolites,” *ACS Appl. Mater. Interfaces*, vol. 10, no. 15, pp. 12364–12373, 2018.

[334] W. J. Thrift *et al.*, “Driving Chemical Reactions in Plasmonic Nanogaps with Electrohydrodynamic Flow,” *ACS Nano*, vol. 11, no. 11, pp. 11317–11329, 2017.

[335] D. U. Yildirim *et al.*, “Colorimetric and Near-Absolute Polarization-Insensitive Refractive-Index Sensing in All-Dielectric Guided-Mode Resonance Based Metasurface,” *J. Phys. Chem. C*, vol. 123, no. 31, pp. 19125–19134, 2019.

[336] O. Yavas, M. Svedendahl, P. Dobosz, V. Sanz, and R. Quidant, “On-a-chip Biosensing Based on All-Dielectric Nanoresonators,” *Nano Lett.*, vol. 17, no. 7, pp. 4421–4426, 2017.

[337] N. Bontempi *et al.*, “Highly sensitive biosensors based on all-dielectric nanoresonators,” *Nanoscale*, vol. 9, no. 15, pp. 4972–4980, 2017.

[338] F. Yesilkoy *et al.*, “Ultrasensitive hyperspectral imaging and biodetection enabled by dielectric metasurfaces,” *Nat. Photonics*, vol. 13, no. 6, pp. 390–396, 2019.

[339] A. Ghobadi, H. Hajian, M. Gokbayrak, B. Butun, and E. Ozbay, “Bismuth-based metamaterials: From narrowband reflective color filter to extremely broadband near perfect absorber,” *Nanophotonics*, vol. 8, no. 5, pp. 823–832, 2019.

[340] S. Ayas, G. Bakan, E. Ozgur, K. Celebi, G. Torunoglu, and A. Dana, “Colorimetric detection of ultrathin dielectrics on strong interference coatings,” *Opt. Lett.*, vol. 43, no. 6, pp. 2–5, 2018.

[341] M. Serhatlioglu, S. Ayas, N. Biyikli, A. Dana, and M. E. Solmaz, “Perfectly absorbing ultra thin interference coatings for hydrogen sensing,” *Opt. Lett.*, vol. 41, no. 8, p. 1724, 2016.

[342] M. Elkabbash *et al.*, “Hydrogen Sensing Using Thin-Film Perfect Light Absorber,” *ACS Photonics*, vol. 6, no. 8, pp. 1889–1894, 2019.

[343] A. F. Koenderink, A. Alù, and A. Polman, “Nanophotonics: Shrinking light-based technology,” *Science*, vol. 348, no. 6234. American Association for the Advancement of Science, pp. 516–521, May-2015.

[344] A. F. Koenderink, “Single-Photon Nanoantennas,” *ACS Photonics*, vol. 4, no. 4. American Chemical Society, pp. 710–722, Apr-2017.

[345] A. V. Akimov *et al.*, “Generation of single optical plasmons in metallic nanowires coupled to quantum dots,” *Nature*, vol. 450, no. 7168, pp. 402–406, Nov. 2007.

[346] S. Schietinger, M. Barth, T. Aichele, and O. Benson, “Plasmon-enhanced single photon emission from a nanoassembled metal - Diamond hybrid structure at room temperature,” *Nano Lett.*, vol. 9, no. 4, pp. 1694–1698, Apr. 2009.

[347] V. Giannini, A. I. Fernández-Domínguez, S. C. Heck, and S. A. Maier, “Plasmonic nanoantennas: Fundamentals and their use in controlling the radiative properties of nanoemitters,” *Chemical Reviews*, vol. 111, no. 6. American Chemical Society, pp. 3888–3912, Jun-2011.

[348] L. Novotny and N. Van Hulst, “Antennas for light,” *Nat. Photonics*, vol. 5, no. 2, pp. 83–90, Feb. 2011.

[349] J. A. Schuller, E. S. Barnard, W. Cai, Y. C. Jun, J. S. White, and M. L. Brongersma, “Plasmonics for extreme light concentration and manipulation,” *Nat. Mater.*, vol. 9, no. 3, pp. 193–204, 2010.

[350] T. T. Tran, K. Bray, M. J. Ford, M. Toth, and I. Aharonovich, “Quantum emission from hexagonal boron nitride monolayers,” *Nat. Nanotechnol.*, vol. 11, no. 1, pp. 37–41, 2016.

[351] T. T. Tran, C. Bradac, A. S. Solntsev, M. Toth, and I. Aharonovich, “Suppression of spectral diffusion by anti-Stokes excitation of quantum emitters in hexagonal boron nitride,” *Appl. Phys. Lett.*, vol. 115, no. 7, p. 071102, Aug. 2019.

[352] N. Chejanovsky *et al.*, “Structural Attributes and Photodynamics of Visible Spectrum Quantum Emitters in Hexagonal Boron Nitride,” *Nano Lett.*, vol. 16, no. 11, pp. 7037–7045, Nov. 2016.

[353] T. T. Tran *et al.*, “Robust multicolor single photon emission from point defects in hexagonal boron nitride,” *ACS Nano*, vol. 2017-Janua, pp. 1–2, 2017.

[354] A. L. Exarhos, D. A. Hopper, R. R. Grote, A. Alkauskas, and L. C. Bassett, “Optical Signatures of Quantum Emitters in Suspended Hexagonal Boron Nitride,” *ACS Nano*, vol. 11, no. 3, pp. 3328–3336, Mar. 2017.

[355] T. T. Tran *et al.*, “Quantum Emission from Defects in Single-Crystalline Hexagonal Boron Nitride,” *Phys. Rev. Appl.*, vol. 5, no. 3, p. 034005, Mar. 2016.

[356] I. Aharonovich, D. Englund, and M. Toth, “Solid-state single-photon emitters,” *Nature Photonics*, vol. 10, no. 10. Nature Publishing Group, pp. 631–641, Oct-2016.

[357] S. Choi *et al.*, “Engineering and Localization of Quantum Emitters in Large Hexagonal Boron Nitride Layers,” *ACS Appl. Mater. Interfaces*, vol. 8, no. 43, pp. 29642–29648, Nov. 2016.

[358] N. Mendelson *et al.*, “Engineering and Tuning of Quantum Emitters in Few-Layer Hexagonal Boron Nitride,” *ACS Nano*, vol. 13, no. 3, pp. 3132–3140, Mar. 2019.

[359] N. V. Proscia *et al.*, “Near-deterministic activation of room-temperature quantum emitters in hexagonal boron nitride,” *Optica*, vol. 5, no. 9, p. 1128, Sep. 2018.

[360] T. T. Tran *et al.*, “Deterministic Coupling of Quantum Emitters in 2D Materials to Plasmonic Nanocavity Arrays,” *Nano Lett.*, vol. 17, no. 4, pp. 2634–2639, 2017.

[361] N. V. Proscia, R. J. Collison, C. A. Meriles, and V. M. Menon, “Coupling of deterministically activated quantum emitters in hexagonal boron nitride to plasmonic surface lattice resonances,” *Nanophotonics*, vol. 8, no. 11, pp. 2057–2064, 2019.

[362] M. Nguyen *et al.*, “Nanoassembly of quantum emitters in hexagonal boron nitride and gold nanospheres,” *Nanoscale*, vol. 10, no. 5, pp. 2267–2274, Feb. 2018.

[363] M. S. Tame, K. R. McEnery, Ş. K. Özdemir, J. Lee, S. A. Maier, and M. S. Kim, “Quantum plasmonics,” *Nature Physics*, vol. 9, no. 6. Nature Publishing Group, pp. 329–340, Jun-2013.

[364] Z. Wang *et al.*, “Giant photoluminescence enhancement in tungsten-diselenide-gold plasmonic hybrid structures,” *Nat. Commun.*, vol. 7, p. 11283, 2016.

[365] J. G. Endriz and W. E. Spicer, “SURFACE-PLASMON-ONE-ELECTRON DECAY AND ITS OBSERVATION IN PHOTOEMISSION*,” *Phys. Rev. Lett.*, vol. 22, pp. 64–68, 1969.

[366] R. Fuchs and K. L. Kliewer, “Surface Plasmon in a Semi-Infinite Free-Electron Gas,” *Phys. Rev. B*, vol. 3, pp. 2270–2278, 1971.

[367] S. Mubeen, J. Lee, N. Singh, S. Krämer, G. D. Stucky, and M. Moskovits, “An autonomous photosynthetic device in which all charge carriers derive from surface plasmons,” *Nat. Nanotechnol.*, vol. 8, no. 4, pp. 247–251, 2013.

[368] S. Mukherjee *et al.*, “Hot electrons do the impossible: Plasmon-induced dissociation of H 2 on Au,” *Nano Lett.*, vol. 13, no. 1, pp. 240–247, 2013.

[369] Y. Zhang, Y. R. Zhen, O. Neumann, J. K. Day, P. Nordlander, and N. J. Halas, “Coherent anti-Stokes Raman scattering with single-molecule sensitivity using a plasmonic Fano resonance,” *Nat. Commun.*, vol. 5, pp. 1–7, 2014.

[370] R. Zhang *et al.*, “Chemical mapping of a single molecule by plasmon-enhanced Raman scattering,” *Nature*, vol. 498, no. 7452, pp. 82–86, 2013.

[371] R. M. Ma, S. Ota, Y. Li, S. Yang, and X. Zhang, “Explosives detection in a lasing plasmon nanocavity,” *Nat. Nanotechnol.*, vol. 9, no. 8, pp. 600–604, 2014.

[372] Y. Fang and M. Sun, “Nanoplasmonic waveguides: Towards applications in integrated nanophotonic circuits,” *Light Sci. Appl.*, vol. 4, no. December 2014, pp. 1–11, 2015.

[373] N. I. Zheludev, S. L. Prosvirnin, N. Papasimakis, and V. A. Fedotov, “Lasing spaser,” *Nat. Photonics*, vol. 2, no. 6, pp. 351–354, 2008.

[374] A. Kristensen *et al.*, “Plasmonic colour generation,” *Nat. Rev. Mater.*, vol. 2, no. 1, p. 16088, 2016.

[375] C. Clavero, “Plasmon-induced hot-electron generation at nanoparticle/metal-oxide interfaces for photovoltaic and photocatalytic devices,” *Nat. Photonics*, vol. 8, no. 2, pp. 95–103, 2014.

[376] W. Li and J. G. Valentine, “Harvesting the loss: Surface plasmon-based hot electron photodetection,” *Nanophotonics*, vol. 6, no. 1, pp. 177–191, 2017.

[377] T. G. U. Ghobadi, A. Ghobadi, E. Ozbay, and F. Karadas, “Strategies for Plasmonic Hot-Electron-Driven Photoelectrochemical Water Splitting,” *ChemPhotoChem*, vol. 2, pp. 161–182, 2018.

[378] T. Gong and J. N. Munday, “Materials for hot carrier plasmonics [Invited],” *Opt. Mater. Express*, vol. 5, no. 11, p. 2501, 2015.

[379] S. Ishii, S. L. Shinde, and T. Nagao, “Nonmetallic Materials for Plasmonic Hot Carrier Excitation,” *Adv. Opt. Mater.*, vol. 7, no. 1, pp. 1–13, 2019.

[380] A. O. Govorov, H. Zhang, and Y. K. Gun’Ko, “Theory of photoinjection of hot plasmonic carriers from metal nanostructures into semiconductors and surface molecules,” *J. Phys. Chem. C*, vol. 117, no. 32, pp. 16616–16631, 2013.

[381] A. Manjavacas, P. Nordlander, V. Kulkarni, and J. G. Liu, “Plasmon-Induced Hot Carriers in Metallic Nanoparticles,” *ACS Nano*, vol. 8, no. 8, pp. 7630–7638, 2014.

[382] M. W. Knight, H. Sobhani, P. Nordlander, and N. J. Halas, “Photodetection with active optical antennas,” *Science (80-.).*, vol. 332, no. 6030, pp. 702–704, 2011.

[383] I. Goykhman, B. Desiatov, J. Khurgin, J. Shappir, and U. Levy, “Locally-oxidized silicon surface-plasmon Schottky detector for telecom wavelengths,” *Nano Lett.*, vol. 11, pp. 2219–2224, 2011.

[384] A. Sobhani *et al.*, “Narrowband photodetection in the near-infrared with a plasmon-induced hot electron device,” *Nat. Commun.*, vol. 4, pp. 1643–1646, 2013.

[385] B. Gerislioglu and A. Ahmadivand, “Towards infrared toroidal photodevices : A Review,” *ArXiv:1908.04804*, pp. 1–37, 2019.

[386] N. J. Halas, “Spiers Memorial Lecture: Introductory lecture: Hot-electron science and microscopic processes in plasmonics and catalysis,” *Faraday Discuss.*, vol. 214, pp. 13–33, 2019.

[387] Z. Fang, Z. Liu, Y. Wang, P. M. Ajayan, P. Nordlander, and N. J. Halas, “Graphene-antenna sandwich photodetector,” *Nano Lett.*, vol. 12, no. 7, pp. 3808–3813, 2012.

[388] F. H. L. Koppens, T. Mueller, P. Avouris, A. C. Ferrari, M. S. Vitiello, and M. Polini, “Photodetectors based on graphene, other two-dimensional materials and hybrid systems,” *Nat. Nanotechnol.*, vol. 9, no. 10, pp. 780–793, 2014.

[389] W. Wang, A. Klots, D. Prasai, Y. Yang, K. I. Bolotin, and J. Valentine, “Hot Electron-Based Near-Infrared Photodetection Using Bilayer MoS2,” *Nano Lett.*, vol. 15, no. 11, pp. 7440–7444, 2015.

[390] M. Tanzid *et al.*, “Combining Plasmonic Hot Carrier Generation with Free Carrier Absorption for High-Performance Near-Infrared Silicon-Based Photodetection,” *ACS Photonics*, vol. 5, no. 9, pp. 3472–3477, 2018.

[391] K. Watanabe, D. Menzel, N. Nilius, and H. J. Freund, “Photochemistry on metal nanoparticles,” *Chem. Rev.*, vol. 106, no. 10, pp. 4301–4320, 2006.

[392] Y. Zhang *et al.*, “Surface-Plasmon-Driven Hot Electron Photochemistry,” *Chem. Rev.*, vol. 118, no. 6, pp. 2927–2954, 2018.

[393] J. Lee, S. Mubeen, X. Ji, G. D. Stucky, and M. Moskovits, “Plasmonic photoanodes for solar water splitting with visible light,” *Nano Lett.*, vol. 12, no. 9, pp. 5014–5019, 2012.

[394] M. Murdoch *et al.*, “The effect of gold loading and particle size on photocatalytic

hydrogen production from ethanol over Au/TiO2 nanoparticles," *Nat. Chem.*, vol. 3, no. 6, pp. 489–492, 2011.

[395] P. Christopher, H. Xin, and S. Linic, "Visible-light-enhanced catalytic oxidation reactions on plasmonic silver nanostructures," *Nat. Chem.*, vol. 3, no. 6, pp. 467–472, 2011.

[396] W. H. Hung, M. Aykol, D. Valley, W. Hou, and S. B. Cronin, "Plasmon resonant enhancement of carbon monoxide catalysis," *Nano Lett.*, vol. 10, no. 4, pp. 1314–1318, 2010.

[397] C. Zhang *et al.*, "Al-Pd Nanodisk Heterodimers as Antenna-Reactor Photocatalysts," *Nano Lett.*, vol. 16, no. 10, pp. 6677–6682, 2016.

[398] D. F. Swearer *et al.*, "Heterometallic antenna-reactor complexes for photocatalysis," *PNAS*, vol. 113, no. 32, pp. 8916–8920, 2016.

[399] Y. Zhang *et al.*, "Ultrathin polarization-insensitive wide-angle broadband near-perfect absorber in the visible regime based on few-layer MoS2 films," *Appl. Phys. Lett.*, vol. 111, no. 111109, pp. 1–5, 2017.

[400] D. Jariwala, A. R. Davoyan, G. Tagliabue, M. C. Sherrott, J. Wong, and H. A. Atwater, "Near-Unity Absorption in van der Waals Semiconductors for Ultrathin Optoelectronics," *Nano Lett.*, vol. 16, pp. 5482–5487, 2016.

[401] F. F. Schlich and R. Spolenak, "Strong interference in ultrathin semiconducting layers on a wide variety of substrate materials," *Appl. Phys. Lett.*, vol. 103, no. 213112, pp. 1–4, 2013.

[402] S. S. Mirshafieyan, H. Guo, and J. Guo, "Zeroth Order Fabry-Perot Resonance Enabled Strong Light Absorption in Ultrathin Silicon Films on Different Metals and Its Application for Color Filters," *IEEE Photonics J.*, vol. 8, no. 5, p. 6804912, 2016.

[403] G. Liu *et al.*, "Semiconductor meta-surface based perfect light absorber," *Nanotechnology*, vol. 28, no. 165202, pp. 1–7, 2017.

[404] H. Song *et al.*, "Nanocavity enhancement for ultra-thin film optical absorber," *Adv. Mater.*, vol. 26, no. 17, pp. 2737–2743, 2014.

[405] M. Casalino *et al.*, "Vertically Illuminated, Resonant Cavity Enhanced, Graphene − Silicon Schottky Photodetectors," *ACS Nano*, vol. 11, no. 11, pp. 10955–10963, 2017.

[406] M. Selim and S. Strite, "Resonant cavity enhanced photonic devices," *Appl. Phys. Rev.*, vol. 78, no. 2, pp. 607–639, 1995.

[407] K. C. Balram, R. M. Audet, and D. A. B. Miller, "Nanoscale resonant-cavity-enhanced germanium photodetectors with lithographically defined spectral response for improved performance at telecommunications wavelengths," *Opt. Express*, vol. 21, no. 8, pp. 226–229, 2013.

[408] A. Ghobadi, H. Hajian, A. R. Rashed, B. Butun, and E. Ozbay, "Tuning the metal filling fraction in metal-insulator-metal ultra-broadband perfect absorbers to maximize the absorption bandwidth," *Photonics Res.*, vol. 6, no. 3, pp. 168–176, 2018.

[409] C.-J. Lee, C.-H. Won, J.-H. Lee, S.-H. Hahm, and H. Park, "GaN-Based Ultraviolet Passive Pixel Sensor on Silicon (111) Substrate," *Sensors*, vol. 19, no. 1051, pp. 1–8, 2019.

[410] T. G. Ulusoy, A. Ghobadi, and A. K. Okyay, "Surface engineered angstrom thick ZnO-sheathed TiO_2 nanowires as photoanodes for performance enhanced dye-sensitized solar cells," *J. Mater. Chem. A*, vol. 2, no. 40, pp. 16867–16876, 2014.

[411] A. Ghobadi, T. Gamze, U. Ghobadi, A. K. Okyay, and E. Ozbay, “Emerging Photoluminescence from Defective Vanadium Diselenide Nanosheets,” *Photonic Res.*, vol. 6, no. 4, pp. 244–253, 2018.

[412] T. G. Ulusoy Ghobadi, A. Ghobadi, T. Okyay, K. Topalli, and A. K. Okyay, “Controlling luminescent silicon nanoparticle emission produced by nanosecond pulsed laser ablation: role of interface defect states and crystallinity phase,” *RSC Adv.*, vol. 6, no. 113, pp. 112520–112526, 2016.

[413] W. Hou and S. B. Cronin, “A review of surface plasmon resonance-enhanced photocatalysis,” *Adv. Funct. Mater.*, vol. 23, no. 13, pp. 1612–1619, 2013.

[414] A. M. Brown, R. Sundararaman, P. Narang, W. A. Goddard, and H. A. Atwater, “Nonradiative plasmon decay and hot carrier dynamics: Effects of phonons, surfaces, and geometry,” *ACS Nano*, vol. 10, pp. 957–966, 2016.

[415] G. Liu *et al.*, “Plasmon-dominated photoelectrodes for solar water splitting,” *J. Mater. Chem. A*, vol. 5, no. 9, pp. 4233–4253, 2017.

[416] A. Ghobadi, T. G. Ulusoy Ghobadi, F. Karadas, and E. Ozbay, “Semiconductor Thin Film Based Metasurfaces and Metamaterials for Photovoltaic and Photoelectrochemical Water Splitting Applications,” *Adv. Opt. Mater.*, vol. 7, no. 14, p. 1900028, 2019.

[417] Y. H. Chiu, T. F. M. Chang, C. Y. Chen, M. Sone, and Y. J. Hsu, “Mechanistic insights into photodegradation of organic dyes using heterostructure photocatalysts,” *Catalysts*, vol. 9, no. 5, 2019.

[418] Y. H. Chiu, T. H. Lai, M. Y. Kuo, P. Y. Hsieh, and Y. J. Hsu, “Photoelectrochemical cells for solar hydrogen production: Challenges and opportunities,” *APL Mater.*, vol. 7, no. 8, 2019.

[419] Z. Zhan, J. An, H. Zhang, R. V. Hansen, and L. Zheng, “Three-dimensional plasmonic photoanodes based on Au-embedded TiO2 structures for enhanced visible-light water splitting,” *ACS Appl. Mater. Interfaces*, vol. 6, no. 2, pp. 1139–1144, 2014.

[420] Z. Liu, W. Hou, P. Pavaskar, M. Aykol, and S. B. Cronin, “Plasmon resonant enhancement of photocatalytic water splitting under visible illumination,” *Nano Lett.*, vol. 11, no. 3, pp. 1111–1116, 2011.

[421] Y. C. Pu *et al.*, “Au nanostructure-decorated TiO2 nanowires exhibiting photoactivity across entire UV-visible region for photoelectrochemical water splitting,” *Nano Lett.*, vol. 13, no. 8, pp. 3817–3823, 2013.

[422] P. A. Desario, J. J. Pietron, D. E. Devantier, T. H. Brintlinger, R. M. Stroud, and D. R. Rolison, “Plasmonic enhancement of visible-light water splitting with Au-TiO2 composite aerogels,” *Nanoscale*, vol. 5, no. 17, pp. 8073–8083, 2013.

[423] Z. Zhang, L. Zhang, M. N. Hedhili, H. Zhang, and P. Wang, “Plasmonic gold nanocrystals coupled with photonic crystal seamlessly on TiO2 nanotube photoelectrodes for efficient visible light photoelectrochemical water splitting,” *Nano Lett.*, vol. 13, no. 1, pp. 14–20, 2013.

[424] T. G. Ulusoy Ghobadi, A. Ghobadi, F. Karadas, and E. Ozbay, “Large scale compatible fabrication of gold capped titanium dioxide nanoantennas using a shadowing effect for photoelectrochemical water splitting,” *Int. J. Hydrogen Energy*, vol. 45, no. 3, pp. 1521–1531, 2020.

[425] A. Naldoni *et al.*, “Influence of TiO2 electronic structure and strong metal-support interaction on plasmonic Au photocatalytic oxidations,” *Catal. Sci. Technol.*, vol. 6, no. 9, pp. 3220–3229, 2016.

[426] S. Farsinezhad, H. Sharma, and K. Shankar, “Interfacial band alignment for photocatalytic charge separation in TiO2 nanotube arrays coated with CuPt nanoparticles,” *Phys. Chem. Chem. Phys.*, vol. 17, no. 44, pp. 29723–29733, 2015.

[427] H. C. Ho, K. Chen, T. Nagao, and C. H. Hsueh, “Photocurrent Enhancements of TiO2-Based Nanocomposites with Gold Nanostructures/Reduced Graphene Oxide on Nanobranched Substrate,” *J. Phys. Chem. C*, vol. 123, no. 34, pp. 21103–21113, 2019.

[428] N. Wu, “Plasmonic metal-semiconductor photocatalysts and photoelectrochemical cells: A review,” *Nanoscale*, vol. 10, no. 6, pp. 2679–2696, 2018.

[429] D. Hu, P. Diao, D. Xu, and Q. Wu, “Gold/WO3 nanocomposite photoanodes for plasmonic solar water splitting,” *Nano Res.*, vol. 9, no. 6, pp. 1735–1751, 2016.

[430] P. Subramanyam, B. Meena, G. N. Sinha, M. Deepa, and C. Subrahmanyam, “Decoration of plasmonic Cu nanoparticles on WO3/Bi2S3 QDs heterojunction for enhanced photoelectrochemical water splitting,” *Int. J. Hydrogen Energy*, no. xxxx, pp. 1–10, 2019.

[431] P. Mishra, S. Patnaik, and K. Parida, “An overview of recent progress on noble metal modified magnetic Fe3O4 for photocatalytic pollutant degradation and H2 evolution,” *Catal. Sci. Technol.*, vol. 9, no. 4, pp. 916–941, 2019.

[432] A. J. Cheah *et al.*, “Facile synthesis of a Ag/MoS2 nanocomposite photocatalyst for enhanced visible-light driven hydrogen gas evolution,” *Catal. Sci. Technol.*, vol. 5, no. 8, pp. 4133–4143, 2015.

[433] K. C. Hung, Y. H. Lai, and T. W. Lin, “Enhancement of photocatalytic hydrogen formation under visible illumination by integrating plasmonic Au nanoparticles with a strongly catalytic Ni3S2/carbon nanotube composite,” *Catal. Sci. Technol.*, vol. 6, no. 11, pp. 4020–4026, 2016.

[434] J. M. Li, H. Y. Cheng, Y. H. Chiu, and Y. J. Hsu, “ZnO-Au-SnO2 Z-scheme photoanodes for remarkable photoelectrochemical water splitting,” *Nanoscale*, vol. 8, no. 34, pp. 15720–15729, 2016.

[435] Y. L. Huang *et al.*, “Tunable photoelectrochemical performance of Au/BiFeO3 heterostructure,” *Nanoscale*, vol. 8, no. 34, pp. 15795–15801, 2016.

[436] J. M. Li, C. W. Tsao, M. J. Fang, C. C. Chen, C. W. Liu, and Y. J. Hsu, “TiO2-Au-Cu2O Photocathodes: Au-Mediated Z-Scheme Charge Transfer for Efficient Solar-Driven Photoelectrochemical Reduction,” *ACS Appl. Nano Mater.*, vol. 1, no. 12, pp. 6843–6853, 2018.

[437] Y. H. Chiu *et al.*, “Yolk-shell nanostructures as an emerging photocatalyst paradigm for solar hydrogen generation,” *Nano Energy*, vol. 62, pp. 289–298, 2019.

[438] K. H. Chen *et al.*, “Ag-nanoparticle-decorated SiO 2 nanospheres exhibiting remarkable plasmon-mediated photocatalytic properties,” *J. Phys. Chem. C*, vol. 116, no. 35, pp. 19039–19045, 2012.

[439] M. Valenti, M. P. Jonsson, G. Biskos, A. Schmidt-Ott, and W. A. Smith, “Plasmonic nanoparticle-semiconductor composites for efficient solar water splitting,” *J. Mater. Chem. A*, vol. 4, no. 46, pp. 17891–17912, 2016.

[440] C. N. Van *et al.*, “Heteroepitaxial approach to explore charge dynamics across Au/BiVO4 interface for photoactivity enhancement,” *Nano Energy*, vol. 15, pp. 625–633, 2015.

[441] Z. Zheng, W. Xie, B. Huang, and Y. Dai, “Plasmon-Enhanced Solar Water Splitting on

Metal-Semiconductor Photocatalysts," *Chem. - A Eur. J.*, vol. 24, no. 69, pp. 18322–18333, 2018.

[442] L. Wang, X. Zhou, N. T. Nguyen, and P. Schmuki, "Plasmon-enhanced photoelectrochemical water splitting using au nanoparticles decorated on hematite nanoflake arrays," *ChemSusChem*, vol. 8, no. 4, pp. 618–622, 2015.

[443] H. Bai *et al.*, "Reasonable regulation of kinetics over BiVO4 photoanode by Fe–CoP catalysts for boosting photoelectrochemical water splitting," *Int. J. Hydrogen Energy*, vol. 44, no. 52, pp. 28184–28193, 2019.

[444] S. Kim *et al.*, "Plasmonic gold nanoparticle-decorated BiVO4/ZnO nanowire heterostructure photoanodes for efficient water oxidation," *Catal. Sci. Technol.*, vol. 8, no. 15, pp. 3759–3766, 2018.

[445] B. Chen, Z. Zhang, M. Baek, S. Kim, W. Kim, and K. Yong, "An antenna/spacer/reflector based Au/BiVO4/WO3/Au nanopatterned photoanode for plasmon-enhanced photoelectrochemical water splitting," *Appl. Catal. B Environ.*, vol. 237, no. June, pp. 763–771, 2018.

[446] L. Wang, H. Hu, N. T. Nguyen, Y. Zhang, P. Schmuki, and Y. Bi, "Plasmon-induced hole-depletion layer on hematite nanoflake photoanodes for highly efficient solar water splitting," *Nano Energy*, vol. 35, no. February, pp. 171–178, 2017.

[447] Z. Xu *et al.*, "Interface Manipulation to Improve Plasmon-Coupled Photoelectrochemical Water Splitting on A-Fe2O3 Photoanodes," *ChemSusChem*, vol. 11, no. 1, pp. 237–244, 2018.

[448] G. C. Li, Q. Zhang, S. A. Maier, and D. Lei, "Plasmonic particle-on-film nanocavities: A versatile platform for plasmon-enhanced spectroscopy and photochemistry," *Nanophotonics*, vol. 7, no. 12, pp. 1865–1889, 2018.

[449] Q. Pan *et al.*, "Boosting Charge Separation and Transfer by Plasmon-Enhanced MoS2/BiVO4 p-n Heterojunction Composite for Efficient Photoelectrochemical Water Splitting," *ACS Sustain. Chem. Eng.*, vol. 6, no. 5, pp. 6378–6387, 2018.

[450] S. Y. Jeong *et al.*, "Plasmonic Silver Nanoparticle-Impregnated Nanocomposite BiVO4 Photoanode for Plasmon-Enhanced Photocatalytic Water Splitting," *J. Phys. Chem. C*, vol. 122, no. 13, pp. 7088–7093, 2018.

[451] A. Kushwaha and M. Aslam, "Defect controlled water splitting characteristics of gold nanoparticle functionalized ZnO nanowire films," *RSC Adv.*, vol. 4, no. 40, pp. 20955–20963, 2014.

[452] H. Kim *et al.*, "Plasmonic Au nanoparticles on 8 nm TiO2 nanotubes for enhanced photocatalytic water splitting," *J. Renew. Sustain. Energy*, vol. 5, no. 5, p. 053104, 2013.

[453] D. U. Yildirim *et al.*, "Disordered and Densely Packed ITO Nanorods as an Excellent Lithography-Free Optical Solar Reflector Metasurface," *ACS Photonics*, vol. 6, no. 7, pp. 1812–1822, 2019.

[454] M. C. Soydan *et al.*, "Lithography-Free Random Bismuth Nanostructures for Full Solar Spectrum Harvesting and Mid-Infrared Sensing," *Adv. Opt. Mater.*, vol. n/a, no. n/a, p. 1901203, Dec. 2019.

[455] T. G. Ulusoy Ghobadi *et al.*, "A Robust Precious Metal-free Dye-sensitized Photoanode for Water Oxidation: Nanosecond Long Excited State Lifetime via a Prussian Blue Analogue," *Angew. Chemie - Int. Ed.*, vol. 59, no. 10, pp. 4082–4090, 2020.

[456] T. G. Ulusoy Ghobadi *et al.*, "A Noble-Metal-Free Heterogeneous Photosensitizer-Relay

Catalyst Triad That Catalyzes Water Oxidation under Visible Light," *Angew. Chemie - Int. Ed.*, vol. 57, no. 52, pp. 17173–17177, 2018.

[457] J. Yu and A. Kudo, "Effects of structural variation on the photocatalytic performance of hydrothermally synthesized BiVO4," *Adv. Funct. Mater.*, vol. 16, no. 16, pp. 2163–2169, 2006.

[458] R. L. Frost, D. A. Henry, M. L. Weier, and W. Martens, "Raman spectroscopy of three polymorphs of BiVO4: Clinobisvanite, dreyerite and pucherite, with comparisons to (VO4) 3-bearing minerals: namibite, pottsite and schumacherite," *J. Raman Spectrosc.*, vol. 37, no. 7, pp. 722–732, 2006.

[459] A. K. Bhattacharya, K. K. Mallick, and A. Hartridge, "Phase transition in BiVO4," *Mater. Lett.*, vol. 30, no. 1, pp. 7–13, 1997.

[460] M. Guo *et al.*, "Enhanced photocatalytic activity of S-doped BiVO4 photocatalysts," *RSC Adv.*, vol. 5, no. 72, pp. 58633–58639, 2015.

[461] C. Regmi, D. Dhakal, and S. W. Lee, "Visible-light-induced Ag/BiVO4 semiconductor with enhanced photocatalytic and antibacterial performance," *Nanotechnology*, vol. 29, no. 6, p. 64001, 2018.

[462] S. Bao, Q. Wu, S. Chang, B. Tian, and J. Zhang, "Z-scheme CdS-Au-BiVO4 with enhanced photocatalytic activity for organic contaminant decomposition," *Catal. Sci. Technol.*, vol. 7, no. 1, pp. 124–132, 2017.

[463] J. Qi *et al.*, "Bimetallic phosphide decorated Mo-BiVO4 for significantly improved photoelectrochemical activity and stability," *RSC Adv.*, vol. 9, no. 27, pp. 15629–15634, 2019.

[464] N. Kruse and S. Chenakin, "XPS characterization of Au/TiO2 catalysts: Binding energy assessment and irradiation effects," *Appl. Catal. A Gen.*, vol. 391, no. 1–2, pp. 367–376, 2011.

[465] S. Nayak and K. M. Parida, "Dynamics of Charge-Transfer Behavior in a Plasmon-Induced Quasi-Type-II p-n/n-n Dual Heterojunction in Ag@Ag3PO4/g-C3N4/NiFe LDH Nanocomposites for Photocatalytic Cr(VI) Reduction and Phenol Oxidation," *ACS Omega*, vol. 3, no. 7, pp. 7324–7343, 2018.

[466] F. Su *et al.*, "Dendritic Au/TiO2 nanorod arrays for visible-light driven photoelectrochemical water splitting," *Nanoscale*, vol. 5, no. 19, pp. 9001–9009, 2013.

[467] A. Ghobadi, T. G. U. Ghobadi, F. Karadas, and E. Ozbay, "Angstrom Thick ZnO Passivation Layer to Improve the Photoelectrochemical Water Splitting Performance of a TiO2 Nanowire Photoanode: The Role of Deposition Temperature," *Sci. Rep.*, vol. 8, no. 1, p. 16322, 2018.

[468] X. Zhang *et al.*, "Effect of aspect ratio and surface defects on the photocatalytic activity of ZnO nanorods," *Sci. Rep.*, vol. 4, pp. 4–11, 2014.

[469] J. C. Dupin, D. Gonbeau, P. Vinatier, and A. Levasseur, "Systematic XPS studies of metal oxides, hydroxides and peroxides," *Phys. Chem. Chem. Phys.*, vol. 2, no. 6, pp. 1319–1324, 2000.

[470] S. Wang, P. Chen, Y. Bai, J. H. Yun, G. Liu, and L. Wang, "New BiVO4 Dual Photoanodes with Enriched Oxygen Vacancies for Efficient Solar-Driven Water Splitting," *Adv. Mater.*, vol. 30, no. 20, pp. 1–7, 2018.

[471] F. Liu, L. Lu, P. Xiao, H. He, L. Qiao, and Y. Zhang, "Effect of oxygen vacancies on photocatalytic efficiency of Tio 2 nanotubes aggregation," *Bull. Korean Chem. Soc.*, vol.

33, no. 7, pp. 2255–2259, 2012.

[472] M. Zhang *et al.*, “Carbon-modified BiVO4 microtubes embedded with Ag nanoparticles have high photocatalytic activity under visible light,” *Nanoscale*, vol. 4, no. 23, pp. 7501–7508, 2012.

[473] M. Barzgar Vishlaghi, A. Kahraman, and S. Kaya, “Increasing Charge Separation Property and Water Oxidation Activity of BiVO4 Photoanodes via a Postsynthetic Treatment,” *J. Phys. Chem. C*, vol. 124, no. 2, pp. 1337–1345, 2020.

[474] T. Li, J. He, B. Peña, and C. P. Berlinguette, “Curing BiVO4 Photoanodes with Ultraviolet Light Enhances Photoelectrocatalysis,” *Angew. Chemie - Int. Ed.*, vol. 55, no. 5, pp. 1769–1772, 2016.

[475] H. L. Tan *et al.*, “Enhancing the Photoactivity of Faceted BiVO4 via Annealing in Oxygen-Deficient Condition,” *Part. Part. Syst. Charact.*, vol. 34, no. 4, 2017.

[476] A. Ghobadi, H. I. Yavuz, T. G. Ulusoy, K. C. Icli, M. Ozenbas, and A. K. Okyay, “Enhanced Performance of Nanowire-Based All-TiO<inf>2</inf>Solar Cells using Subnanometer-Thick Atomic Layer Deposited ZnO Embedded Layer,” *Electrochim. Acta*, vol. 157, 2015.

[477] T. Wei *et al.*, “Multi-electric field modulation for photocatalytic oxygen evolution: Enhanced charge separation by coupling oxygen vacancies with faceted heterostructures,” *Nano Energy*, vol. 51, no. March, pp. 764–773, 2018.

[478] Q. T. Liu, D. Y. Liu, J. M. Li, and Y. B. Kuang, “The impact of crystal defects towards oxide semiconductor photoanode for photoelectrochemical water splitting,” *Front. Phys.*, vol. 14, no. 5, 2019.

[479] F. S. Hegner, D. Forrer, J. R. Galán-Mascarós, N. López, and A. Selloni, “Versatile Nature of Oxygen Vacancies in Bismuth Vanadate Bulk and (001) Surface,” *J. Phys. Chem. Lett.*, vol. 10, no. 21, pp. 6672–6678, 2019.

[480] S. Selim *et al.*, “Impact of Oxygen Vacancy Occupancy on Charge Carrier Dynamics in BiVO4 Photoanodes,” *J. Am. Chem. Soc.*, vol. 141, no. 47, pp. 18791–18798, 2019.

[481] Z. Wang *et al.*, “Understanding the Roles of Oxygen Vacancies in Hematite-Based Photoelectrochemical Processes,” *Angew. Chemie - Int. Ed.*, vol. 58, no. 4, pp. 1030–1034, 2019.

[482] W. J. Yin, S. H. Wei, M. M. Al-Jassim, J. Turner, and Y. Yan, “Doping properties of monoclinic BiVO4 studied by first-principles density-functional theory,” *Phys. Rev. B - Condens. Matter Mater. Phys.*, vol. 83, no. 15, pp. 1–11, 2011.

[483] G. Wang *et al.*, “Computational and photoelectrochemical study of hydrogenated bismuth vanadate,” *J. Phys. Chem. C*, vol. 117, no. 21, pp. 10957–10964, 2013.

[484] L. Liu *et al.*, “Gold photosensitized SrTiO3 for visible-light water oxidation induced by Au interband transitions,” *J. Mater. Chem. A*, vol. 2, no. 25, pp. 9875–9882, 2014.

[485] J. K. Cooper *et al.*, “Electronic structure of monoclinic BiVO 4,” *Chem. Mater.*, vol. 26, no. 18, pp. 5365–5373, 2014.

[486] L. Mascaretti *et al.*, “Plasmon-Enhanced Photoelectrochemical Water Splitting for Efficient Renewable Energy Storage,” *Adv. Mater.*, vol. 31, no. 31, pp. 1–23, 2019.

[487] M. Haro, R. Abargues, I. Herraiz-Cardona, J. Martínez-Pastor, and S. Giménez, “Plasmonic versus catalytic effect of gold nanoparticles on mesoporous TiO2 electrodes for water splitting,” *Electrochim. Acta*, vol. 144, pp. 64–70, 2014.

[488] X. An *et al.*, “New Insights into Defect-Mediated Heterostructures for Photoelectrochemical Water Splitting,” *Adv. Energy Mater.*, vol. 6, no. 8, p. 1502268, 2016.

[489] Y. H. Lu *et al.*, “A facile green antisolvent approach to Cu2+-doped ZnO nanocrystals with visible-light-responsive photoactivities,” *Nanoscale*, vol. 6, no. 15, pp. 8796–8803, 2014.

[490] Y. H. Chiu *et al.*, “Fully Depleted Ti-Nb-Ta-Zr-O Nanotubes: Interfacial Charge Dynamics and Solar Hydrogen Production,” *ACS Appl. Mater. Interfaces*, vol. 10, no. 27, pp. 22997–23008, 2018.

[491] F. S. Hegner, I. Herraiz-Cardona, D. Cardenas-Morcoso, N. López, J. R. Galán-Mascarós, and S. Gimenez, “Cobalt Hexacyanoferrate on BiVO4 Photoanodes for Robust Water Splitting,” *ACS Appl. Mater. Interfaces*, vol. 9, no. 43, pp. 37671–37681, 2017.

[492] B. Moss *et al.*, “Unraveling Charge Transfer in CoFe Prussian Blue Modified BiVO 4 Photoanodes,” *ACS Energy Lett.*, pp. 337–342, 2018.

[493] J. H. Kim and J. S. Lee, “Elaborately Modified BiVO4 Photoanodes for Solar Water Splitting,” *Adv. Mater.*, vol. 31, no. 20, pp. 1–35, 2019.

[494] H. S. Han *et al.*, “Boosting the solar water oxidation performance of a BiVO4 photoanode by crystallographic orientation control,” *Energy Environ. Sci.*, vol. 11, no. 5, pp. 1299–1306, 2018.

[495] Y. Pihosh *et al.*, “Photocatalytic generation of hydrogen by core-shell WO3/BiVO4 nanorods with ultimate water splitting efficiency,” *Sci. Rep.*, vol. 5, no. February, pp. 1–2, 2015.

[496] H. Cao, X. Qiu, Y. Liang, M. Zhao, and Q. Zhu, “Sol-gel synthesis and photoluminescence of p-type semiconductor Cr2O3 nanowires,” *Appl. Phys. Lett.*, vol. 88, no. 24, pp. 1–4, 2006.

[497] A. Devilez, X. Zambrana-Puyalto, B. Stout, and N. Bonod, “Mimicking localized surface plasmons with dielectric particles,” *Phys. Rev. B - Condens. Matter Mater. Phys.*, vol. 92, no. 24, pp. 24–28, 2015.

[498] K. Sekizawa, K. Oh-Ishi, and T. Morikawa, “Photoelectrochemical water-splitting over a surface modified p-type Cr2O3 photocathode,” *Dalt. Trans.*, vol. 49, no. 3, pp. 659–666, 2020.

[499] K. Park and A. M. Kolpak, “Optimal methodology for explicit solvation prediction of band edges of transition metal oxide photocatalysts,” *Commun. Chem.*, vol. 2, no. 79, pp. 1–10, 2019.